Interaction of Graphene and Templated Cluster Arrays with CO, H_2, and O_2

Inaugural-Dissertation

zur
Erlangung des Doktorgrades
der Mathematisch-Naturwissenschaftlichen Fakultät
der Universität zu Köln

vorgelegt von

Dipl.-Phys. Timm Gerber

aus Offenbach am Main

Abstract

Interaction of graphene and templated cluster arrays with CO, H_2 and O_2 was studied by means of scanning tunneling microscopy (STM) and X-ray photoemission spectroscopy (XPS). The experimental data was complemented by ab initio density functional theory (DFT) calculations. As a prerequisite for studies of gas interaction, the binding mechanism of the clusters to graphene, as well as the growth and structure of Pt clusters, was investigated in detail.

The formation of cluster lattices on graphene on Ir(111) has been explained by graphene rehybridization. This DFT picture was tested by comparing calculated core level spectra to XPS measurements. For pristine graphene, DFT and XPS agree on a 140 meV modulation of the C 1s core level shifts (CLS), which correlates with the height modulation of the graphene layer above the Ir surface. With Pt clusters adsorbed, measured Pt 4f CLS of the adsorbed clusters also support the calculations. The modulation of the C 1s spectrum is strengthened with clusters adsorbed, and C atoms both under and in the vicinity of the Pt clusters are experimentally distinguished as a broad shoulder of positive C 1s CLS. The calculations suggest that the sp^2 to sp^3 rehybridization of graphene displaces the involved C atoms closer to the Ir(111) surface, implying chemical bond formation. The signature of these bonds in the Ir 4f spectrum was identified.

The growth of Pt clusters, their structure, and their interaction with the graphene layer was studied as a function of Pt coverage. STM measurements revealed that once Pt clusters are two-layered, their further growth is restricted to two dimensions. The threshold for sintering was found to be at 0.75 ML Pt, so that the upper size limit for Pt clusters arranged in a lattice is 65 atoms. The cluster-graphene interaction, as well as the graphene-Ir surface interaction was investigated with spectra of the C 1s and the Ir 4f regions, respectively. It was found that the related components, namely the C 1s shoulder and the Ir interface component, agree regarding their relative intensities. Combining these results, schematic representations of the clusters and

their binding geometry with the graphene layer was derived.

Pt cluster arrays were tested for their stability with respect to CO gas exposure. Cluster stability and adsorption-induced processes were analyzed as a function of cluster size. Small clusters containing fewer than 10 atoms are unstable upon CO adsorption. They sinter through Smoluchowski ripening – cluster diffusion and coalescence – rather than the frequently reported Ostwald ripening mediated by metal-adsorbate complexes. Larger clusters remain immobile upon CO adsorption, but become more three-dimensional. An implication of the CO-induced cluster mobility is the sensitivity of Pt cluster array growth to the CO background pressure. In order to generalize the results, the study was extended to the adsorption of other gases (H_2, O_2) on Pt clusters, as well as to the adsorption of CO on other metal clusters (Ir, Au).

The temperature, time and flake-size-dependent intercalation phases of oxygen underneath graphene on Ir(111) formed upon exposure to molecular oxygen were studied. Through the applied pressure of molecular oxygen, the atomic oxygen created on the bare Ir terraces is driven underneath the graphene flakes. The importance of substrate steps and of the unbinding of graphene flake edges from the substrate for the intercalation is identified. Using CO titration to selectively remove oxygen from the bare Ir terraces, the energetics of intercalation were uncovered. Cluster decoration techniques were used as an efficient tool to visualize intercalation processes in real space. To give an outlook, the study was extended to the intercalation of hydrogen.

Intercalation of graphene often leads doping of graphene. Comparing XPS and angular resolved photoemission spectroscopy (ARPES) data for various systems, it was found that the Dirac point and the C 1s core level shift in the same direction. These shifts can be described in terms of a rigid band model and the C 1s core level shift may be used to estimate the level of doping. It was found that graphene/Ir(111) is p-doped by H and O intercalation, whereas it is n-doped after Eu intercalation. The graphene layer is also doped by Pt and Ir clusters on top of it. The smallest clusters n-dope the graphene by charge spill-out. The largest Pt coverage results in a slight p-doping of the graphene layer. When Pt clusters coalesce upon CO exposure, the level of doping is reduced.

Contents

1 Introduction

Graphene is a single atomic layer of graphite and thereby represents a two dimensional allotrope of carbon. We witness a continuously growing research interest in graphene [1, 2] which is both due to its rich physics and to a variety of possible applications.

A few examples for the former are the ambipolar electric field effect [3], charge carriers which mimic relativistic particles [4], and the unusual half-integer quantum Hall effect [5].

The envisioned applications for graphene-based devices are numerous including high-frequency transistors [6], efficient gas sensors [7], and transparent electrodes for displays [8] or solar cells [9].

One way to fabricate graphene sheets is epitaxial growth on metal surfaces by decomposition of hydrocarbons [10, 11]. In this way, graphene layers of exceptional quality can be synthesized on the Ir(111) surface [12, 13]. The success of this method stimulated attempts to transfer these layers from the substrate onto the desired device [14]. Furthermore, there is a unique characteristic of the graphene on Ir(111) system, which will be exploited in this thesis: Graphene/Ir(111) is a versatile template for the growth of cluster lattices of unmatched quality [15].

Clusters represent an interesting state of matter. Their structure as well as their electronic, chemical and magnetic properties change with size, and often differ from that of the solid [16, 17]. Prominent examples are ferromagnetic clusters of Rh (which is paramagnetic as bulk material) [18], and the unusual reactivity of nanometer-sized Au particles [19].

Moreover, most heterogeneous, industrial catalysts are made of metal particles, a few nanometer in size, dispersed on a porous support [20]. In these systems, the size distribution of the particles is rather broad and their morphology as well as the surface or interface structure is often not known. These variables may not concern an industrial chemist who desires a more efficient catalyst, but who is not disinclined

1

to improve it by trial and error. However, it is the surface scientist's aspiration to unfold all effects that are involved. Therefore, studies are often performed on supported *model catalysts* [21]. This term refers to metal clusters prepared on clean surfaces under ultra high vacuum (UHV) conditions which can be examined by surface science techniques. Following this approach, impressive results have been achieved [22]. To name one example, the catalytic activity for the oxidation of carbon monoxide depends on the exact number of atoms constituting Pt clusters supported on MgO [23].

The reactivity of supported clusters is often influenced by their support. For Au clusters supported by oxide surfaces, it was shown that this influence can be at least two-fold: Firstly, by changing the cluster's electronic structure through charge transfer from the substrate [24], and secondly, by the presence of reactive sites at the cluster oxide interface [25, 26]. Therefore, substrates that do not alter the cluster's properties are desired, and that are inert with respect to molecules involved in the reaction under consideration. These requirements are fulfilled by graphite and thus, clusters on this support have been extensively studied [21].

As a consequence of the exploding interest in graphene, studies of graphene supported clusters appeared. Some examples are the growth of clusters on solution-based graphene nanosheets [27–29], on few-layer [30] or single layer [31] graphene films cleaved from graphite crystals, as well as on graphene grown on Si-terminated SiC surfaces [32–34]. In some cases, these graphene-supported clusters show interesting properties as enhanced electrocatalytic activity for methanol oxidation [27], or enhanced CO tolerance in the hydrogen oxidation reaction in polymer electrolyte fuel cells [28], compared to clusters supported on graphite. The common feature of all mentioned examples is that – as on graphite surfaces – the clusters are randomly dispersed.

For this reason, graphene supported on lattice-mismatched metal substrates is an even more interesting support for clusters. Moiré patterns, which arise from the lattice mismatch between graphene and the metal surface, act as a template for self-assembly of metal clusters. The templating effect of the moiré allows the creation of cluster lattices of equally sized and spaced clusters each residing in an identical environment. Examples include Pt and other metal clusters on the graphene/Ru(0001) moiré [35–42], Ni clusters on the graphene/Rh(111) moiré [43], and a variety of metallic and bimetallic clusters on graphene/Ir(111) [15, 44–46]. Nevertheless,

the perfection of the cluster lattice strongly depends on the metal supporting the graphene film [11]. Of the above mentioned, graphene/Ir(111) induces cluster arrays whose exceptional order and narrow size distribution makes them particularly attractive laboratories for fundamental studies of nanocatalysis.

A prerequisite to such studies is the investigation of the stability of the cluster/support system at elevated temperatures and in the presence of reactants, i.e. under reaction conditions. Sintering, a decrease in particle number and corresponding increase of particle size, is a process that deactivates catalysts [47–49].

Case studies of various cluster support systems have shed light on sintering mechanisms at the atomic level. An important one [50–60] is that under reaction conditions, clusters are disrupted and form mobile metal-reactant species which cause mass transport and associated ripening. For example, disruption into single adatoms and formation of mobile surface carbonyls [such as $Ir(CO)_2$] have been observed for clusters of Pt [50, 51], Ir [52–54] and Rh [55] grown on TiO_2. Decay of epitaxial Cu islands on Cu(111) and Co islands on Au(111) was found to be promoted in the presence of S through formation of mobile Cu_3S_3 and Co_3S_4 complexes [56–58]. The lower sublimation energy of Pd-H compared to Pd was proposed to explain the Ostwald ripening of Pd clusters deposited on SiO_2 in a hydrogen atmosphere [59]. Lastly, mobile Pt_xO_y species were identified as the source of Oswald ripening of Pt-particles on Al_2O_3 [60]. But for clusters supported by graphene, no such studies are available yet.

In the case of graphene supported clusters, exposure to gases may not only influence the particles, but have an impact on the graphene itself. A common interaction of gases with graphene is intercalation. This refers to the insertion of an adlayer of molecules or atoms between the graphene sheet and its substrate. Examples are H and O intercalation under graphene/SiC [61–63] and O intercalation under Graphene/Ru(0001) [64–66].

Beyond gaseous intercalants, graphene can also be intercalated by metals [67–73] or by semiconductors [74–77]. The strong interest in intercalation of graphene stems from unique possibilities to decouple [61–63, 67–69, 74–76] or even electrically insulate [77] it from the substrate, or to enable its exfoliation [14]. Furthermore, the graphene may be doped by the intercalated layer [72, 78], which increases the number of charge carriers and thus enhances the conductivity of graphene. Finally, even the properties of the intercalated film may be altered due to the presence of

graphene on top of it [73]. In order to control intercalation precisely, a detailed understanding of the process is desired.

In the following, the content of this thesis is outlined. Before these results are presented, the necessary background information is given (Chapter 2), and the experimental methods are described (Chapter 3). The outstanding ability of graphene on Ir(111) to act as a template for cluster lattices originates from a particular binding mechanism of the clusters to the graphene [79, 80]. In Chapter 4, the existing theoretical model of this binding mechanism is experimentally substantiated. Chapter 5 studies the growth mode of Pt clusters, their structure and their interaction with the graphene layer in detail. In Chapter 6, the stability of clusters on graphene/Ir(111) in the presence of gases is investigated, with a focus on the impact of CO onto Pt clusters. The intercalation of graphene by oxygen, and the impact of this process on clusters on the graphene is described in Chapter 7. Finally, Chapter 8 describes how the graphene layer is doped by the presence of intercalated oxygen underneath, or by cluster lattices on top of it, and how this doping is manifested in the C 1s core level shift.

2 Background

2.1 Graphene/Ir(111)

Graphene (abbreviated Gr) can be grown in exceptional quality by decomposition of hydrocarbons on the Ir(111) surface [44, 81, 82]. Several growth recipes yielding either graphene flakes [81] or a closed monolayer of graphene are available [13, 83]. Details on these processes are given in Section 3.4.
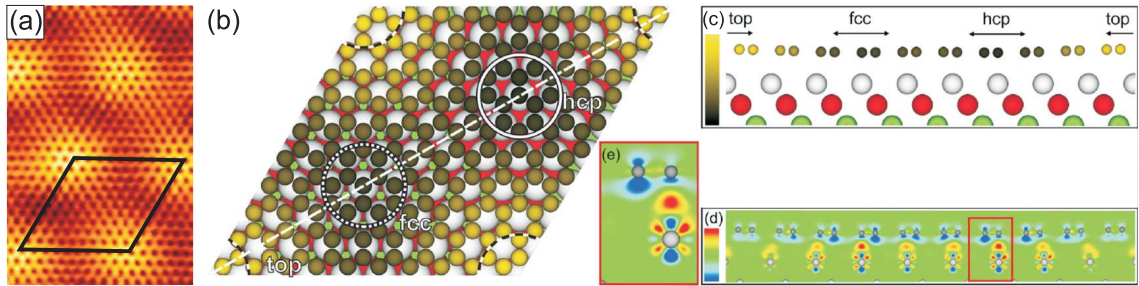
Figure 2.1 (a) STM topograph (59 Å × 84 Å, U = 1 V, I = 7 nA) of the graphene moiré on Ir(111). Reproduction from [84]. (b) Top view and (c) side view [cut along the dashed line in (b)] of the relaxed structure of graphene/Ir(111) obtained by DFT including vdW interactions. Regions of high-symmetry stacking (fcc, hcp, top) are marked by circles (b) or arrows (c) and (d). The color scale in (b) and (c) ranges from $h = 3.20$ Å (dark) to $h = 3.65$ Å (yellow). (d) Charge transfer upon adsorption. The color scale ranges from $\Delta\rho$ = -0.0138e Å^{-3} (blue) over light green to $\Delta\rho = +0.013e$ Å^{-3} (red). A negative value indicates loss of electron density. (e) Magnified view of red box in (d). Reproduction from [85].

Figure 2.1 (a) shows a scanning tunneling microscopy (STM) topograph of Gr/Ir(111). The small black dots represent the centers of the carbon rings. The long range pattern is a moiré superstructure resulting from the mismatch of the graphene and the iridium lattice. The moiré is an incommensurate pattern of (10.32 x 10.32) carbon rings over (9.32 x 9.32) Ir atoms [86].

Figure 2.1 (b) shows a ball model of the moiré unit cell as calculated by nonlocal van

der Waals density functional theory (vdW-DFT) [85]. For the calculations the unit cell was approximated by (10 x 10) unit cells of graphene on (9 x 9) cells of Ir(111). Three high-symmetry domains exist which are labeled top, hcp, and fcc according to the location of the center of the carbon rings with respect to the Ir(111) surface. The largest distance of graphene over the Ir surface of 3.62 Å is found in the top regions. These regions correspond to the bright areas in Fig. 2.1 (a). The hcp and fcc regions have a height of 3.27 Å and 3.29 Å, respectively. The average height of 3.41 Å corresponds very well with the experimental value of 3.38 Å as determined by the x-ray standing waves (XSW) method. This distance is similar to the interlayer distance in graphite of 3.36 Å, and indicates that bonding of graphene to the Ir surface is weak. The height corrugation is due to the fact that bonding is not uniform over the unit cell. While the average height gives the impression of pure vdW interaction, a small charge transfer from graphene towards the substrate takes place in the hcp and fcc regions (Fig. 2.1 (d) and (e)). In conclusion, the binding with an average binding energy of E_b = -50 meV/C consists of weak chemical bonds in the hcp and fcc areas and chemical repulsion in the top areas.

As we will see, this binding energy inhomogeneity of graphene on Ir(111) influences the process of intercalation (Chapter 7).

The on average weak bonding of the graphene layer to the Ir(111) surface is manifested in X-ray photoemission spectroscopy (XPS). Figure 2.2 shows C 1s spectra of graphite and graphene on various lattice-mismatched metal substrates by Preobrajenski and coworkers [87]. The spectrum for graphene/Ir(111) can be reproduced with a single peak which is only slightly broader than the one of graphite. This indicates that the bond strength as well as the corrugation are comparable in both systems. We will see in Chapter 4 that the width of the C 1s peak for graphene/Ir(111) correlates with the height distribution of the carbon atoms in the graphene unit cell.

Contrarily, the strong chemisorption of graphene on both Rh(111) [88] and Ru(0001) [89] leads to a splitting of the C 1s peak into a weakly bonding and a strongly bonding component.

Before we turn to the description of cluster growth on graphene/Ir(111), we will briefly discuss the morphology of graphene islands on graphene/Ir(111). The model shown in Figure 2.1 was obtained assuming that the graphene layer is of infinite extension. Lacovig et al. [90] investigated how the morphology of small graphene islands differs from that of an infinite layer. Using a combination of DFT and
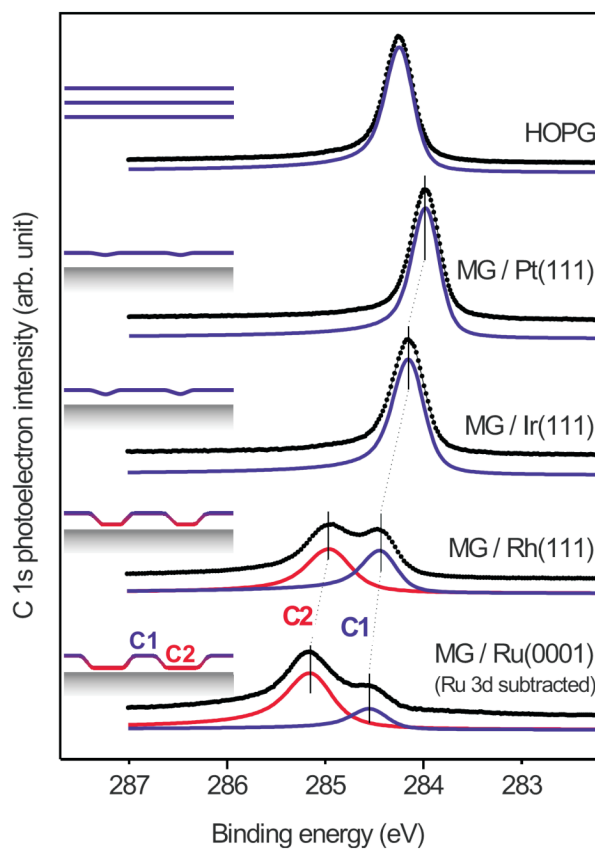
Figure 2.2 C 1s photoelectron spectra from graphene (here referred to as MG i.e. monolayer graphite) adsorbed on several lattice-mismatched metal surfaces. The photon energy is 400 eV. The C 1s photoelectron spectrum from highly oriented pyrolytic graphite (HOPG) is shown for comparison. Schematics illustrate the resulting graphene morphology. Reproduction from [87].

XPS they found that graphene nanoislands adopt a particular domelike shape and that their edges are strongly bound to the substrate (see Figure 2.3). According to these results, one would expect that large graphene islands (consisting of several moiré unit cells) are predominantly bound to the substrate by the carbon atoms at their edges, too. This view is, however, challenged by findings of Li and coworkers [91], who reported that the edges of graphene islands on Ir(111) are terminated by hydrogen. The issue of how the dangling carbon bonds at the edges of graphene islands are saturated is the subject of ongoing research and not settled so far. As the termination of the graphene edges is likely to influence the pathway of intercalation, this will become important in Chapter 7.
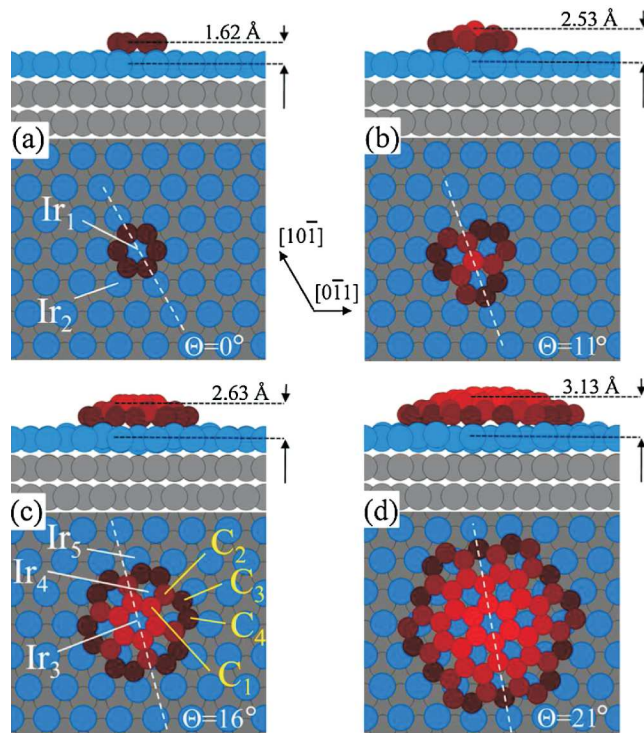
Figure 2.3 Calculated structural models of the carbon clusters formed by n honeycomb rings with (a) $n = 1$, (b) $n = 3$, (c) $n = 7$, and (d) $n = 19$. Ir_i and C_j represent different local configurations of Ir and C atoms respectively. The distance of the central C atoms from the Ir substrate as well as the orientation of the cluster with respect to the $[10\bar{1}]$ direction of Ir(111) is indicated. Reproduction from [90].

2.2 Clusters on Graphene/Ir(111)
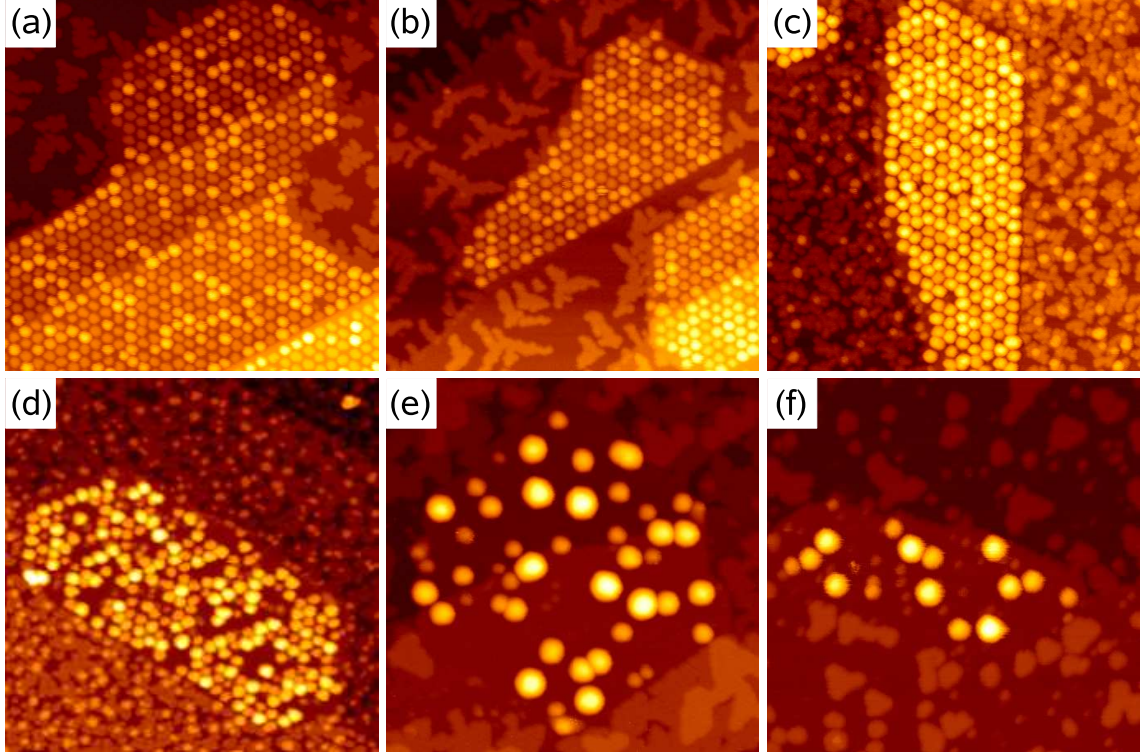
Figure 2.4 STM topographs of Ir(111) with graphene flakes after deposition of an amount Θ of various metals at 300 K. (a) $\Theta = 0.20$ ML Ir, average cluster size $s_{av} = 17$ atoms; (b) $\Theta = 0.25$ ML Pt, $s_{av} = 22$ atoms; (c) $\Theta = 0.44$ ML W, $s_{av} = 38$ atoms; (d) $\Theta = 0.53$ ML Re, $s_{av} = 60$ atoms; (e) $\Theta = 0.77$ ML Fe, s av $= 420$ atoms; (f) $\Theta = 0.25$ ML Au, $s_{av} = 100$ atoms. Note that $s_{av} = \Theta \cdot A_m/n$ with $A_m = 87$ atoms the number of Ir atoms in the moiré unit cell and n the fraction of moiré cells occupied by a cluster (the filling factor). Image size 700 Å x 700 Å. Reproduction from [15].

Figure 2.4 shows STM topographs after room temperature deposition of the indicated metals on Ir(111) partly covered with graphene flakes. Ir, Pt, and W deposition yields cluster lattices close to perfection. At least Ir and Pt cluster grow epitaxially with the (111) cluster planes parallel to the substrate surface. The $\langle 1\bar{1}0 \rangle$ cluster directions are parallel to the $\langle 1\bar{1}0 \rangle$ directions of the Ir substrate and the $\langle 1\bar{1}20 \rangle$ directions of graphene [15]. The epitaxy of Ir clusters on the graphene moiré is supported by a DFT-based model of cluster binding [79, 80].
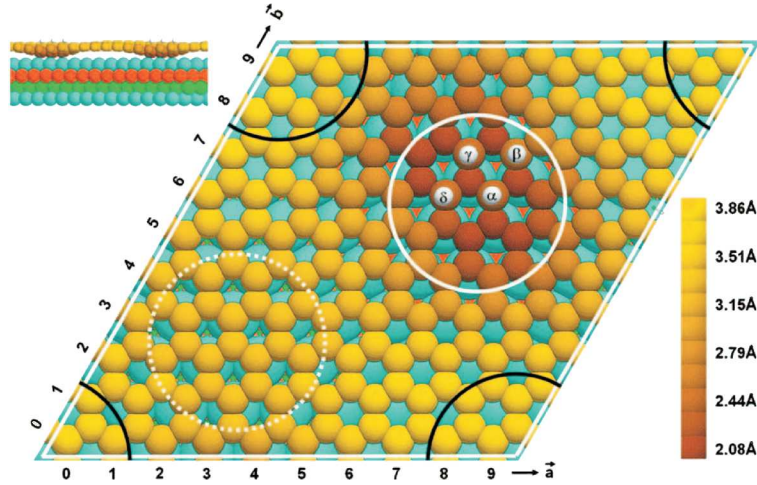
Figure 2.5 Ball model of DFT optimized structure for a four-atom flat Ir cluster on graphene/Ir(111). The unit cell was approximated as (10 x 10) unit cells of graphene on (9 x 9) cells of Ir(111). First, second, and third substrate layer Ir atoms are colored blue, red, and green, respectively. Solid and dotted white circles mark the hcp and fcc regions of the moiré. Top regions, which are delimited by the black arcs, are located in the cell corners. The radii of the Ir adatoms are reduced to reveal the substrate. Local island-induced depression of the graphene layer is shown by the C atom coloring; the color scale denotes heights measured from the Ir surface. Upper left: Side view. Reproduction from [79].

Figure 2.5 shows a ball model of an Ir_4 cluster adsorbed on graphene on Ir(111). The energetically preferred adsorption site is the hcp region. There the graphene rehybridizes from its characteristic sp^2 configuration to diamond-like sp^3. The graphene layer moves closer to the substrate, with every second carbon atom binding (with its fourth bond normal to the average carbon plane) to Ir surface atoms, while the other half of the carbon atoms bind to the cluster. DFT calculations predict that chemical bonds form between carbon and metal atoms which significantly reduce the local C atom height above the Ir surface from $\sim3.4\,\text{Å}$ to $\sim2.1\,\text{Å}$. We note that a similar DFT based scenario has been proposed for patterned adsorption of hydrogen on the graphene/Ir(111) moiré [92, 93].

The favored adsorption site of the Ir cluster (i.e. the hcp region) nicely agrees with the experimental data [86]. Except for this agreement on the adsorption site there has been no experimental proof for this rehybridization model so far. This will be the topic of Chapter 4.

This DFT calculation was performed for an Ir cluster. However, the STM data in Fig. 2.4 shows that there is a huge difference in cluster growth for different metals.

We conclude that whether the graphene rehybridizes or not strongly depends on the deposited metal. In previous work [15] we considered three factors as heuristic guidelines for the suitability of a material to form a cluster lattice:

(i) A large cohesive strength of the material as an indicator for the ability to form strong chemical bonds.

(ii) A large extension of a localized valence orbital of the deposit material allowing it to efficiently interact with the graphene p-bond and thus to initiate rehybridization to diamond-like carbon underneath the cluster.

(iii) A certain match of the graphene unit cell repeat distance on Ir(111) (2.452 Å [86]) and the nearest-neighbor distance of the deposit material to fit the first layer cluster atoms atop every second C atom.

Table 2.1 compares these parameters for the studied materials. The guidelines agree with the ability of Ir, Pt, and W to form a cluster lattice and with the inability of Au, Fe, and Ni to do so. The poor quality of the Re cluster lattice is, however, not expected.

Zhou and coworkers [37] suggested that a single parameter suffices to predict cluster lattice formation, namely the (M-C) metal-carbon bond strength. This parameter can be estimated by the M-C bond dissociation energy which is also listed in Table 2.1. Ir, Pt and W show indeed large dissociation energies, whereas the values for Au, Fe, and Ni are much lower. No dissociation energy for Re is indicated as it is well established that rhenium does not form stoichiometric carbides at ambient pressure [94]. Thus, the M-C bond strength is actually a good parameter to predict cluster lattice formation on graphene/Ir(111).

Material	a	r_{d}	E_{coh}	D(M-C)
	(Å)	(pm)	(eV)	(eV)
Ir	2.715	70.8	6.94	6.54 [95]
W	2.741	77.6	8.90	6.14 [95]
Re	2.761	73.9	8.03	no Re-C
Pt	2.775	65.9	5.84	6.32 [95]
Au	2.884	63.5	3.81	2.73 - 3.51 [96]
Fe	2.483	38.2	4.28	3.76 [97]
Ni	2.492	33.8	4.44	4.05 [98]

Table 2.1 Nearest-neighbor distance a, valence d-orbital radius r_{d}, cohesive energy E_{coh} as well as metal-carbon bond dissociation energy D(M-C) of the tested materials for cluster lattice formation on the graphene moiré on Ir(111). Partly reproduced from [15].

In the following we will compare cluster lattices grown on graphene/Ir(111) to such grown on graphene/Ru(0001). As pointed out in the introduction to this thesis, graphene supported by Ir(111) is the template which fabricates cluster lattices of the highest quality in terms of order and size distribution. Its outstanding performance as a template is compared in Figure 2.6 (a) to cluster formation on graphene/Ru(0001) [Fig. 2.6 (b)]. Both samples were prepared by room temperature deposition of $\sim 0.3\,\mathrm{ML}$ Pt onto the graphene pre-covered metal surface. Fig. 2.6 (a) shows an almost defect free lattice of equally sized clusters. In (b) the moiré pattern of graphene/Ru(0001) is still visible (green pattern) as it is only partially occupied by Pt clusters, which even show a broader size distribution compared to (a).
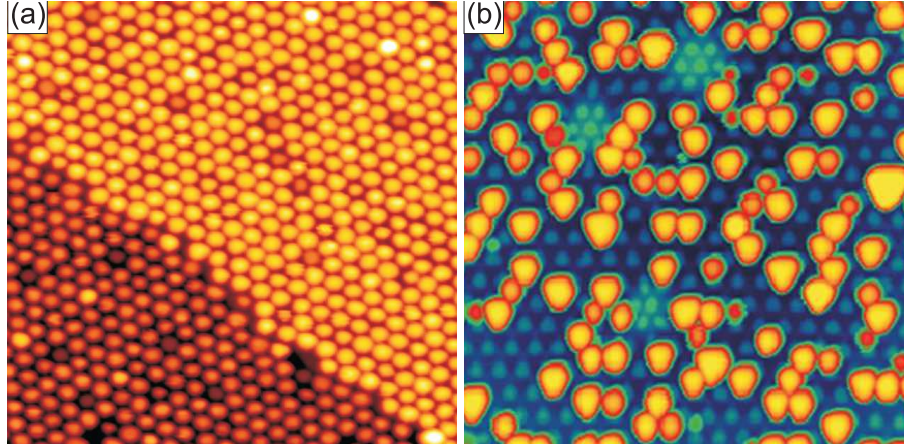
Figure 2.6 STM topographs after room temperature deposition of (a) $\Theta = 0.30$ ML Pt on graphene/Ir(111) and (b) $\Theta = 0.36$ ML Pt on graphene/Ru(0001). Image size 540 Å x 540 Å. (b) is reproduced from [35].

We note that well arranged Pt cluster arrays on graphene/Ru(0001) can be obtained by Pt deposition at a growth temperature $T = 140$ - 180 K [36]. Apparently, also for the graphene/Ru(0001) system, there is a preferred nucleation site in the moiré unit cell. However, the variation of adsorption strength over different sites is not as pronounced as for the graphene/Ir(111) system. In the following we will briefly discuss differences in cluster binding on both substrates.

As described above, the clusters grown on graphene/Ir(111) are stabilized in the hcp regions of the moiré unit cell by graphene rehybridization. Underneath the clusters the graphene moves from its vdW bond distance of $\sim$3.4 Å into chemical contact with the substrate. In contrast, the bonding between a pristine graphene layer and the Ru(0001) is strong and cannot be caused by vdW bonds [87, 89] (compare Fig. 2.2). Cluster formation on graphene/Ru(0001) can therefore not be analogous to the case of graphene/Ir(111). Indeed, Sutter at al. [38] showed that Ru clusters adsorb in the low-lying regions of graphene/Ru(0001) where they lift the graphene layer from 1.8 Å to 2.1 Å with respect to the Ru surface (Figure 2.7). This binding mechanism is fundamentally different from the one for clusters on graphene/Ir(111) suggested by Feibelman. The latter is apparently a unique property of the graphene on Ir(111) system and most likely the reason for the unmatched quality of the cluster lattices on this template.
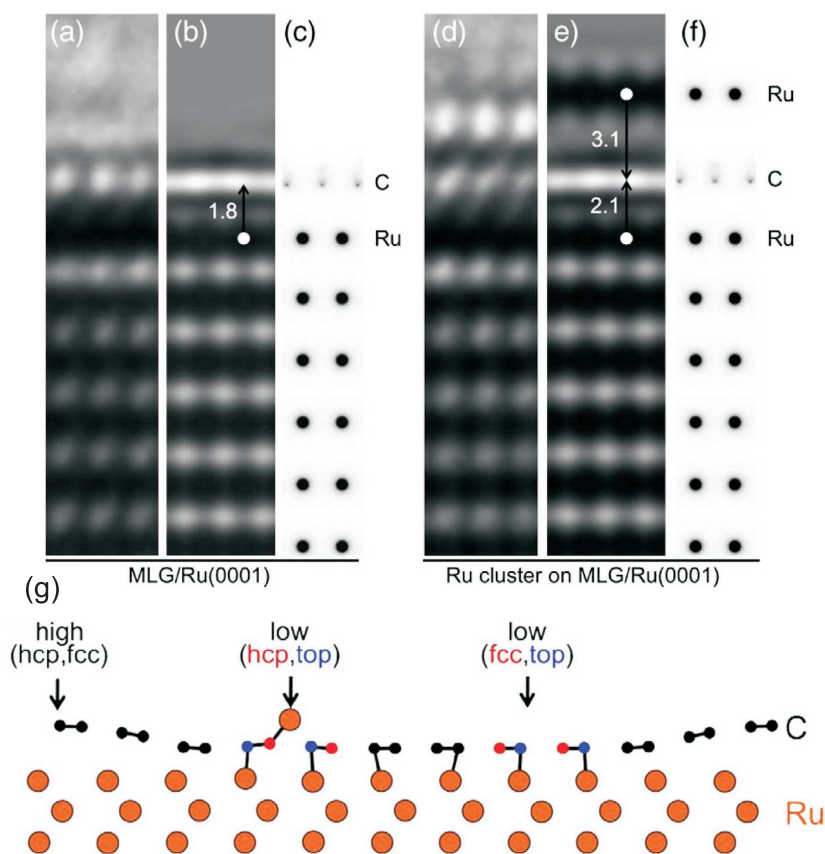
Figure 2.7 Graphene-Ru separation and its modification by an adsorbed Ru cluster. (a) High-resolution TEM image of monolayer graphene on Ru(0001). (b) Calculated high-resolution TEM image for a graphene-Ru separation of 1.8 Å, giving the best match between experiment and simulation. (c) Projected potential, showing the positions of C and Ru atoms for the simulation in (b). (d) High-resolution TEM image of a Ru cluster graphene/Ru(0001). (e) Calculated high-resolution TEM image for a separation of 2.1 Å between graphene and the Ru substrate, with the Ru cluster 3.1 Å above the graphene layer, giving the best match between experiment and simulation. (f) Projected potential showing the positions of C and Ru atoms for the simulation in (e). (g) Side view along the diagonal of the graphene/Ru(0001) moiré cell of single Ru adatom adsorption in the fcc low region, computed by DFT. Reproduced from [38].
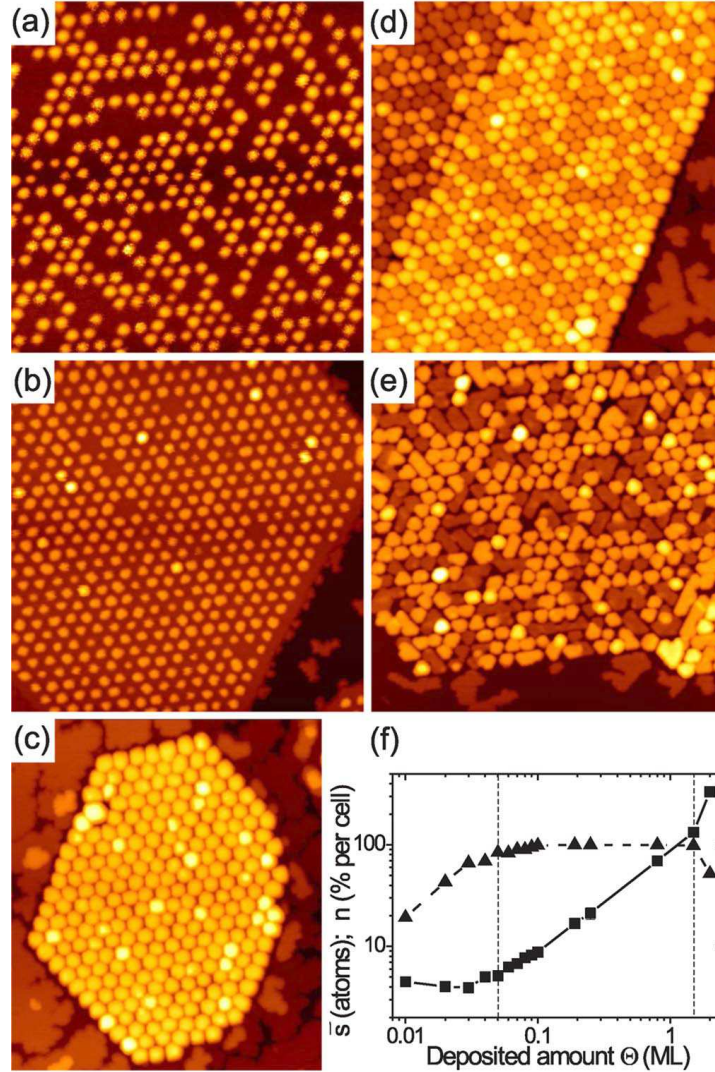
Figure 2.8 Cluster lattices on graphene flakes. The Ir coverages are (a) 0.03, (b) 0.10, (c) 0.80, (d) 1.50, and (e) 2.00 ML, respectively. Image height is always 550 Å. (f) Filling factor n in percent clusters per moiré cell (triangles) and average cluster size in atoms $\bar{s}$ versus deposited amount Θ in ML (squares). Lines are to guide the eye. Reproduction from [44].

We conclude this section by taking a closer look at the growth mode of Ir cluster on graphene/Ir(111). Figure 2.8 (a)-(e) shows a series of STM topographs obtained by increasing the deposited amount of Ir. The quantitative analysis [Fig. 2.8 (f)] of the filling factor n and the average cluster size in atoms s_{av} versus deposited amount Θ suggests three regimes of cluster growth [44]: (i) A nucleation regime where n increases nearly linearly with Θ, while s_{av} is almost independent of the coverage. (ii) A growth regime for coverages $0.05 \leq \Theta \leq 1.50\,\mathrm{ML}$ in which n is

close or equal to one while the average cluster size increases proportionally with Θ. (iii) A coalescence or sintering regime for $\Theta \geq 1.50\,\mathrm{ML}$, which is characterized by the onset of cluster coalescence. The coalesced clusters extend typically over several unit cells [Fig. 2.8 (e)]. In Chapter 5 a similar study for Pt clusters is presented and their growth mode will be compared to that of Ir clusters.

2.3 Electronic Structure of Graphene
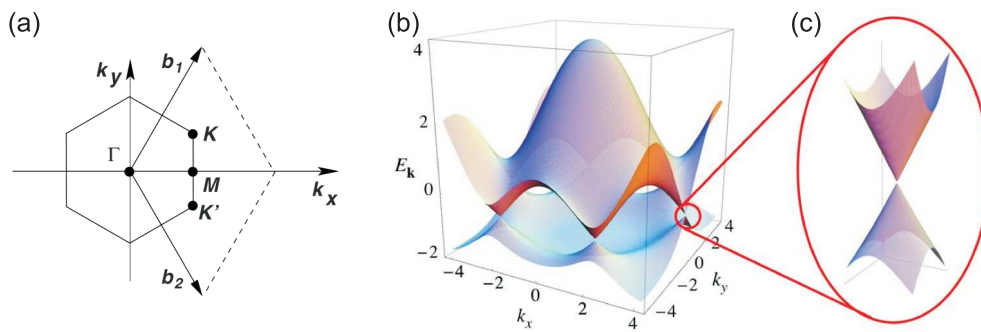
Figure 2.9 (a) Brillouin zone of the graphene honeycomb lattice. The Dirac cones are located at the K and K' points (called Dirac points). (b) Electronic dispersion of graphene (π and $\pi^\star$ bands) over the first Brillouin zone. The bands cross the Fermi level at the Dirac points. (c) Zoom of the energy bands close to one of the Dirac points. Reproduced from [99].

Graphene shows a number of interesting electronic effects [1, 3], which originate from its particular band structure (Fig. 2.9). The occupied π and the unoccupied $\pi^\star$ touch at the Fermi level E_F at the K-points of the first Brillouin zone, where the density of states vanishes [99] - the so-called Dirac points. As the density of states is zero at E_F, graphene is often referred to as a 'zero gap semiconductor'. The bands show a linear dispersion around E_F so that the dispersion resembles two touching cones. They are referred to as Dirac cones and are the electronic signature feature of graphene.

The electronic structure of graphene may, however, be altered by its support. This is especially the case for graphene supported by metal surfaces like Ni(111) or Ru(0001). On both surfaces, graphene is bound strongly through hybridization of graphene states with those of the metal [100, 101]. On the contrary, weakly interacting metal surfaces like Pt(111) or Ir(111) show but a little disturbance of the

electronic structure of graphene [102, 103]. For the case of graphene/Ir(111) this is demonstrated in Fig. 2.10.
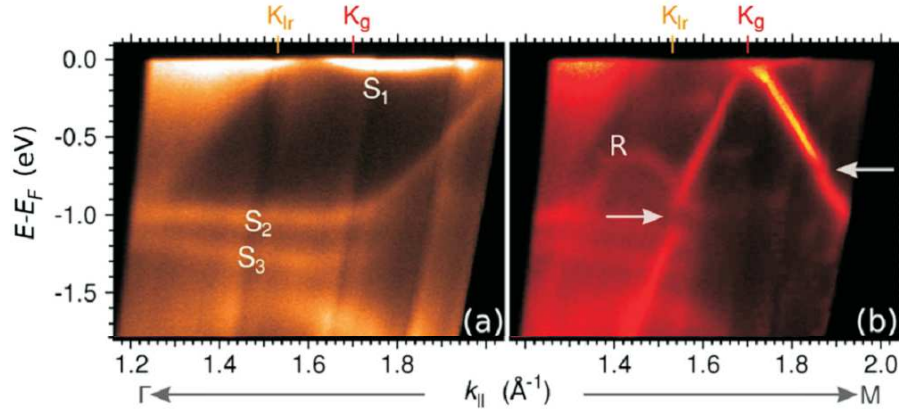
Figure 2.10 (a) ARPES spectrum of clean Ir(111) taken $\phi = 0.5° \pm 0.1°$ off the Γ-M direction. The positions of the K points of iridium and graphene are marked as K_{Ir} and K_g, respectively. S_1 - S_3 are surface states. (b) ARPES spectrum of Ir(111) covered by graphene along the same azimuth as in (a). Horizontal arrows denote minigaps in the primary Dirac cone. A visible replica band is labeled R. Reproduced from [103].

Figure 2.10 (a) shows the ARPES spectrum of the clean Ir(111) surface [103]. Conveniently, the region where the graphene Dirac cone is expected, coincides with an energy gap in the Ir(111) electronic structure. Only three weakly dispersing surface states exist in this gap. Figure 2.10 (b) shows the spectrum for graphene on Ir(111). The linear branches of the Dirac cone are clearly visible. We can identify only faint substrate related features in the spectrum: A marginal doping of 0.10 eV, additional replica bands and the opening of minigaps. The latter two can be attributed to the periodic potential created by the moiré superstructure. Altogether, the band structure strongly resembles that of freestanding graphene (compare Fig. 2.9 (c)) and shows no sign of hybridization with substrate electronic bands.

The doping of graphene and how it can be tailored by intercalation will be the topic of Chapter 8. Another way to engineer the band structure of graphene/Ir(111) will be described in the following: Rusponi et al. [104] demonstrated that an Ir cluster lattice grown on the moiré pattern (as described in Section 2.2) gives rise to the opening of a band gap E_{gap}. Figure 2.11 (a) shows an ARPES spectrum of graphene on Ir(111). This spectrum is similar to the one in Fig. 2.10 (b) except for the fact that a small band gap is observed at the Fermi level. As the unoccupied $\pi^{\star}$ band is not visible in ARPES, only a lower limit of E_{gap} can be estimated:

$E_{\text{gap,gr/Ir(111)}} \geq 70\,\text{meV}$. Figure. 2.11 (b) shows that the cluster lattice noticeably enlarges the graphene band gap to $E_{\text{gap,Ir/gr/Ir(111)}} \geq 200\,\text{meV}$. The question whether a band gap occurs upon cluster growth is, however, beyond the scope of this thesis. Nevertheless, Rusponi et al. report that upon cluster deposition the C 1s core and the top of the σ band both shift $30\,\text{meV}$ to higher binding energies (Fig. 2.12). They conclude that the Dirac point E_{D} also shifts by the same amount - a fact that will be considered in Section 8.2.

A feature, which Rusponi and coworkers do not address, is that the C 1s peak becomes asymmetric after cluster growth [red curve in Fig. 2.12 (a)]. A shoulder develops at the high binding energy side of the peak. The origin of this shoulder will be discussed in detail in Chapter 4.
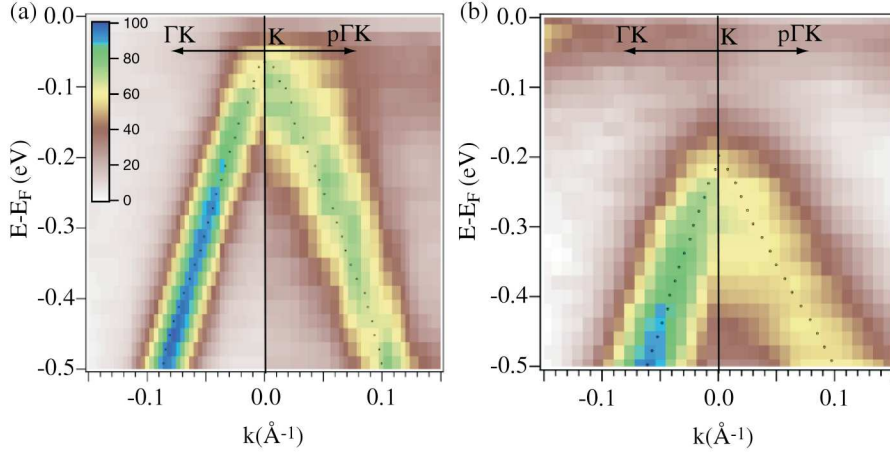
Figure 2.11 (a) ARPES intensity of the π band of graphene on Ir(111), close to the K point, along the pΓK and the ΓK directions. A linear dispersion is observed along both directions. (b) ARPES intensity of the π band of graphene after growth of Ir clusters on graphene/Ir(111) along the same two directions. In (a) and (b) the dots represent the result of fitting the momentum distribution curves (MDCs). Note that the enlargement of the band gap is accompanied by an enhancement of the anisotropy in the energy dispersion of the Dirac cones. Reproduced from [104].
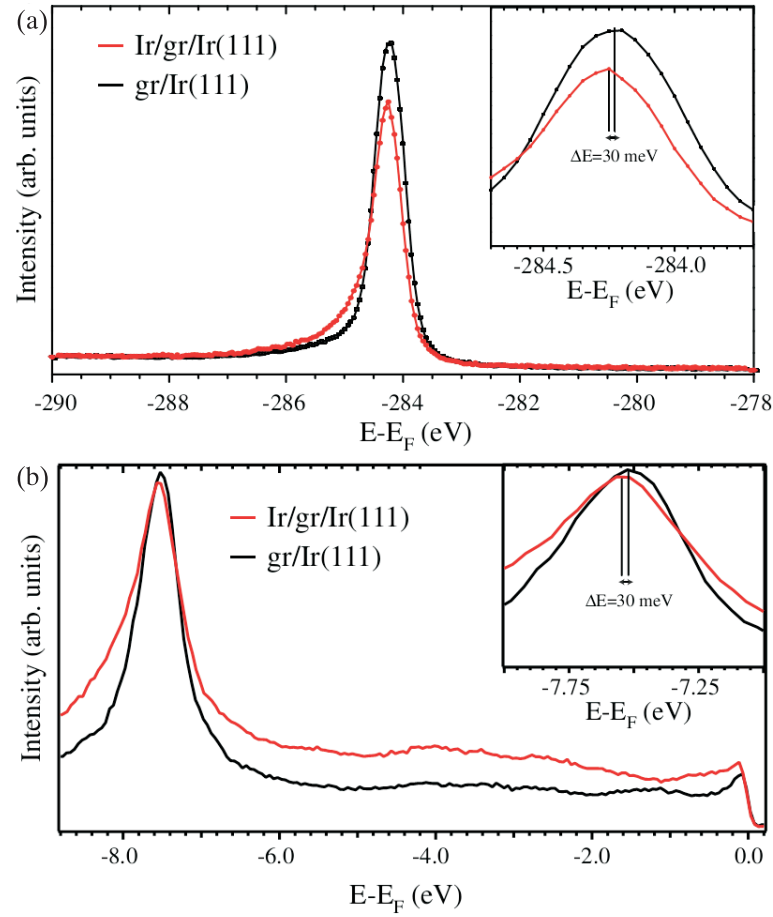
Figure 2.12 (a) C 1s core levels for clean graphene (black) and after deposition of 0.15 ± 0.05 ML Ir (red). Inset: Zoom on the C 1s peak showing a shift of 30 ± 30 meV after cluster growth (normal emission, photon energy 450 eV). (b) Energy distribution spectra corresponding to the situations in (a). Measured at the M point of the second Brillouin zone. Inset: The top of the σ-band shifts by 30 ± 30 meV after cluster growth. Reproduced from [104].

2.4 Intercalation of Graphene
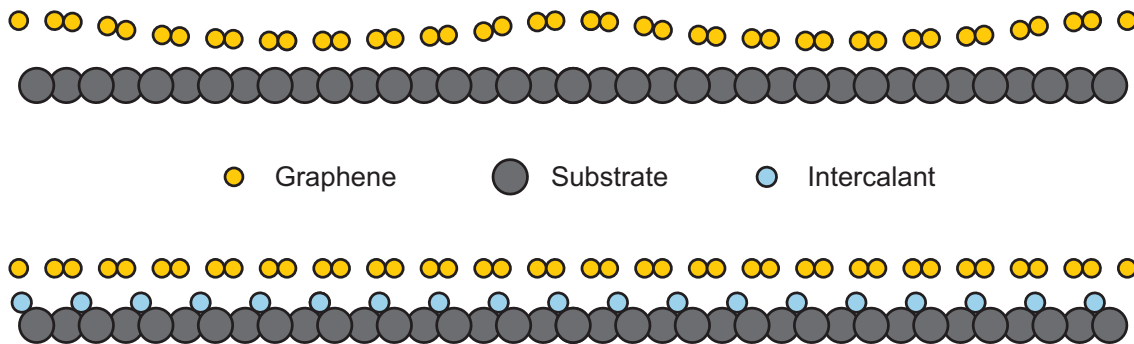
Figure 2.13 Schematic illustration of graphene before (upper panel) and after intercalation of atoms between the graphene layer and the substrate (lower panel). Redrawn from [66].

Intercalation refers to the insertion of molecules, atoms or ions into a chemical compound. Well known examples are graphite intercalation compounds [105, 106]. In the case of graphene, intercalation signifies the insertion of an adlayer of molecules or atoms between the graphene sheet and its substrate. This is sketched in Figure 2.13: The upper panel shows a pristine graphene layer on a substrate. The graphene is slightly corrugated which is typical for graphene supported by a weakly interacting, lattice-mismatched transition metal surface (compare Fig. 2.2). The lower panel shows a layer of adatoms intercalated between the graphene sheet and the substrate. As depicted, the adlayer may reduce the corrugation of the graphene layer by passivating the substrate surface. This is one example how intercalation might affect the properties of graphene. Another example will be given in the following.
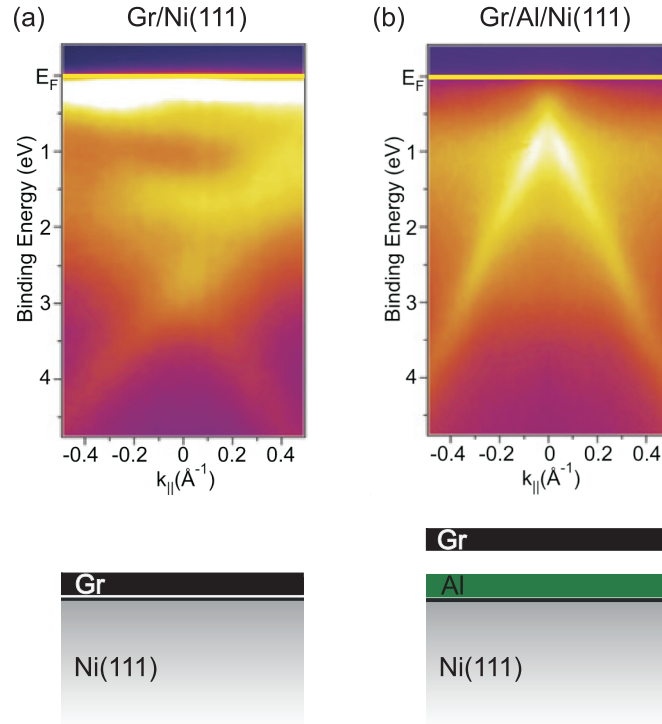
Figure 2.14 ARPES intensity maps around the K-point along the direction perpendicular to Γ-K in the Brillouin zone for (a) graphene/Ni(111) and (b) the graphene/Al/Ni(111) system. Reproduced from [72].

Figure 2.14 (a) shows the ARPES spectrum of graphene on Ni(111). We note that the original electronic structure of the free-standing graphene is strongly perturbed. The Dirac cone is heavily distorted and graphene-derived electronic bands are shifted to higher binding energies [72]. The reason is that graphene is strongly bound to the Ni surface by hybridization of the graphene π and Ni 3d states [100, 107, 108].

Figure 2.14 (b) shows the ARPES spectrum after intercalation of Al between the graphene layer and the Ni surface. Contrary to the graphene/Ni(111) system, the Dirac cone is fully restored. After Al intercalation, the electronic structure resembles that of the free-standing graphene. Evidently, the Al layer effectively decouples graphene from the substrate. In addition, electron doping shifts the Dirac point below E_F by 0.64 eV. Doping of graphene by an intercalated layer will be discussed in detail in Chapter 8.
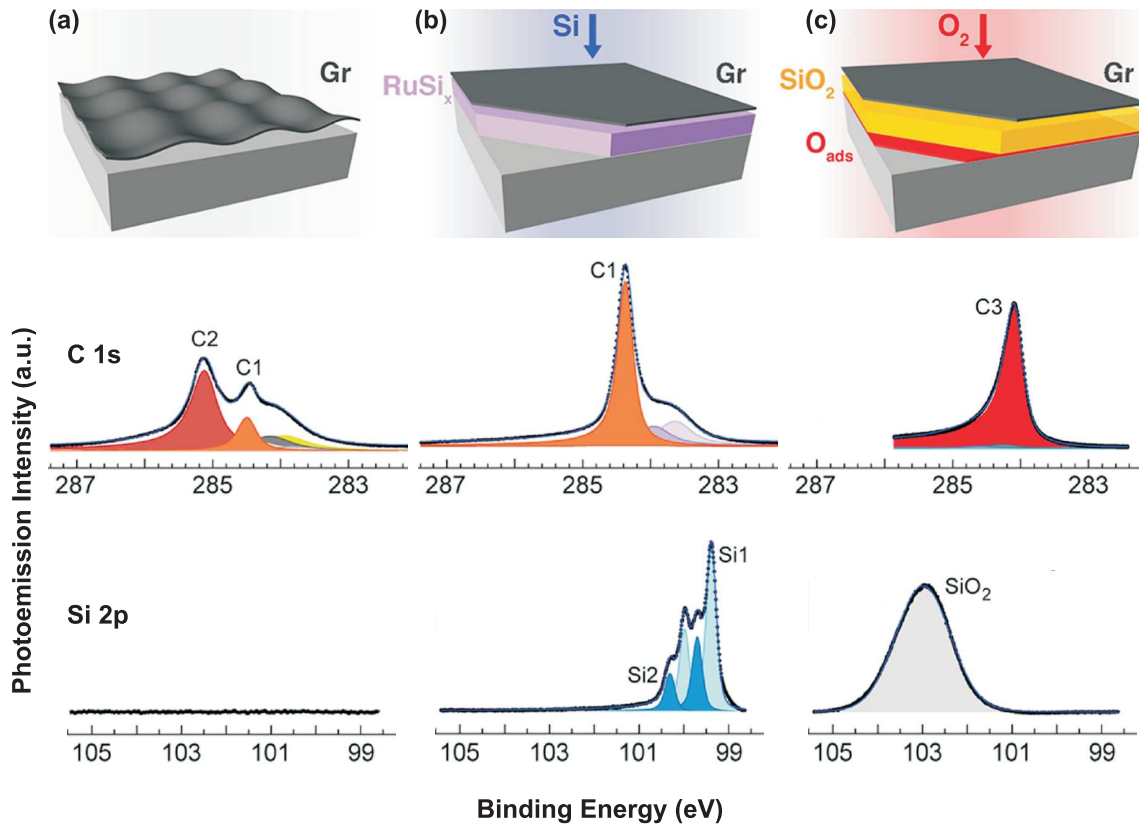
Figure 2.15 Step of SiO$_2$ synthesis under epitaxial graphene on Ru(0001). (a) Formation of epitaxial graphene. (b) Exposure of the sample surface to silicon at 720 K. Si intercalates and forms a silicide with the metal substrate. (c) The metal silicide is oxidized to form an insulating SiO$_2$ layer that separates the metal from graphene ($p_{O_2} = 4 \times 10^{-3}$ mbar, 640 K). The metal surface is terminated with chemisorbed oxygen. Schematics (upper panel) as well as photoemsision spectra from C 1s (middle panel) and Si 2p (lower panel) respectively. Note that the C 1s signal and that of the Ru 3d$_{3/2}$ (minor components in the middle panel) overlap energetically in the XPS spectrum. Modified from [77].

For most technological applications, graphene has to be supported by an insulator, or at least by an insulating layer. In order to use graphene grown on metals, one possibility is to transfer it from the metal onto the desired substrate. In this context, it was shown that Br$_2$ intercalation is an efficient method to enable exfoliation of graphene grown on Ir(111) by adhesive tape [14].

Going one step further, Lizzit et al. developed a process which inserts an insulating layer in between the graphene sheet and the metal substrate [77]. It is sketched in Figure 2.15.

Firstly, graphene is prepared by epitaxial growth on Ru(0001) [Fig. 2.15 (a)]. The corresponding C 1s core level spectrum shows two peaks (C1 and C2). C2 arises

from the strong coupling of the graphene layer to the Ru surface in parts of the moiré unit cell, C1 is the signature of the nonbonding parts (compare Fig. 2.2 and [87]). The additional minor components visible in the spectrum stem from photoemisson of the Ru $3d_{3/2}$ orbital.

Secondly, the sample surface is exposed to silicon under conditions allowing for intercalation [Fig. 2.15 (b)]. The C 1s spectrum consists of a single narrow component C1 signaling that the graphene layer is decoupled from the substrate. The Si 2p core level (as well as the Ru 3d, data not shown) indicates that the intercalated Si forms a silicide with the metal substrate. The total quantity of intercalated silicon atoms can be varied by adjusting the Si exposure time. Here, the Si coverage corresponds to approximately 4 ML.

Finally, the sample is exposed to O_2: Oxygen intercalates below graphene and progressively oxidizes the silicide layer. During oxidation, the silicide is consumed and the Si 2p spectrum transforms into a broad peak at higher binding energy, indicative of Si in SiO_2 environment. The C 1s intensity converts into the single and narrow C3 peak, interpreted as graphene supported by SiO_2. The C 1s spectrum does not show any sign of oxidation, demonstrating that graphene does not react with O_2 during intercalation, and that during decomposition of the Ru silicide, oxygen binds exclusively to silicon.

By using a nanoscale four-point probe technique, the authors showed that the SiO_2 layer provides electrical insulation of the graphene layer against the metallic substrate.

3 Experimental

All experiments described in this thesis were performed in ultra-high vacuum (UHV). They were carried out in two laboratories: STM was done in the TuMA III laboratory at the Institute of Physics II at the University of Cologne, XPS was done at beamline I311 of the MAX IV Laboratory in Lund, Sweden. Both setups will be described briefly. An introduction to XPS is given and illustrated by several examples.

3.1 The Ultra High Vacuum System TuMA III
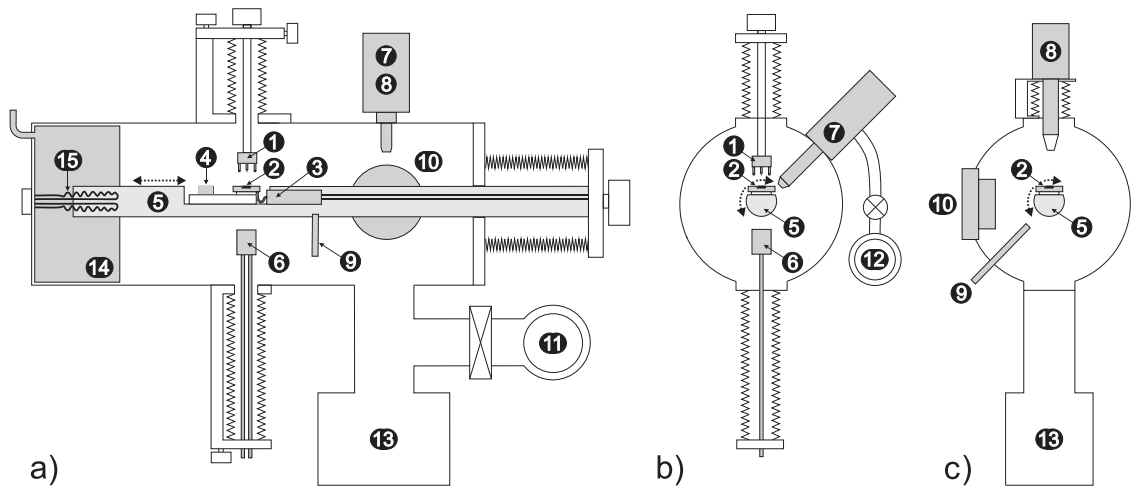
Figure 3.1 TuMA III UHV system [(a) sideview, (b),(c) cross sections]: (1) STM, (2) Ir(111) sample, (3) cooling reservoir, (4) Faraday cup, (5) manipulator, (6) e-beam evaporator, (7) ion gun, (8) mass spectrometer with Feulner cup, (9) gas doser, (10) LEED system, (11,12) turbo molecular pumps, (13) ion pump, (14) cooling trap, (15) titanium sublimation pump. Figure modified from [109].

STM experiments were performed in the variable temperature UHV system TuMA III with a base pressure of 10^{-10} mbar. Several pumps are used to achieve such a

low pressure: a turbomolecular pump, an ion pump, a titanium sublimation pump and a cooling trap on the main chamber as well as a second turbomolecular pump for differential pumping of the ion gun.

The STM is of the beetle type with a homemade Ir tip. Low-energy electron diffraction (LEED) is used to determine the surface structure. The quadrupole mass spectrometer (QMS) is used for residual gas analysis as well as for thermal desorption spectroscopy (TDS). To obtain a better signal to noise ratio in TDS measurements the mass spectrometer was equipped with a Feulner cup in the course of this thesis [110].

The sample used for all experiments is an iridium single crystal with an (111) oriented surface which is mounted in a transferable and rotatable manipulator. The sample is heated by electron bombardment and is connected to a liquid nitrogen reservoir for cooling. The temperature is measured by a type K (chromel-alumel) thermocouple.

The system is further equipped with an ion gun including a mass filter and a Faraday cup to measure the ion flux. A gas dosing system is used to dose gases in proximity of the sample. The local pressure in front of the gas doser was estimated to be 80 times higher than the measured pressure of the chamber [109]. Pressures given in this thesis always refer to the local pressure at the sample.

A four pocket e-beam evaporator (EGN4, Oxford Applied Research) is used for metal deposition. It is equipped with a manual shutter and an ion flux monitor. Typical evaporation rates are e.g. 3×10^{-2} ML/s for the evaporation of Pt. During evaporation the pressure remained in the low 10^{-10} mbar range.

A detailed description of the TuMA III setup is given in [111].

3.2 Principle of X-ray Photoemission Spectroscopy

In this section the principle of XPS and its experimental realization is described. Peculiarities of the beamline I311 are described in the next section.
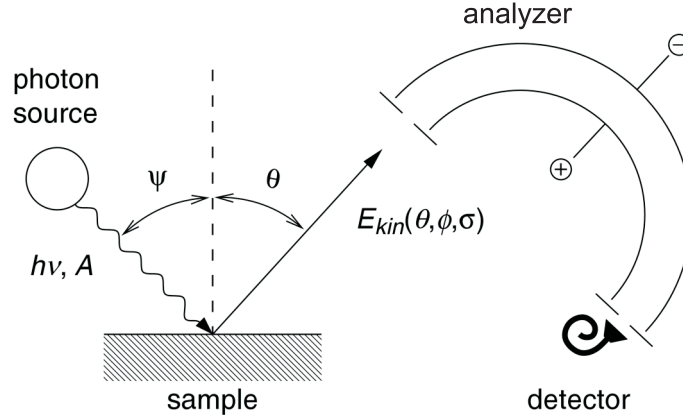
Figure 3.2 Principle of photoemission spectroscopy. Monochromatic photons with energy $h\nu$ are produced by a light source and hit the sample surface under an angle Ψ with respect to the surface normal. The kinetic energy E_{kin} of the photoelectrons can be analyzed by use of electrostatic analyzers (usually by an additional retarding field) as a function of the experimental parameters. The whole setup is evacuated to ultra high vacuum (UHV) (from [112]).

XPS is a surface sensitive technique used to investigate the composition of a sample and the chemical state of the constituting atoms. The principle of photoemission spectroscopy (PES) is shown in Figure 6.5. Monochromatic light – which can be either generated by a lab source (e.g. Al-K_α X-ray anode) or preferably by a synchrotron radiation facility – is directed onto the sample. If the energy of the light is in the X-ray regime (100 eV to 10 keV), the technique is referred to as X-ray photoemission spectroscopy (XPS). Due to the photoelectric effect the impinging photons create photoelectrons with an kinetic energy E_{kin} of

$$E_{\mathrm{kin}} = h\nu - \phi - E_{\mathrm{B}} \qquad (3.1)$$

where $h\nu$ is the photon energy, ϕ the work function of the sample, and E_{B} the binding energy of the electron in the sample. The kinetic energy E_{kin} of the photoelectron is typically measured by using hemispherical analyzers. The analyzer is usually operated in the fixed transmission mode. This means that the photoelectrons are decelerated by a retarding voltage and pass the hemisphere with a constant kinetic
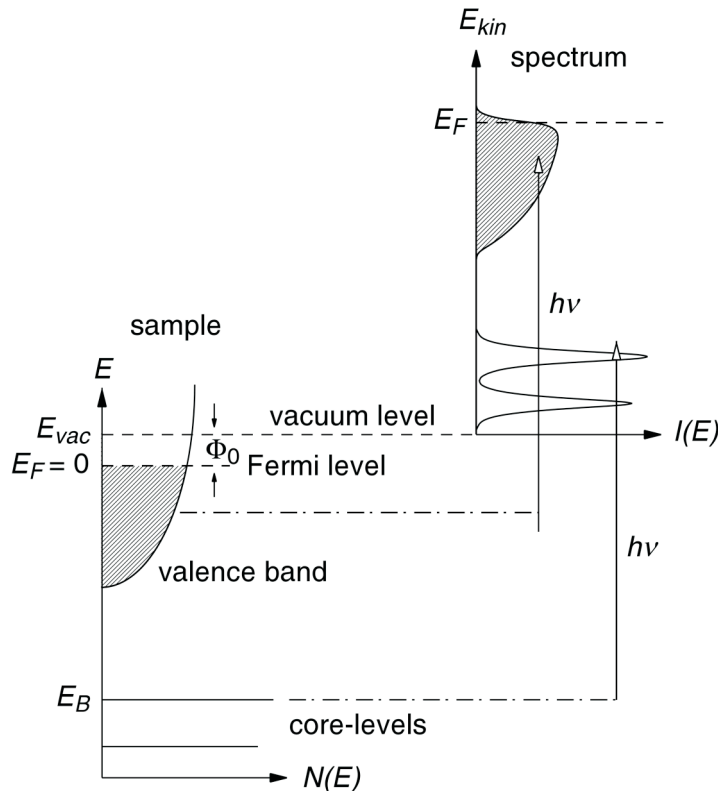
Figure 3.3 Schematic view of the photoemission process. Electrons with binding energy E_B can be excited above the vacuum level E_{vac} by photons with energy $h\nu > E_B + \Phi_0$. The photoelectron distribution $I(E_{kin})$ can be measured by the analyzer and is (in first order) an image of the occupied density of electronic states $N(E_B)$ in the sample. The discrete core level states of the sample give rise to peaks of a finite width in the spectrum. Note that also the Fermi level is also broadened. (from [112])

energy (the so-called pass energy). A spectrum over an energy range is obtained by varying the retarding voltage. The quantity of interest is the binding energy E_B, which can in principle be calculated with the help of Eq. 3.1 once the kinetic energy of the photoelectrons E_B is measured. For this calculation the photon energy $h\nu$ and the work function ϕ have to be known very precisely. It is therefore more convenient to calibrate the binding energy scale directly to the Fermi energy E_F (see Fig. 3.3). A schematic view of the photoemission process is given in the energy diagram shown in Fig. 3.3. This simplified picture shows the purpose of photoemission spectroscopy: the properties of the photoelectrons basically reflect the electronic structure of the investigated system [112]. The discrete core level states of the sample give rise to peaks of a finite width in the spectrum. The peak positions are defined by electron

binding energies which are characteristic for the atomic species under investigation. In other words the presence of a peak at a certain binding energy is a sign for the presence of a certain element in the sample. Photoemission spectroscopy can therefore be used to investigate the composition of a sample. However, XPS is a much more powerful tool: It is not only able to reveal the composition of the sample but also the chemical bonding state of the atoms in the sample. The latter is due to the fact that core level binding energies vary depending on the chemical environment of the atom. These variations are called *chemical shifts* or *core level shifts*. An overview of the theory and of various approaches to the interpretation of core level shifts can be found in the review by Egelhoff [113].

The surface sensitivity of XPS is due to the mean free path of the photoelectrons (Fig. 3.4). For kinetic energies of around 100 eV the mean free path is of the order of only a few Å. If measurements are performed at a synchrotron facility, the user can tune the energy $h\nu$ of the photons to a value that the kinetic energy of the photoelectrons becomes $E_{\text{kin}} \approx 100\,\text{eV}$ so that a maximum of surface sensitivity is achieved. This is done by setting $h\nu$ to the binding energy E_{B} of the core level under investigation plus $\sim 100\,\text{eV}$ (compare Eq. 3.1). For example we have chosen a photon energy of 390 eV to investigate the carbon 1s core level that has a binding energy of $E_{\text{B,C 1s}} \approx 284\,\text{eV}$ (compare Section 3.4). We will see below that - with the appropriate photon energy - the XPS signal originating from the surface of our Ir crystal equals the signal originating from the bulk of the Ir crystal in intensity.
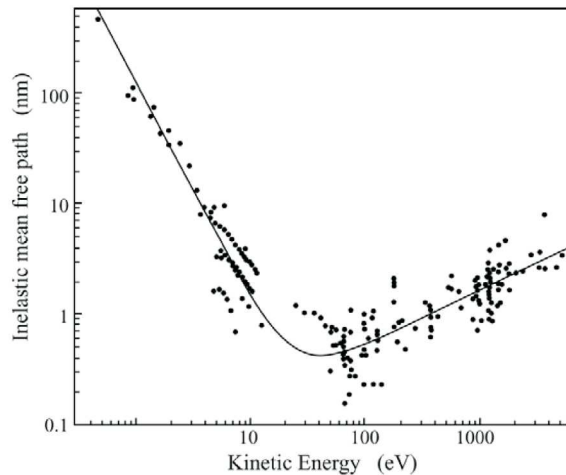
Figure 3.4 Mean free path of excited electrons in solids against kinetic energy. This so-called *universal* curve shows a minimum of approximately 5 Å at 20 - 100 eV kinetic energy (Figure from [114], original data from [115]).

3.3 The Beamline I311 at Max-lab

XPS measurements were carried out at beamline I311 of the MAX II storage ring of the MAX IV Laboratory in Lund, Sweden. MAX II is a third generation synchrotron source with a circumference of 90 m and a maximum stored current of 300 mA [116]. Inside the storage ring electrons are accelerated until they reach an energy of 1500 MeV. At this energy the electrons have a speed of 99.99999 % of the speed of light. Bending magnets, wigglers, and undulators are used to generate photons in the X-ray regime by deflecting the electrons in a magnetic field.

I311 is an undulator based soft X-ray beamline with two end stations: One dedicated to XPS and NEXAFS, the other used for LEEM and PEEM measurements. Figure 3.5 shows a sketch of a typical beamline setup for XPS measurements.
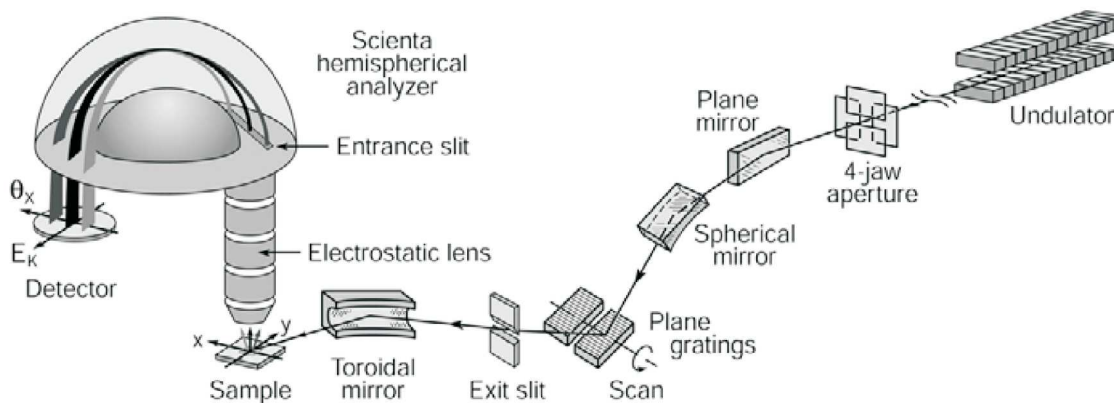
Figure 3.5 Sketch of a typical beamline setup for XPS measurements including (among others) an undulator, a plane grating monochromator, an exit slit behind the grating, and an entrance slit in front of the analyzer, the sample and a detector as well as several mirrors and lenses (from [114]).

Photoemission spectroscopy requires monochromatic X-rays of a certain energy (see Section 3.2 for how this energy is selected to achieve a maximum of surface sensitivity). However, the undulator emits light of a characteristic spectrum depending on the undulator gap [Fig. 3.6 (b)]. This gap is tuned to maximize the intensity of the light at the desired photon energy.
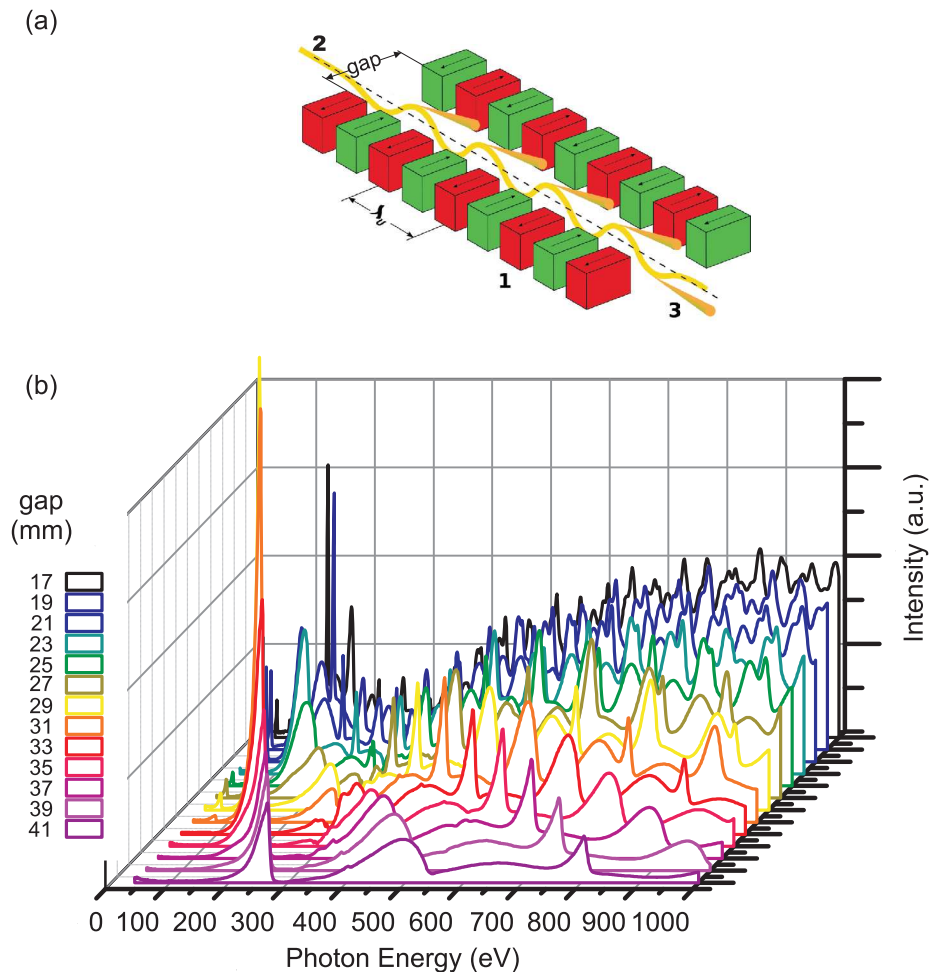
Figure 3.6 (a) Principle of an undulator. Permanent magnets (1) seperated by a tunable gap generate a static magnetic alternating along the length of the undulator with a wavelength λ_u. The electrons (2) traversing the periodic magnet field are forced to undergo oscillations and radiate (3). (from [117])
(b) Photon energy spectra generated by the undulator at I311 for different settings of the gap (from [116]). Note that for small gaps the undulator mimics the behaviour of a wiggler, giving high output with only weak undulator features over a large photon energy.

Afterwards the light is monochromated by an optical grating (Zeiss SX-700, 1220 lines/mm) and passes an adjustable exit slit. Fig. 3.7 displays the resolution of the grating as a function of photon energy for different settings of the slit. It is evident that for a given photon energy the resolution can be improved by narrowing the exit slit. However, a reduction of the slit size also reduces the number of photons reaching the sample so that measuring time is increased. A compromise must be found for each spectrum.
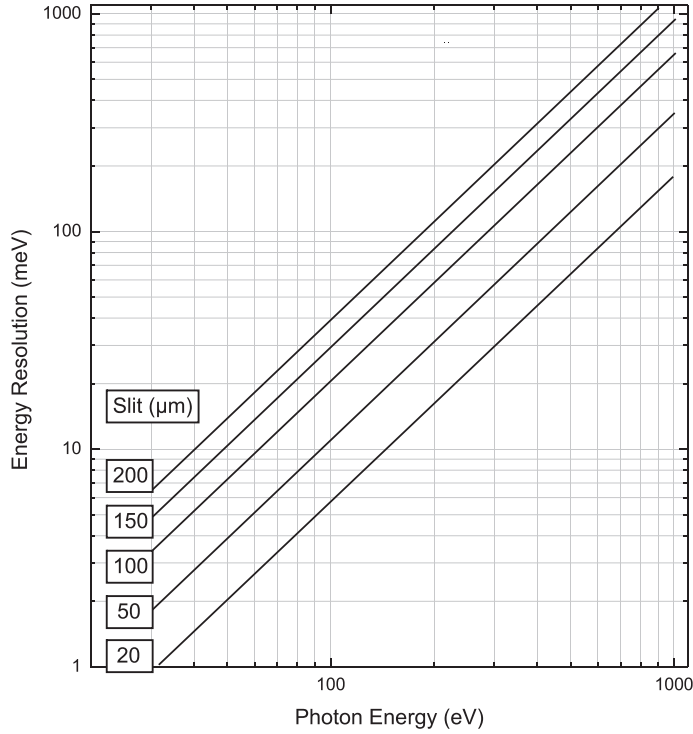
Figure 3.7 Energy resolution of the Zeiss SX-700 grating at I311 as a function of photon energy for different settings of the exit slit (modified from [116]).

The light is focused by mirrors onto the grating and from there onto the sample. The spot size on the sample is about 0.5 mm horizontally and 0.1 mm vertically, thus the area that is probed is 0.05 mm². The exited photoelectrons are analyzed by a hemispherical Scienta SES200 Analyzer and detected by a CCD camera. The analyzer is operated in the fixed analyzer transmission mode. The energy resolution of the analyzer is given by

$$Res(eV) = \frac{E_{pass} \cdot s}{2R}$$

where s is the width of the entrance slit of the analyzer and R its radius (200mm). The resolution can be improved by reducing the width of the entrance slit or the pass energy on the expense of intensity. A balance between intensity and resolution has to be found.

3.4 Experimental Procedures and Calculations

The Ir(111) crystal was cleaned by cycles of Ar^+ (XPS) or Xe^+ (STM) sputtering at room temperature with subsequent O_2 treatment at 1200 K (1×10^{-7} mbar, 10 min), followed by vacuum annealing to above 1400 K. No subsurface Ar gas bubbles were observed with STM.

The growth of partial graphene layers with 0.2 ML, 0.5 ML or 0.95 ML coverage was performed by 1, 3 or 10 cycles of ethylene (C_2H_4) adsorption till saturation at room temperature followed by thermal decomposition at 1400 K [44, 86, 118]. 1 ML (monolayer) graphene corresponds here to full coverage of the Ir(111) substrate. The resulting 0.5 ML graphene layer is not yet percolated and consists of flakes and coalesced flakes with a broad size distribution with circle equivalent (CE) diameters of 10 nm to 100 nm. The 0.95 ML graphene layer is percolated and displays uncovered Ir(111) patches at distances of the order of micrometers in STM.

The perfectly closed 1 ML graphene layer was grown by one cycle of adsorption and thermal decomposition followed by chemical vapor deposition of ethylene (p = 1×10^{-7} mbar) for 2400 s at 1170 K [13]. Graphene layers of comparable quality can also be achieved by CVD alone if the growth temperature is chosen high enough [83]. We dismissed the latter method as it would require prolonged sample heating. For all graphene coverages these growth recipes only yield the well-known incommensurate (9.32 x 9.32) moiré superstructure with the dense packed rows of graphene and Ir(111) in parallel with a scatter of less than $\pm$ 0.5° [86]. Consequently, the film displays no graphene edge atoms and only a marginal concentration of point defects, which accommodate the small tilts. The quality and uniqueness of orientation of the prepared graphene and the absence of differently oriented domains was checked by LEED in both the STM and the XPS chamber. In the XPS chamber the absence of CO adsorption at room temperature confirmed the closure of the 1 ML graphene layer. In the STM chamber the full coverage with graphene was directly confirmed by low magnification STM imaging all over the sample.

High purity metals (Pt, Ir, Au) were sublimated with a commercial e-beam evaporator, resulting in a typical deposition rate of e.g. 3×10^{-2} ML/s for Pt. Coverages are defined, such that 1 ML corresponds to the surface atomic density of Ir(111). During deposition the sample was kept at 300 K if not indicated otherwise, and the pressure remained in the low 10^{-10} mbar range. The evaporator was calibrated in the STM chamber by determination of the fractional area of monolayer metal is-

lands deposited onto clean Ir(111). At the I311 beamline the same evaporator as in the TuMA-III Lab was used with identical settings and distance to the sample. For Pt evaporation the STM rate calibration was confirmed in the XPS setup using the Ir 4f surface peak which vanishes at 1 ML coverage. Both calibrations agree within 10 %.

STM imaging was conducted at room temperature if not indicated otherwise. STM topographs were post-processed using the WSxM software [119]. Tunneling resistances of $\approx 2 \times 10^{10} \, \Omega$ are used to avoid tip-cluster interaction. Moreover, owing to the convolution of the tip shape with the clusters, multilayered clusters tend to display a larger base area compared to 1-layered ones.

All XP-spectra were collected in normal emission. If not specified otherwise, all spectra are taken with photon energies of 190 eV for Ir 4f, Pt 4f, and Au 4f, 390 eV for C 1s, and 650 eV for O 1s, respectively. The total energy resolution of the light and analyzer is better than 45 meV, 60 meV and 200 meV for the respective core level spectra. The spectra were fitted with Doniach-Sunjic (DS) functions [120] convoluted with Gaussians. The parameters α and the Lorentzian full width at half maximum (LFWHM) of the DS functions account for the asymmetry of the peaks, due to inelastic scattering of photoelectrons, and for the finite lifetime of the core hole, respectively. The Gaussian full width at half maximum (GFWHM) accounts for the experimental broadening. A linear background was used for the curve fitting. All spectra are normalized to the background, and core binding energies, defined to have positive values, are referenced to the Fermi edge. Accordingly, a positive core level shift (CLS) corresponds to a binding energy increase.

Density functional theory (DFT) calculations were done by Peter J. Feibelman in order to optimize structures and to calculate core level shifts. Calculated core-level shifts were obtained in the fully-screened hole approximation, in which the total energy of the system plus core hole is computed by setting the core potential of the ionized atom to that of the same atom with the appropriate core electron missing. Total energies were evaluated using the VASP DFT code [121, 122], with a LDA Functional, based on the Ceperley-Alder Local Density Functional [123], as parametrized by [124], in the Projector Augmented Wave (PAW) Approximation [125, 126]. The LDA Functional was chosen for the present work since it describes the binding of Ir islands on graphene better than the PW91-GGA Functional [79].

As in Ref. [79], graphene/Ir(111) was modeled as a 10×10 graphene adlayer on the

upper surface of a 9×9, 4-layer, Ir(111) crystalline slab. This is a very good approximation to the experimentally observed incommensurate 10.3×10.3 graphene layer on a 9.3×9.3 substrate mesh. In structural optimizations, with and without overlying Pt islands, the atoms of the bottom Ir layer were fixed in a (111) bulk, crystal plane, with an Ir-Ir nearest neighbor distance equal to 2.701 Å, the theoretical optimum. Positions of all remaining atoms were relaxed until none experienced a force of magnitude $> 45\,\mathrm{meV/\text{Å}}$. Electronic relaxation was accelerated using Methfessel-Paxton Fermi-level smearing (width = 0.2 eV) [127], and corrected for the unphysical contact potential difference associated with having a graphene adlayer on one side of the Ir slab only [128]. A 400 eV plane-wave basis cutoff was used as well as a 3×3 surface brillouin zone sample for the sake of good accuracy.

4 How Pt Clusters Bind to the Graphene Moiré on Ir(111)

The results of this chapter (except Section 4.3) are published in Physical Review B 85, 035407 (2012) [84]. I was strongly involved in the XPS measurements and conducted the STM experiments. I was involved in discussion and analysis of the data as well as in commenting and editing of the manuscript. Section 4.3 was added by myself.

In Section 2.2 the DFT based scenario of cluster binding to the graphene moiré was described [79, 80]. Despite its plausibility, there is as yet no experimental evidence for the rehybridization picture beyond agreement of the experimentally-determined binding site preference of the metal clusters with what DFT calculations predict. A way to proceed is suggested by previous investigations of the binding of graphene to different metals [87, 129] and of how differently sized graphene flakes bind to the Ir(111) substrate [90]. In this chapter, we will show XPS measurements of C 1s core level shifts for graphene/Ir(111) with and without adsorbed clusters present, and we compare them to calculated shifts based on the rehybridization picture.

To set a standard for agreement between DFT theory and XPS data, we will first compare measured and calculated C 1s CLS of graphene on Ir(111) without adclusters (Section 4.1). The effect of cluster adsorption is the subject of Sections 4.2 - 4.4, where we analyze experimental and calculated results of the C 1s CLS of graphene with Pt adclusters, and of the Pt $4f_{7/2}$ CLS of the adsorbed clusters themselves. Further, we present Ir 4f spectra showing a signature of graphene interaction with the Ir surface.

4.1 A Test Case: Core Level Spectrum of Pristine Gr/Ir(111)

Figure 4.1(a) shows an STM topograph of graphene on Ir(111) with the moiré unit cell indicated. Both the honeycomb structure formed by the carbon atoms and the moiré's different high symmetry domains are visible. The latter are labeled top, hcp or fcc according to the position of the center of the carbon rings [44]. A ball model of the DFT optimized structure in Fig. 4.1(b) shows the geometry of the high symmetry domains and the undulation of the graphene. C-atoms in top domains reside 3.85 Å above the Ir surface, whereas those in hcp/fcc domains lie about 0.6 Å lower. The C-atoms are grouped in Fig. 4.1(b) according to their height and binding geometry. Those in threefold hollow sites are labeled by $\diamond$ and $\triangle$, in bridge sites by $\square$ and in atop sites by $\circ$ and $\triangleright$.

To understand how the graphene-Ir(111) distance and the local geometry of C-atoms affect the C 1s core level we calculated the CLS of the 200 C-atoms in the moiré unit cell using the core ionization potential of a C-atom in a isolated graphene layer as a reference. The results are shown in Fig. 4.1(c) using the same colored symbols as in Fig. 4.1(b) to distinguish atoms at different heights and adsorption sites. Comparing C-atoms in threefold hollow [$\diamond$ and $\triangle$ in Figs. 4.1(b-c)] or bridge sites [$\square$ in Figs. 4.1(b-c)] it is clear that there is an approximate linear correlation between the graphene-Ir(111) distance and the C 1s core level binding energy, which is lower for atoms farther from the substrate. Core shifts estimated in the initial state approximation [113], which are the main contributions to the numbers we calculated, offer insight into the sign of this effect. The key idea is that CLS's are more negative on atoms that gain electronic charge, and more positive on those that lose it. Thus, the CLS's on C atoms farther from the metal imply that they are somewhat negatively charged, while the atoms that lie lowest are positive. This charge redistribution is consistent with an electrostatic interaction between the mobile electrons of the graphene and the electron spillout charge of the underlying metal. That is, the positive charge of the low-lying moiré regions is favorable by virtue of attraction to the metal's spillout electrons. Equally, the negative charge of the high-lying regions is favorable by virtue of repulsion from them.

Although this explanation of the CLS's is convincing we want to offer an alternative interpretation. A consequence of charge transfer to or from the graphene layer is
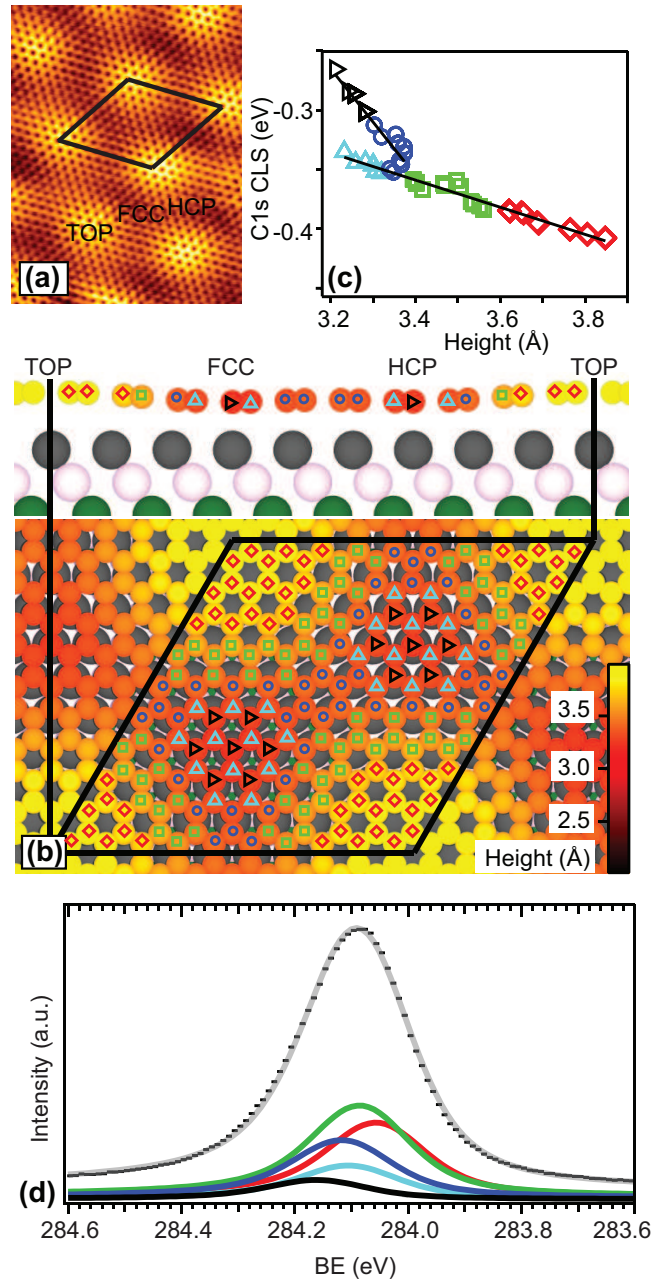
Figure 4.1 (a) STM topograph (59×84 Å², U= 1V, I=7nA) of the graphene moiré on Ir(111). The three high symmetry domains top, fcc and hcp are indicated. (b) Schematic illustration of the DFT optimized C(10×10)/Ir(9×9) moiré unit cell showing a top view, and a side view along the unit cell diagonal. The height of the C atoms is given by the color scale. The C-atoms in threefold hollow sites are labeled by ◇ and △, in bridge sites by □ and in atop sites by ○ and ▷ (see text). (c) Calculated C 1s CLS for the 200 atoms in the moiré unit cell. (d) Black dots represent the experimental C 1s spectrum. The gray curve is the superposition of 200 peaks with a binding energy distribution according to the DFT calculated CLS. The 5 colored components are the sums of peaks originating from C atoms marked with ◇, △, □, ○, and ▷ in panel (b), respectively.

doping. In Chapter 8 we will see that this doping leads to a C 1s CLS which is positive on atoms that gain electronic charge, and negative on those that lose it. Applying this model to the undulated graphene layer one must conclude that the CLS's on C atoms farther from the metal imply that they are somewhat positively charged, while the atoms that lie lowest are negative. In the future, local work function measurements might show how the charge is actually distributed over the moiré unit cell and in which way our CLS's should be interpreted.

Similarly to C-atoms in threefold/bridge sites we observe an approximately linear height-BE correlation for C-atoms positioned atop Ir atoms and marked with ○ and ▷ in Fig. 1(b-c). The slope, however, is a factor of 4 steeper for C atoms atop Ir (-0.45 eV/Å) compared to atoms in threefold/bridge sites (-0.11 eV/Å), consistent with a stronger interaction between C atoms' π orbitals and the $d_{3z^2-r^2}$ orbitals of the underlying Ir atoms for atop positioned C atoms. This interaction seems a likely candidate for an explanation of why it is the hcp and fcc regions of the graphene film that lie low, and not the top region. In the former, weak hybridization effects pull C atoms directly above Ir's toward the metal. In the top region, there are no C atoms directly above Ir's [85, 130].

Figure 4.1(d) shows the experimental C 1s spectrum obtained on pristine graphene / Ir(111). We observe a single C 1s peak at 284.09 eV with an experimental full width at half maximum (FWHM) of 0.25 eV. The experimental C 1s spectrum was fitted with 200 peaks with identical intensity and C 1s CLSs according to our DFT calculations. Both the Gaussian and Lorentzian full width at half maximum (GFWHM and LFWHM) were constrained to one common fitting parameter for all 200 peaks during the fitting procedure. The result was a GFWHM and LFWHM of 0.15 eV and 0.12 eV, respectively. As shown by the gray curve in Fig. 4.1(d), the superposition of the 200 peaks is an excellent approximation to the experimental spectrum and the LFWHM is, furthermore, in good agreement with studies on HOPG [131]. To illustrate how atoms in different domains/adsorption sites contribute to the experimental spectrum, the C 1s sum spectrum of each of the 5 sets of atoms shown in Fig. 4.1(b-c) is included in Fig. 4.1(d).

The C1s graphene/Ir(111) peak position of 284.09 eV measured here is similar to previously measured values of 284.16 eV [87], 284.10 eV [90] and 248.15 eV [132]. The measured experimental FWHM of 0.25 eV is lower than any reported value (0.40 eV [87] and 0.30 eV [132]) consistent with the excellent quality of our graphene

and the absence of defects and edge atoms. It is worth noting, incidentally, that because we only captured photoelectrons within an acceptance angle of $+/- 5^o$ about the surface normal, dispersion, such as was attributed in Ref. [132] to formation of C 1s bands, cannot have contributed to the broadening of our C 1s XPS feature.

4.2 C 1s Core Level Shifts of Gr/Ir(111) with Pt Clusters

Satisfied that DFT calculations provide a faithful description of the C 1s spectrum of pristine graphene/Ir(111), we now wish to use them to test the rehybridization/buckling model of metal cluster array binding on the graphene. To that end, Fig. 4.2(a) shows an STM image obtained after room temperature deposition of 0.18 ML Pt. The large majority of Pt clusters in the Figure are one layer high, though a few bright two-layer islands are also apparent. All clusters are adsorbed in hcp domains, with the following occupation numbers: 1-layered clusters (80±2%), 2-layered clusters (12±2%), 3-layered clusters (2±1%), and empty cells (5±1%). As, on average, 94% of the moiré unit cells contain a cluster, and each unit cell contains 87 Ir atoms [44], the average Pt island is comprised of 17 atoms. Given an approximate Poisson size distribution [44], clusters of size 15-19 atoms are all very similar in probability, ranging from 8.6 % to 9.6 %. Thus, to limit computational effort, we conducted DFT calculations for planar, highly symmetric, magic Pt_{19} clusters. As for Ir clusters supported by graphene [79] our calculations imply that the Pt_{19} clusters are stabilized in hcp domains with the Pt atoms positioned atop C atoms. The optimized Pt_{19}/graphene/Ir(111) structure is shown in Fig. 4.2(b). Comparison of the side view of pristine graphene in Fig. 4.1(b) and of graphene supporting Pt_{19} clusters in Fig. 4.2(b) shows that C atoms below and in the vicinity of the Pt_{19} cluster move closer to the Ir(111) surface, while C atoms in top domains moved slightly away from the Ir surface (3.98 Å). Based on the observed height-BE correlation established for pristine graphene we expect a CLS to higher binding energies for the C atoms that have moved closer to the Ir(111) surface upon Pt deposition. The DFT calculated C 1s CLS for the C atoms in the Pt_{19}/graphene/Ir(111) structure, shown in Fig. 4.2(c), confirm the expected positive CLS below and in the vicinity of the Pt_{19} cluster.

In more detail we find that the C atoms surrounding the Pt cluster [∘ in Fig. 4.2(c)]

have a linear BE-height correlation with an even steeper slope (-1.6 eV/Å) than for pristine graphene (-0.11 eV/Å threefold hollow and bridge, -0.45 eV/Å atop). Coordination directly to Pt atoms ($\diamond$) adds an additional CLS of +0.6 eV on top of the CLS expected from the C-Ir(111) distance, while C-atoms atop Ir atoms ($\triangledown$) below the Pt_{19} cluster have an extra CLS of -0.5 eV. As the observed negative and positive shifts are approximately equal in magnitude, Pt deposition evidently leads to charge transfer of electrons from Pt bonded C atoms to Ir bonded C atoms below the Pt clusters [see the small schematic drawing in Fig. 4.2(c)]. Based on the DFT calculations the Pt clusters' effect on the C 1s CLS is therefore twofold: (i) The polarization of charge toward the Ir substrate as C-Ir bonds form increases the average C 1s CLS. (ii) The $sp^2 \rightarrow sp^3$ rehybridization induces a transfer of electrons from Pt bonded C atoms to Ir bonded C atoms.

Towards confirming that our Pt_{19} model and the $sp^2 \rightarrow sp^3$ rehybridization are faithful to nature, let us compare the DFT and measured C 1s spectra after deposition of 0.18 ML Pt in Fig. 4.2(d). Relative to the C 1s spectrum of pristine graphene, shown with black dots, Pt deposition shifts the main peak by +0.06 eV (blue dots), while a broad shoulder develops at high binding energies. Comparing with Figs. 4.2(b) and (c), we identify the shoulder with three groups of C atoms: immediate neighbors of Pt atoms($\diamond$), contributing CLS in a width of 0.24 eV, immediate neighbors of Ir atoms ($\triangledown$), with CLS covering 0.10 eV, and C atoms bordering the Pt island ($\circ$), with CLS ranging over 1.04 eV. Using the peak shape from pristine graphene and the C 1s CLS from DFT we calculated the C 1s peak originating from each of the 200 C-atoms in a graphene unit cell supporting a Pt_{19} cluster. Further, we used these calculated C 1s peaks as input to calculate the shape of the 3 components assigned to the experimental shoulder. As Fig. 4.2(d) shows, the addition of these three components ($\diamond$, $\triangledown$, $\circ$) results in a broad shoulder largely matching the experimental one in width.

Still, the overall intensity of the simulated shoulder is too high, particularly the component with the highest binding energies, from C atoms directly bound to Pt cluster atoms [marked $\diamond$ in Figs. 4.2(b)-(d) and component shaded black in Fig. 4.2(d)]. The overestimate of the overall intensity of the shoulder in the calculated spectrum is a likely consequence of the attenuation of the photoelectron signal originating from C atoms below the Pt_{19} clusters. In fact attenuation of the calculated shoulder components by 40% – the attenuation of one layer of Pt in the Pt(111) surface at E_{kin}
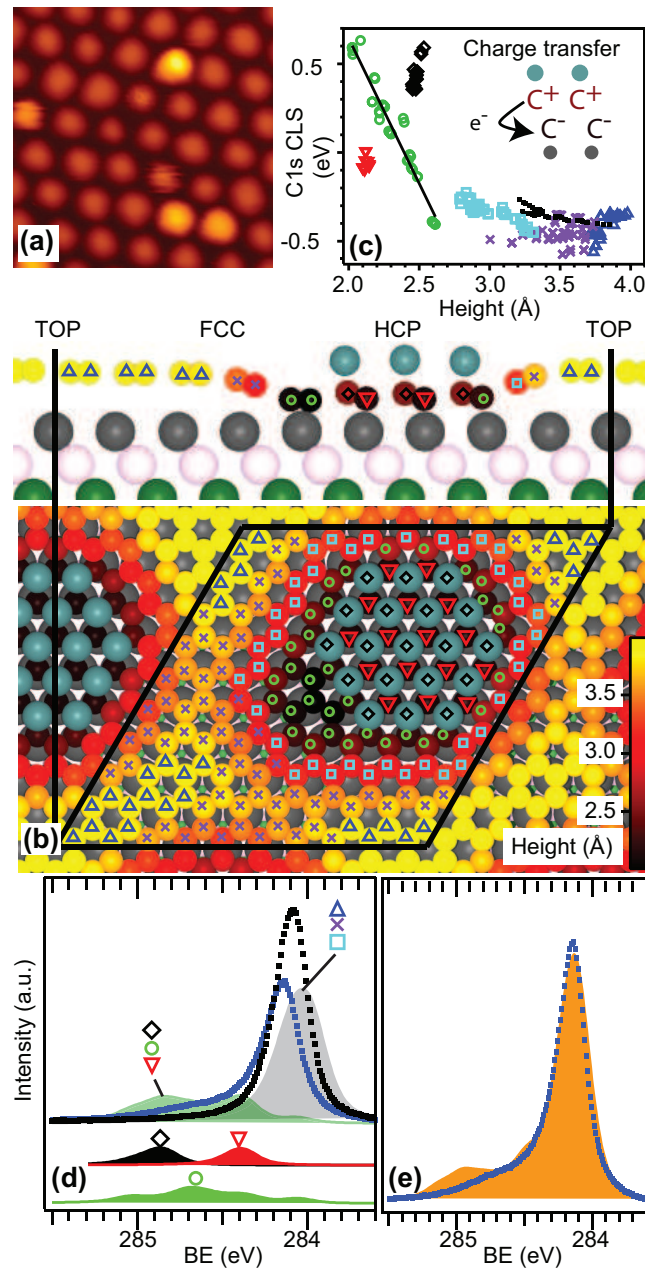
Figure 4.2 (a) STM topograph (U=1V, I=0.05nA, 150×150 Å^2) after deposition of 0.18 ML Pt on graphene. (b) Schematic illustration of the DFT optimized C(10×10)/Ir(9×9) moiré unit cell with an adsorbed Pt$_{19}$ cluster showing the top view and the side view along the unit cell diagonal. The height of the C atoms is given by the color scale. C atoms are grouped into 6 sets based on their position in the moiré unit cell ($\diamond$, $\triangledown$, $\circ$, $\square$, $\times$, and $\triangle$). (c) Calculated C 1s CLS for the atoms in graphene supporting a Pt$_{19}$ cluster. Symbols used as in panel (b). The shift is given relative to a C atom in isolated graphene. The black dots are the data of pristine graphene as in Fig. 1(c). (d) Experimental C 1s spectrum before (black dots) and after (blue dots) deposition of 0.18 ML Pt. The curves marked with ($\diamond$), ($\triangledown$) and ($\circ$) symbols are the DFT calculated components corresponding to Pt bonded C atoms, Ir bonded C atoms, and C atoms close to the Pt$_{19}$ cluster, respectively. The light gray and light green curves are the DFT calculated C 1s component of atoms far away from and close to the Pt cluster, respectively. (e) Comparison of the experimental C 1s spectrum after deposition of 0.18 ML Pt and the overall DFT simulated spectrum shifted +0.1 eV and corrected for attenuation of the photoelectrons (see text).

= 390 eV - 284 eV = 106 eV – brings the overall intensity to reasonable match with the experiment [see below and Fig. 4.2(e)]. Further, we find that the area of the experimental shoulder is increased a factor of 1.3 when the C 1s spectrum is acquired with hν=390 eV compared to spectra taken with hν = 350 eV and hν = 450 eV indicating that diffraction effects are important for the shoulder area at low kinetic energy of the photoelectrons. The area of the shoulder component is, however, increased again when the C 1s spectrum is measured with hν = 500 eV and hν = 600 eV. At high kinetic energy of the photoelectron, attenuation and diffraction effects will be less important and we are, therefore, unable to explain the overweighting of the high binding energy shoulder ["discrepancy (A)" in what follows].

Addition of the remaining calculated components ($\square$, $\times$, $\triangle$) results in a *negative* shift for the main peak upon cluster adsorption as the gray curve in Fig. 4.2(d) demonstrates. This calculated negative shift of the main component contradicts its experimentally observed positive shift by 0.06 eV ["discrepancy (B)" in the following discussion].

Although calculations and experiment agree on the formation of a high-energy binding energy shoulder in the C 1s CLS upon cluster adsorption, the sources of discrepancies (A) and (B) are, given current knowledge, a matter of speculation. For example, we will see in Chapter 8 that cluster formation causes systematic shifts of the C 1s core level most probably related to doping. A minute difference between actual and calculated doping might thus account for discrepancy (B). Such a difference could result from neglect of the cluster size distribution in our calculations. On that basis, we shifted all theoretical peaks by +0.1 eV and additionally scaled down the shoulder components by 40% to account for photoelectron attenuation by the Pt$_{19}$ clusters. The resulting spectrum, shaded orange in Fig. 4.2(e), is a reasonable match to the experimental one. Nonetheless, discrepancy (A) remains.

According to the correlation we have established between C-atom height and C 1s binding energy, excess weight theoretically attributed to the highest binding energy peak [discrepancy (B)] means that in the region between the Pt islands, the graphene sheet lies too close to the underlying Ir substrate. Given the tendency of the LDA to overbind, it is easy to imagine that a more faithful density functional would mitigate this problem. Still, for graphene/Ir(111) with no island present, the predicted C 1s spectrum agrees well with experiment (cf. Fig. 4.1). Thus, a geometric solution of discrepancy (B) is not straightforward, and the answer may lie entirely elsewhere.

4.3 Ir 4f Signature of Graphene Interaction with the Ir Surface

Our calculation imply that C atoms below and in the vicinity of the Pt_{19} cluster are displaced closer to the Ir(111) surface with every second C atom binding to substrate Ir atoms directly below them. These Ir atom which bind to carbon atoms should display a core level shift compared to Ir surface atoms unaffected by the graphene layer. To test our model with respect to this graphene-surface-interaction we investigated the Ir $4f_{7/2}$ core level spectrum.

Fig. 4.3 shows Ir $4f_{7/2}$ spectra for a clean Ir surface (a), the Ir surface covered with graphene (b) and after deposition of 0.18 ML Pt on graphene/Ir(111) (c). The spectrum of the clean surface consists of two components, the Ir bulk component located at 60.87 eV and the Ir surface component at 60.33 eV consistent with the data of Bianchi et al. [133] and Ng et al. [93]. Both components were fitted with DS-functions (see Table 4.1 for details of the fit parameter).

Fig. 4.3 (b) shows the Ir $4f_{7/2}$ spectrum of 1 ML graphene/Ir(111). The spectrum remains virtually unchanged compared to that of the clean surface (consistent with [90]). The fitting parameters of the graphene-covered surface display only small variations compared to the clean surface. The fact that the spectrum remains unchanged by the presence of the graphene layer is in line with our findings displayed in Fig. 4.1 namely that the Ir-C distance is large (ranging from 3.2 Å to 3.8 Å) for all carbon atoms indicating that they interact only weakly with the Ir surface.

The spectrum changes after deposition of 0.18 ML Pt onto the graphene layer [Fig. 4.3 (c)]. The intensity of the surface component is noticeably reduced and a third component has to be introduced for a reasonable fit of the data. The position and fit parameters of the bulk and surface components were kept as they were obtained from fitting the spectrum of the graphene-covered surface before Pt deposition. The third component was found to be located at 60.52 eV with the same LFWHM and α as the surface component. However, a larger GFWHM had to be allowed for a reasonable reproduction of the spectrum. Regarding the relative intensities of our components we find that after Pt deposition the sum of the surface component and the third component is almost equal to the intensity of the surface component for the clean graphene layer ($I_{surface}$(graphene) = 0.62 and $I_{surface}$(0.18 ML Pt) + I_{3rd}(0.18 ML Pt) = 0.58, when I_{bulk} is defined to be equal to 1). Obviously spectral weight has
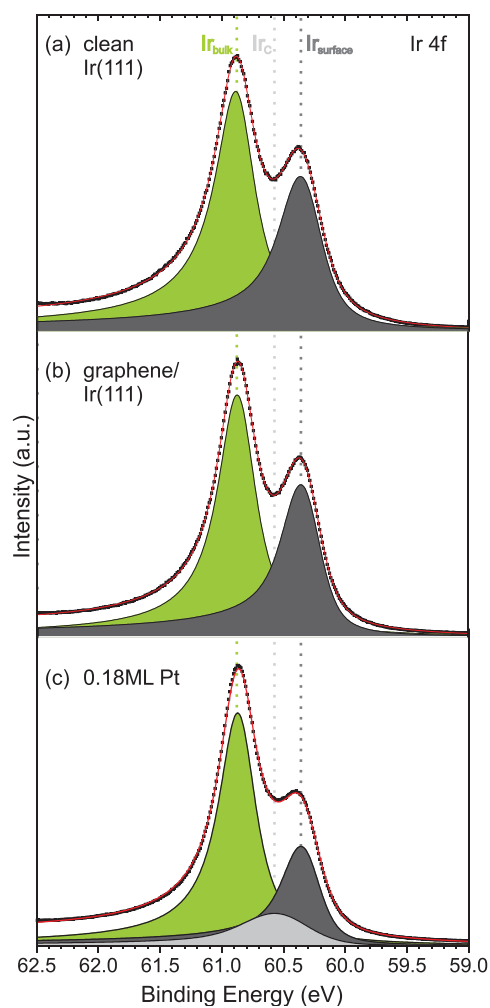
Figure 4.3 (a) Ir $4f_{7/2}$ core level spectra for a clean Ir(111) surface, (b) covered with graphene and (c) after deposition of 0.18 ML Pt on graphene. The experimental spectra are shown as black dots, the fits as solid red lines, and the filled curves represent the components of the fit (green = Ir bulk, dark gray = Ir surface, light gray = Ir interface, see text)

	Ir$_{bulk}$ clean	**Ir$_{bulk}$** graphene with/without clusters	**Ir$_{surface}$** clean	**Ir$_{surface}$** graphene with/without clusters	**Ir$_C$** graphene with clusters
Binding Energy (eV)	60.86	60.86	60.33	60.33	60.52
LFWHM (eV)	0.360	0.327	0.240	0.170	0.170
α	0.100	0.071	0.160	0.175	0.175
GFWHM (eV)	0.065	0.100	0.225	0.234	0.500

Table 4.1 Fit parameters of the DS-functions used to fit the Ir 4f spectra in Figures 4.3 and 5.3.

been shifted from the surface component to the third component so that we assign this component to surface atoms binding to carbon atoms which moved closer to the Ir(111) surface in the presence of the Pt cluster. In the following we will call this component Ir$_C$. This component is the Ir 4f signature of graphene rehybridization. The larger GFWHM signals that the interaction with the Ir surface atoms in the region where the graphene binds to the substrate is not homogeneous. This is due to slight misalignments of the involved C and Ir atoms as visible in the cross section of Fig. 4.2 (b). Note that Cavallin et al. [46] recently investigated Ir 4f and C 1s spectra after growth of Rh clusters on graphene/Ir(111). In Section 5.2 their findings will be discussed in detail.

4.4 Pt 4f Core Level Shifts of Pt Clusters Adsorbed on Gr/Ir(111)

For separate confirmation that our Pt_{19} model and the $sp^2 \rightarrow sp^3$ rehybridization describe the experimentally observed situation correctly, we compared the DFT calculated CLS of Pt 4f with the experimental spectrum. Figure 4.4(a) shows the calculated Pt $4f_{7/2}$ CLS of the 19 Pt atoms in the cluster using the CLS of a Pt bulk atom as reference with a known BE of 70.9 eV [134]. Our calculations show that the Pt atoms at the perimeter of the cluster have Pt $4f_{7/2}$ CLS of -0.1 to -0.2 eV relative to bulk Pt, while the 6 atoms surrounding the central atom have an additional shift of ~0.4 eV and the central Pt atom has an additional shift of ~0.8 eV.

To understand the significance of these CLSs, in a first experiment we have grown 0.5 ML Pt at 580 K directly on Ir(111). At this coverage and temperature Pt forms monolayer islands with the large majority of the Pt atoms 6-fold coordinated to Pt and 3-fold coordinated to the Ir(111) substrate [15]. Fig. 4.4(b) displays the experimental Pt 4f spectrum. We deconvoluted the experimental spectrum with one single Pt $4f_{7/2}$ and Pt $4f_{5/2}$ component. The curve fitting reveals that the Pt $4f_{7/2}$ component has a binding energy of 70.88 eV, a GFWHM (0.29 eV), and LFWHM (0.31 eV).

Fig. 4.4(c) displays the experimental Pt 4f spectrum of 0.18 ML Pt deposited onto graphene. The Pt peaks are much broader than for Pt deposited onto clean Ir(111). To test if our DFT calculated CLS are able to explain the observed peak broadening we fitted the experimental Pt 4f spectrum of Pt/graphene with 19 Pt $4f_{7/2}$ and 19 Pt $4f_{5/2}$ components with similar intensities and binding energies fixed to the DFT calculated values. Further, the GFWHM and LFWHM were fixed to the values obtained for Pt adsorbed on clean Ir(111) during the fitting procedure. The light blue curve in Fig. 4.4(c) shows the result of the curve fitting. It is apparent that the experimental broadening of the Pt 4f peaks is well reproduced by the DFT calculated CLS. Also the absolute DFT calculated binding energy positions of the Pt 4f components, match excellently with the experimental spectrum. The only discrepancy between the experimental Pt 4f spectrum and the fit is that the overall width of Pt 4f peaks in the fit is slightly too small. If the GFWHM is increased from 0.29 eV to 0.6 eV during the fitting procedure the fit reproduces the experimental curve almost perfectly. An increased GFWHM could be the result
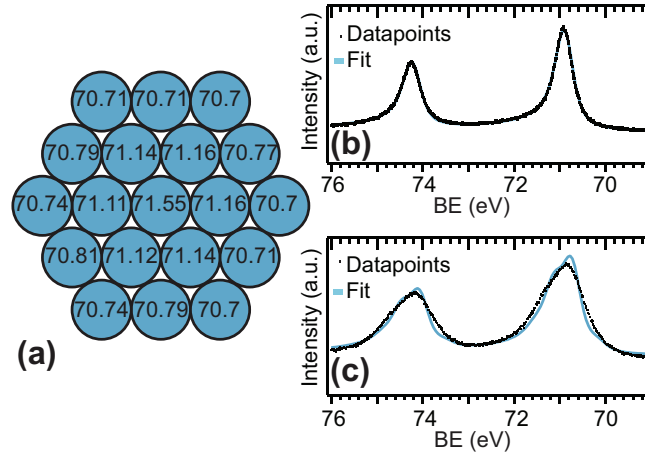
Figure 4.4 (a) Calculated Pt $4f_{7/2}$ core levels for the Pt_{19} cluster. The atomic configuration used to calculate the Pt $4f_{7/2}$ core levels is identical to Fig. 4.2(b). (b) Experimental Pt 4f spectrum (dots) of monolayer Pt-islands (0.5 ML) adsorbed on a clean Ir(111) surface. The light blue line shows the result of the curve fitting, when one Pt $4f_{7/2}$ and Pt $4f_{5/2}$ component were used. (c) Experimental Pt 4f spectrum (dots) of 0.18 ML Pt deposited onto graphene. The light blue curve is the result of the curve fitting, with CLS fixed to the DFT calculated values in (a), and the LFWHM and GFWHM fixed to the values for Pt adsorbed on clean Ir(111).

of less symmetric clusters, the experimental cluster size distribution, and a larger vibrational broadening of Pt/graphene than on Pt/Ir(111).

4.5 Conclusions

In summary, we have demonstrated a linear correlation between C-atom height and 1s binding energy in a graphene adlayer on Ir(111), reflecting an electron charge redistribution depending on the adlayer's undulation geometry. Upon deposition of 0.18 ML Pt we observed well-ordered, single-layer clusters in the graphene hcp domains, by STM. The corresponding changes in XPS spectra match an interpretation based on DFT modeling of the clusters as highly symmetric, flat and comprised of 19 Pt atoms. Specifically, a broad C 1s shoulder develops upon Pt deposition, and, using DFT calculated CLS, we showed that this shoulder must be assigned to C-atoms both under and in the vicinity of the Pt cluster. In more detail calculations revealed that the $sp^2 \rightarrow sp^3$ rehybridization further broadens the shoulder because of electron transfer from Pt bonded C atoms to Ir bonded C atoms. However, the calculations imply a larger weight of the highest binding energy component and a

slight positive shift of the main component of the C 1s CLS relative to experimental observation. Of considerable interest would be to learn whether these discrepancies are attributable to limitations of our physical model, i.e., assuming clusters of just one size and shape, or to systematic error in our DFT implementation. Further the sp^3 hybridized C atoms which move closer to the Ir surface give rise to the Ir_C component in the Ir 4f spectrum. Lastly, we compared measured and calculated Pt $4f_{7/2}$ CLS and found an excellent agreement, offering a solid starting point for future gas adsorption studies. In particular, the CLS of the edge atoms of the Pt_{19} clusters are shifted -0.4 eV with respect to terrace atoms affording the opportunity to distinguish step and terrace site adsorption.

5 Growth and Structure of Pt Clusters

In the previous Chapter, the cluster binding to the graphene layer was examined for a specific cluster size: Calculation were carried out for a Pt_{19} cluster and the experiments were done with $\Theta = 0.18$ ML Pt which corresponds to $s_{av} = 17$ atoms. The purpose of this chapter is to extend the study to the growth of Pt clusters, their structure and their interaction with the graphene layer as a function of Pt coverage. First of all, we will analyze the STM data (Section 5.1) before we turn to XPS measurements of the C 1s and Ir 4f regions (Section 5.2). Combining these results, schematic representations of the clusters and their binding geometry with the graphene layer will be derived (Section 5.3).

5.1 Growth Mode of Pt Clusters on Gr/Ir(111)

Fig. 5.1 shows a sequence of STM topographs obtained by deposition of Pt on 1 ML graphene/Ir(111) at $300\,\mathrm{K}$. The deposited amount was increased from 0.05 ML up to 1 ML. The average cluster size ranges from $s_{av} = 5$ atoms to $s_{av} = 174$ atoms respectively. The average cluster size s_{av} is obtained from the known deposited amount Θ (compare Section 2.2), the fraction n of moiré cells occupied by a cluster (the filling factor), and the number of Ir atoms in one moiré unit cell $A_{\mathrm{m}} = 87$ atoms via $s_{av} = \frac{\Theta \cdot A_{\mathrm{m}}}{n}$.
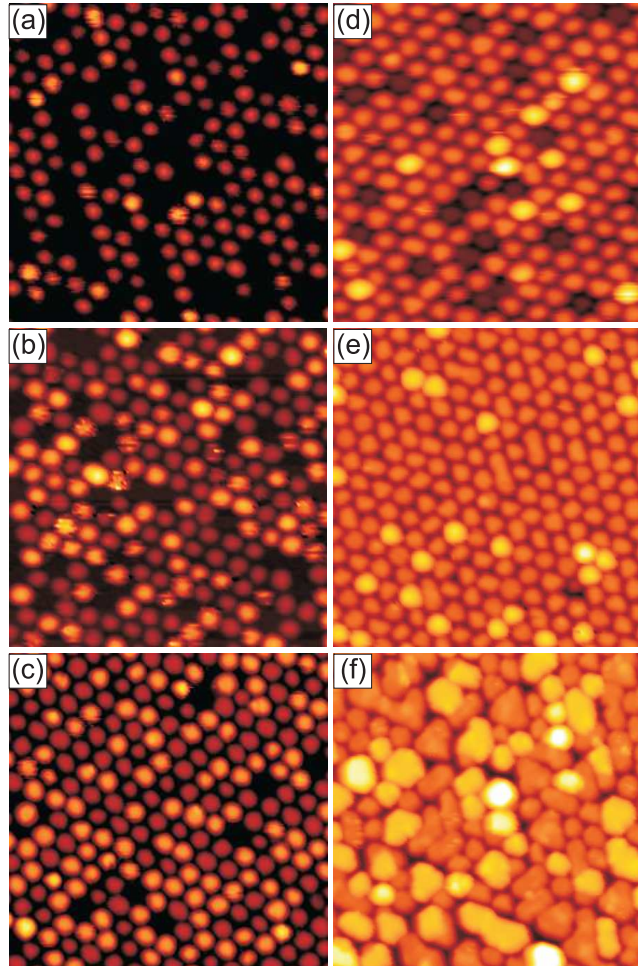
Figure 5.1 STM topographs of Pt cluster arrays on Gr/Ir(111). The Pt coverages and average cluster sizes s_{av} are (a) 0.05 ML, 5 atoms (b) 0.10 ML, 11 atoms (c) 0.20 ML, 19 atoms (d) 0.44 ML, 39 atoms (e) 0.75 ML, 65 atoms and (f) 1 ML, 174 atoms. The image size is always 290 Å × 290 Å.

As the Pt clusters grow in a layer-by-layer mode [15], the distinct height levels in the topographs correspond to one-, two- and three-layered clusters. Four-layered clusters can only be observed occasionally and only for the highest coverages (0.75 and 1 ML). Below the threshold coverage for sintering, the clusters are confined to one moiré unit cell. After deposition of 0.75 ML Pt [Fig. 5.1 (e)], a few elongated clusters can be observed which result from sintering of two neighboring clusters. Apparently a coverage of 0.75 ML Pt (corresponding to $s_{av} = 65$ atoms) marks the onset of sintering. At 1 ML Pt coverage, the majority of clusters has sintered so that the resulting particles extend over several moiré cells. The height distribution of the clusters as well as their average size s_{av} and the fraction of occupied moiré
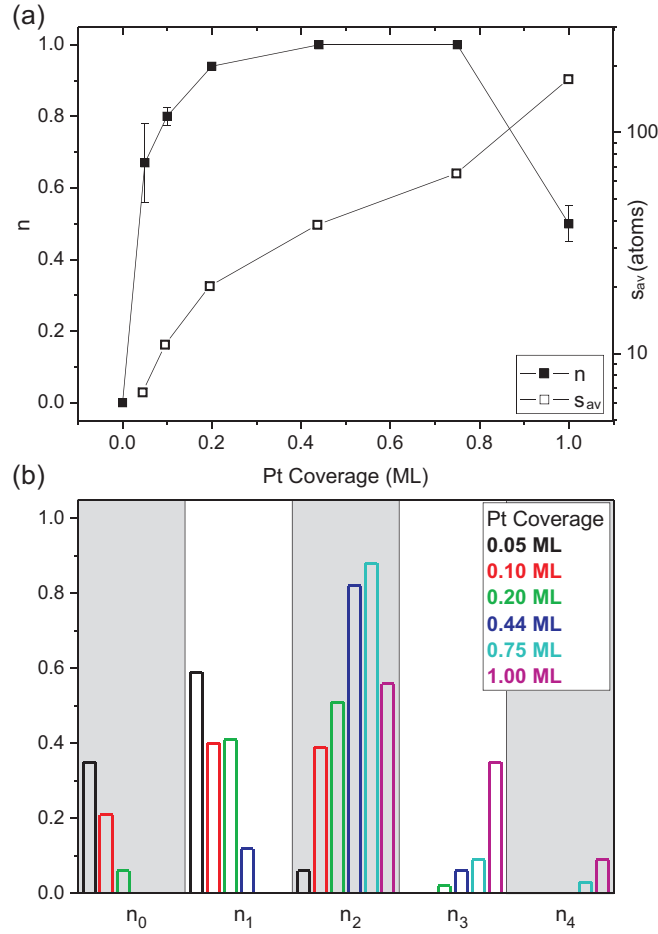
Figure 5.2 (a) Fraction of occupied moiré cells n and average cluster size s_{av} against deposited amount of Pt [135]. (b) partial filling factors of the moiré n_0, n_1, n_2, n_3 and n_4 with no, 1-, 2-, 3- and 4-layered clusters, respectively. Colors correspond to indicated Pt coverages.

cells n is presented in Fig. 5.2.

This data suggests three regimes of cluster growth: a *nucleation* regime up to 0.1 ML coverage characterized by a steep increase of n and by the presence of predominantly one-layered clusters. For coverages between 0.20 ML and 0.75 ML, n increases only slowly from 0.8 to 1. In this *growth* regime the clusters evolve to almost exclusively two-layered forms. For higher coverages we observe cluster *sintering* as indicated by a strong reduction of n and a noticeable increased number of three-layered clusters. Although the described growth of Pt clusters resembles the growth of Ir clusters (compare Fig. 2.8 and ref. [44]), there are slight differences which will be discussed in the following:

(i) The *nucleation* regime is more distinct for Ir clusters: n reaches 1 at a deposited amount of 0.1 ML Ir (compared to 0.4 ML for Pt). Also Ir clusters remain one-layered until all moiré cells are occupied, whereas two-layered Pt clusters are already observed *before* all cells are filled.

(ii) Ir clusters strongly increase their height in the *growth* regime. After deposition of 1.5 ML Ir (which is just below the threshold for sintering [44]) we observe four- and five-layered clusters. On the contrary, Pt clusters of more than two layers are rarely observed even for the highest Pt coverages studied. Apparently, two-layered Pt clusters grow only laterally, whereas Ir clusters grow in all three dimensions thereby also increasing in height. As a consequence, the threshold for sintering is much lower for Pt clusters (0.75 ML) than for Ir clusters (1.5 ML).

In the following we try to explain our observations using the differences in metal-carbon adhesion and metal cohesive energy for Pt compared to Ir. Observation (i) can be explained by a stronger metal-carbon adhesion for Ir than for Pt. The metal-carbon bond dissociation energy is indeed larger for Ir than for Pt. However, the difference only amounts to approx. 3% (6.54 eV (Ir) compared to 6.32 eV (Pt) per metal-carbon bond[95]). In addition this reasoning seems to contradict observation (ii): if metal-carbon adhesion is stronger for Ir, we do not expect Ir clusters to switch to a three-dimensional growth mode as soon as all moiré cells are occupied. Yet it might be the case that the stronger metal-carbon adhesion of Ir is over-compensated by a larger cohesive energy compared to Pt (6.94 eV to 5.84 eV [136]) so that a more three-dimensional shape is probably favored for Ir clusters if they are larger than a critical cluster size. The fact that the metal-carbon adhesion is the strongest in the center of the hcp area (i.e. where positions of Ir and C atoms match best) is probably the reason why the preference of a three-dimensional shape depends on the cluster size.

Finally we will address the role of the STM tip on imaging the clusters: in Fig. 5.1 (d)-(f) the underlying graphene is not visible any more and the clusters appear to be touching each other. If we consider the amount of Pt being deposited, we find that the average cluster size e.g. in (d) is 38 atoms/cluster. As the majority of the clusters are two-layered, we will consider a typical cluster to consist of 23 atoms in the first layer and 15 in the second layer. So its lateral extension is much smaller than the moiré unit cell which consist of 9 x 9 Ir atoms. It is therefore obvious that the lateral extension of the particles is largely overestimated due to the convolution

of their shape with that of the STM tip.

5.2 Cluster-Graphene Interaction Monitored in Ir 4f and C1 s

In Chapter 4 we established that the XPS fingerprints of Pt cluster adsorption on the graphene moiré are as follows:

(i) The development of a shoulder on the high binding energy side of the C 1s peak due to rehybridization of graphene atoms from sp^2 to sp^3.

(ii) A shift of the main C 1s peak which we tentatively assigned to doping.

(iii) The appearance of an Ir_C interface component in the Ir 4f spectrum due to Ir surface atoms interacting with the graphene sheet in the areas where the graphene is pinned to the substrate.

In this section we will see how the features (i) and (iii) evolve with increasing Pt cluster size. The shift of the main C 1s peak will be discussed in Chapter 8.

Figure 5.3 shows Ir 4f spectra for Pt coverages from 0 ML to 0.75 ML. As in Section 4.3 these spectra are fitted with three components: Ir_{bulk}, $Ir_{surface}$ and Ir_C (for the fit parameter see Table 4.1).

Figure 5.3 (g) shows how the relative intensities of these components develop with Pt coverage. The intensity of Ir_{bulk} remains constant except for small fluctuations. However, spectral weight is shifted continuously from $Ir_{surface}$ to Ir_C. Apparently the area where graphene interacts strongly with the Ir surface expands at the expense of the area where the interaction is only weak. This is as expected because the larger the Pt cluster, the larger the area of graphene which it can potentially pin to the Ir surface. A detailed discussion on which fraction of the Ir surface is involved will be given at the end of this section.
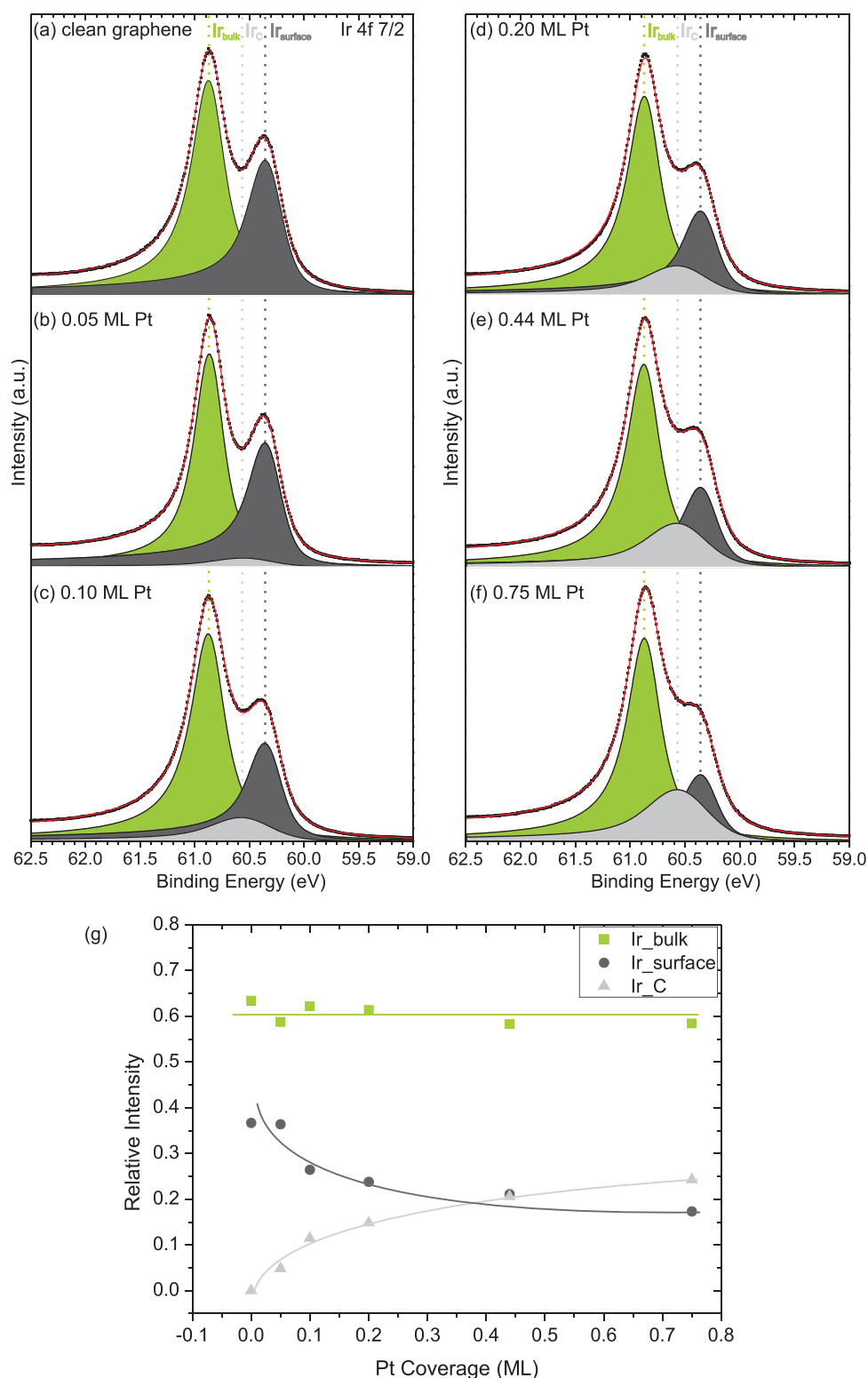
Figure 5.3 Ir $4f_{7/2}$ core level spectra for (a) clean graphene on Ir(111) and after Pt deposition of (b) 0.05 ML, (c) 0.10 ML, (d) 0.20 ML, (e) 0.44, (f) 0.75 ML respectively. The experimental spectra are shown as black dots, the fits as solid red lines, and the filled curves represent the components of the fit (green = Ir_{bulk}, light gray = $Ir_{surface}$, dark gray = Ir_C) same fit parameters as in Table 4.1 (g) Relative intensities of the three components against Pt coverage. The lines are to guide the eye.
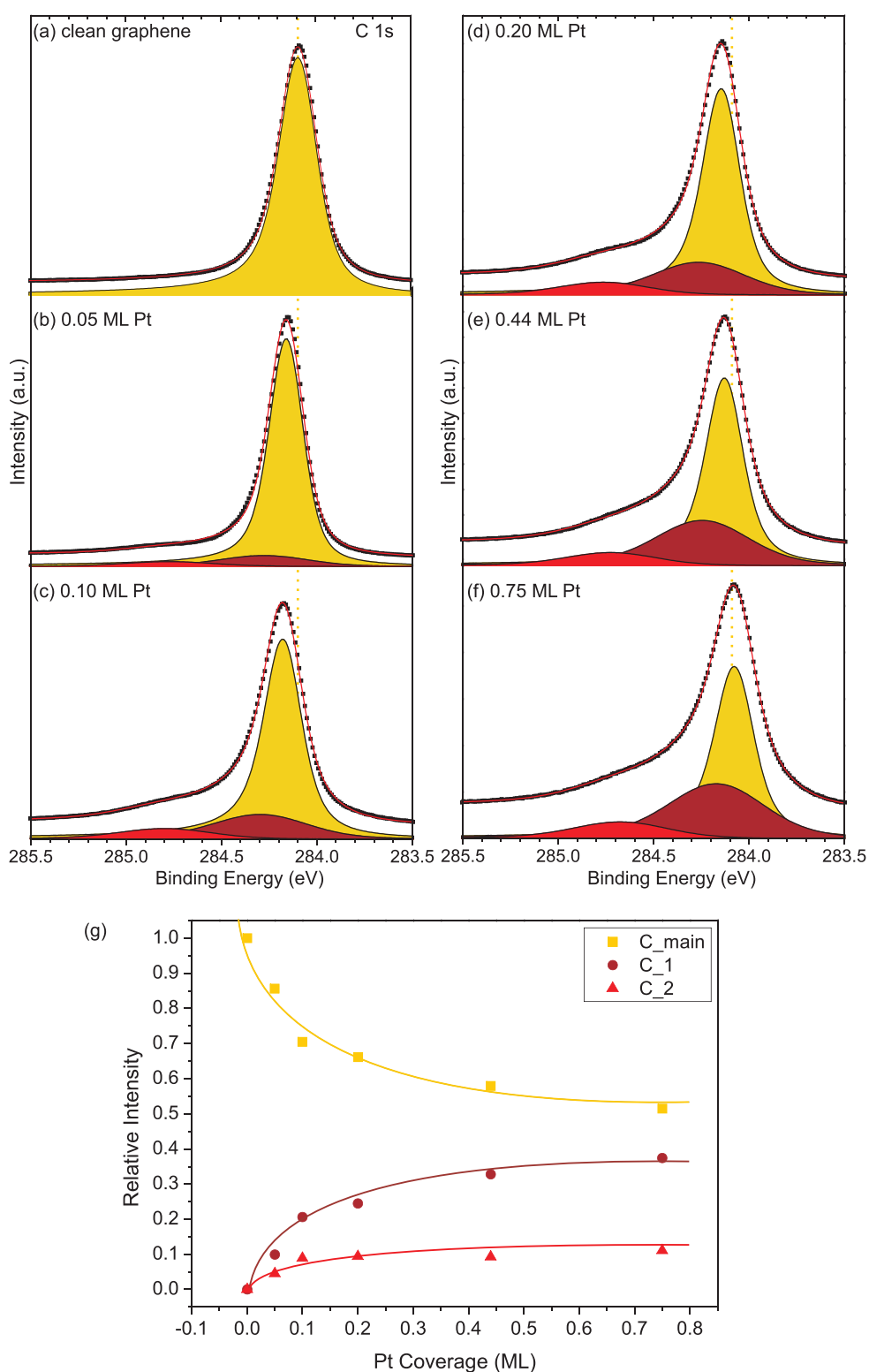
Figure 5.4 C 1s core level spectra for (a) clean graphene on Ir(111) and after Pt deposition of (b) 0.05 ML, (c) 0.10 ML, (d) 0.20 ML, (e) 0.44, (f) 0.75 ML respectively. The experimental spectra are shown as black dots, the fits as solid red lines, and the filled curves represent the components of the fit (yellow = C_{main}, dark red = C_1, light red = C_2), fit parameters as in Table 5.1. The dotted line indicates the BE position of pristine graphene. (g) Relative intensities of the three components against Pt coverage. The lines are to guide the eye.

Figure 5.4 shows the corresponding C 1s spectra. In Section 4.2 we have seen that these graphene spectra result of a superposition of 200 single peaks which extend over a binding energy interval of 0.14 eV for the case of clean graphene and of ~ 1 eV for 0.18 ML Pt on graphene. As it is not very convenient to work with 200 single peaks, we tested if a simplified analysis might also reproduce our spectra reasonably well. Indeed the spectrum of clean graphene [Fig. 5.4 (a)] can be fitted with a single DS-function located at 284.09 eV which is only slightly broader than the peaks used in Section 4.2 (it is called C_{main} in the following, see Table 5.1 for fit parameter). When fitting the spectra with clusters, the shape of this peak was kept constant. However, the peak was allowed to shift in binding energy which is necessary to fit the spectra correctly. The origin of this shift will be discussed in Chapter 8.

In order to reproduce the shoulder reasonably well, a minimum of two components had to be introduced (called C_1 and C_2 in the following, same parameter as C_{main} except for a larger GFWHM). Their position was fixed at binding energies of $+0.1$ resp. $+0.6$ eV relative to the C_{main} component. The choice of these components is the consequence of an iterative fitting procedure which aimed at reproducing the data very well by using the same set of components in all of the spectra. No deeper physical meaning should be assigned to C_1 and C_2. We will consider them just a measure for the intensity of the shoulder compared to the main carbon peak. These relative intensities are plotted in Figure 5.4 (g). With increasing Pt coverage spectral weight is shifted from C_{main} to C_1 and C_2.

	C_{main}	C_1	C_2
Relative Binding Energy (eV)	0	+0.1	+0.6
LFWHM (eV)	0.130	0.130	0.130
α	0.05	0.05	0.05
GFWHM (eV)	0.160	0.500	0.500

Table 5.1 Fit parameters of the DS-functions used to fit the C 1s spectra in Figure 5.4.

We expect a relation between the fraction of the graphene layer which is pinned to the substrate and the fraction of the Ir surface which is in close contact with this layer. This fraction of the graphene layer can be calculated as $\frac{C_1+C_2}{C_1+C_2+C_{main}}$, the fraction of the Ir surface as $\frac{Ir_C}{Ir_C+Ir_{surface}}$. These relative intensities are compared in Figure 5.5. Assuming errors of 10% the results agree. This agreement supports the fitting procedures described above.
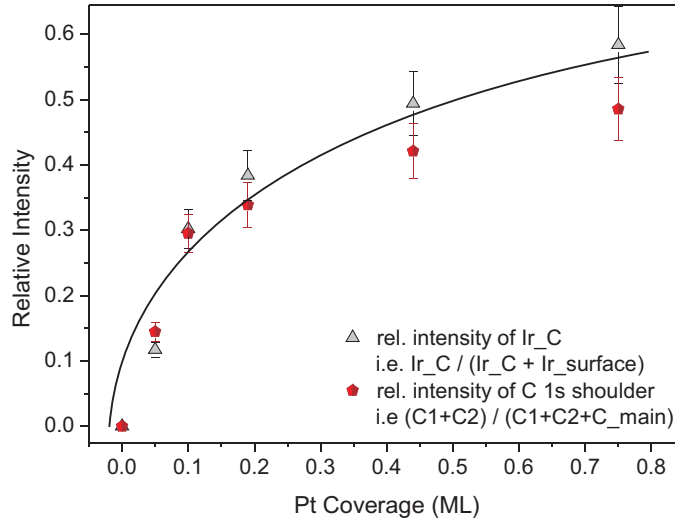
Figure 5.5 Relative intensities of the Ir 4f interface component (Ir$_C$, gray) and the C 1s shoulder components (C$_1$ + C$_2$, red) against Pt coverage. The line is to guide the eye.

At this point we want to discuss the findings of Cavallin et al. [46] who analyzed the growth of Rh clusters on the graphene/Ir(111) moiré by STM and XPS. In particular they also observe a shoulder at the high binding energy side of the main carbon peak in the C 1s spectrum which they refer to as C$_M$ (corresponding to C$_1$ + C$_2$ in our analysis) as well as an Ir interface component Ir$_C$. This is qualitatively the same finding as reported in this work. In contrast to our observation that the intensities of Ir$_C$ and C$_1$ + C$_2$ match very well, Cavallin et al. do not find such an agreement for their components. After deposition of 0.37 ML Rh at 90 K and subsequent annealing to 200 K they find the relative intensity of C$_M$ to be $\sim$ 30%, whereas the corresponding intensity of Ir$_C$ is below 10%. We can think of no reason why 30% of the carbon atoms should rehybridize to sp^3 without interacting with an equal fraction of Ir surface atoms. We can therefore not exclude that either the intensity of Ir$_C$ was underestimated or the intensity of C$_M$ was overestimated by the fitting procedure the authors applied.

5.3 Correction for Damping and Schematic Representation

For a quantitative analysis of the results, we have to consider that the intensity of Ir_C as well as the intensities of C_1 and C_2 are damped by the presence of the Pt cluster which lies above the corresponding Ir and C atoms. In the following these intensities will be corrected for damping and then used to calculate the number of involved C and Ir atoms in cluster binding.

The Pt clusters are mostly one or two layers high (compare Figures 5.1 and 5.2 respectively). C and Ir atoms below the cluster are therefore attenuated by one or two layers Pt. As seen in Figure 4.2 the graphene area which is pinned down by the cluster is larger than the base of the cluster. These carbon atoms and the Ir atoms below are not damped by the cluster. We will therefore assume that the intensity of Ir_C as well as the intensities of C_1 and C_2 are attenuated by one layer Pt in average i.e. by 40% regardless of the Pt coverage. The C and Ir atoms not taking part in the cluster binding are not damped at all. The intensities $Ir_{surface}$ and C_{main} are therefore not affected by the cluster.

Let I_{damp} be the measured intensity we want to correct (i.e. the intensity of Ir_C or the intensity of the shoulder components C_1 and C_2). If we assume that the signal is attenuated by 40%, it has to be corrected as follows: $I_{damp} \cdot \frac{100}{60}$. If we assume the main signal $I_{main} = 1 - I_{damp}$ (C_{main} or $Ir_{surface}$) to be undamped, the relative intensity of the considered component after correction for damping is:

$$I_{corr} = \frac{I_{damp} \cdot \frac{100}{60}}{I_{damp} \cdot \frac{100}{60} + (1 - I_{damp})}$$

After this treatment we are able to calculate the number of carbon atoms taking part in cluster binding. The number of involved carbon atoms per occupied moiré cell is

$$\#C = I_{C_1 + C_2, corr} \cdot \frac{200}{n}$$

where 200 is the number of carbon atoms in the approximated 10×10 over 9×9 moiré unit cell and n the fraction of occupied moiré cells. In the same way the number of involved Ir atoms is

$$\#Ir = I_{\mathrm{Ir_C,corr}} \cdot \frac{81}{n}$$

The results are presented in Table 5.2.

Coverage (ML)	n	s_{av} (atoms)	$I_{\mathrm{C_1+C_2}}$ fit	corr.	#C (atoms)	$I_{\mathrm{Ir_C}}$ fit	corr.	#Ir (atoms)
0.05	0.67	6	0.14	0.22	66	0.12	0.18	22
0.10	0.80	11	0.30	0.41	103	0.30	0.42	42
0.20	0.94	19	0.34	0.46	98	0.38	0.51	44
0.44	1	38	0.42	0.55	110	0.49	0.62	50
0.75	1	65	0.49	0.61	122	0.58	0.70	57

Table 5.2 n and s_{av} for different Pt coverages as derived from the STM data shown in Figure 5.1, corresponding fitting results for C 1s and Ir 4f spectra (i.e. relative intensity $I_{\mathrm{C_1+C_2}}$ and $I_{\mathrm{Ir_C}}$ of the components $C_1 + C_2$ and Ir_C respectively before and after correction for damping) and the number of corresponding carbon and iridium atoms #C and #Ir in the approximated moiré unit cell.

We used these results to derive the ball models of the approximated moiré unit cell shown in Figure 5.6. Models for representative clusters of average or close to average size and of typical height are shown for each coverage and a representative number of involved C and Ir atoms are accentuated. Pt cluster atoms are shown in blue, sp^2 carbon in yellow, sp^3 carbon in red, Ir bulk in green, Ir surface in dark gray and Ir$_{\mathrm{C}}$ interface in light gray (colors correspond to the components of the fit in Figures 5.3 and 5.4 respectively). The position of the cluster is as derived by DFT for the Pt$_{19}$ in the previous Section. Also the slight asymmetry, i.e. that the graphene is pinned down more strongly in between hcp and fcc regions than in between hcp and top regions, is inspired by DFT.
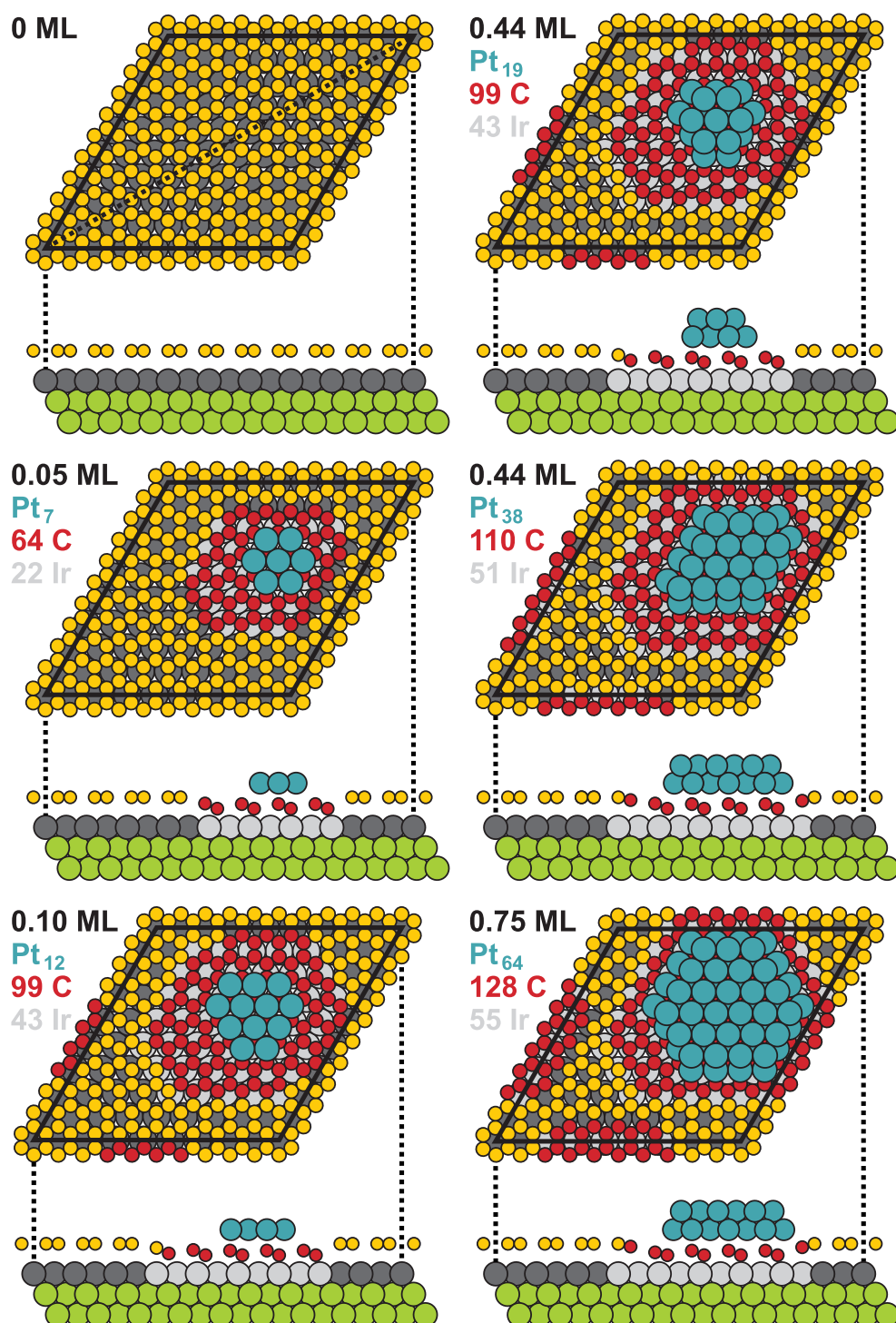
Figure 5.6 Representative ball models as derived from the results in Table 5.2. Shown is a top view as well as a side view along the unit cell diagonal. Pt cluster atoms are blue, sp^2 carbon atoms yellow, sp^3 carbon red, Ir surface dark gray, Ir interface light gray, Ir bulk light green. Colors correspond to the fit components in Figures 5.3 and 5.4 respectively. The Pt coverages and the cluster size is indicated. The number of Ir and C atoms affected by the rehybridization is given in the corresponding color.

The main finding is that the pinned graphene area is always larger than the cluster's base area. This effect is the stronger the smaller the clusters are in size. For the Pt_7 for example the pinned graphene area is 3 times larger than the cluster's base. For the Pt_{64} this area is still 1.5 times larger than the cluster's base. Thus, one could think of using a more sophisticated model of damping by the clusters than assuming a constant damping factor of 40% for all cluster sizes. However, an improved model must include an iterative procedure of estimating the damping factors. As we do not believe that our results would change significantly we refrain from such an effort.

For the largest Pt coverage of 0.75 ML the pinned areas of neighboring cells are almost touching each other. If they touch one can easily imagine the cluster coalescing with the neighboring cluster. This is in line with the finding that 0.75 ML Pt coverage is the threshold for coalescence [compare Figure 5.1 (e)].

We want to stress that these models were drawn ab-initio just using the results shown in Table 5.2 and the DFT results for a flat Pt_{19} cluster (compare Section 4.2) and are not meant to be more than schematic visualizations of our STM and XPS results. Of course DFT calculation for all cluster sizes or surface X-ray diffraction (SXRD) measurements would be desirable for confirmation of these models. The latter technique was recently employed to determine the structure of Ir_{80} clusters on the graphene/Ir(111) moiré [137]. It would be of interest to extend such studies to Pt and Ir clusters of different sizes to confirm the differences in growth mode between those two as they are described above.

5.4 Pt 4f Spectra

For the sake of completeness we will conclude this chapter by taking a look at the
Pt 4f spectra corresponding to the different cluster sizes discussed above. They are
shown in Figure 5.7. All spectra show the same complex shape as the spectrum
shown in Figure 4.4. The shape was successfully described by DFT and originates
from differently coordinated Pt atoms having different core level shifts (compare Fig.
4.4 and [46] respectively). Thus the spectra result from a superposition of various
components and we do not attempt to deconvolute them. As expected, the intensity
scales with coverage.
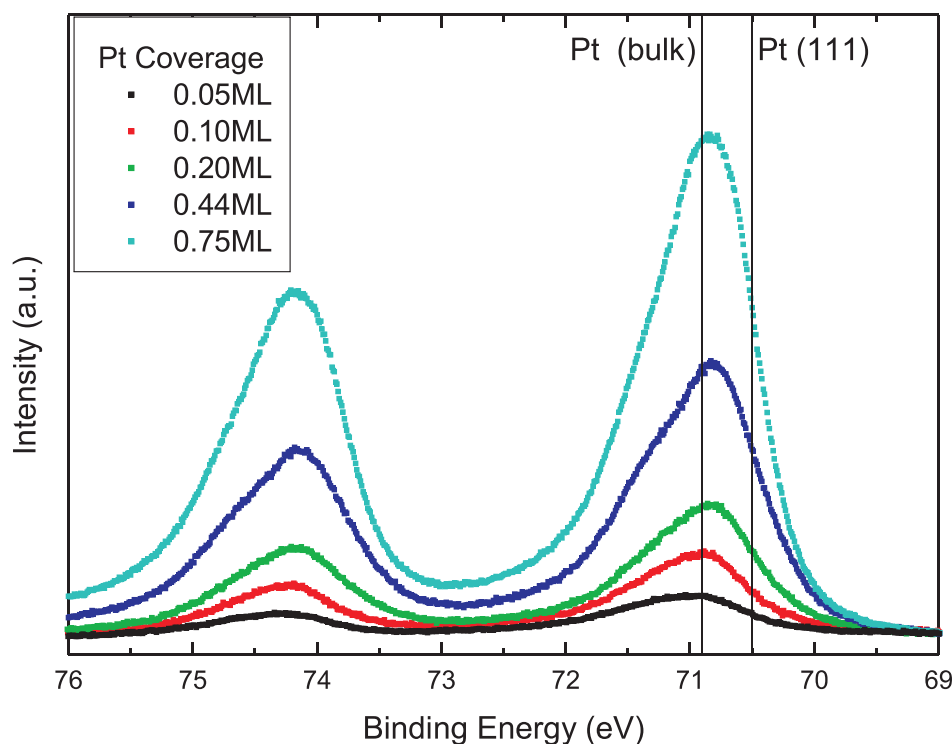
Figure 5.7 Pt 4f spectra for the indicated Pt coverages. Spectra are normalized to the
background and a linear background was subtracted. The binding energies for bulk Pt
(70.9 eV) and Pt(111) (70.5 eV) are indicated.

5.5 Conclusions

The growth mode and structure of Pt clusters on the graphene/Ir(111) moiré was investigated by means of STM and XPS. STM measurements revealed that once Pt clusters are two-layered their further growth is restricted to two dimensions which is different from the growth of Ir clusters [44]. The threshold for sintering was found to be at 0.75 ML Pt so that the upper size limit for Pt clusters arranged in a lattice is 65 atoms.

The cluster-graphene interaction as well as the graphene-Ir surface interaction was investigated with spectra of the C 1s and the Ir 4f regions respectively. It was found that the related components, namely the C 1s shoulder and the Ir interface component, agree regarding their relative intensities. This further confirms our bonding picture of rehybridized carbon atoms that are pinned to the Ir substrate by the Pt clusters. The intensities were corrected for damping by the Pt clusters.

Combining the information gathered with STM and XPS representative ball models of Pt clusters and how they bind to the graphene were derived.

The Pt 4f spectra were found to be a superposition of several components. The resulting spectra are of complex shape and were not further investigated.

6 CO-Induced Smoluchowski Ripening of Pt Cluster Arrays

In this chapter, cluster arrays grown on Gr/Ir(111) are tested for their stability with respect to gas exposure, with a focus on Pt clusters exposed to CO. Firstly, we will analyze the STM data (Section 6.1) and find that small Pt clusters, containing fewer than 10 atoms, are unstable upon CO adsorption. They sinter through Smoluchowski ripening - cluster diffusion and coalescence - rather than the frequently reported Ostwald ripening mediated by metal-adsorbate complexes. Larger clusters remain immobile upon CO adsorption, but become more three-dimensional. Careful analysis of the XPS data complemented by DFT calculations provide inside into the origin of the CO induced Pt cluster ripening and shape transformations (Section 6.2 - 6.4).

The "skyhook" effect on surface diffusion is a concept with a long history [56, 57, 139–141]; promotion of diffusion by atop adsorption of hydrogen on a metal adatom is the classic example [140, 141]. But, the skyhook effect is also known in the diffusion of clusters. For example, Cu transport on Cu(111) speeds up dramatically in the

presence of small surface concentrations of S. The reason is that Cu_3S_3 adclusters have a low formation energy, and are mobile because their strong internal binding weakens their attachment to the substrate [56, 57]. It seems plausible that adsorbed CO molecules act similarly as a skyhook for a Pt cluster on a graphene-covered Ir(111) surface. Our working hypothesis is that CO adsorption raises the cluster to a height where the potential of the underlying graphene is relatively weakly corrugated. Thus diffusion should be facile, and the observed Smoluchowski ripening a consequence.

Section 6.5 deals with the growth of Pt particles in the presence of CO, before we extend our study to adsorption of other gases (H_2, O_2) on Pt clusters, as well as to adsorption of CO on other metal clusters (Ir, Au) (Section 6.6).

6.1 STM View of Pt Cluster Arrays Exposed to CO

Fig. 6.1(a),(c),(e),(g),(i) and (k) displays STM topographs after Pt deposition onto Gr/Ir(111). The deposited amount is increased from of 0.05 ML to 1.00 ML Pt so that the average cluster sizes is tuned from $s_{av} = 5$ atoms to $s_{av} = 174$ atoms (see Table 6.1). Note that this data is similar data or in some cases the same data as shown in Figure 5.1 of Section 5.1.

With CO exposure the cluster arrays are transformed to the ones shown in the topographs on the right side of each panel [Fig. 6.1(b),(d),(f),(h),(j) and (l)]. Full time lapse sequences of the experiments with Pt coverages of 0.05, 0.20, and 0.44 ML, respectively are available on the internet ([142], movies 1-3). For clarity, locations of cluster disappearance are marked in each of the related topographs by thin white circles. Table 6.1 summarizes the changes by listing before and after CO exposure: the average cluster height $\bar{h}$, the fraction of moiré cells occupied n (the filling factor), as well as partial filling factors of the moiré n_1, n_2, n_3 and n_4 with 1-, 2-, 3- and 4-layered clusters, respectively. The data represented in Table 6.1 after CO exposure were obtained from STM topographs at late times, when cluster sintering had terminated and a stationary state was reached.

Analysis of Fig. 6.1 together with Table 6.1 yields the following conclusions: (i) CO exposure causes substantial sintering of small clusters [compare Fig. 6.1(a) and (b), (c) and (d)] while the effect is negligible for large clusters [compare Fig. 6.1 (g) and (h), (i) and (j), (k) and (l)]. With increasing initial cluster size s_{av} the reduction
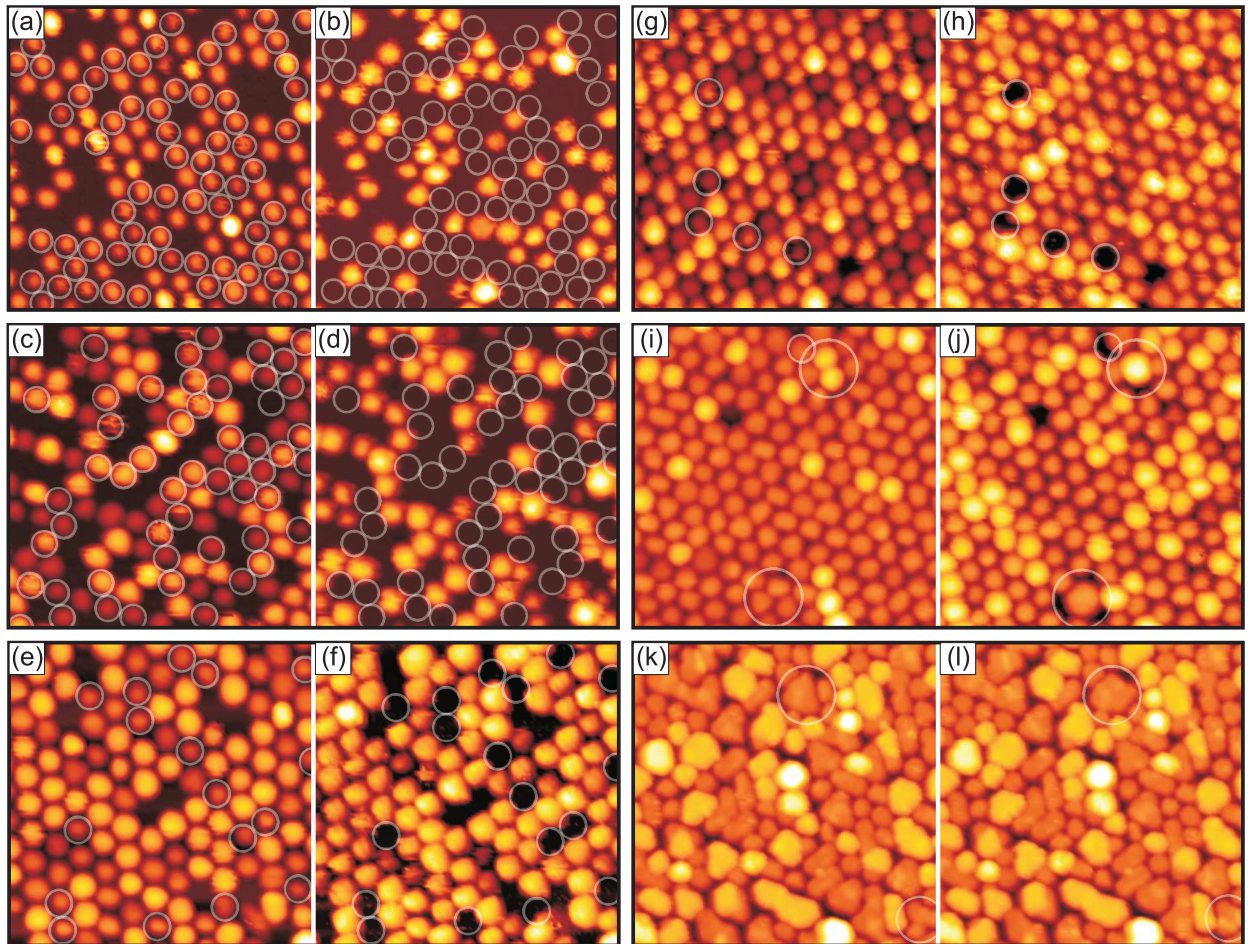
Figure 6.1 STM topographs of Pt cluster arrays on Gr/Ir(111) taken at the same sample location before and after exposure to CO. (a) Deposited amount $\theta = 0.05\,\text{ML}$ Pt; (b) as in (a), but after additional exposure to $1.1\,\text{L}$ CO at $p_{\text{CO}} = 1 \times 10^{-9}\,\text{mbar}$. (c) $0.10\,\text{ML}$ Pt, (d) + $32\,\text{L}$ CO, $p_{\text{CO}} = 1 \times 10^{-8}\,\text{mbar}$. (e) $0.20\,\text{ML}$ Pt, (f) + $16\,\text{L}$ CO, $p_{\text{CO}} = 1 \times 10^{-8}\,\text{mbar}$. (g) $0.44\,\text{ML}$ Pt, (h) + $20\,\text{L}$ CO, $p_{\text{CO}} = 1 \times 10^{-8}\,\text{mbar}$. (i) $0.75\,\text{ML}$ Pt, (j) + $39\,\text{L}$ CO, $p_{\text{CO}} = 1 \times 10^{-8}\,\text{mbar}$. (k) $1.00\,\text{ML}$ Pt, (l) + $12\,\text{L}$ CO, $p_{\text{CO}} = 1 \times 10^{-8}\,\text{mbar}$. Clusters which disappear during CO exposure and their former location are marked with small circles. Events of sintering in (i) and (j) resp. (k) and (l) are marked by large circles. Image size is always $290\,\text{Å} \times 290\,\text{Å}$.

Table 6.1 Pt amounts θ, average cluster size s_{av}, average cluster height $\bar{h}$, filling factors n_1, n_2, n_3 and n_4 of the moiré lattice with Pt clusters of one, two, three and four layers height, respectively, as well as their sum n before and after CO exposure. Analysis based on sample areas containing more than 600 moiré cells of the experiments visualized by 6.1. Data after CO exposure were obtained when sintering had terminated.

θ	s_{av} (atoms)	$\bar{h}$ (ML)	n_1	n_2	n_3	n_4	n
0.05 ML	5	1.09	0.75	0.07	0.00	0.00	0.82
0.05 ML + CO	10	1.24	0.30	0.10	0.00	0.00	0.40
0.10 ML	11	1.50	0.40	0.40	0.00	0.00	0.80
0.10 ML + CO	19	1.66	0.16	0.31	0.00	0.00	0.47
0.20 ML	19	1.54	0.43	0.51	0.00	0.00	0.94
0.20 ML + CO	21	1.85	0.08	0.74	0.00	0.00	0.82
0.44 ML	39	1.99	0.25	0.50	0.24	0.00	0.99
0.44 ML + CO	39	2.38	0.00	0.61	0.37	0.00	0.98
0.75 ML	65	2.15	0.00	0.87	0.09	0.03	0.99
0.75 ML + CO	65	2.45	0.00	0.55	0.43	0.01	0.99
1.00 ML	174	2.53	0.00	0.27	0.18	0.05	0.50
1.00 ML + CO	174	2.53	0.00	0.27	0.18	0.05	0.50

of n diminishes, until cluster sintering vanishes for $s_{av} > 50$ atoms. (ii) Cluster disappearance is primarily due to 1-layered clusters, i.e. the smallest clusters in the size distribution. Note that the few clusters that disappear for $s_{av} = 39$ [white circles in Fig. 6.1(g) and (h)] are all 1-layered ones. (iii) While for $s_{av} = 5$ atoms the decrease of n_1 is primarily due to cluster disappearance, for $s_{av} = 39$ the decrease is almost exclusively by transformation of 1-layer to multi-layer clusters without affecting n. (iv) In consequence of the substantial decrease of n_1 the average cluster height $\bar{h}$ increases upon CO exposure. Note that for $s_{av} = 19$ and $s_{av} = 39$ the cluster height distribution narrows upon CO exposure, i.e. the clusters become more uniform in height. (v) For $s_{av} = 65$ the average cluster height $\bar{h}$ increases by transformations from 2-layer to 3-layer clusters. (vi) For $s_{av} = 174$ the cluster lattices is not changed except for very rare sintering events.

Time lapse sequences of STM images taken during CO exposure provide insight into the mechanisms of cluster disappearance and transformation. Fig. 6.2 (a) and (b) are two consecutive topographs during 1×10^{-9} mbar CO exposure of a 0.05 ML Pt cluster array (full sequence is provided as movie 4 on the internet [142]). Event (i) is a movement of a cluster to a neighboring *empty* moiré unit cell. Event (ii) is a movement of a cluster to an adjacent *occupied* moiré unit cell. The 1-layered clusters coalesce and form a 2-layered cluster. While with adsorbed CO such cluster motion to empty and occupied neighboring moiré unit cells takes place at 300 K, substantially higher temperatures are required for cluster motion without CO [15]. The obvious conclusion from these observations is that CO exposure causes Smoluchowski ripening (diffusion and coalescence) of clusters and thereby the reduction of n.

Figures 6.2 (c) and (d) are two consecutive STM topographs during 1×10^{-8} mbar CO exposure of a 0.20 ML Pt cluster array (full sequence is provided as movie 2 [142]). The two encircled clusters transform from 1-layered to 2-layered clusters without any other changes in their environment. We name such a change towards a more 3-dimensional shape *without* supply of material from other moiré cells a shape transformation.

CO-induced cluster mobility and CO-induced shape transformations are two distinct, essentially unrelated effects. It is obvious from event (i) in Fig. 6.2 (b) that small clusters are set in motion without a shape transformation. Also the 0.05 ML data in Table 6.1 make plain that coalescence of two small 1-layered clus-
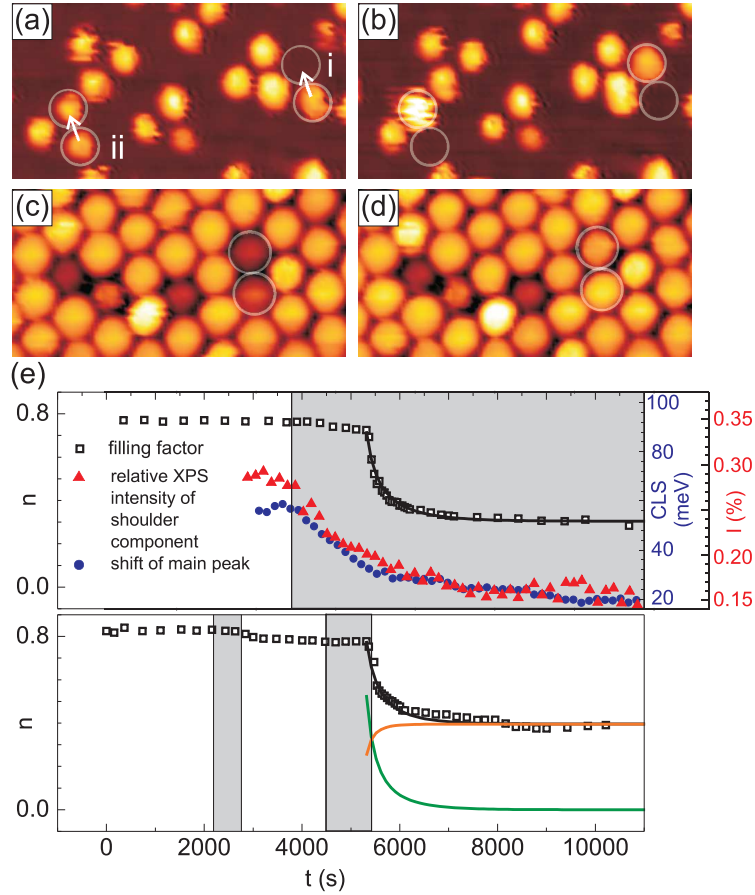
Figure 6.2 (a),(b) Consecutive STM topographs after deposition of 0.05 ML Pt during CO exposure with 1×10^{-9} mbar. Time between images $\Delta t = 53$ s. Stills from movie 4 [142]. (c),(d) Consecutive STM topographs after deposition of 0.20 ML Pt during 1×10^{-8} mbar CO exposure. Time between images $\Delta t = 53$ s. Stills from movie 2 [142]. (e) Filling factor n (black open squares) as a function of time t for cluster arrays formed by deposition of 0.05 ML Pt. Times of exposure to 1×10^{-9} mbar CO are indicated by gray shading. Full black lines are model fits (see text). Data for upper and lower panel taken from movie 4 and movie 1, respectively. In upper panel additionally the relative XPS intensity I of the C 1s component related to cluster binding (right axis, red up triangles) and the core level shift (CLS) of the main C 1s peak (right axis, blue full dots) are plotted versus t for a 0.05 ML Pt cluster array. Data shifted on t-axis such that start of 1×10^{-9} mbar CO exposure matches with the one from STM movie in same panel. In lower panel additionally fractions n_m of mobile (green line) and n_i of immobile (orange line) clusters according to model fit are plotted (see text).

ters mostly results in a 1-layered coalesced cluster. For clusters with more than 10 atoms CO-induced cluster mobility dies off and shape transformations become the more frequent, the larger the clusters are. This can be inferred from Fig. 6.2(c) and (d), Table 6.1 and the movies of the 0.20 ML and 0.44 ML cluster arrays [142].

Figure 6.2 (e) displays the analysis of the filling factor n versus time t based on STM movies of 0.05 ML Pt cluster arrays (movies 4 and 1 [142]). In the upper panel initially n (open squares) is constant with time within the limits of error (error primarily from STM drift). Start of exposure to 1×10^{-9} mbar CO, indicated by the gray shading, causes only a slight gradual decrease of n. It is caused by rare coalescence events. About 1500 s after the start of CO exposure (after 1.1 L CO dosed) a sharp decrease of n signifies onset of high cluster mobility and a large number of coalescence events. 2000 s later the cluster density stabilizes at about half of its initial value.

In the lower panel a similar experiment is analyzed, where dosing of CO was performed in two parts. After a first dose of 0.4 L only a slight decrease of n is observed. Continued imaging after pumping out CO reveals no further change in the cluster array. Reopening the CO valve and dosing of CO also displays no significant changes in n until the second dose reaches 0.7 L (the integral dose reaches 1.1 L). Closing the CO valve immediately after the onset of cluster mobility and coalescence does not impede the ripening process. Instead, n continues to decrease with the same time behavior and to a similar level, as observed in the upper panel in the presence of CO.

It must be concluded that after a threshold exposure of about 1.1 L the properties of the Pt clusters are changed to an extent that they are mobile, irrespective of the continued presence of gas. As CO is known to adsorb on Pt at 300 K and to desorb only with negligible rates, we conclude that the threshold dose is related to a threshold coverage. Moreover, our experiment makes clear that the heat of CO adsorption on the Pt clusters is irrelevant for cluster mobility.

6.1.1 Relevance of Tip-Cluster Interactions

Donner and Jacob [36] investigated tip induced cluster manipulation in some detail and pointed out that high tunneling resistances $R \approx 2 \times 10^9 \, \Omega$ are necessary to avoid Pt cluster pick-up, and lateral displacement, on graphene on Ru(0001). Early on, we used an STM tip similarly, as a tool for Ir cluster removal from graphene on Ir(111)

[44]. Thus, it is natural to ask how significantly the results we present in Figures 6.1 and 6.2 were affected by tip cluster interaction. Indeed, we found as well that the probability for tip cluster interaction decreases monotonically with R and therefore used $R \geq 2 \times 2^{10}\,\Omega$ throughout. The tunneling parameters chosen ($U = 1\,\mathrm{V}$ and $I = 32 - 52\,\mathrm{pA}$) are a trade-off between minimizing tip cluster interaction on the one hand and maintaining a reasonable lateral resolution plus speed of the feedback loop for time resolution of the processes on the other hand. Under these conditions cluster manipulation by the STM tip is a very rare event. Indeed, close inspection of the movies 1-4 reveals that occasional tip cluster interaction events were present, specifically once the clusters are mobilized by CO. Evidence for cluster pick-up and rare events of material deposition was found. Also cluster motion to another moiré unit cell and cluster height changes are observed while the tip is scanning the respective clusters. However, since cluster motion and cluster height changes are frequent in the related coverage regimes, such events must take place occasionally when the tip is just scanning the cluster under concern and need not to be due to a tip cluster interaction. Areas scanned only twice, before CO exposure and after sintering had terminated, show only slight differences for n and the n_i compared to areas that were continuously scanned more than 150 times during CO exposure.

In order to settle this issue, Fig. 6.3 provides a quantitative analysis for an $0.05\,\mathrm{ML}$ cluster array related to the experiment of movie 1. Small clusters, as here with an initial $s_{av} = 5$, are least strongly bound and therefore most susceptible to tip cluster interaction. Fig. 6.3(a) displays a large scale topograph, in which the locations of the first frame of movie 1 (gray square) and the last frame of movie 1 (blue square) have been indicated. In between the squares the image frame gently drifted from frame to frame. The lower part of the topograph has not been scanned before, the left part only once, prior to CO exposure. It is apparent that close to the step edge in the scanned area (blue square) n is somewhat lower and an extraordinary large cluster is present. These facts are indeed related to tip cluster interaction. However, the other area in the blue square and its surrounding display very similar appearance and filling factors. Figure 6.3(b) provides a bar chart, where n_1, n_2 and n are compared before CO exposure [gray bar, evaluated from area of gray square in Fig. 6.3(a)], after CO exposure in the last frame of movie 1 [blue bar, evaluated from blue square in Fig. 6.4(a)] and after CO exposure in an area never scanned before [yellow bar, evaluated from yellow rectangle in Fig. 6.3(a)]. In total, the filling
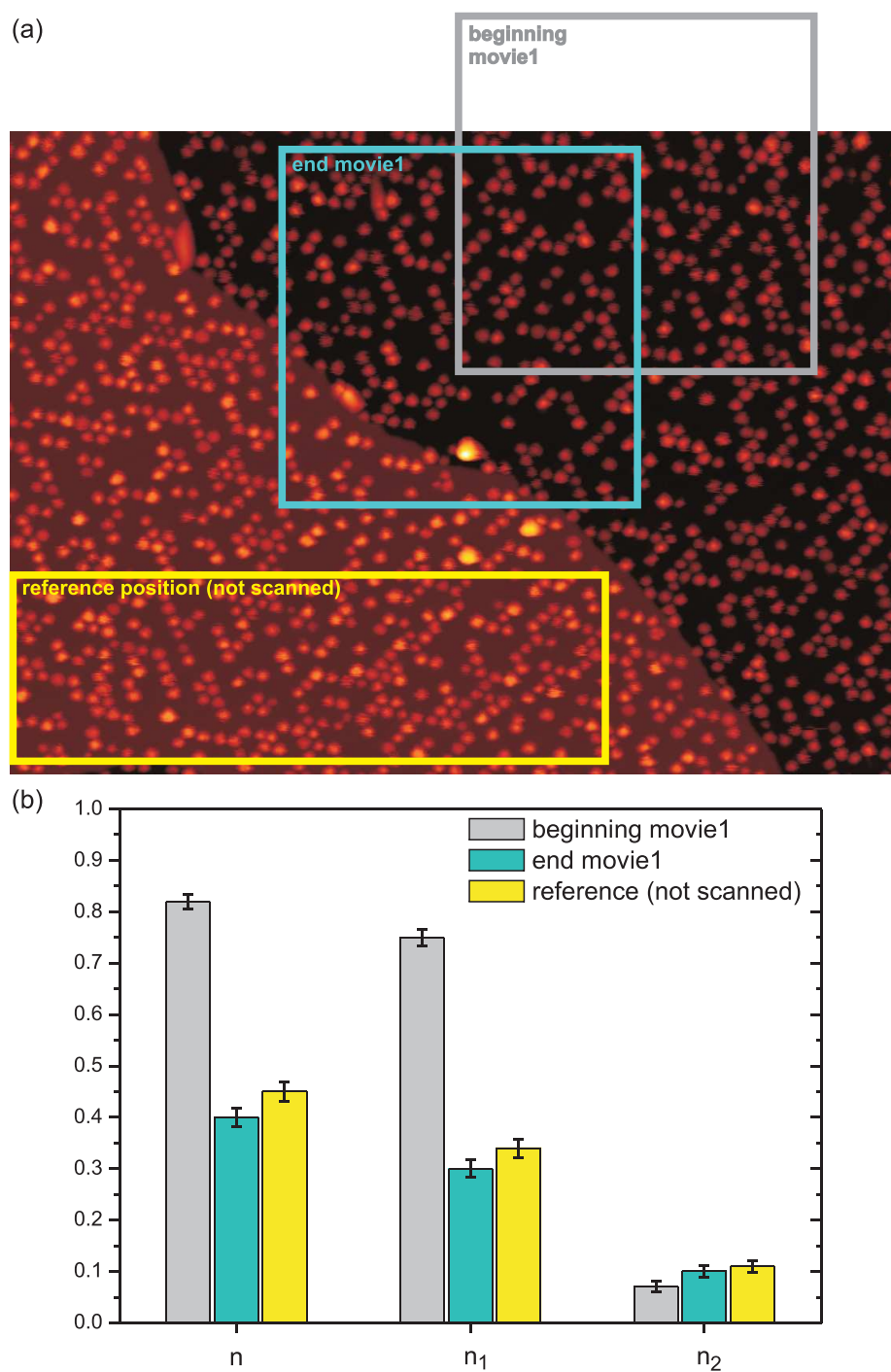
Figure 6.3 (a) 0.05 ML Pt cluster array imaged after movie 1 was recorded and sintering had ceased. The boxes mark the positions of the first frame of movie 1 (gray), of the last frame of movie 1 (blue) as well as a location of the sample not scanned before (yellow). Image size is 1400Å × 1000Å. (b) Corresponding filling factors n_1, n_2 and n of the clusters in the regions marked in (a).
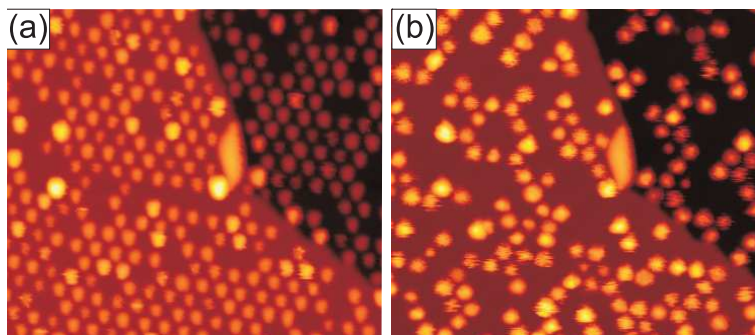
Figure 6.4 0.05 ML Pt cluster array imaged (a) before and (b) after movie 1 was recorded (thus before and long time after CO exposure), but not imaged in between. Image size is 460Å x 400Å.

factor decreased from $n = 0.82$ before CO exposure to $n = 0.40$ in the continuously scanned area as compared to $n = 0.45$ in the area never scanned before. Though there is a small and noticeable tip cluster interaction effect, based on this analysis it must be concluded that the STM movies provide a proper qualitative view of CO adsorption-induced dynamic effects in the cluster arrays.

In support of this conclusion, Fig. 6.4 displays side-by-side the same location prior to CO exposure [6.4(a)] and after clustering sintering had ceased [6.4(b)]. The location has not been scanned in between. Figure 6.4(b) is indeed the upper left corner of Fig. 6.3(a). Qualitatively and quantitatively it displays the same changes as shown in Fig. 6.1 (a) and (b) and as apparent from movie 1.

Thereby it can be ruled out that the Smoluchowski ripening observed dynamically in the STM movies was caused by tip cluster interactions. The quantitative analysis provided in Table 6.1 was conducted on areas that were at most scanned twice, before CO exposure and after sintering had terminated. Thereby tip effects are eliminated. All general features derived from Table 6.1 are present in all experiments conducted. However, specifically for 0.05 ML cluster arrays some variation in the initial filling factors n and n_i were observed from experiment to experiment, depending on the graphene quality and the deposition conditions (see below).

To summarize, our experiments provide unambiguous evidence that cluster sintering proceeded by Smoluchowski ripening only. In the entire data taken not a single event of a gradual disappearance of a cluster was observed. Clusters always moved and disappeared as integral entities as shown in Fig. 6.2. The observation that clustering sintering ceases, irrespective of whether CO is supplied continuously or

not, is consistent with this view. If Smoluchowski ripening prevails, cluster sintering stops once the clusters have become too large to detach from the substrate to move (see below for a more detailed discussion), as observed. If Ostwald ripening would prevail, it would be hard to understand why the formation of mobile carbonyl species abruptly stops, if clusters have reached a certain size.

6.1.2 Quantitative Analysis of Cluster Mobility

In previous work we described [15] cluster hopping with a rate ν as a thermally activated process: $\nu = \nu_0 e^{E_a/k_B T}$. Here k_B, T, E_a and ν_0, are the Boltzmann constant, temperature, activation energy and attempt frequency for a move. With the simplifying assumption of identical diffusion properties for the entire cluster ensemble we were to able obtain quantitative estimates for E_a and ν_0 using the temperature dependence of ν as obtained from isochronal annealing sequences. Here we extend this approach to describe adsorption-induced cluster mobility. After the threshold exposure of CO we assume a cluster to be within one of the two classes: it belongs either to the fraction n_m of mobile clusters or to the fraction n_i of clusters that could not be mobilized by CO. The decrease of n_m with time is then

$$\frac{dn_m}{dt} = -\nu n_m n_i - \nu 2 n_m n_m$$

The first term describes the decrease by coalescence of a mobile cluster with an immobile cluster, the second term the decrease by coalescence of two mobile clusters. Similarly, the increase of n_i is then

$$\frac{dn_i}{dt} = \nu n_m n_m$$

This system of non-linear differential equations is solved numerically. The sum of the starting values $n_i(0) + n_m(0)$ equals the initial filling factor $n(0)$ obtained from the experimental data. The ratio $\frac{n_m(0)}{n_i(0)}$ as well as ν are fitting parameters.

The black lines in Fig. 6.2 (e) are excellent fits to the experimental $n(t)$. The fit parameters are $\nu = 4 \times 10^{-3} Hz$ and $\frac{n_m(0)}{n_i(0)} = 6.2$ for the upper panel as well as $\nu = 4 \times 10^{-3} Hz$ and $\frac{n_m(0)}{n_i(0)} = 2.12$ for the lower panel. The fact that the same hopping rate fits both experiments lends credence to our description. In the lower panel the solution $n(t)$ is also separated into its constituents $n_m(t)$ (green) and $n_i(t)$ (orange). The ratio $\frac{n_m(0)}{n_i(0)}$ differs between the upper and the lower panel fit. Inhomogeneities in

the initial cluster size distribution or the fact that CO was pumped out after reaching the threshold dose in the lower panel experiment might cause this difference.

In addition, we performed an experiment similar to the one shown in Fig. 6.1 (a) and (b) but at lower temperature. We exposed $0.05\,\mathrm{ML}$ Pt to $22\,\mathrm{L}$ of CO at $90\,\mathrm{K}$. In this experiment the filling factor n was reduced from 0.66 to 0.51 after CO exposure which is a reduction of n by 23%. This is much less than the reduction of n by 50% as in the room temperature experiment [Fig. 6.1 (a) and (b)]. This result is fully consistent with our assumption that the CO induced cluster hopping is a thermally activated process.

6.2 Adsorption Site Determination by XPS
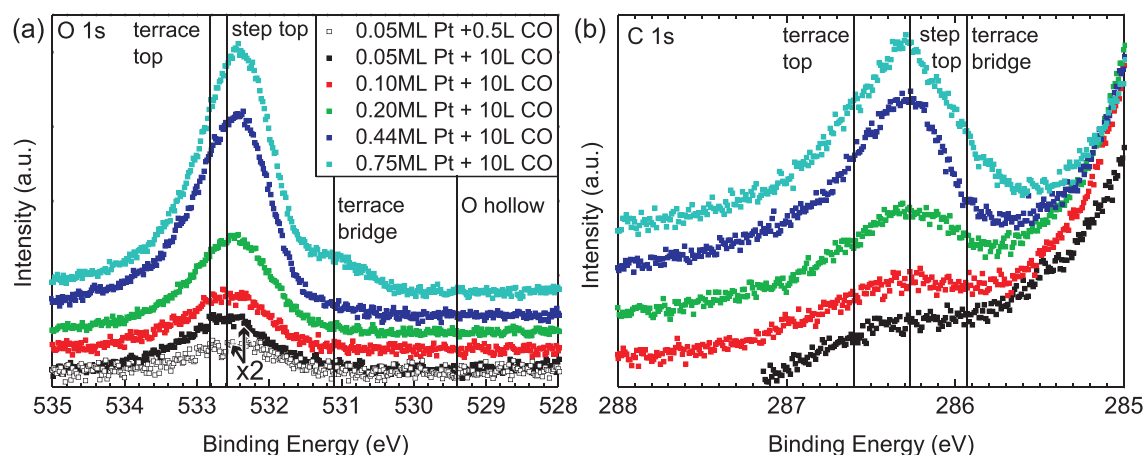
Figure 6.5 (a) O 1s spectra of $0.5\,\mathrm{L}$ CO adsorbed on $0.05\,\mathrm{ML}$ (open black) and $10\,\mathrm{L}$ CO adsorbed on $0.05\,\mathrm{ML}$ (black), $0.10\,\mathrm{ML}$ (red), $0.20\,\mathrm{ML}$ (green) $0.44\,\mathrm{ML}$ (blue) and $0.75\,\mathrm{ML}$ (cyan) Pt cluster arrays. Core level binding energies for CO adsorbed in terrace atop, terrace bridge and step atop sites on Pt(355) [143] as well as for oxygen adsorbed in hollow sites on Pt(111) [134] are indicated. Spectra are shifted vertically for clarity. Both spectra for $0.05\,\mathrm{ML}$ Pt are multiplied by a factor of 2. (b) C 1s fingerprint region of C atoms in CO after exposure of $0.05\,\mathrm{ML}$, $0.10\,\mathrm{ML}$, $0.20\,\mathrm{ML}$, $0.44\,\mathrm{ML}$ and $0.75\,\mathrm{ML}$ Pt cluster arrays to $10\,\mathrm{L}$ CO. Binding energies for CO adsorbed in terrace atop, terrace bridge and step atop sites on Pt(332) [144] are indicated. Spectra are shifted vertically for clarity. All $10\,\mathrm{L}$ CO exposures were done at $p_{\mathrm{CO}} = 1 \times 10^{-7}\,\mathrm{mbar}$, $0.5\,\mathrm{L}$ CO was dosed at $p_{\mathrm{CO}} = 1 \times 10^{-9}\,\mathrm{mbar}$.

To relate the CO exposure induced Pt cluster dynamics to adsorption properties we conducted high resolution XPS experiments and measured O 1s spectra of the O atoms in CO and C 1s spectra of the C atoms in CO. No O 1s peak intensity was

detected on pristine Gr/Ir(111) after CO exposure, consistent with the absence of CO adsorption on Gr/Ir(111). The lowest spectrum in Figure 6.5 (a) (open black squares) displays the O 1s region of the photoemission spectrum measured after exposure of a 0.05 ML cluster array to 0.5 L CO. It corresponds to the situation before cluster coalescence, which sets in only after exposure to the threshold dose of 1.1 L. The other spectra were measured after 10 L CO exposure of 0.05 ML, 0.10 ML, 0.20 ML, 0.44 ML and 0.75 ML Pt cluster arrays. They correspond to situations where cluster coalescence has already taken place [Fig. 6.1 (b),(d),(f),(h),(j) and (l)]. With increased Pt-deposition the O 1s peak area and thus the amount of adsorbed CO increases, as might be expected. The O 1s peak position is independent of whether cluster coalescence has taken place or not (0.05 ML array, lower two spectra) and of the deposited amount (upper three spectra). This suggests an identical CO adsorption site for all situations. We indicate the O 1s binding energies for CO adsorbed in terrace atop, terrace bridge and step atop sites on Pt(355) [143] by vertical lines in Fig. 6.5 (a)[1]. Since the O 1s photoemission binding energies are rather sensitive to the adsorption geometry of CO, the comparison with our measured value suggests the CO-molecules to be adsorbed atop at the cluster edge atoms. Adsorption of oxygen (and thus dissociation of the CO-molecule) can be ruled out by absence of a feature at 529.4 eV [134] [vertical line "O hollow" in Fig. 6.5 (a)], which would be present for O adsorbed in the threefold hollow sites on Pt. Note that when clusters start to develop larger terraces, owing to their size and by coalescence, a shoulder at the terrace bridge bound position starts to develop in the O 1s spectrum. We observed this for the 0.75 ML cluster array [cyan spectrum in Fig. 6.5 (a)]. Since bridge bonding is present on Pt(111) terraces after saturation with CO, this could have been anticipated.

Figure 6.5 (b) displays the C 1s fingerprint region of C atoms in CO after exposing the Pt cluster arrays to 10 L CO. The strongly asymmetric shape of the background is due to the C 1s peak of graphene located at 284.1 eV as described in Chapter 4 [see also Fig. 6.7]. Consistent with the O 1s spectra, also for the C 1s spectra the peak position is independent of the deposited amount and confirms identical adsorption sites for all situations. The comparison between our C 1s spectra and those measured for CO adsorbed in terrace atop, step atop, and bridge sites on

---

[1]Note that the O 1s binding energy for step adsorption from Tränkenschuh et al. [143] can only be assigned to atop sites at step edges with the help of a second article by the same authors [145].

Pt(332) [144] indicates that CO adsorbs on step atop Pt sites, consistent with our inferences based on the O 1s spectra. However, adsorption on terrace atop sites cannot be excluded entirely.

We also investigated the corresponding Pt 4f spectra acquired after CO exposure of the Pt clusters. Due to the complex structure of the Pt 4f signal (compare Figures 4.4 and 5.7) these spectra can not be used to gain further information about the adsorption site. For the sake of completeness they are shown in Fig. A.1 of the Appendix.

In conclusion, our photoemission spectra provide evidence that for cluster arrays with sizes $s_{av} < 40$ atoms CO adsorbs atop. This finding is consistent with the adsorption behavior of CO on small, free Pt clusters in a beam with sizes up to 22 atoms. Gruene et al. demonstrated that for such Pt clusters the CO adsorption is exclusively atop [146]. Also the work of Tränkenschuh et al. [143, 145] provides unambiguous evidence that the atop site is the preferred adsorption site of CO molecules at steps and on terraces.

An estimate for the average number of adsorbed CO-molecules per cluster after saturation was obtained from O 1s intensities calibrated to the O 1s signal originating from a CO $(\sqrt{3} \times \sqrt{3})R30°$ layer on bare Ir(111) with a coverage of 0.33 ML [147]. We obtain 8, 16, 15, 27 and 32 CO-molecules per Pt cluster for the 0.05 ML, 0.10 ML, 0.20 ML, 0.44 ML and 0.75 ML arrays, respectively. According to Table 6.1 we find 8 CO-molecules adsorbed to a cluster with $s_{av} = 10$ atoms, 16 CO-molecules to one with $s_{av} = 19$ atoms, 15 CO-molecules to one with $s_{av} = 21$ atoms, 27 CO-molecules to one with $s_{av} = 39$ atoms and 32 CO-molecules to one with $s_{av} = 65$ atoms. Ball models for representative clusters of average or close to average size after CO exposure are shown in Fig. 6.6. For all cases, the number of edge atoms coincides very well with the estimated number of adsorbed CO-molecules. We conclude that at saturation to good approximation each cluster edge atom accommodates one CO-molecule. For the highest coverage of 0.75 ML Pt a rare population of terrace sites cannot be excluded.
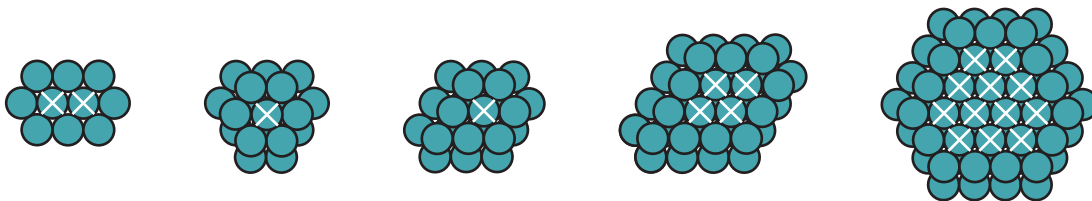
Figure 6.6 Ball models for Pt clusters containing 10, 19, 22, 38 and 64 atoms. Terrace atoms are marked by white crosses.

6.3 Weakening of Cluster-Graphene-Interaction Monitored in C 1s and Ir 4f

To relate the CO exposure induced Pt cluster dynamics to cluster binding, we investigated C 1s and Ir 4f core level spectra.

Figure 6.7 displays the C 1s region of 0.05 ML, 0.20 ML, and 0.75 ML Pt cluster arrays on Gr/Ir(111) before (left) and after (right) exposure to 10 L CO. For Gr/Ir(111) the C 1s spectrum can be fitted with a single peak located at 284.1 eV with a full width at half maximum (FWHM) of 0.22 eV (Section 5.2). The Pt deposition is associated with the development of a broad shoulder in the binding energy range of 284.3 - 285 eV. We showed that this shoulder is due to rehybridized C atoms both under and in the vicinity of the Pt clusters. In consequence of cluster binding these C atoms are sp^3 hybridized and closer to the Ir surface, at chemical rather than van der Waals binding distance. For these atoms we demonstrated a linear relationship between their core level shift and their height above Ir(111). In addition, we observe a +50 meV shift of the main peak which we assign to doping by the Pt clusters (see Chapter 8). The C 1s spectrum after exposing the 0.05 ML cluster array to 10 L CO is displayed in Fig. 6.7 (b): The rehybridization shoulder largely disappeared and the main peak shifts back to the position of Gr/Ir(111) without Pt clusters. Similar data is shown in Fig. 6.7 (c) and (d) for 0.20 ML, and in (e) and (f) for 0.75 ML Pt cluster arrays. Figure 6.7 (g) shows the intensity of the rehybridization shoulder before and after CO exposure. It is evident that the shoulder intensity decreases for all Pt coverages.

The diminished rehybridization shoulder and the backshift of the Gr main peak are not a consequence of cluster mobility, i.e. they do not originate from the decrease of n and the ensuing reduced contact area of the clusters with Gr. The time-dependent
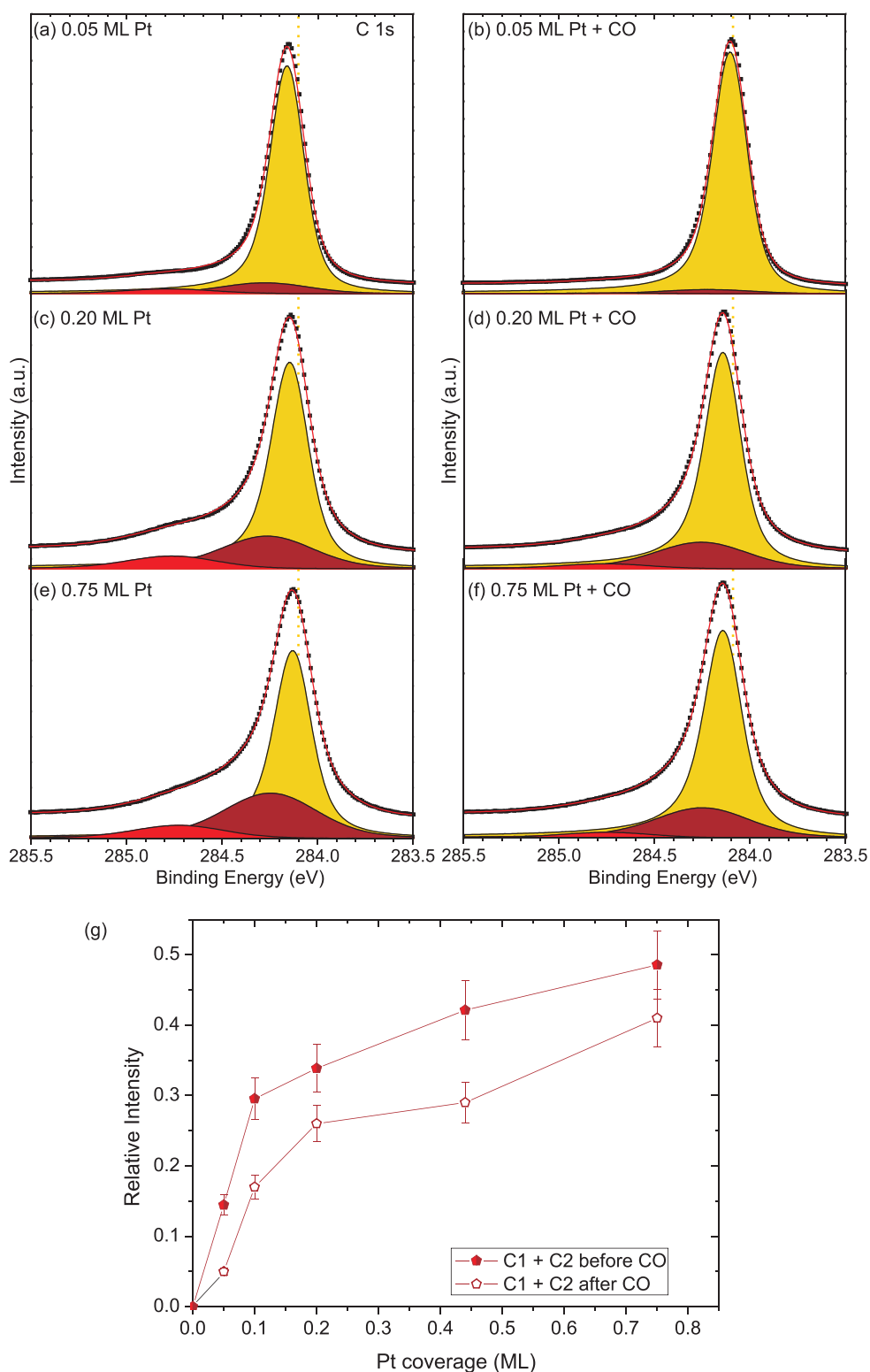
Figure 6.7 C 1s spectra before (left) and after $10\,\mathrm{L}$ CO exposure at $p_{CO} = 1 \times 10^{-7}\,\mathrm{mbar}$ (right). (a) $0.05\,\mathrm{ML}$ Pt, (b) $0.05\,\mathrm{ML}$ Pt + CO, (c) $0.20\,\mathrm{ML}$ Pt, (d) $0.20\,\mathrm{ML}$ Pt + CO, (e) $0.75\,\mathrm{ML}$ Pt, (f) $0.75\,\mathrm{ML}$ Pt + CO [(a),(c), and (e) are reproductions from Fig.5.3]. The experimental spectra are shown as black dots, the fits as solid red lines, and the filled curves represent the components of the fit (yellow = C_{main}, dark red = C_1, light red = C_2), fit parameters as in Table 5.1. The dotted line indicates the BE position of pristine graphene. (g) Relative intensities of the shoulder components $C_1 + C_2$ against Pt coverage before (filled symbols) and after CO exposure (open symbols).
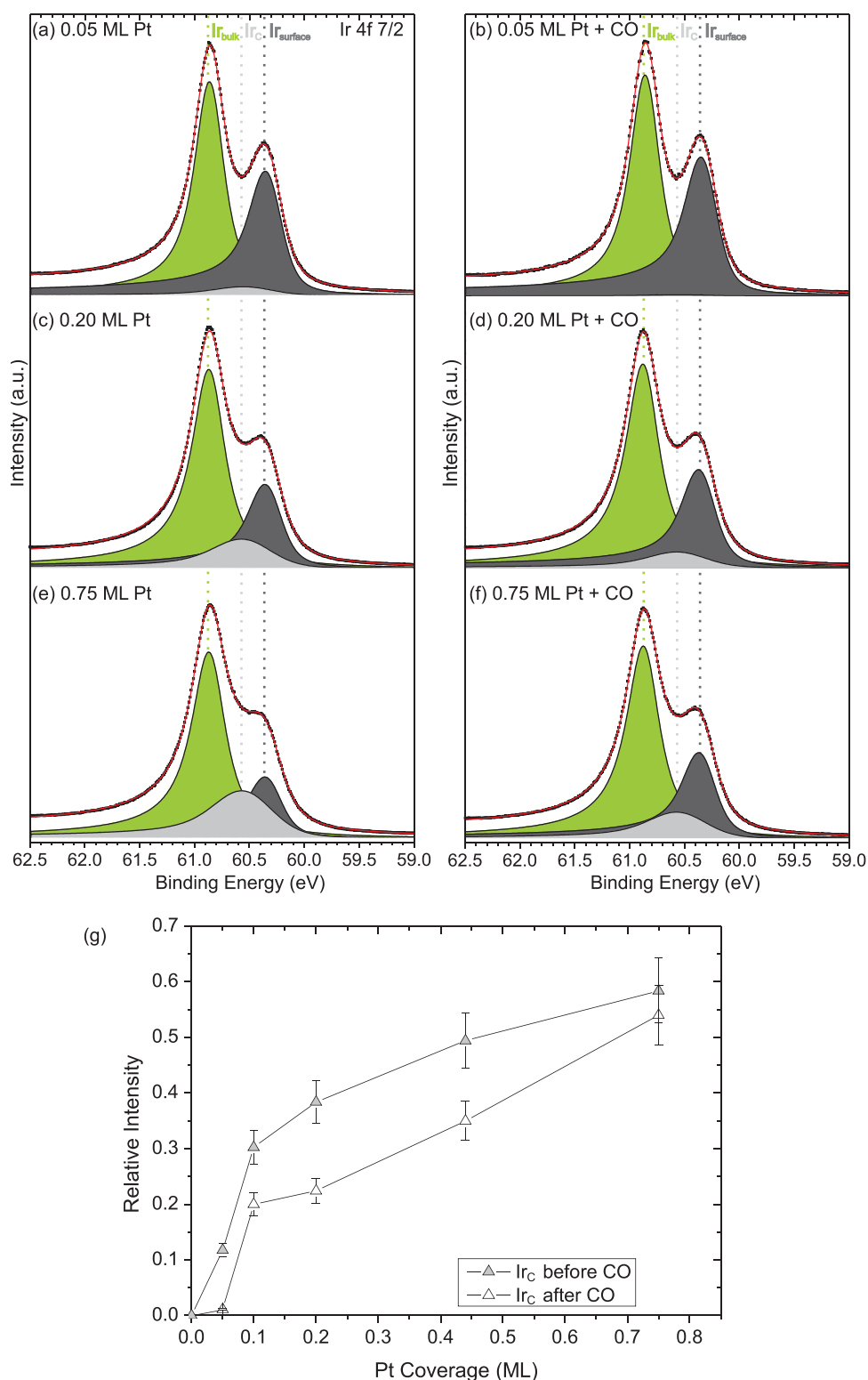
Figure 6.8 Ir $4f_{7/2}$ spectra before (left) and after $10\,\mathrm{L}$ CO exposure at $p_{\mathrm{CO}} = 1{\times}10^{-7}\,\mathrm{mbar}$ (right). (a) $0.05\,\mathrm{ML}$ Pt, (b) $0.05\,\mathrm{ML}$ Pt + CO, (c) $0.20\,\mathrm{ML}$ Pt, (d) $0.20\,\mathrm{ML}$ Pt + CO, (e) $0.75\,\mathrm{ML}$ Pt, (f) $0.75\,\mathrm{ML}$ Pt + CO [(a),(c), and (e) are reproductions from Fig.5.3]. The experimental spectra are shown as black dots, the fits as solid red lines, and the filled curves represent the components of the fit (green = $\mathrm{Ir_{bulk}}$, dark gray = $\mathrm{Ir_{surface}}$, light gray = $\mathrm{Ir_C}$), fit parameters as in Table 4.1. (g) Relative intensities of the $\mathrm{Ir_C}$ components against Pt coverage before (filled triangles) and after CO exposure (open triangles).

analysis of the integral intensity of the C 1s rehybridization shoulder [red triangles in Fig. 6.2(e) upper panel, fitting as described in Section 5.2] and the binding energy shift of the C 1s Gr main peak [blue dots in Fig. 6.2(e)] show that both quantities decrease immediately after the start of CO exposure, while n remains nearly constant. When cluster mobility sets in both quantities are already reduced by more than 50 %.

In Section 5.2 we observed a correlation between the intensity of the C 1s shoulder ($C_1 + C_2$) and the Ir 4f interface component (Ir_C, compare Fig. 5.5). Therefore, we expect the weakening of the C 1s shoulder upon CO adsorption to be paralleled by a decrease of the Ir_C component. Figure 6.8 displays the Ir 4f region of 0.05 ML, 0.20 ML, and 0.75 ML Pt cluster arrays on Gr/Ir(111) before (left) and after (right) exposure to 10L CO. It is evident that the intensity of the interface component Ir_C decreases upon CO exposure for all Pt coverages [Fig. 6.8 (g)].

6.4 DFT Results and the Diffusion Mechanism

So far, our experiments show that the adsorption of CO-molecules on Pt cluster edge atoms largely undoes graphene rehybridization beneath the cluster before sintering starts. What can be the origin of this effect?

Consistent with studies on vicinals to Pt(111) and Pt clusters, where CO prefers to reside in 1-fold edge sites [143, 145, 146], our XPS experiments show that CO binds atop Pt cluster edge atoms. In such sites, one can expect that a graphene C atom, the cluster Pt atom and the CO-molecule will be almost collinear. According to Blyholder, CO-Pt bond formation then occurs as a result of charge donation from the σ molecular orbital of CO to Pt sp-bands and back donation of Pt d-electrons into the $2\pi^*$ CO orbital [148, 149].

But, such bonding *cannot lead to a skyhook effect*. The problem, as Föhlisch et al.'s elaboration of the Blyholder model makes clear, is that CO adsorption in a 1-fold site does not imply a competition for $Pt(5d_{3z^2-r^2})$ electrons [150, 151]. The $Pt(5d_{3z^2-r^2})$ orbital is involved in binding the Pt to the underlying graphene. So, a weakening of the interaction of the $Pt(5d_{3z^2-r^2})$ - $C(2p_z)$ might well lead to a mobilization of a Pt island. But based on our current understanding of CO binding to Pt atop sites, such weakening does not occur.

The reason is that "back-donation" into the CO $2\pi^*$ orbital is the result of hy-

bridization with $Pt(5d_{xz})$ and $Pt(5d_{yz})$ electrons, i.e., $5d_{\pi}$ electrons, not $Pt(5d_{3z^2-r^2})$ electrons. They have the wrong (5σ) azimuthal symmetry for forming hybrids with the CO $2\pi^*$. In fact, Föhlisch, et al. showed that the interaction between the CO σ and the $Pt(5d_{3z^2-r^2})$ orbital is repulsive. Thus, there is no competition that would weaken the Pt bond to the graphene below.

First-principles calculations based on the Local Density Approximation confirm this picture, but, as we will explain, do not yet permit a definitive interpretation of the Smoluchowski coarsening we have observed, given available experimental information and the theoretical state-of-the-art.

In Chapter 4 we have used DFT calculations successfully to gain insight into cluster binding on graphene on Ir(111), and were even able to reproduce core level shifts of graphene atoms due to Pt cluster binding with good accuracy. Therefore, despite experience suggesting DFT will not show a preference for CO bonding in the observed 1-fold edge sites on the Pt/Gr/Ir(111) clusters [152], we undertook ab initio calculations to see whether they might, nevertheless, help to explain how CO mobilizes our Pt islands. The particulars of our calculations are as described in Section 3.4 except that six CO molecules were added to an island comprising 7 Pt atoms in the Gr/Ir(111)-(9x9) moiré unit cell.

Figure 6.9(a) displays the geometry resulting from a DFT optimization of a pristine Pt-heptamer. Note that the graphene beneath the cluster is buckled. Directly below each Pt atom is a relatively yellow (i.e., high-lying) C atom, to which it is bound at a distance of about $2.16\,\text{Å}$, the sum of the covalent radius of C and the metallic radius of Pt. Between the raised C atoms are relatively brown (i.e., lower lying) ones. They are bound to Ir atoms below, and lie at chemical bonding distances from them. The buckling implies that underneath the cluster, the graphene has locally rehybridized from sp^2 to diamond-like sp^3 carbon [79].

In Figure 5(b), we show the results of optimizing a Pt cluster with CO molecules 1-fold bound to cluster-edge atoms, the coordination required for correspondence with our XPS data. The molecules did not shift away from the 1-fold sites in the course of structural relaxation, indicating a relative minimum in the energy. But CO adsorption only caused distances between Pt atoms and C atoms to increase marginally, by less than 0.07 Å on average, and left the Pt-C chemical bonds intact for all seven Pt atoms. Correspondingly, the underlying Gr remained buckled, locally, with C atoms alternately yellowish, because they have moved up to bind to Pt

atoms, and brown, because they have moved down to bind to underlying Ir atoms. Thus, if the pristine cluster is immobile, then the cluster decorated by CO-molecules in 1-fold edge sites is equally so, according to DFT. This result is entirely consistent with the conclusions we have drawn from the study of CO binding in 1-fold sites on Pt(111) by Föhlisch, et al. [150, 151], although, regrettably, the weight of the experimental evidence implies that atop CO is what undoes the binding of Pt to C, mobilizing the Pt clusters.

Despite the experimental evidence for 1-fold CO adsorption on the edges of our Pt clusters, we also investigated CO in edge bridge sites, which, based on DFT studies of CO on vicinals to Pt(111), we expected to provide stronger bonding [152]. As expected, the bridging geometry was energetically preferred over 1-fold cluster decoration, the preference amounting to 81 meV per CO, or 0.49 eV/island. Surprisingly, however, the bonding within the graphene and between graphene and the Pt cluster as shown in Fig. 6.9(c) changed remarkably compared to Fig. 6.9(a) and (b). Upon bridging CO adsorption, distances between Pt atoms and C atoms increased substantially, by more than 0.90 Å on average. Four of the Pt atoms moved too far from the nearest C atoms to be chemically bound to them, and correspondingly, the underlying graphene unbuckled. Only two edge Pt atoms remained at a chemical binding distance (still about 0.25 Å higher than for the pristine case), for instance, in Fig. 6.9(c), the one at the front of the cluster labeled "2.28". The unbuckling of the underlying graphene implies diminished rehybridization of graphene, in line with our experimental observations [compare Fig. 6.5(c)], and, likely, with facile cluster mobilization.

Incidentally, despite the dramatically increased bond distances between the Pt- and the underlying C atoms, the effect of adsorption on the bond lengths within the Pt cluster is marginal. The average Pt-Pt distance increased upon CO adsorption by just 2%, from 2.62 Å to 2.67 Å. Apparently, the cluster integrity was not affected by CO adsorption.

Thus the DFT calculation for what appears to be the experimentally wrong, 2-fold adsorption site is consistent with a skyhook effect, whereas that for the observed 1-fold adsorption geometry offers no explanation for CO-induced cluster mobilization. In the DFT optimization, bridging CO adsorption caused (i) substantially weakened and lengthened bonds between Pt atoms and the underlying C atoms, (ii) a lifting of the rehybridization or an unbuckling of the graphene and (iii) an only negligible
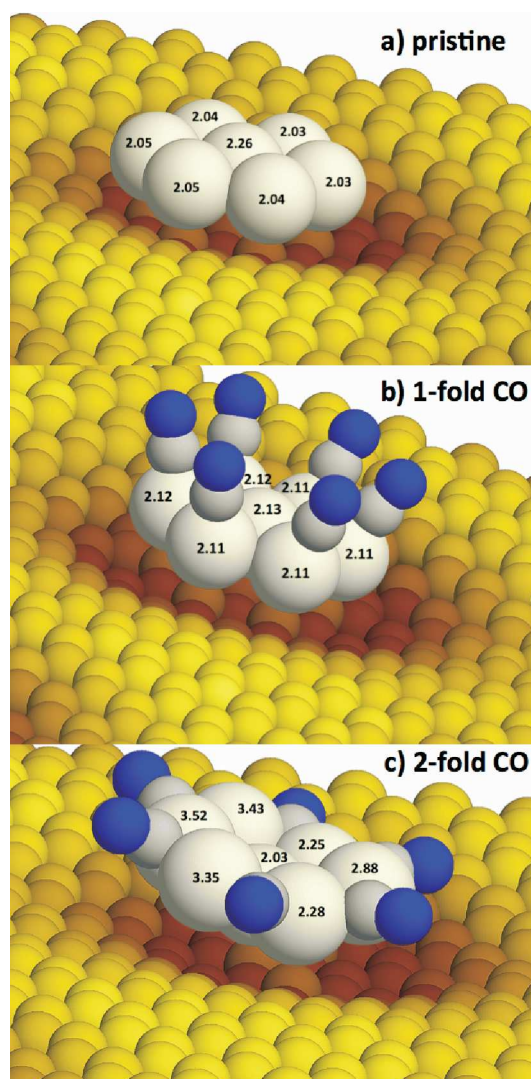
Figure 6.9 Geometries of a planar Pt-heptamer adsorbed to the hcp-area of graphene on Ir(111). (a) Pristine Pt-heptamer; (b) Pt-heptamer decorated by CO molecules in 1-fold (atop) sites; (c) Pt-heptamer decorated by CO molecules in 2-fold (bridge) sites. Gray and blue spheres represent C and O atoms of the CO molecules. White spheres are Pt atoms, and small, yellow to brown ones are the C atoms of the Gr layer. Browner means closer to the underlying Ir(111) substrate, and yellower means higher above it. The numbers are computed distances, in Å, of each Pt atom from the nearest C atom below it.

effect on the bond strength within the cluster itself. These three observations imply cluster mobility, as observed. The Pt atoms moved away from the graphene. At the same time the underlying substrate potential presumably became less corrugated, and lateral diffusion more facile.

This discussion underlines a need for technical improvements in theory, and further experiments. The by now well-known deficiency of approximate density functionals has once again manifested itself in our prediction that CO will prefer to bind in a higher rather than a lower coordination geometry on a metallic substrate, in this case a 7 atom Pt island. On the other hand, the calculated preference for the two-fold bonding geometry is small, and there is no reason to assume that the nature of the CO bonds would be appreciably different in an improvement over current DFT more faithful to observed binding energies. Assuming DFT does describe the nature of the CO-Pt bonds in a qualitatively correct way, and assuming that the edge-saturated 7 Pt atom islands are representative, then it seems necessary to conclude that island mobilization occurs when CO transiently resides in edge bridge sites. On the other hand, we have no experimental evidence for transient, bridge-bonded CO. Further experiments, perhaps in the nature of IR spectroscopy, would be helpful in this regard. They might reveal a population of CO in bridge sites, or rule that possibility out.

Before leaving the DFT results, we wish to remark on the locality of the unbinding effect and its likely relation to the cluster-size dependence of CO-induced mobility. The key observation is that only Pt atoms on which CO is adsorbed lose their coordination to the underlying graphene.

Given this locality of the unbinding effect let us revisit Table 6.1. It says that after CO exposure sintering terminates and clusters are immobile once they reached a size of $s = 10$ atoms. As shown in Fig. 6.6, a compact 10 atom cluster has 8 edge atoms. In agreement with our XPS coverage analysis these 8 edge atoms possess 8 adsorbed CO-molecules, either atop bonded (as found in experiment) or bridge bonded (as predicted by DFT). Now we postulate that the effect of the adsorbed CO-molecules is localized to their Pt atom counterparts, which unbind from the graphene. This means a 10 Pt atom cluster, whose edges are saturated by CO, is immobilized by its two terrace atoms. From that we deduce that a cluster of as few as two Pt atoms will not diffuse, and that one should expect the initial CO-free system, with an average cluster size of $s_{av} = 5$ atoms for the 0.05 ML cluster array, to be stable.

By contrast, after enough CO has been deposited that there are decorated clusters with just one undecorated Pt atom, or none, then these decorated clusters will be mobilized. Smoluchowski ripening will proceed, accordingly, until their coalescence creates larger clusters with at least two CO-free Pt atoms. At that point, ripening will cease.

A 38 atom 2-layered Pt cluster, characteristic for the 0.44 ML Pt cluster arrays with $s_{av} = 39$ possesses 9 atoms in the first layer, which are buried by second layer Pt atoms (compare Fig. 6.6). These atoms are protected against CO adsorption and thus the stability of the 0.44 ML cluster array is well understandable. In the 0.10 ML and in the 0.20 ML cluster array still some CO induced mobility is observable for $s_{av} = 11$ atoms resp. $s_{av} = 19$ atoms initially. We attribute this to the tail of the cluster size distributions extending below 10 atoms. The observation that most of the clusters that become mobile upon CO adsorption in the 0.20 ML case are 1-layered clusters is at least consistent with the assumption that these are the smallest ones in the distribution.

While lateral motion is the most relevant CO-induced process for small clusters, for those with more than 20 Pt atoms shape transformations to more three-dimensional arrangements dominate, and proceed without mass exchange between clusters. Generally, the shape of a supported cluster is determined by the balance of substrate surface, cluster surface and interface energy [153]. The substrate surface energy can be neglected here, as the surface free energy of graphene is very low owing to its inertness. Even without CO adsorbed, upon cluster growth initially 1-layered clusters transform to 2-layered clusters [15, 80]. As the rehybridization area of graphene is limited in size, at some point in the growth process the increase of the interface area is disfavored compared to an increase of cluster cohesion (lowering of total surface energy). Therefore arriving Pt atoms do not stay at the cluster edge in contact with graphene, but prefer to increase their coordination with other Pt atoms by forming a second layer [80]. Consider now a cluster somewhat below the critical size s_c, which is around 19 atoms for a Pt cluster on Gr/Ir(111) (compare Table 6.1). CO adsorption will change its shape, because the binding of the edge atoms to their underlying C atom counterparts is substantially weakened. Therefore interface formation is disfavored compared to an increase of Pt cohesion. Thus, a 2-layered configuration will already be preferred for a smaller size $s_c' < s_c$. Note that CO adsorption will also affect Pt-Pt bonding. However, since in Pt-Pt bonding all valence

electrons are already involved, the effect of an adsorbed CO will be much smaller than for the Pt-C bonding.

The preferential adsorption of CO to low coordinated atoms has an additional effect on cluster energetics and also tends to favor more 3 dimensional shapes. Consider a 19 atom planar cluster with CO saturated edges and a surplus of a few less strongly bound terrace CO-molecules. Transformation of the 1-layered cluster into a 2-layered cluster increases the number of strongly binding edge atoms. Through this shape transformation the terrace surplus CO-molecules can bind more strongly, to the newly formed edge atoms, which in turn reduces the cluster surface energy. The cluster thus reshapes to provide as many favorable adsorption sites as possible.

Reshaping of stepped Pt surfaces into nanometer-sized Pt clusters was found under an applied CO pressure in the mbar-range [154]. This reshaping was interpreted to be driven by a reduction of the repulsion of adjacent CO-molecules. While we can not entirely rule out a contribution of this effect, the CO induced Pt-C bond weakening and the enhanced CO binding by cluster reshaping appear to be a straightforward explanation for the similar phenomenon we observe here.

Except for very rare sintering events the 1 ML Pt cluster array is neither affected by cluster diffusion nor by shape transformations. The former observation can again be explained by the abundance of buried Pt atoms which are protected against CO adsorption. The absence of shape transformations in this array is however unexpected.

Finally, we consider why the majority of Pt clusters in the 0.05 ML arrays are set in motion after a well-defined threshold exposure [compare Fig. 6.2(e)]. Above we argued that clusters begin to move, when fewer than 2 atoms are left without a CO-molecule atop. This requires a larger cluster (e.g. a flat 8 atom cluster) to collect more CO-molecules than a smaller one needs (e.g. a 5 atom cluster). The larger CO capture efficiency of a larger cluster - most likely in proportion to its area - helps to synchronize the moment when larger and smaller clusters become mobile. However, it is questionable whether this compensation effect is fully able to explain the observed synchronization for the onset of cluster motion. One possibility is that the local graphene strain field associated with a moving cluster might slightly affect clusters in its vicinity and thereby help to synchronize cluster mobility.

6.5 Growth of Pt Clusters in the Presence of CO

An implication of CO-induced cluster mobility is the sensitivity of Pt cluster array growth to the CO background pressure. Small clusters of a few Pt atoms are abundant during growth and become more mobile by CO adsorption. In consequence, in a poor vacuum with residual CO, arrays that are less regular form, with a smaller filling factor.
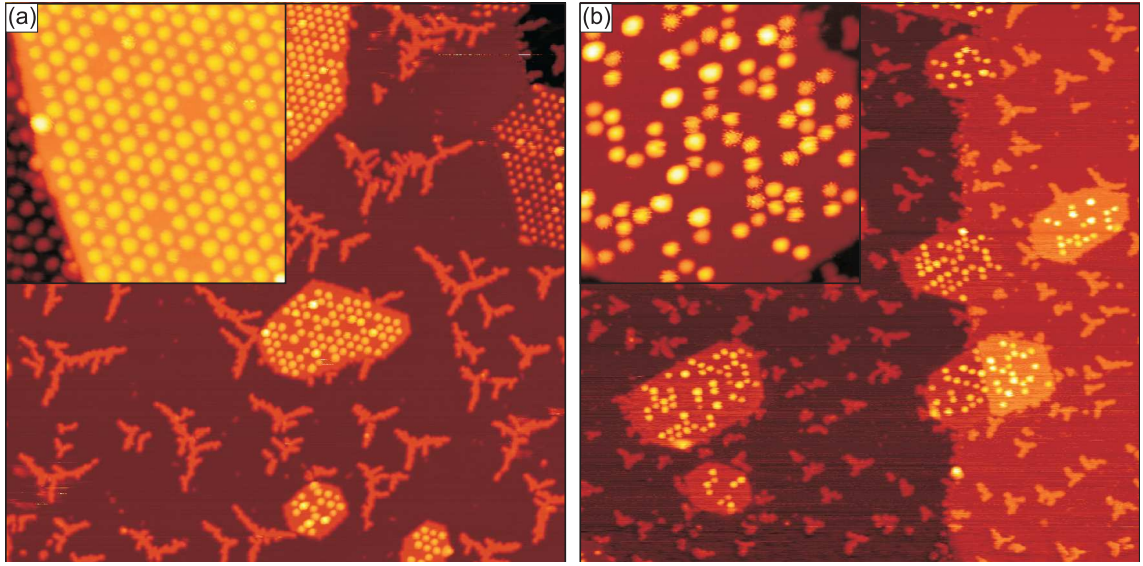
Figure 6.10 STM topographs after deposition of $0.10\,\text{ML}$ Pt on Gr/Ir(111). (a) Deposition in a partial CO pressure of $p_{CO} < 2 \times 10^{-10}$ mbar. (b) Deposition with $p_{CO} = 5 \times 10^{-9}$ mbar. Image sizes $1650\,\text{Å} \times 1650\,\text{Å}$, inset sizes $375\,\text{Å} \times 375\,\text{Å}$.

Figure 6.10(a) displays an STM topograph after deposition of $0.10\,\text{ML}$ Pt under ultra high vacuum conditions with the total background pressure during deposition below 2×10^{-10} mbar. Here graphene was prepared by room temperature ethylene adsorption till saturation, thermal decomposition at $1450\,\text{K}$, but without additional exposure to ethylene at elevated temperatures. This results in graphene flakes covering a fractional surface area of about $20\,\%$ [81]. The inset shows the cluster array with a filling factor $n = 0.92$, and with predominantly 1-layered clusters, as expected under these conditions [15]. On the bare Ir surface fractal dendritic Pt islands are visible.

Figure 6.10(b) displays an STM topograph of the same experiment, except that during Pt growth a CO pressure of $p_{CO} = 5 \times 10^{-9}$ mbar was applied. The inset highlights the poor filling of the moiré with $n = 0.42$ and with a larger relative

fraction of 2-layered clusters. The Pt islands on the bare Ir surface are smaller and display a significantly higher island number density. This is expected for epitaxial growth of Pt in the presence of CO [155].

6.6 Generalization to Other Gases and Other Metal Clusters

We have shown that small Pt clusters on Gr/Ir(111) are unstable upon CO adsorption and sinter through Smoluchowski ripening. In order to test if this behavior is a particularity of CO adsorption on Pt clusters or rather a general phenomenon that arises when metal clusters on Gr/Ir(111) are exposed to gases, we extended our study to the adsorption of other gases (H_2, O_2) on Pt clusters as well as to the adsorption of CO on other metal clusters (Ir, Au).

6.6.1 Pt Clusters Exposed to H_2 and O_2

We exposed $0.05\,$ML Pt cluster arrays on Gr/Ir(111) to H_2 and O_2 (Fig. 6.11). In both cases even large exposures of the order of $100\,$L did not induce cluster mobility. Fig. 6.11 (a) and (b) show the same sample location before and after $100\,$L H_2 exposure at $90\,$K exposure, respectively. The clusters lattice is virtually unchanged.

Fig. 6.11 (c) and (d) shows the same sample location before and after $80\,$L O_2 exposure at $300\,$K. After exposure, we observe height transformations of the Pt clusters as well as one single event of a cluster disappearing [circles in (c) and (d)]. The height transformations might trace back to contamination by CO which is easily generated e.g. at the pressure gauge while dosing O_2. Apparently, small Pt clusters are stable in the presence of O_2 and H_2, whereas they are unstable in the presence of CO (compare Fig. 6.1).
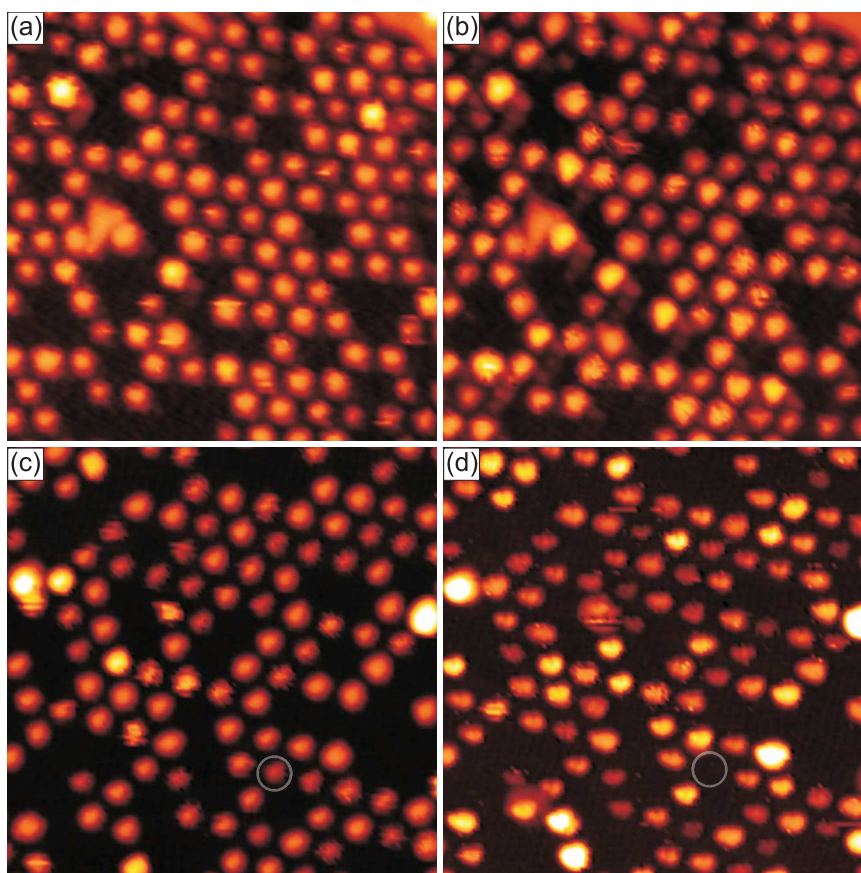
Figure 6.11 0.05 ML Pt before (a) and after (b) 100 L H_2 exposure at 90 K with $p_{H_2} = 2 \times 10^{-7}$ mbar, same sample location. (a) and (b) are imaged at 90 K. 0.05 ML Pt before (c) and after (d) 80 L O_2 exposure at 300 K $p_{O_2} = 1 \times 10^{-7}$ mbar, same sample location. Image size is always 380 Å x 380 Å.

Figure 6.12 shows C 1s spectra of 0.2 ML Pt before and after exposure to H_2 and O_2, respectively. We find that in both cases the intensity of the shoulder components $(C_1 + C_2)$ is reduced by 10% upon gas adsorption. For comparison: The shoulder intensity was reduced by 25% when 0.20 ML Pt were exposed to CO (Fig. 6.7). We conclude that the cluster binding to the graphene is weakened by O_2 and H_2 adsorption but not to such an extent that the clusters are mobilized.

The question arises why the behavior of Pt clusters with respect to these gases differs from the ripening induced by CO exposure. Let us recall the results of our DFT calculations: Despite their ambiguous outcome, the calculations at least showed that the stability of the clusters crucially depends on the adsorption site. Thus, the different impact of CO, H_2, and O_2 on the clusters might be due to different adsorption geometries. As mentioned above, CO prefers one-fold coordinated adsorption sites
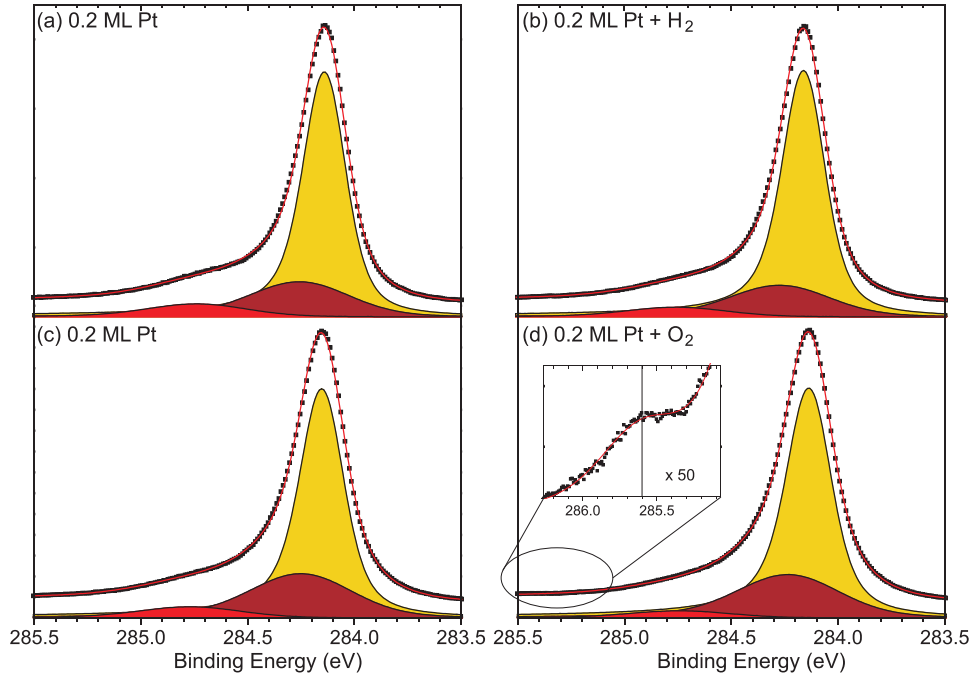
Figure 6.12 C 1s of 0.2 ML Pt before (left) and after (right) 750 L H_2 exposure at 120 K with $p_{H_2} = 5 \times 10^{-6}$ mbar (a,b) and 10 L O_2 exposure at 300 K with $p_{O_2} = 1 \times 10^{-7}$ mbar (c,d), respectively. Inset in (d) is enlarged 50 times.

[143, 145, 148]. Contrarily, O_2 and H_2 adsorb dissociatively on Pt surfaces and the O and H atoms occupy three-fold coordinated hollow sites [156, 157], even at step edges [144].

For another attempt to explain our findings, let us consider the adsorption energy of a molecule or atom as a measure for the strength of its interaction with the surface. On the Pt(111) surface, the CO molecule is adsorbed with a binding energy of -1.43 eV (for adsorption at low coordinated sites the adsorption energy can be even higher [148]), an H atom is adsorbed with an energy of -0.76 eV [156], and an O atom is adsorbed with an energy of -3.51 eV [158]. However, we have to consider the adsorption energy *per* Pt atom. For example, O adsorbs in three-fold coordinated sites forming a 2x2 overlayer. In this structure, each Pt atom is one-fold coordinated with O. Thus, the adsorption energy per Pt atom is $E_{O,norm.} = -3.51$ eV $\times$ 1 / 3 = -1.17 eV. Hydrogen forms a 1x1 overlayer, so that both, the Pt and the H atoms, are threefold coordinated: $E_{H,norm.} = -0.76$ eV $\times$ 3 / 3 = -0.76 eV. For small clusters, we found that the CO saturation coverage is almost one molecule per atom, thus $E_{CO,norm.} \geq -1.43$ eV $\times$ 1 / 1 = -1.43 eV. If we do not consider an O structure denser

than 2x2, these values are in line with the stronger impact of CO adsorption onto the cluster compared to the other gases.

An interesting feature appears in the C 1s spectrum after O_2 exposure [inset in Fig. 6.12 (d)]: we observe a small peak at 285.6 eV. Similar features are found by Vinogradov et al. (285.6 eV [159]) as well as by Larciprete et al. (285.8 eV [160]) after exposing Gr/Ir(111) to a beam of atomic oxygen. Both authors assign this component to the formation of epoxy groups (C-O-C) in the graphene layer. Thus after exposing Pt clusters to molecular oxygen we observe a feature previously assigned to epoxy groups formed by atomic oxygen. This indicates that some of the oxygen which is adsorbed dissociatively on the Pt clusters is spilled over from the cluster onto the graphene layer where it forms epoxy species. This effect is, however, rather small. The intensity of the epoxy feature amounts to only 2% of the total C 1s intensity. This means that on average four carbon atoms per moiré cell are affected which is equivalent to the formation of two epoxy groups (each consisting of two C atoms and one O atom) per moiré unit cell.

6.6.2 Ir and Au Clusters Exposed to CO

In the previous section we have seen that small Pt clusters which sinter upon CO exposure are stable in the presence of O_2 and H_2. As CO is apparently the molecule interacting in the strongest manner with the clusters, we use it to test the stability of Ir and Au clusters.

Figure 6.13 $0.05\,\mathrm{ML}$ Ir before (a) and after (b) $5\,\mathrm{L}$ CO exposure at $300\,\mathrm{K}$ with $p_{CO} = 1 \times 10^{-9}\,\mathrm{mbar}$, same sample location. Image size is always $380\,\mathrm{Å}$ x $380\,\mathrm{Å}$. C 1s of $0.08\,\mathrm{ML}$ Ir before (c) and after (d) $10\,\mathrm{L}$ CO exposure at $300\,\mathrm{K}$ with $p_{CO} = 1 \times 10^{-7}\,\mathrm{mbar}$.

Figure 6.13(a) and (b) show the same sample location before and after an array of $0.05\,\mathrm{ML}$ Ir clusters was exposed to CO. Before CO exposure we observe a partially filled cluster array ($n = 0.74$) consistent with previous results [44]. We note that CO exposure causes substantial sintering of small Ir clusters. The filling n is reduced from 0.74 to 0.4.

Figure 6.13(c) displays the C 1s spectrum of $0.08\,\mathrm{ML}$ Ir before CO exposure. We observe a shoulder on the low binding energy side of the carbon main peak which we can assign to sp^2 to sp^3 rehybridization of the carbon atoms. The relative intensity

of the shoulder amounts to 0.36 (if the total C 1s intensity is set to 1), which is comparable to the case of Pt clusters (i.e. 0.30 for 0.10 ML Pt, see Section 5.2). After CO exposure [Fig. 6.13(d)] the intensity of the shoulder is reduced by 33% signaling that rehybridization is weakened which is consistent with the observation that the small Ir clusters are unstable in the presence of CO (for comparison: -43% for 0.10 ML Pt exposed to CO).

All in all, the behavior of Ir clusters is highly similar to that of Pt clusters:

(i) We observe the same shoulder in the C 1s spectrum due to the fact that Ir cluster bind to the graphene layer in a similar fashion as Pt clusters (compare [79] and Chapter 4).

(ii) They show the same ripening behavior [compare Fig. 6.1 (a),(b)].

(iii) For both metals the intensity of the C 1s shoulder is noticeably reduced upon CO exposure (compare Fig. 6.7).

After the study of Ir clusters let us turn to Au clusters. Figure 6.14 (a) shows an STM topograph after deposition of 0.05 ML Au onto Gr/Ir(111) at 90 K. The deposition temperature had to be lowered because room temperature Au deposition does not yield an Au cluster array [15]. Even so, we observe a cluster array not as well ordered as the Ir and Pt cluster arrays.

Figure 6.14(b) shows the same sample location after exposure to 18 L CO at 90 K (note that CO does not adsorb on the Au particles at 300 K). This array is only slightly affected by CO exposure. Only a few sintering events occur, marked by circles (compare Fig. 6.13 and 6.1 for the impact of CO on Ir and Pt clusters).

Figure 6.14(c) displays the C 1s spectrum of 0.10 ML Au before CO exposure. In addition to the main carbon peak we again observe the rehybridization shoulder with a relative intensity of 0.15. We note that the intensity is lower than for comparable Pt and Ir coverages (0.30 for 0.10 ML Pt and 0.36 for 0.08 ML Ir). This finding implies that the interaction of Au with graphene is much weaker than that of Pt and Ir with graphene, which is in line with the lower thermal stability of Au clusters on Gr/Ir(111) [15].

Upon CO exposure the spectrum shows but a little change. The intensity of the shoulder is reduced by only 14% (for comparison: -43% for 0.10 ML Pt, -33% for 0.08 ML Ir).

We also recorded spectra of the Au 4f region displayed in Fig. 6.14(e) and (f). In (e) we observe the Au $4f_{7/2}$ and $4f_{5/2}$ peaks of the Au clusters before exposure. Both
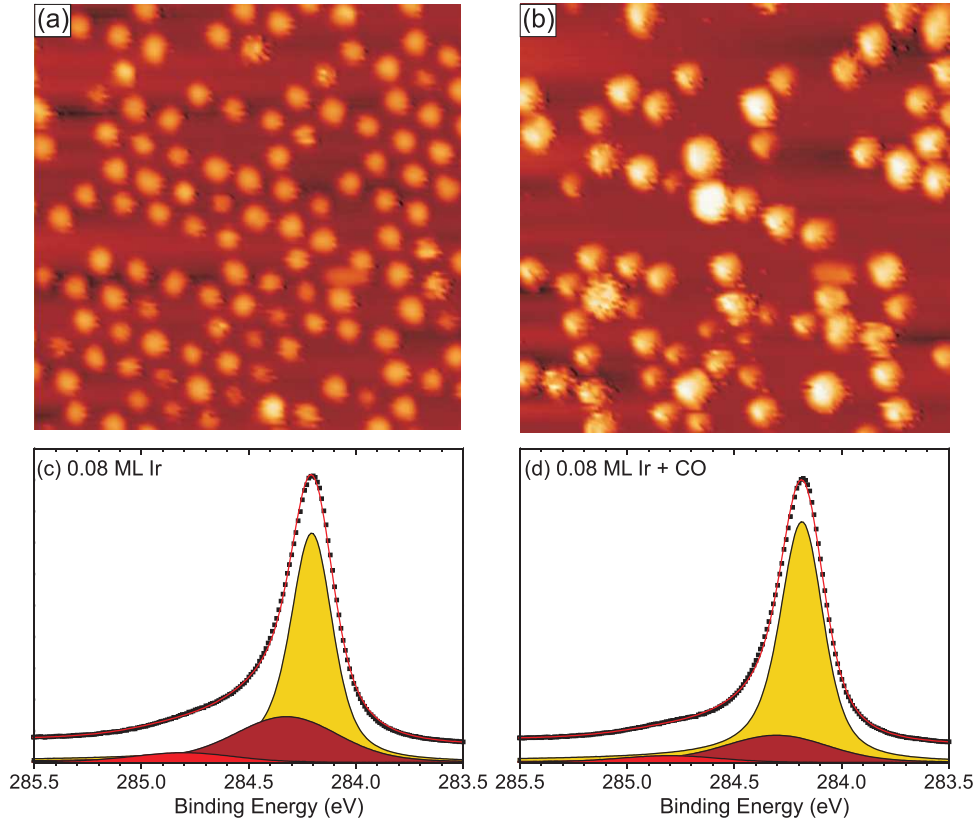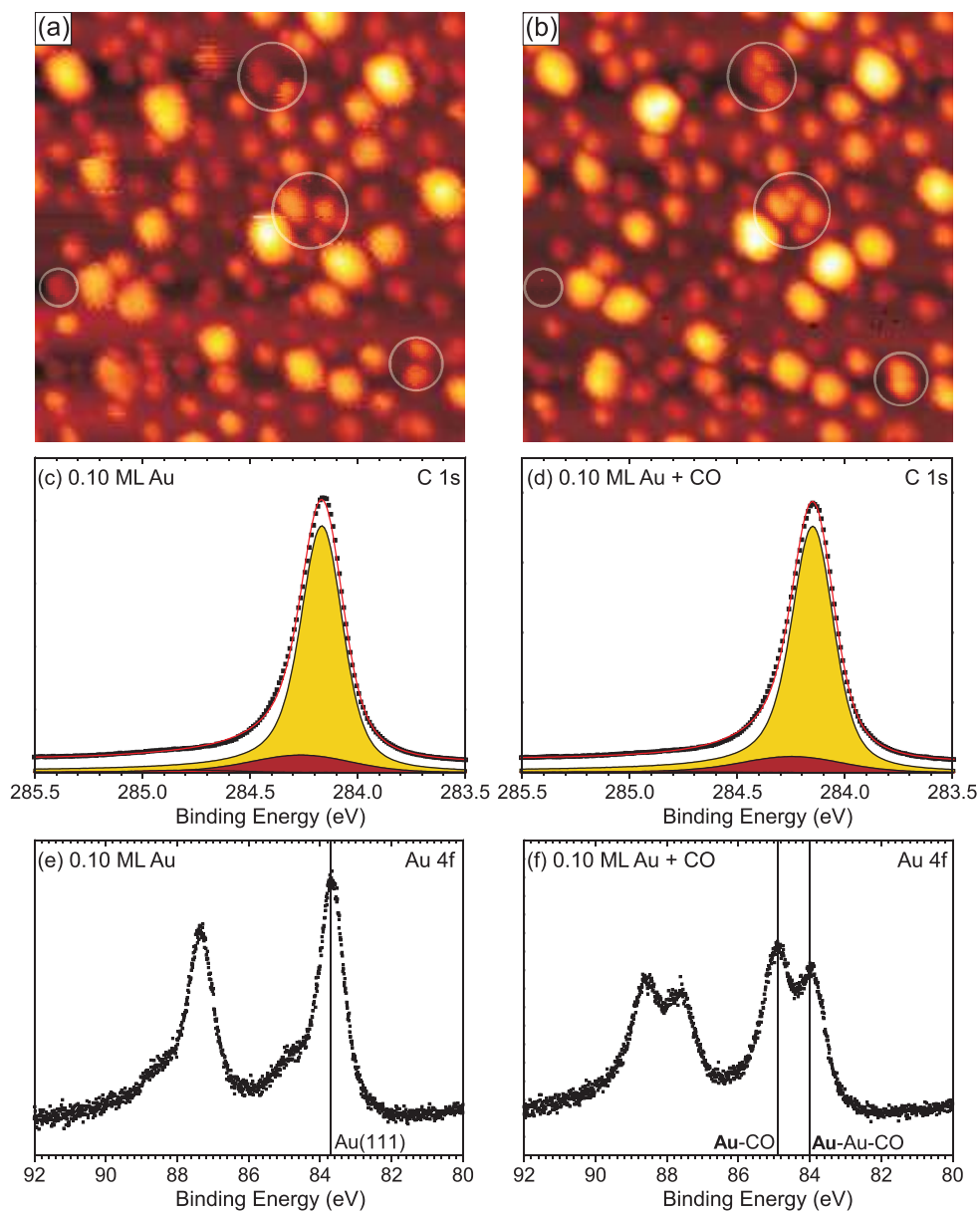
Figure 6.14 0.05 ML Au before (a) and after (b) 18 L CO exposure at 90 K with $p_{CO} = 1 \times 10^{-8}$ mbar, same sample location. Image size is 380 Å x 380 Å. C 1s [Au 4f] of 0.1 ML Au before (c) [e] and after (d) [f] 10 L CO exposure at 120 K with $p_{CO} = 1 \times 10^{-7}$ mbar. In (e) the binding energy for Au(111) is indicated. In (f) binding energies for Au atoms adsorbing a CO molecule (**Au**-CO) and Au atoms neighboring such an Au atom (**Au**-Au-CO) are indicated [161].

peaks are dominated by a sharp component. The binding energy of the Au $4f_{7/2}$ main component of 83.7 eV exactly matches that reported for the Au(111) surface [161]. In addition, we observe a small shoulder at the high binding energy side, which is due to contamination by CO (see description below). Figure 6.14(f) shows the Au 4f spectra after CO exposure. The Au $4f_{7/2}$ is now split into two components. One is shifted by +0.3 eV (with respect to main component before exposure) to 84.0 eV, the other displays a very large shift of +1.2 eV to 84.9 eV. According to Weststrate et al. [161] the strongly shifted components can be assigned to Au atoms with an adsorbed CO molecule (**Au**-CO), the other component to Au atoms neighboring an Au atom with CO adsorbed (**Au**-Au-CO). The Au 4f spectrum implies that CO molecules are adsorbed onto the clusters. However, this adsorption does not destabilize the Au clusters.

To summarize this section, we note that Ir clusters behave quite similar to Pt clusters: Clusters of both metals are destabilized upon CO exposure accompanied by a decrease in the intensity of the C 1s shoulder components. In contrast, Au clusters are stable in the presence of CO.

Ir is a platinum group metal and has similar chemical properties as Pt. As an example, let us compare the chemisorption of CO on the (111) surfaces of these metals: On both surfaces the CO molecule adsorbs preferentially in atop positions [147, 157]. Only at CO coverages higher than $\sim$0.2 ML the less favored bridge sites become populated. Also the initial adsorption energy is almost the same: -1.43 eV/molecule on Pt(111) [162] and -1.55 eV/molecule on Ir(111) [147], respectively. As the interaction of CO with the (111) surfaces of Ir and Pt is very much alike, we are not surprised that the interaction of CO with clusters of both metals is also analogous.

Contrarily, Au is considered the noblest of all metals and its chemical properties differ from those of the platinum group metals [163, 164]. Let us consider that the interaction of CO with the Au(111) surface is different: The adsorption energy is slightly *positive* (0.15 eV/molecule [165]) which means that CO does not adsorb on this surface except for step and kink sites. At kinks, the adsorption energy is -0.3 eV/molecule which is almost one order of magnitude smaller than for kinks of a Pt surface (-2.1 eV/molecule [148]). We therefore expect the CO molecule to interact also in a much weaker manner with a Au cluster than with an Ir or Pt cluster. Even though the Au cluster is bound only weakly to the graphene layer, the interaction of CO with the particle is not strong enough to destabilize it.

6.6.3 Stability of Clusters at Atmospheric Pressure

We have seen that CO exposure has a strong impact on the stability of Ir and Pt clusters, whereas exposure to gases like H_2 and O_2 is harmless. We wondered if the clusters are stable when exposed to air at atmospheric pressure. For this test we chose an array of medium-sized Ir clusters ($\Theta = 0.45$ ML, $s_{av} = 39$ atoms) on a partially graphene-covered Ir surface (0.2 ML graphene). Figure 6.15(a) shows the Ir cluster array on a graphene flake which extends over two terraces of the Ir(111) substrate separated by a mono-atomic step edge. As expected, the quality of the lattice is very high. Fig. 6.15(b) shows the sample after having been exposed to air at atmospheric pressure. Imaging is also performed under ambient conditions which explains the poorer image quality compared to (a). Still the cluster lattice is well visible indicating that the clusters are stable when exposed to air even at atmospheric pressure. We kept the sample under ambient conditions for several weeks before transferring it back to UHV conditions. Prior to mounting, the sample was cleaned by rinsing it in isopropyl alcohol. Fig. 6.15(c) shows this sample imaged under UHV conditions. Regardless of the very poor image quality the cluster lattice is still recognizable. This proves that medium-sized Ir clusters are stable even upon long exposure to ambient conditions. Based on the reported similarities between Ir and Pt clusters, we predict stability under ambient conditions also for Pt clusters.
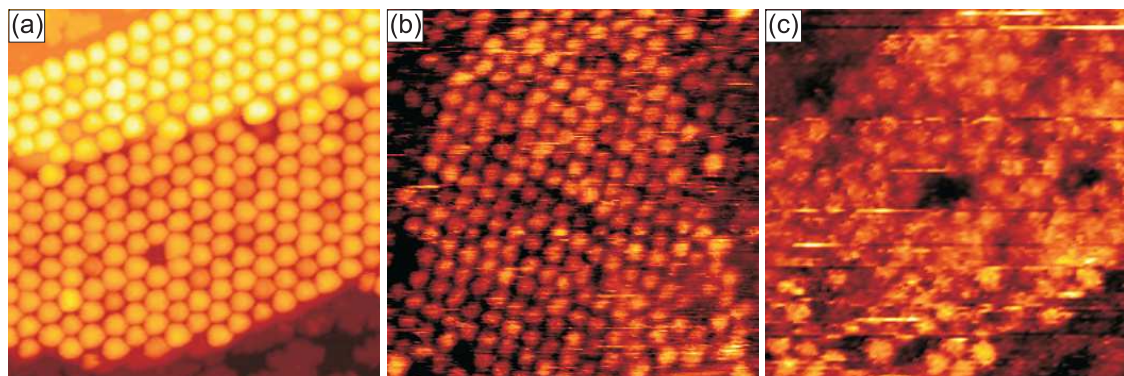

Figure 6.15 (a) 0.45 ML Ir imaged in UHV, (b) after short exposure to air (1 bar), imaged under ambient conditions, and (c) after weeks of exposure to air and cleaning with isopropyl alcohol, imaged under UHV conditions. Image size is always 400 Å x 400 Å.

6.7 Conclusions

We have shown that CO-induced sintering of small Pt clusters on Gr/Ir(111) can be traced back to Smoluchowski ripening. Even if clusters stay immobile upon adsorption, they often transform to a more three-dimensional shape. In photoemission spectroscopy, the CO adsorption on the Pt clusters is accompanied by a pronounced decrease of both the shoulder in the C 1s peak and the Ir 4f interface component Ir_C, which are characteristic for graphene rehybridization. CO is found to be adsorbed atop on Pt cluster edge atoms. We had hoped that DFT calculations would help to interpret our discovery of island mobility, but instead they left us in a quandary. Either we disbelieve the DFT result that CO in one-fold island-edge sites has little effect on the bonding of the Pt to the graphene below, or we must assume that a CO-decorated island can adopt a transient structure in which Pt-graphene bonds are broken and the island is mobilized. In the first case we lack theoretical evidence to justify the disbelief. In the latter, we lack experimental confirmation of transient configurations.

An implication of CO-induced cluster mobility is the sensitivity of Pt cluster array growth to the CO background pressure. We have seen that with residual CO, less regular cluster arrays with a smaller filling factor form.

In order to test if the observed sintering of clusters is a particularity of CO adsorption on Pt clusters or rather a general phenomenon that arises when metal clusters on Gr/Ir(111) are exposed to gases, we extended our study to the adsorption of other gases (H_2, O_2) on Pt clusters as well as to the adsorption of CO on other metal clusters (Ir, Au). We have seen that adsorption of H_2 and O_2 does not destabilize small Pt clusters. We found that CO is the molecule showing the strongest interaction with the clusters, so that we used it to test the stability of Ir and Au clusters. We showed that small Ir clusters sinter upon CO exposure, paralleled by a decrease of C 1s shoulder intensity. Both observations are the same as for Pt cluster. Au clusters behave differently: Although their binding to graphene is much weaker than that of Ir and Pt clusters, they are not destabilized by CO adsorption. This is explained by the much weaker interaction of CO with Au surfaces compared to Ir and Pt surfaces.

Finally, medium sized Ir clusters were tested for their stability under ambient conditions. It was shown that the clusters are stable even after they have been exposed to air at atmospheric pressure for weeks, and after cleaning with alcohol, respectively.

7 Oxygen Intercalation under Graphene on Ir(111)

In this chapter, we resolve the temperature and time dependent intercalation phases of oxygen underneath graphene on Ir(111) formed upon exposure to molecular oxygen, as well as the XPS fingerprints of these phases (Section 7.1). Using STM we study the flake-size-dependence of intercalation, and the importance of substrate steps and of the unbinding of graphene flake edges from the substrate (Section 7.2). Using CO titration to selectively remove oxygen from the bare Ir terraces, the energetics of intercalation are uncovered (Section 7.3). In Section 7.4, the study will be extended to the intercalation of hydrogen. Cluster decoration techniques are used as an efficient tool to visualize intercalation processes in real space.

In the following, we will review previous work on graphene-oxygen interaction: For graphene flakes on Ru(0001) - strongly bound to the substrate - oxygen intercalation upon exposure to molecular oxygen has been intensely studied by microscopy and spectroscopy [64–66]. For temperatures around $600\,\mathrm{K}$ and below - where oxygen etching is absent - intercalation proceeds from the edges of graphene flakes towards the interior with a phase boundary separating intercalated and non-intercalated graphene areas [64, 65]. The saturated intercalation phase is assigned to a p(2x1)-O structure sandwiched between Ru(0001) and graphene [64, 68]. During intercalation, Starodub et al. [65] observed two well-defined fronts in low energy electron

microscopy (LEEM), which they speculate to be linked to O-phases below graphene with low and high O concentrations. From their LEEM movies Sutter et al. [64] concluded that the rate-limiting step for oxygen intercalation is the decoupling of graphene from the substrate at the reaction front.

For graphene on Ir(111), intercalation of oxygen upon exposure to molecular oxygen has only been studied in the context of graphene etching by Starodub et al. [65]. Based on their observations at elevated temperatures, the authors concluded that direct attack of graphene by intercalated oxygen is the main route for graphene etching on Ir(111).

In addition, two independent studies by Vinogradov et al. [159] and Larciprete et al. [160] used reactive O radicals to study the oxidation of graphene resting on Ir(111). Both studies concluded that epoxy groups (C-O-C) are formed, but they disagreed about the existence and XPS-fingerprints of intercalated oxygen.

Here, for graphene on Ir(111), we investigate the intercalation of oxygen underneath graphene in a temperature range below the onset of graphene etching. Moreover, we take advantage of our ability to tailor the morphology of graphene on Ir(111) in a controlled way. We prepare a perfectly closed graphene layer as a reference and investigate intercalation underneath graphene flakes with circle equivalent (CE) diameters of the order of 10 nm to 100 nm, two to three orders of magnitude less than the size of the flakes investigated in the LEEM studies mentioned above [64, 65]. At the temperatures, pressures and exposures investigated, oxygen does not dissolve into the bulk of Ir and therefore the system under concern is a true two dimensional (2D) system [167].

Armed with such a well-defined system, the chemical sensitivity of XPS, and the detailed atomic scale view of STM we are able to answer the following fundamental questions: What are the fingerprints of intercalation in XPS and STM? Are there several distinguishable intercalation phases and what are their characteristics? What is the rate-limiting step for oxygen intercalation and how does it depend on flake morphology? Is the intercalation probability a function of graphene flake size? Is there an effect of substrate steps on intercalation? Is there an energy gain associated with the intercalation of oxygen? How does intercalation depend on an applied molecular oxygen pressure?

7.1 Kinetics of Intercalation and XPS Fingerprints

Firstly, we determine the XPS fingerprints of intercalation under graphene flakes with CE diameters of 10 nm to 100 nm. In Fig. 7.1 we display the C 1s spectra of a 0.5 ± 0.1 ML graphene/Ir(111) surface before (lowest spectra) and after oxygen exposure at stepwise increasing temperatures. If not specified otherwise, oxygen exposure in this chapter is conducted in an O_2 pressure of 10^{-5} mbar for 100 s. The resulting dose of 750 L is more than an order of magnitude larger than what is necessary to reach saturation coverage on Ir(111) [133, 168].
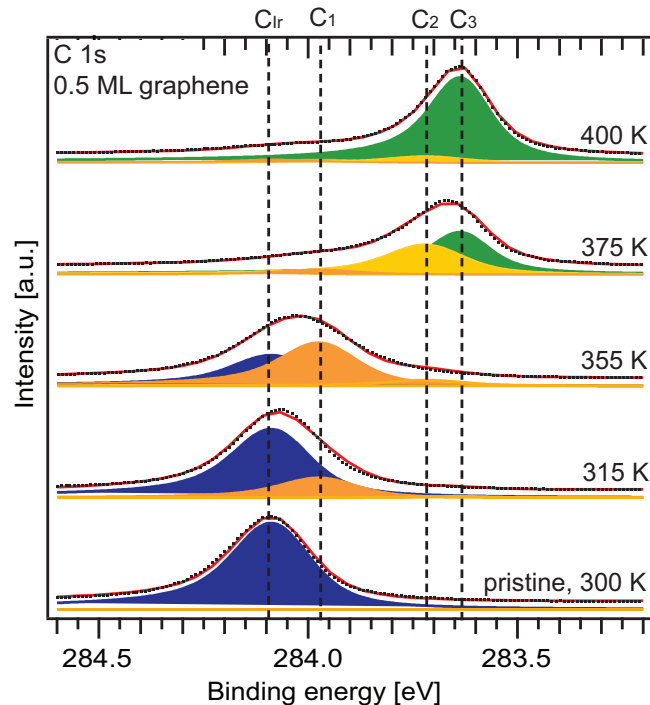
Figure 7.1 XP-spectra of the C 1s region of 0.5 ML graphene/Ir(111). The sample was exposed to 750 L of O_2 at stepwise increasing temperature, as indicated in the figure. The pristine graphene film is shown in the lowest spectra. The experimental spectra are shown as black dots, the fits as solid lines and the filled curves represent the components of each fit. The dashed lines are the fitted binding energy positions.

Before oxygen exposure, the 0.5 ML spectrum can be fitted by a single component C_{Ir} at 284.09 ± 0.05 eV with identical GFWHM and LFWHM of 0.16 eV. Note that this component corresponds to the one which is called C_{main} in Chapter 5. The width is due to the height modulation of the graphene layer, which can be correlated with a 140 meV modulation of the C 1s CLS (Chapter 4).

For the 0.5 ML graphene flakes oxygen exposure up to 355 K leads to the development of a low binding energy shoulder, whereas higher temperatures result in a new C 1s component (C_3) positioned at 283.64 ± 0.02 eV, a shift of -0.45 ± 0.02 eV compared to the C_{Ir} component of pristine graphene. The two intermediate components C_1 and C_2 (shifted -0.17 ± 0.03 eV, resp. -0.34 ± 0.03 eV compared to C_{Ir}), also seen in Fig. 7.1, were introduced since it is impossible to fit the C 1s spectra after oxygen exposure with only one C_{Ir} and one C_3 component. They both have the same width parameters as the C_{Ir} component. We note that binding energies and estimated error bars of the C_{Ir}, C_1, C_2, and C_3 components are based on a number of experiments. The assignment of the C_1 and C_2 components will be discussed below, after we analysed the nature of the C_3 component. Following oxygen exposure at 400 K the C_3 component fully dominates the spectrum. The GFWHM of the new C_3 component is 0.11 eV and thus reduced 31% with respect to the C_{Ir} component of pristine graphene. Since the GFWHM of graphene is coupled to the height modulation of the film above the Ir(111) surface (Chapter 4), the decreased width suggests that the height modulation is reduced upon oxygen exposure at 400 K. The peak area of the C_3 component after oxygen exposure at 400 K is, within the error limits, identical to the peak area of the C_{Ir} component of the pristine graphene. Therefore, we conclude that etching of graphene has not yet started. Since O_2 dosing at 400 K leads to one single C 1s component, with a -0.45 eV CLS, we conclude that all C-atoms are chemically equivalent after oxygen exposure. Further, the identical intensity of pristine and oxygen exposed graphene and the decreased C 1s width after oxygen exposure suggest that the chemically equivalent C-atoms are located in an intact graphene film. Finally, it is obvious from Fig. 7.1 that the development of the C_3 component is strongly temperature dependent and only fully developed at 400 K.

For a perfectly closed 1 ML graphene layer with no bare Ir, we find after oxygen exposure at temperatures up to 700 K that the peak position, FWHM and peak area remains unchanged (see Fig. 7.2). This holds for oxygen pressures up to 10^{-5} mbar. After oxygen exposure at 700 K STM imaging confirms the structural and chemical integrity of the 1ML graphene, being indistinguishable from pristine graphene (data not shown). However, for a graphene layer with small pinholes always a C_3 component arises well below 700 K. Thus, the C_3 component as well as the C_2 and C_1 components are unique for a situation where at least small patches of Ir(111) are
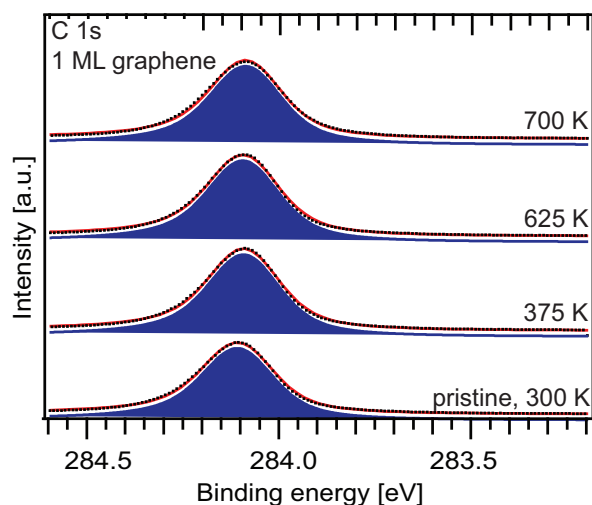
Figure 7.2 XP-spectra of the C 1s region of a perfectly closed 1 ML graphene layer on Ir(111). The sample was exposed to $750\,L$ of O_2 at stepwise increasing temperature, as indicated in the figure. The pristine graphene film is shown in the lowest spectra. The experimental spectra are shown as black dots, the fits as solid lines and the filled curves represent the components of each fit

uncovered by graphene.

In earlier XPS studies of atomic oxygen adsorption onto graphene/Ir(111) [159, 160] epoxy groups were identified and assigned to a C 1s component with a binding energy of 284.6 - 285.9 eV. The absence of any peak in this energy interval shows that no epoxy groups are formed when monolayer and sub-monolayer graphene films are exposed to molecular oxygen. The C_3 component we observe at 283.64 eV must therefore originate from another oxygen related carbon species on the surface.

Fig. 7.3(a) and (b) show the Ir $4f_{7/2}$ core level spectra of Ir(111) supporting 0.5 ML graphene and clean Ir(111), before (lower) and after oxygen exposure at $400\,K$ (upper). Initially both spectra consist of one Ir $4f_{7/2}$ bulk component (Ir_B) at 60.81 eV and one surface component (Ir_0) shifted -0.50 eV with a GFWHM of 0.25 eV and a LFWHM of 0.21 eV (these components correspond to Ir_{bulk} and $Ir_{surface}$, respectively, as introduced in Section 4.3). Upon oxygen exposure of the 0.5 ML film the iridium surface component, Ir_0, decreases to 3% of its initial value. Therefore, 97% of all Ir(111) surface atoms - with and without graphene atop - are affected by the oxygen dosing. As the Ir_0 component disappears two new components appear, one at lower binding energy (-0.19 eV) compared to bulk, called Ir_1, and one at higher binding energy (+0.30 eV), called Ir_2. The CLS of the two new oxygen-induced features Ir_1
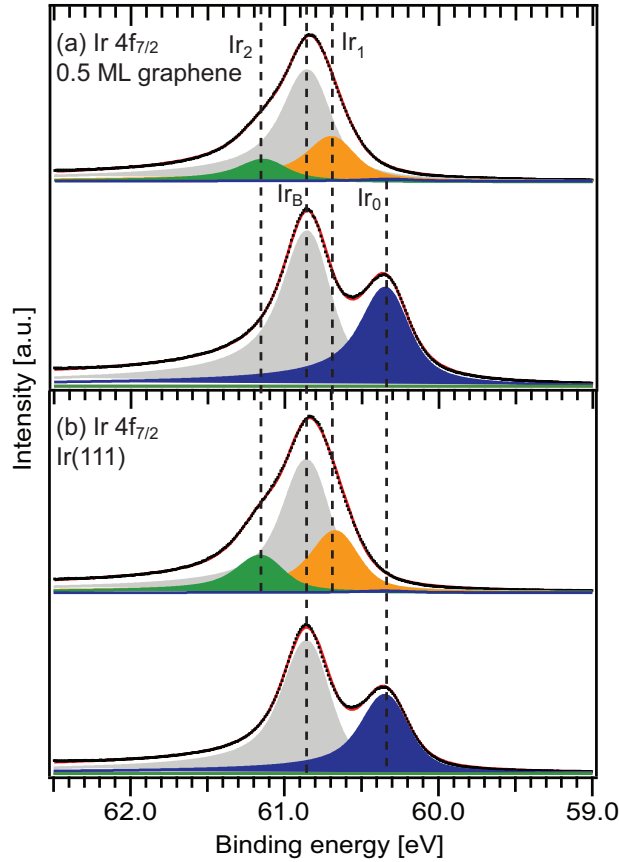
Figure 7.3 Ir $4f_{7/2}$ spectrum of (a) 0.5 ML graphene/Ir(111) and (b) clean Ir(111). The lower spectra of (a) and (b) are taken before, and the upper ones after exposure to $750\,L$ of O_2. The 0.5 ML graphene was exposed at $400\,K$ and the Ir(111) at room temperature. The experimental spectra are shown as black dots, the fits as solid lines and the filled curves represent the components of the fit.

and Ir_2 in Fig. 7.3(a) are identical with those measured for oxygen on Ir(111) upon room temperature oxygen exposure, seen in Fig. 7.3(b). Previous studies [133, 168] have shown that exposure of molecular oxygen onto Ir(111) leads to dissociation and formation of rotated micro-domains of a defective p(2x1) structure with oxygen atoms adsorbed in the three fold hollow sites. In a p(2x1) structure Ir surface atoms are bound either to one oxygen atom or to two oxygen atoms. This gives rise to the two components, Ir_1, and Ir_2 [133] We therefore tentatively conclude that oxygen intercalated the graphene flakes with a defective p(2x1) structure the same structure as formed on bare Ir(111) and substantiate this conclusion in the following by a careful analysis of the Ir components for situations with different graphene coverages. By normalizing the intensity of the Ir_0, Ir_1 and Ir_2 components in Fig. 7.3(a) to the
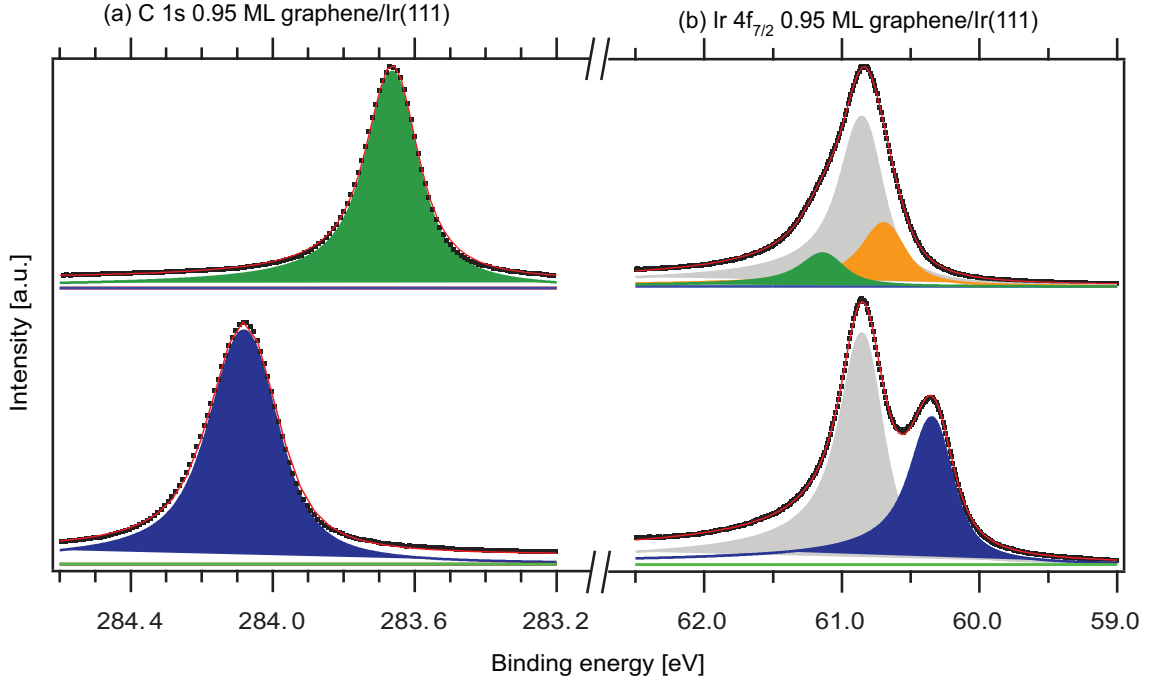
Figure 7.4 C 1s (a) and Ir $4f_{7/2}$ (b) spectra of 0.95 ML graphene/Ir(111). The lower spectra are taken before, and the upper ones after exposure to 750 L of O_2 at 460 K. The experimental spectra are shown as black dots, the fits as solid red lines and the gray, blue, orange, and green curves represent the components of the fit.

total surface intensity, the coverage of the respective types of Ir surface atoms can be calculated to be: $\Theta_0 = 0.03$ ML, $\Theta_1 = 0.70$ ML, and $\Theta_2 = 0.27$ ML. Since each oxygen atom adsorbed forms three bonds with the Ir surface atoms, the oxygen coverage Θ_{Ox} is simply one third of the sum of the coverages of surface atoms, each multiplied by their number of bonds to oxygen atoms: $\Theta_{Ox} = \frac{1}{3} \cdot (0 \cdot \Theta_0 + 1 \cdot \Theta_1 + 2 \cdot \Theta_2) = 0.41 \pm 0.02$ ML. In a similar experiment for a graphene coverage of 0.95 ML exposed to 750 L O_2 at 460 K we get $\frac{1}{3} \cdot (0 \cdot 0$ ML $+ 1 \cdot 0.71$ ML $+ 2 \cdot 0.29$ ML$) = 0.43 \pm 0.02$ ML (see Fig. 7.4).

Note, for the 0.95 ML coverage photoelectron attenuation by graphene atop is not an issue as we compare relative intensities of Ir atoms nearly all underneath graphene. The coexistence of Ir_1 and Ir_2 atoms on O-saturated samples with 0.5 ML and 0.95 ML graphene coverage is unambiguous evidence for a defective p(2x1)-O structure. These components only appear when oxygen atoms are placed with single and double Ir-Ir spacing to Ir(111) three-fold hollow sites. Further, the existence of large areas of p(2x2)-O structure is ruled out by the complete disappearance of the Ir_0 component,

as it would give rise to a significant amount of Ir_0 atoms [25% for 1 ML of p(2x2)-O]. For reference, curve fitting of the oxygen exposed Ir(111) surface without graphene [Fig. 7.3(b)] reveals the following coverages: $\Theta_0 = 0.01$ ML, $\Theta_1 = 0.62$ ML, and $\Theta_2 = 0.37$ ML which results in $\Theta_{Ox} = 0.45 \pm 0.02$ ML. Thus, within the error limits we obtain the identical oxygen coverages, independent of graphene coverage.

Bianchi et al. [133] found a slightly lower saturation coverage of $\Theta_{Ox} = 0.38$ ML at 80 K on Ir(111). In contrast to our method this saturation coverage was found by extrapolating the Ir_0 curve to zero coverage and fixing the corresponding O 1s signal to $\frac{1}{3}$ ML. The intensity of the Ir_0, Ir_1, and Ir_2 components at saturation coverage are, however, also reported in the work of Bianchi et al. Based on their values and our method for calculating the oxygen coverage we obtain $\frac{1}{3} \cdot (0 \cdot 0.06$ ML $+ 1 \cdot 0.58$ ML $+ 2 \cdot 0.37$ ML) = 0.44 ML, within the error limits identical to our value.
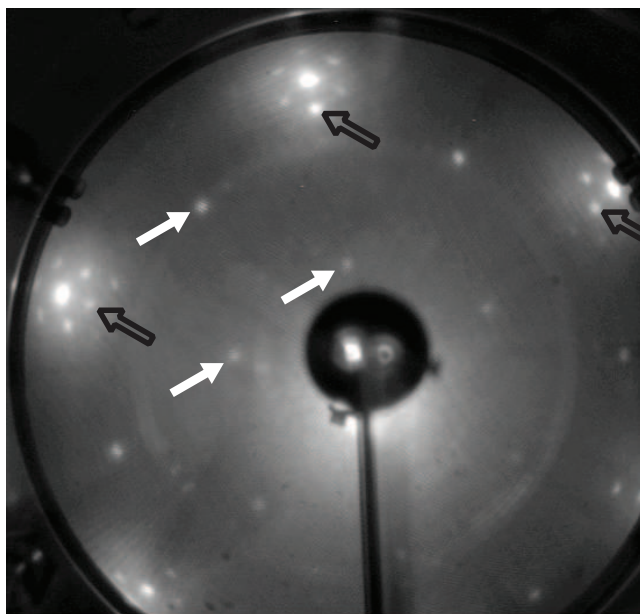
Figure 7.5 LEED image taken at 76 eV of a 0.95 ML graphene film exposed 750 L of O_2 at 460 K. Half order diffraction spots (white filled arrows) with respect to the first order Ir reflections (black unfilled arrows) are well visible. They are consistent with rotated micro domains of p(2x1) underneath the graphene

The fact that oxygen exposure at 400 K (0.5 ML) 460 K (0.95 ML) leads to chemically equivalent C-atoms, with a CLS of -0.45 eV, a disappearance of the Ir_0 component on graphene-covered Ir(111), within the limits of error identical oxygen coverages and binding energy positions Ir_1 and Ir_2 irrespective of the graphene coverage up to 0.95 ML can only be explained if oxygen intercalates the graphene flakes at

these temperatures. Based on these observations we assign the C_3 component in the C 1s spectrum to graphene detached from the Ir(111) surface by an intercalated, defective, p(2x1)-O layer. Further evidence for the structural assignment of the C_3 component comes from the low energy electron diffraction (LEED) image of the O-intercalated 0.95 ML graphene that displays clearly visible half order diffraction spots with respect to the first order Ir(111) ones (see Fig. 7.5).

In addition, we note that a negative C 1s CLS upon oxygen intercalation is consistent with a net hole doping of the graphene sheet by the oxygen. This will be explained in Chapter 8.

Finally, our assignment is supported by the O 1s core level spectra of fully O-intercalated graphene and O-covered Ir(111), which reveals an identical O 1s peak position at 529.9 eV (see Fig. 7.6). For a perfectly closed 1 ML graphene layer no oxygen signal was observed, neither before nor after oxygen exposure at a temperature up to 700 K. Since the binding energy of the O 1s peak originating from the p(2x1)-O structure on Ir(111) is independent of whether or not a graphene flake is located above we conclude that the oxygen-atoms bind to the Ir substrate and if at all, only interact weakly with graphene. We did not observe any O 1s features at 531.1 eV (epoxy groups) and 532.4 eV (ethers) in contrast to the studies of atomic oxygen on graphene/Ir(111) [159, 160], further confirming that oxygen is not adsorbed on the graphene, but rather on the metal surface.

After assigning the C_3 component we continue with the analysis of the C_1 component that dominates the C 1s spectrum taken after oxygen exposure at 355 K [see Fig. 7.1]. Curve fitting of this C 1s spectrum reveals the following relative intensities: C_{Ir} (43%), C_1 (52%), and C_2 (5%). From fitting the corresponding Ir $4f_{7/2}$ spectrum ($\Theta_0 = 0.39$ ML $\Theta_1 = 0.51$ ML, $\Theta_2 = 0.10$ ML) we find a total oxygen coverage of 0.24 ± 0.02 ML. As half of the surface area is bare Ir with a saturation coverage of 0.45 ML determined above, 0.24 ML 0.5 x 0.45 ML = 0.015 ML of the total oxygen coverage is left for intercalation under the graphene flakes. As the flakes cover only half the surface area, the local coverage under the graphene flakes is twice as large, i.e. amounts to 0.03 ML. Note that we subtract here large numbers with substantial errors resulting in an uncertainty of the order of 100% for the oxygen concentration underneath the graphene flakes. Nevertheless, based on this estimate we assign the C_1 component in Fig. 7.1 to a dilute oxygen lattice gas. Referring to Fig. 7.1 it is evident that the C_1 component develops at temperatures between 315 K and 355 K.

We explain this observation by the onset of mobility of the O-adatoms within this temperature interval.
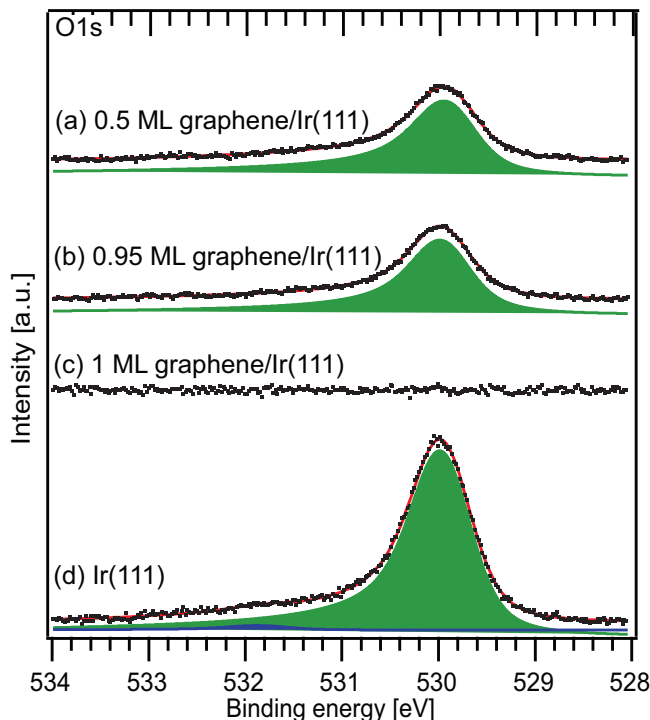
Figure 7.6 The O 1s region after exposure to $750\,\mathrm{L}$ of O_2 for 100 sec. (a) 0.5 ML graphene/Ir(111) at 400 K,(b) 0.95 ML graphene/Ir(111) at 460 K, (c) 1 ML graphene/Ir(111) at $650\,\mathrm{K}$ and (d) Ir(111) at room temperature. The experimental spectra are shown as black dots, the fits as solid red lines and the green and blue curves represent the components of the fit

After oxygen exposure at $375\,\mathrm{K}$ the C 1s spectrum in Fig. 7.1 is dominated by the C_2 (46%) and C_3 (42%) components. Curve fitting of the corresponding Ir 4f spectrum reveals the following relative coverages: $\Theta_0 = 0.10$ ML, $\Theta_1 = 0.83$ ML, and $\Theta_2 = 0.08$ ML, giving $\Theta_{Ox} = 0.33$ ML. As before we can calculate the average O-coverage below graphene at $375\,\mathrm{K}$ as: $(0.33$ ML $- 0.225$ ML$)/0.5 = 0.21$ ML. This oxygen coverage suggests that oxygen intercalates graphene fully at $375\,\mathrm{K}$ and the average O-coverage is similar to the one of a p(2x2) structure. We therefore tentatively assign the C_2 component to a p(2x2) structure formed below graphene.

By exposing a 0.5 ML graphene film to oxygen at $380\,\mathrm{K}$ the intercalation process can be followed in real time by monitoring the C 1s region. Here, we exposed the sample to 1×10^{-7} mbar O_2, the O_2 pressure was stabilized at 300 K, and within 4 minutes it was heated to $380\,\mathrm{K}$ where it was kept during the remaining oxygen
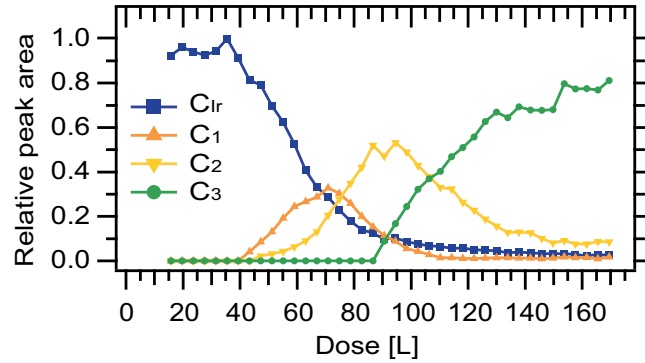
Figure 7.7 The time evolution of the components of the C 1s spectra measured in real time as 0.5 ML graphene on Ir(111) is exposed to 1×10^{-7} mbar, at 380 K. The spectra were fitted using the same components as in Fig. 7.1.

exposure time.

Curve fitting of the C 1s spectra with the same components as described above gives the evolution of the components and the corresponding oxygen phases, as seen in Fig. 7.7 (for a movie of the C 1s spectra during oxygen exposure see [169]). Initially the C_1 component grows, indicating a dilute oxygen phase growing underneath the graphene. As the C_1 component reaches its maximum, the C_2 component starts to increase due to the formation of the p(2x2)-O structure. Finally, the growth of the C_3 initiates once the C_2 component reaches its maximum value.

The intercalation process followed in real time shows the subsequent formation of more and more dense oxygen phases below the graphene flakes. This picture is fully consistent with what is shown in Fig. 7.1, where the same C 1s components are seen to appear at increasing temperatures as more oxygen is able to intercalate the graphene flakes.

Altogether, our observations suggests the following picture of oxygen adsorption on Ir(111) supported graphene. Intercalation requires the presence of bare iridium and therefore no C 1s core level shift is observed on perfectly closed 1 ML graphene films. The absence of any C 1s CLS establishes, that graphene can be grown as a hole-free membrane, impenetrable to molecular oxygen. On the sample with the partial 0.5 ML graphene coverage O_2 dissociation takes place on bare Ir(111) patches, where a p(2x1)-O adlayer is formed. At 300 K this adlayer remains and no oxygen penetrates under the graphene flakes. Increasing the temperature up to 355 K causes more and more graphene flakes to become intercalated by a dilute oxygen adatom gas. At higher temperatures around 375 K graphene flakes become intercalated by

dense oxygen p(2x2)-O and p(2x1)-O adlayers. For $T \geq 400\,\mathrm{K}$ a defective oxygen p(2x1)-O adlayer is present on the entire Ir(111) surface, be it pristine or covered by graphene flakes.

Thus the XPS fingerprints of oxygen intercalation have been determined for the respective core level to be: a C 1s CLS of -0.45 eV to 283.64 eV and a narrowing of the peak in C 1s, disappearance of the Ir_0 component and appearance of Ir_1 and Ir_2 components in Ir $4f_{7/2}$ and an O 1s peak positioned at 529.9 eV, corresponding to oxygen on Ir(111). Armed with these fingerprint values of O-intercalated graphene we revisit the previous XPS-studies of atomic oxygen adsorption on graphene/Ir(111). In the recent work by Vinogradov et al. [159] the authors observed and assigned an O 1s peak at 529.0 eV to intercalated oxygen after exposure to atomic oxygen at room temperature. The authors tentatively explained that the -1 eV CLS with respect to oxygen adsorption on clean Ir(111) is caused by the overlaying graphene film. More recently, Larciprete et al. [160] questioned this assignment (528.8 eV in the work by Larciprete et al.) based on the oxygen peak desorption behaviour. Instead they suggested that the $\sim$529 eV component should be assigned to O-atoms adsorbed in the moiré regions closer to the metal substrate in analogy with the H adsorbates. Since we measure an O 1s binding energy of 529.9 eV for intercalated oxygen, identical to oxygen on clean Ir(111), we can rule out that the O 1s feature at $\sim$529 eV observed after atomic oxygen exposure can originate from intercalated oxygen. Furthermore, we find that intercalation of oxygen is reflected by a -0.45 eV CLS of the C 1s peak of graphene. None of the studies by Vinogradov et al. or Larciprete et al. found C 1s components with a negative shift that occurred simultaneously with the 529 eV peak. We therefore agree with Larciprete et al. and conclude that the O 1s component at 529 eV should be assigned to something else than intercalated oxygen. However, at higher oxygen exposures Larciprete et al. observe a C 1s component at 283.6 eV shifted -0.5 eV with respect to their C 1s binding energy for pristine graphene. This peak is according to the authors assigned to carbon vacancies. In the corresponding O 1s spectrum the authors observe a new component at 530.0 eV, which they assign to double bonded C=O. A shift of -0.5 eV in C 1s spectrum and an O 1s peak position 530 eV is almost identical to what we observe for intercalated oxygen. We, therefore, suspect that a small amount of intercalated oxygen is responsible for the 283.6 eV C 1s component and 530.0 eV O 1s components in the work of Larciprete et al.

7.2 STM View of Intercalation and the Role of Graphene Edges

To gain additional insight into the proposed oxygen intercalation picture we performed STM investigations. Fig. 7.8(a) displays Ir(111) covered with 0.5 ML graphene after oxygen exposure at 355 K. As visualized by the schematic sketch of Fig. 7.8(b) the topography in Fig. 7.8(a) has four Ir substrate levels separated by monatomic steps. The step edges partially act as boundaries of the graphene flakes, but they also grow over the steps. The Ir areas free of graphene are covered by atomic oxygen in the (2x1) structure and have a noisy appearance in Fig. 7.8(a). The graphene-covered areas are rather smooth, but display a moiré of graphene with the underlying Ir(111) substrate with a periodicity of 2.53 nm and a corrugation of 0.45 Å. The moiré is well visible in the contrast enhanced box in the upper right corner of Fig. 7.8(a). Within the graphene-covered area four small islands with an apparent height of 0.9 Å are present [striped red-yellow in Fig. 7.8(b)], three of them next to each other, close to substrate steps. These islands are always found close to substrate steps covered by graphene, often close to the edge of the flake [see Fig. 7.9 which is large scale topograph of the area presented in Fig. 7.8(a)]. The area fraction of these islands is below 5% of the graphene area, consistent with the small intensity of the C_2 and C_3 components for the 355 K C 1s spectrum in Fig. 7.1. We propose that these small islands represent a dense phase of intercalated oxygen underneath graphene, either in the (2x2) or in the (2x1) structure, as visualized in the cross section shown in Fig. 7.8(c) which is taken along the blue line in Fig. 7.8(a). We assume the other graphene-covered areas to be not intercalated or to only possess an oxygen lattice gas intercalation phase consistent with the observation of the C_{Ir} and C_1 components in the XP-spectra.

Additional evidence for this assignment comes from Pt deposition experiments. To understand their outcome, we first review a few previous results related to graphene on Ir(111). The incommensurate moiré unit mesh consists of (10.32 x 10.32) graphene unit cells resting on (9.32 x 9.32) Ir atoms [86]. Due to the varying lateral positioning of the C-atoms with respect to Ir, we identify three high symmetry regions in each moiré unit cell: in an atop-area (fcc- and hcp-area) we find underneath the center of a hexagonal carbon ring an atop Ir site (regular hollow or fcc-site and faulted hollow or hcp-site). In Ref. [85] it was found that the binding
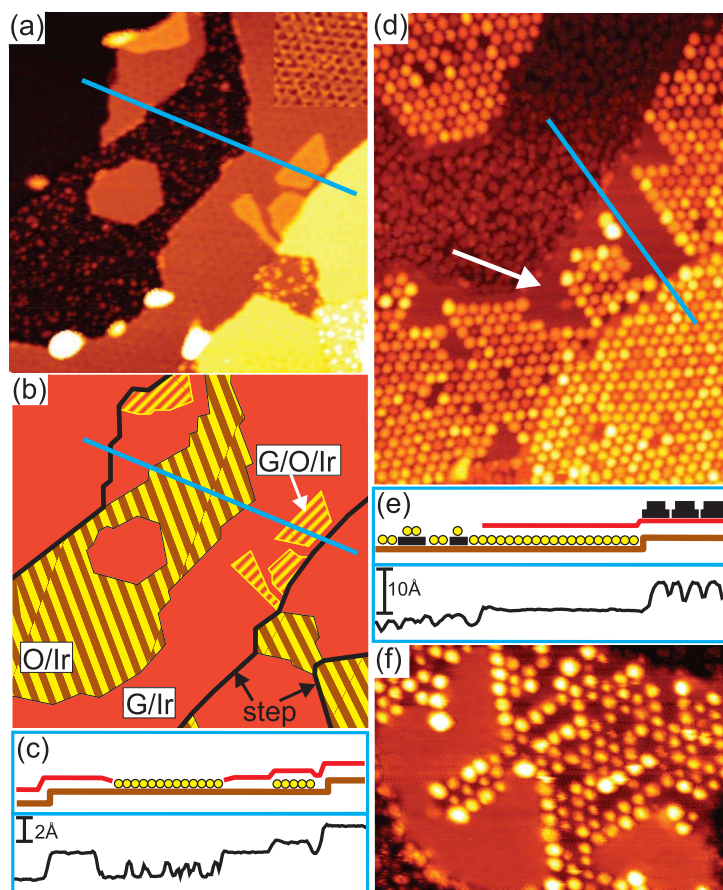
Figure 7.8 (a) STM topograph of Ir(111) covered with 0.5 ML graphene after exposure to 750 L of O_2 at 355 K. In the contrast enhanced box in the upper right corner the moiré is visible. Image size 70 nm x 70 nm. (b) Schematic representation of (a) in top view. Full black line Ir step edge; red graphene on Ir(111) (G/Ir in the schematics); striped brown-yellow Ir with adsorbed O (O/Ir); striped red-yellow graphene with intercalated oxygen(G/O/Ir). (c) Upper panel: schematic cross section along blue line as indicated in (a) and (b). Brown Ir; red graphene; yellow dots - adsorbed oxygen atoms. Lower panel: STM height profile along blue line in (a). (d) STM topograph of the same preparation as in (a), but with additional deposition of 0.3 ML Pt at 300 K. The white arrow indicates an area, where no cluster array was formed on graphene. Image size 70 nm x 95 nm. (e) Upper panel: schematic cross section along the blue line in (d). Black Pt, other colors as in (c). Lower panel: height profile along blue line in (d). (f) STM topograph after similar preparation as in (d), but less Pt was used for post-deposition. Image size 50 nm x 35 nm.

of graphene to Ir is dominated by physisorption with an average binding energy of E_b=50 meV per C-atom and an average height of 3.38 Å (Fig. 2.1). However, this binding is modulated, with weak chemical bonds in the hcp- and fcc-areas and chemical repulsion in the atop-areas. The weak bonds are formed through weak hybridization of Ir($5d_{3z^2-r^2}$) orbitals with C($2p_z$) orbitals, where C atoms of graphene and Ir substrate atoms sit in juxtaposition. In the chemically repelled atop areas (with no C atoms in juxtaposition to Ir atoms) graphene has a larger distance from the substrate resulting in a graphene corrugation of about 0.4 Å. Upon Pt deposition on graphene, the cooperative attack of substrate Ir($5d_{3z^2-r^2}$) orbitals and deposit Pt($5d_{3z^2-r^2}$) orbitals on the graphene π-electronic system causes graphene to locally hybridize from sp^2 to sp^3 in the hcp-areas, implying chemical bond formation between Ir-C and C-Pt and thus cluster binding ([79] and Chapter 4). It is evident that a saturated intercalated oxygen adlayer between Ir and graphene will prevent Ir-C chemical bond formation, thereby inhibit graphene rehybridization and thus impede cluster pinning. Therefore, upon Pt deposition, no Pt cluster arrays are expected to form in graphene areas with dense intercalated oxygen phases underneath.

Fig. 7.8(d) shows the oxygen exposed 0.5 ML graphene sample discussed above after additional deposition of 0.3 ML Pt at room temperature. More than 95% of the graphene-covered area displays a well ordered Pt cluster array, consistent with the absence of a dense oxygen phase corresponding to the C_2 or C_3 components in Fig. 7.1. We have to conclude that the presence of a dilute oxygen adatom gas underneath the graphene flakes (the C_1 component) does not impede cluster growth. It is plausible that the oxygen adatoms of the dilute phase linked to the C_1 component are sitting preferentially in atop- areas underneath the graphene. There, graphene is most distant from the Ir(111) substrate and not even weak bonds between the two exist. Thus, no (or the smallest) energy penalty has to be paid for intercalating oxygen under the atop-areas. Upon Pt deposition, this location of the O adatoms does not disturb the local graphene rehybridization and cluster binding, as it takes place in the hcp-areas where O is absent. Small patches of graphene without an ordered Pt cluster array are also observed in Fig. 7.8(d). These patches are assigned to the areas where a dense phase of intercalated oxygen is present. Our interpretation of the morphology is visualized by the schematic cross section displayed in Fig. 7.8(e), which is taken along the blue line in Fig. 7.8(d). Final evidence for our assignment comes from Fig. 7.8(f). It represents a surface morphology after a similar treatment

Figure 7.9 Large scale topograph (280nm x 170nm) of the area presented in Fig. Fig. 7.8(a) here marked by the square in the center of the ima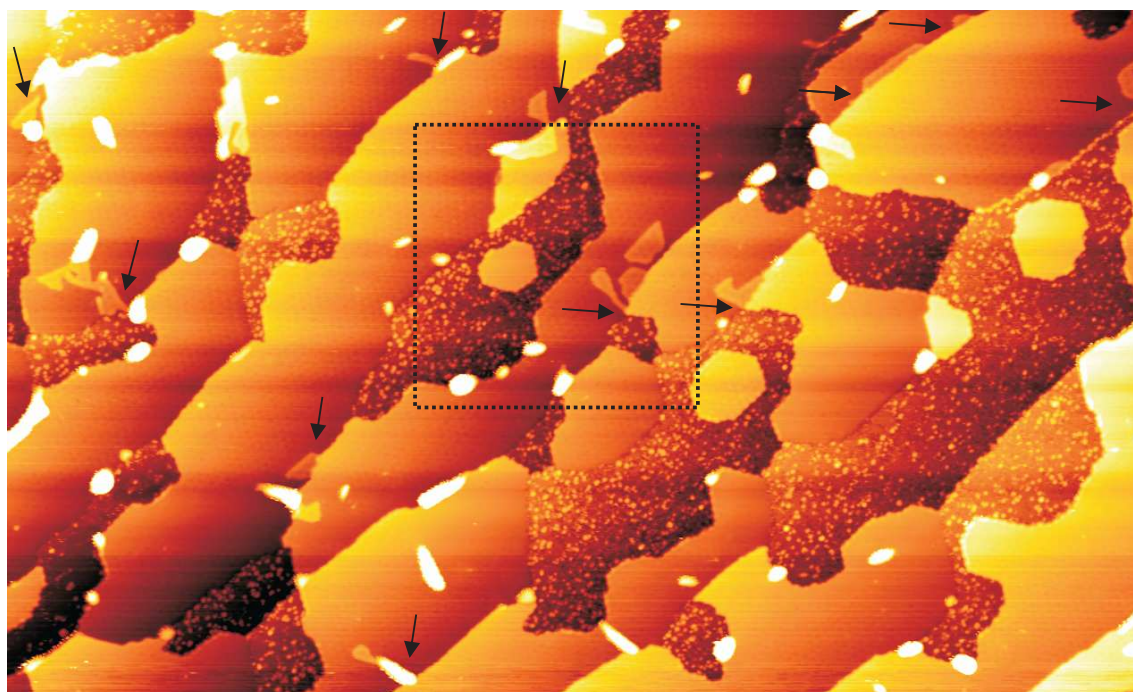ge (Ir(111) covered with 0.5 ML graphene after exposure to 750 L at 355K). Intercalated patches are highlighted by arrows. It is obvious that intercalated patches are always found close to substrate steps covered by graphene, often close to the edge of the flake.

as in Fig. 7.8(c), but with less Pt deposited. As a result the clusters are smaller and it is easier to observe the graphene substrate between the clusters. An analysis of Fig. 7.8(f) reveals that the graphene level is 0.9 Å higher in the cluster free region as compared to the graphene substrate with clusters, thereby confirming our interpretation. We note that to distinguish between intercalated and non-intercalated graphene areas on Ru, Ru post-deposition has been used, though resulting in a weaker contrast and probably not related to graphene rehybridization [38].

Next we give the real space view of the 400 K C 1s spectrum shown in Fig. 7.1, i.e. after exposing an 0.5 ML graphene-covered Ir(111) sample to O_2 at 400 K. Fig. 7.10(a) shows the corresponding STM topograph. The graphene flakes in the lower part of the topograph display no visible moiré contrast. However, the graphene flake in the upper image part attached to an ascending step displays clear moiré contrast. After oxygen exposure at 400 K such flakes with clear moiré contrast are rare in the overall topography. We conclude that the nature of these flakes must be different. An unambiguous interpretation is again possible with the help of Pt deposition. Fig. 7.10(b) shows the sample after an additional 0.3 ML Pt deposited at 300 K. Except for a small flake indicated by an arrow in the lower part of Fig. 7.10(b), no cluster arrays are formed on the graphene flakes. The Pt agglomerates to a few large clusters which are randomly distributed on the flakes. Also decoration of the graphene flake edges by Pt is apparent. This finding is consistent with our conclusions based on the XPS data, namely that at 400 K the vast majority of the graphene area has a dense p(2x1)-O adlayer intercalated, corresponding to the C_3 component.

Before we turn to a detailed discussion on the intercalation behavior of graphene flakes we will address a perfectly closed monolayer of graphene. After exposure of 1 ML graphene to 750 L O_2 at 700 K STM displays the moiré pattern characteristic for the graphene layer everywhere on the sample. Figure Fig. 7.11 (a) is an example image. Using the cluster decoration technique we find after deposition of 0.3 ML Pt on the sample of Figure Fig. 7.11 (a) a uniform and almost defect free cluster array, as shown in Fig. 7.11 (b). It is indistinguishable from a cluster array formed on pristine graphene. The formation of the cluster array is fully consistent with a graphene film with no oxygen intercalated. We, therefore, have to conclude that the closed 1 ML graphene layer is unchanged by the 700 K oxygen treatment and further protects the underlying Ir(111) surface against oxygen adsorption. This conclusion
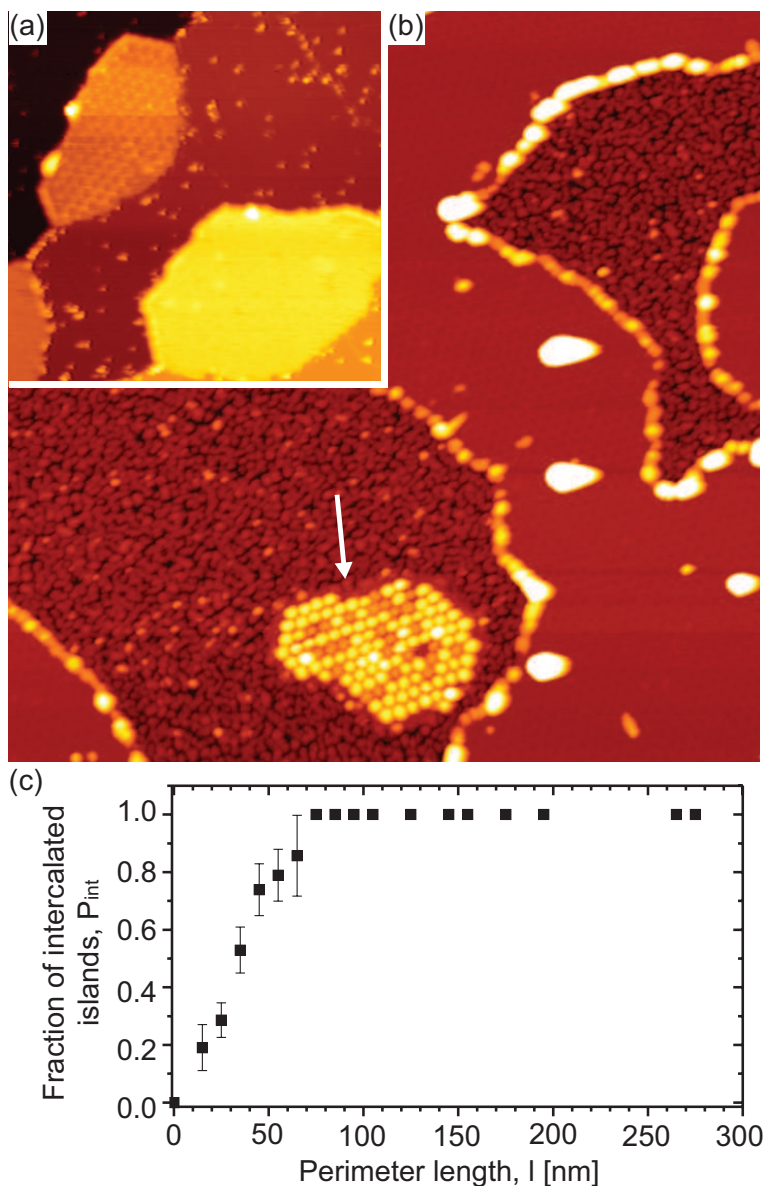
Figure 7.10 (a) STM topograph of Ir(111) covered with 0.5 ML graphene after exposure to 750 L of O_2 at 400 K. Image size 70 nm x 70 nm. (b) STM topograph after same preparation as in (a), but with additional deposition of 0.3 ML Pt at 300 K. The arrow indicates a small graphene flake with Pt cluster array (see text). Image size 140 nm x 140 nm (c) Probability P_{int} for a flake to be intercalated at 400 K by a p(2x1)-O adlayer as a function of flake perimeter length l (see text). The confidence level represented by the error bars is 66%. No errors are given for less than 7 perimeter lengths in a bin.
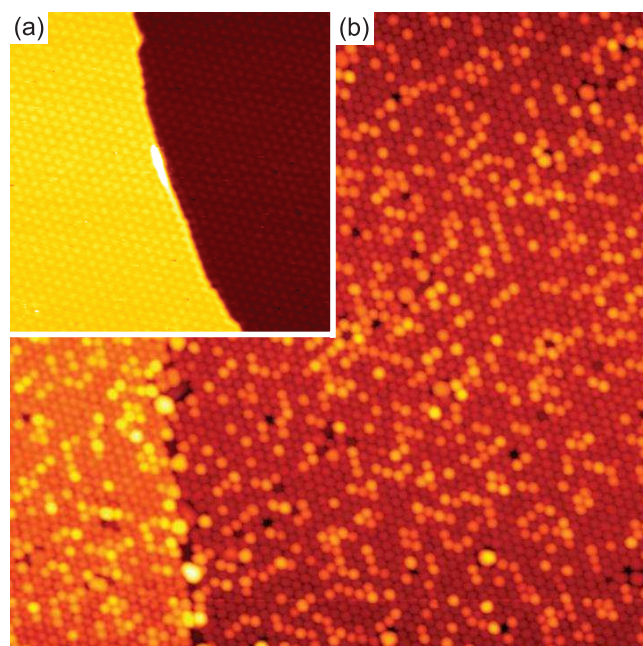
Figure 7.11 (a) STM topograph after exposure of a closed graphene film on Ir(111) to 750 L of O_2 at 700 K. (b) After oxygen exposure, but with additional room temperature deposition of 0.3 ML Pt was performed. Image sizes are (a) 70 nm x 70 nm and (b) 140 nm x 140 nm.

matches perfectly with the XPS data presented in Figures Fig. 7.2 and Fig. 7.6(c).

Analysis of a large number of STM images of oxygen exposed graphene flakes reveals the following features: (i) At 355 K the phase boundaries between dense and dilute intercalation areas are sharp. (ii) At 355 K the phase boundaries largely follow the moiré structure. Densely intercalated areas are mostly quantized laterally in units of the moiré cell. (iii) At 355 K densely intercalated areas are typically attached to substrate steps covered by graphene, mostly close to a location where a graphene flake crosses a substrate step. The intercalated areas are only found under graphene flakes grown over a step edge. (iv) At 400 K graphene flakes are either fully intercalated with a p(2x1)-O intercalation phase or only with a dilute adatom gas. Not a single phase boundary within a graphene flake is observed out of a sample of more than 103 graphene flakes. (v) At 400 K few graphene flakes without a p(2x1)-O intercalation layer remain. They are all among the smallest ones. (vi) At 400 K the apparent moiré corrugation of intercalated flakes is with $\sim$0.1 Å substantially lower than the one of non-intercalated ones with $\sim$0.45 Å.

The sharpness of the phase boundaries at 355 K (i) and their relation to the moiré (ii)

most likely trace back to the binding energy inhomogeneity of graphene on Ir(111) mentioned above. When a dense oxygen adlayer is formed underneath graphene, the more strongly bound hcp- and fcc-areas need to be delaminated from the graphene. In consequence they form an obstacle for the expansion of the intercalated dense O phase and sharp phase boundaries are formed between the oxygen adatom lattice gas (not requiring delamination, as O is located primarily in the atop-areas) and the O-islands in the p(2x2) or p(2x1) phase. Findings (iii)-(v) tell us about the pathway of intercalation. The formation of a dense phase of atomic oxygen on the Ir(111) surface under the graphene flake encompasses two basic steps: (a) delamination of the graphene flake starting at its edge and (b) oxygen transport under the flake through surface diffusion to establish a dense oxygen intercalation phase. The fact that after oxygen exposure at 400 K all large graphene flakes are fully intercalated with a p(2x1)-O oxygen phase, while only a few small graphene flakes are not delaminated, tells us immediately that at this temperature the formation of the p(2x1)-O intercalation layer is not diffusion limited but boundary limited. Diffusion limitation would make it difficult for the phase boundary to reach the center of large graphene flakes (which is not the case), while boundary limitation says that the key process is to propagate the p(2x1)-O ad-layer on the Ir(111) terrace through the flake edge underneath the graphene flake, i.e. to pass the flake edge. Moreover, the absence of phase boundaries underneath graphene flakes tells that the delamination of a flake at 400 K must be considered as a single, fast event.

In Fig. 7.10(c) we plot the observed fraction P_{int} of p(2x1)-O intercalated and delaminated graphene flakes confined to a single Ir terrace as a function of the flake perimeter length l. Graphene flakes that are not confined to a single Ir terrace, i.e. that grow across a substrate step, are not included in the statistics (see below). This implies that our analysis is not valid for a percolated graphene film with holes or even for the perfectly closed layer. For the analysis we evaluated l for a total of 177 graphene flakes. It is obvious from the analysis that P_{int} is a strongly increasing function of l. P_{int} reaches unity for flakes with a perimeter of 80 nm and beyond. Assuming that the propagation of the p(2x1)-O adlayer beyond the flake edge is a process with a small probability that is attempted independently and randomly along the flake edge yields an initial linear increase of P_{int} with l, which has to level off, when approaching $P_{int} = 1$, as observed.

Recent experiments on very small graphene flakes (data not shown) indicate that

flakes smaller than a threshold flake size cannot be intercalated by oxygen. However, the data presented in Fig. 7.10(c) shows no evidence for this threshold flake size.

Why is it difficult for oxygen to propagate the p(2x1)-O adlayer underneath the graphene flake edge and what is the nature of this unlocking-process? As shown by Lacovig et al., the graphene flake edge dangling bonds tend to bind to the Ir substrate([90] and Fig. 2.3). Therefore the flakes bend down at the edge, as indicated in the schematics of Fig. 7.8(c). While single oxygen adsorbates forming an oxygen adatom lattice gas - may diffuse underneath the graphene flake into the unbound atop-areas without lifting the flake edge and the flake itself to a significant extent, the formation of a dense oxygen adlayer requires the entire unbinding of graphene. Unbinding of a graphene moiré unit cell at the flake edge requires unbinding of the flake edge bonds plus unbinding of the graphene moiré unit cell adjacent to the edge. In contrast, unbinding of a moiré unit cell within the flake requires no additional unbinding of edge bonds. The force required for the unbinding of a moiré unit cell at the flake edge is therefore evidently larger than the one for unbinding a cell in the interior of the flake. This explains why even very large flakes are delaminated rapidly, once the phase boundary passed the flake edge. For graphene flakes confined to a single Ir(111) substrate terrace, unbinding of the graphene flake edge may therefore be considered as the rate-limiting step in intercalation at 400 K.

The additional question arises, how the adsorbed oxygen on the terrace may exert the unbinding force at the graphene edge. To answer this question it is of key importance to note that close to saturation the adsorption energy of oxygen on Ir(111) decreases considerably because of repulsive adsorbate-adsorbate interactions [167, 170]. Consider now the saturated p(2x1)-O adlayer at the graphene flake edge. The adlayer exerts a one dimensional pressure (force per unit length) on the graphene flake edge, as a local expansion of the adlayer into the space underneath the flake will increase the binding energy (larger adsorbate separation). Through local fluctuations in coverage (and thus force) at some point along the flake edge, unbinding will occur. The probability for an unbinding event at the flake edge will be proportional to the perimeter of the edge, as observed. It is followed by rapid expansion of the adlayer underneath the flakes. The fixed chemical potential of the gas phase will replenish oxygen on the Ir(111) terrace until eventually the p(2x1)-O adlayer is established on the entire surface, on the bare Ir terrace and under the graphene flakes. These considerations also explain why delamination does not start

in the center of a graphene flake: although some oxygen is present there, its concentration is low and thus the force that can be exerted to unbind. Our experiments related to the energetics of intercalation presented below (Fig. 7.14 and Fig. 7.15 with discussion) are fully consistent with the above picture. However, we are unable to specify the unbinding process in terms of the atomistic reaction pathways and potential energy barriers. To this end density functional theory calculations and more detailed experiments are highly desirable.

In the description of Fig. 7.10(b) we noted that the Pt deposition causes an edge decoration of flakes delaminated by an intercalated (2x1) adsorbate layer. This edge decoration with Pt clusters is absent for small flakes that have not been delaminated and which display a regular cluster array. In the picture proposed above, the Pt edge decoration is expected: After unbinding the graphene edges from the substrate they are likely to be reactive and will consequently act as heterogeneous nucleation sites for Pt.

While our concept of edge unbinding as a rate-limiting step for the formation of dense oxygen adlayers underneath graphene flakes explains all of our observations convincingly, it is worthwhile to consider an alternative scenario based on the oxygen intercalation experiments on Ru(0001). Sutter et al. [64] and Starodub et al. [65] observed that once the oxygen exposure to Ru(0001) stops, O disappears from under graphene flakes already at 550 K and close to the edge of a graphene flake deintercalation takes place first. An alternative interpretation of the Pt decoration experiment of Fig. 7.10(b) would then be that for the small graphene flakes the oxygen has leaked out by the time of the STM analysis, while the edges of the large flakes would, after some oxygen loss at the edges, rebind to the Ir, keeping the O trapped inside. Instead of hindered intercalation under small flakes, our Pt post-deposition experiments would then visualize the more rapid deintercalation of oxygen from under small flakes. The edge decoration of the large flakes would then not be the consequence of reactive flake edges but of graphene rebound to the substrate. This scenario based on oxygen intercalation under graphene on Ru(0001) experiments does not apply for the following two reasons.

(1) Oxygen adsorption on Ir(111) is a true 2D adsorption system. Thus, once the sample is saturated with oxygen in a p(2x1)-adlayer only combustion with graphene (T > 550 K) or oxygen desorption (T > 750 K) might lower the surface coverage. Both processes possess onset temperatures well above 400 K and are thus irrelevant.

As the oxygen adlayer was saturated in a pressure of 1×10^{-5} mbar, an unreasonable amount of energy would be necessary to compress the saturated O adlayer in consequence of deintercalation. There is no space to go for the oxygen from under a flake all surrounding Ir terraces are saturated with oxygen.

(2) A striking proof that the above scenario fails is contained in Fig. 7.12. Fig. 7.12(a) displays Pt clusters grown on the graphene flakes before oxygen exposure. Upon oxygen exposure at 400 K with an oxygen pressure of 1×10^{-7} mbar the Pt cluster arrays of large graphene flakes suddenly disorder after an exposure to 6 L. The final state is shown in Fig. 7.12(f) after 145 L.

Fig. 7.13 displays a small and several larger graphene flakes after a similar experiment. While the large graphene flakes display detached clusters, the array on the small graphene flake indicated by the white arrow is still intact. Our interpretation is as follows: Upon O_2 exposure oxygen adsorbs on the Ir(111) terrace and intercalates under the graphene flakes in the very same way, as if the clusters would not be present. Upon formation of a dense oxygen intercalation layer, graphene becomes detached from the Ir(111) substrate and the local sp^3 hybridization is lifted. In consequence the clusters are unbound, become mobile and aggregate to larger entities which eventually come to rest. Our observations imply that the increased delamination energy due to cluster binding is not a substantial hindrance for the formation of a dense intercalation layer. Our observations also imply that where the cluster array was not destroyed as for the small graphene flake in the lower part of Fig. 7.13 - no dense oxygen layer intercalated. Thereby, the scenario developed above on the basis of observations related to oxygen intercalation under graphene on Ru(0001) is refuted.

Coming back to our list of observations extracted from the STM images, observation (iii) at 355 K indicates that graphene flakes extending over several terraces are somewhat special. At this lower temperature, densely intercalated areas are typically attached to substrate steps covered by graphene, mostly close to a location where a graphene flake crosses a substrate step [compare Fig. 7.8(a) and Fig. 7.9]. Our interpretation is as follows: Where a graphene flake grows over a substrate step a larger graphene-Ir separation is found [81]. Therefore at these locations oxygen more easily unbinds the graphene locally and diffuses in under the flake along the more spacious tunnel formed through the graphene flake and the ascending step. Occasionally oxygen is able to unbind a small area adjacent to the tunnel and spreads
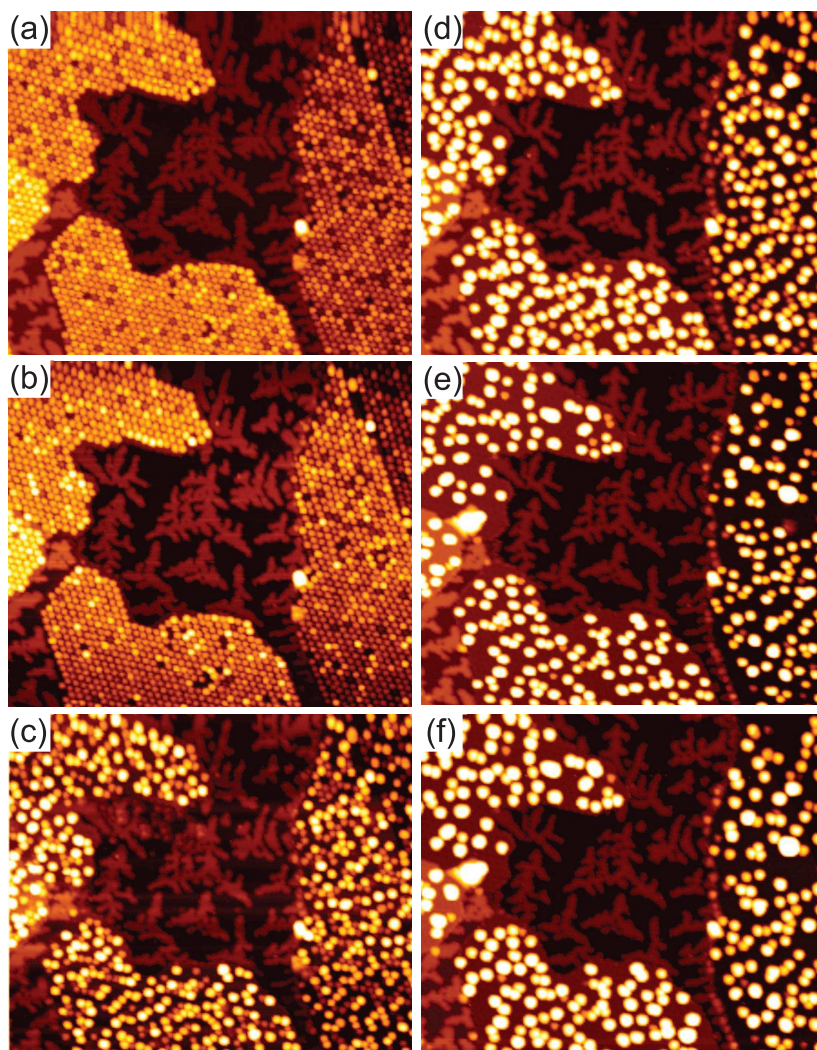
Figure 7.12 STM topographs of 0.3 ML Pt deposited at 300K on 0.5 ML graphene/Ir(111). (a) Imaged at 400 K before oxygen exposure. (b)-(f) Imaged at 400 K during exposure to $1{\times}10^{-7}$ mbar of O_2. (b) After 80 s (6 L); (c) after 250 s (19 L); (d) after 590 s (44 L); (e) after 1260 s (95 L); (f) after 1930 s (145 L). Image size 120nm x 100nm.
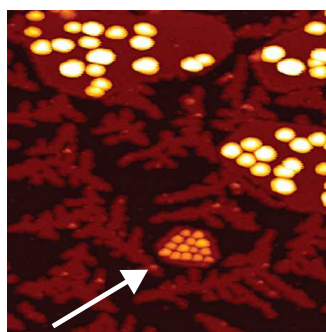
Figure 7.13 STM topograph of 0.3 ML Pt deposited at 300 K on 0.2 ML graphene/Ir(111) after exposure to 750 L of O_2. Arrow indicates non-delaminated graphene flake (see text). Image size 70 nm x 70 nm.

away from the step forming a dense intercalation patch. Note that one of the 4 small intercalation patches in Fig. 7.8(a) has a small gap to the substrate step. We observe that the shape of intercalation patches may fluctuate while imaging. Therefore small intercalation patches may also be pinched of the substrate step or a patch connected to it. We emphasize that single intercalation patches are not found in the central area of a substrate terrace covered by graphene (compare Fig. Fig. 7.9). As at 355 K we never observe entire intercalated flakes, we conclude that at this low temperature the delamination of graphene within the flake is an effective barrier for the spreading of the dense oxygen intercalation phase.

We note that we are unable to identify the rate-limiting step for the formation of the oxygen adatom lattice gas under graphene flakes with certainty. We assume that it is just the onset of the surface diffusion of atomic oxygen on Ir(111) that enables its formation. At least the increase of the p(2x1)-O domain size from room temperature to 400 K as seen by STM is consistent with this assumption.

The substantially reduced corrugation of the moiré (vi) after delamination of the graphene through intercalated oxygen is fully consistent with our XPS experiments. When we discussed Fig. 7.1, we noted that the reduced GFWHM of the new C_3 component representing graphene floating on intercalated oxygen indicates a reduced height modulation. This is exactly what we observe in STM.

7.3 Energetics of Intercalation

Now we address the question whether atomic oxygen, once formed on the bare Ir(111) terraces, is more strongly bound underneath the graphene flakes than on the bare Ir. We already demonstrated that no covalent bonds are formed between oxygen and graphene (absence of XPS signatures for ethers and epoxy groups). However, if intercalated oxygen would cause strong charge transfer of graphene, from electrostatic interaction an enhanced binding energy of oxygen underneath graphene could result.

In a first experiment we exposed 0.5 ML graphene on Ir(111) to $750\,\mathrm{L}$ O_2 at room temperature. As described above, intercalation is absent and the p(2x1)-O structure is present only on the bare Ir(111) patches at this temperature. Subsequently, we heated the sample to $410\,\mathrm{K}$ in the absence of an applied oxygen pressure. The C 1s region was monitored during heating. In Fig. 7.14(a) the first and the last C 1s spectrum of the experiment are displayed. Fig. 7.14(b) shows the result from curve fitting of the C 1s spectra taken during the heating. The components are the same as in Fig. 7.1. Initially, only the C_{Ir} component is present in Fig. 7.14(a). Upon heating the C_{Ir} component is seen to decrease, whereas the C_1 component increases. A very small C_2 component is also seen in the temperature interval 380 - $410\,\mathrm{K}$. After heating to $410\,\mathrm{K}$ a visible shift towards lower binding energy is observed and the spectrum can be deconvoluted by the C_{Ir} (82%) and C_1 (16%) components.

The observation of the C_1 component tells that a dilute oxygen lattice gas formed below many graphene flakes when the surface is heated to $410\,\mathrm{K}$. The absence of the C_3 component implies the absence of a p(2x1)-O adlayer below graphene. The marginal size of the C_2 component implies an only marginal size of p(2x2)-O adlayers below graphene. Oxygen combustion with graphene during the heating can be excluded as we observe that above $550\,\mathrm{K}$. Consistent with these XPS findings regular cluster arrays form on the graphene flakes when Pt is deposited afterwards [compare Fig. 7.14(c)], except in a few locations at the edges of graphene flakes. These disturbed areas [see arrow in Fig. 7.14(c)] may be linked to the small magnitude of the C_2 component.

Without applied oxygen pressure no dense oxygen adlayer forms underneath graphene flake. The outcome of this experiment is consistent with our considerations described above. The dilute adatom gas forms underneath, as this enables to lower the concentration of oxygen on the terrace and thereby to increase the average oxygen binding
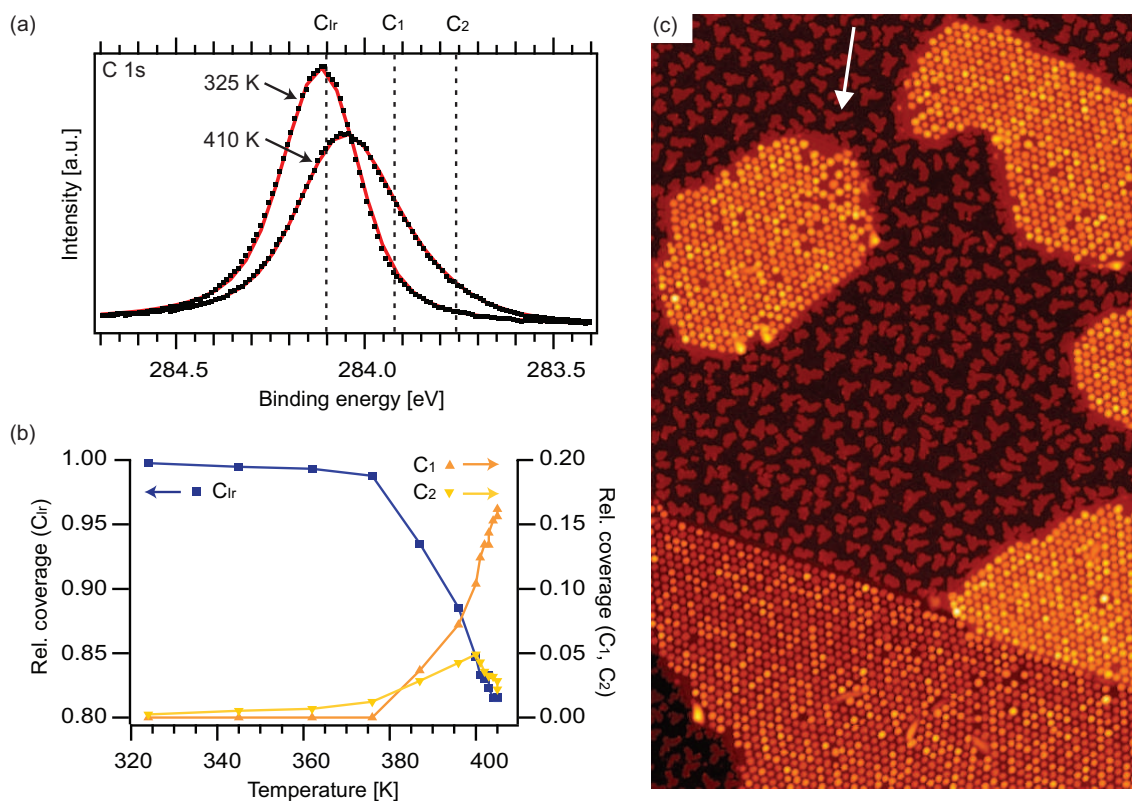
Figure 7.14 0.5 ML graphene/Ir(111) was exposed to 750 L of O_2 at 300 K and subsequently heated to 410 K. In (a) the first (325 K) and last (410 K) C 1s spectra taken during heating are displayed. The experimental data is shown as dots and the fits as red lines. In (b) the partial coverages of the fit components C_{Ir}, C_1, and C_2 for the spectra are plotted as a function of temperature. (c) STM topograph taken after the experiment visualized in (a) and (b), but with additional deposition of 0.3 ML Pt at 300 K. Image size 140 nm x 220 nm.

energy to Ir(111) [167]. As the initially saturated p(2x1)-O adlayer on the Ir terraces decreases in oxygen density, the force exerted by it on the graphene flakes will rapidly drop to an extent that graphene delamination does not take place, or only to a marginal extent. While this experiment is fully consistent with the absence of an energetic preference for oxygen to reside underneath graphene, it does not prove its absence.

In a second experiment we titrated intercalated oxygen with CO, which can be seen as the reverse experiment of oxygen intercalation. Initially, a surface covered with 0.5 ML graphene was exposed to 750 L of O_2 at 410 K to obtain full intercalation. After oxygen intercalation the sample was heated to 490 K and exposed to 5×10^{-9} mbar of CO. The titration was followed in real time by acquisition of the C 1s region and the Ir 4f region. We note that a temperature of 490 K is too low for graphene etching or oxygen desorption. Details about the etching of graphene will be discussed in a forthcoming publication.

The C 1s spectra are shown in Fig. 7.15(a) as an image plot. The CO dose is given on the x-axis, and the binding energy is given on the y-axis, while the intensity is shown with color code. The corresponding Ir 4f spectra were fitted with the same components as in Fig. 7.3 and the resulting peak areas of the surface components are shown in Fig. 7.15(b). Initially, a small negative CLS in the C 1s region develops, simultaneously with the Ir_2 component decrease. Once the Ir_2 component reached zero the C 1s CLS matches extremely well with the fingerprint of graphene intercalated by a p(2x2)-O structure, i.e. with the position of the C_2 component [see Fig. 7.15(a)]. After the Ir_2 component disappeared the Ir_1 component starts to decrease and the C 1s CLS decreases rapidly. This implies that oxygen deintercalates to an extent that graphene adheres again to Ir(111), i.e. relaminates Ir(111). Once, the C 1s peak reaches the C_{Ir} peak position the coverage of Ir_1 atoms has dropped to approximately half of the coverage as compared to the measured coverage of the p(2x2)-O structure just before re-lamination sets in. We conclude that at this point of the titration we have the p(2x2)-O structure on the bare Ir and fully laminated graphene flakes. This is a key finding: despite the fact that the titration reaction removes oxygen only from the bare Ir terraces (CO cannot penetrate under graphene at the low pressure applied [171], at this point the oxygen concentration on the bare Ir terraces is larger than underneath the graphene flakes. Apparently graphene expels oxygen. This finding can only be understood, if oxygen energetically prefers to

reside on the bare Ir rather than underneath graphene flakes. Thus, the CO titration experiment directly proves that O-intercalation weakens the binding of graphene to the substrate, since an overall binding energy gain of graphene bonded to the Ir(111) substrate is the only way to explain the energetic preference of oxygen on the bare Ir(111). Further, titration diminishes the remaining Ir_1 component due to loss of oxygen from the terraces and eventually we are left with clean Ir(111) partly covered by non-intercalated graphene.
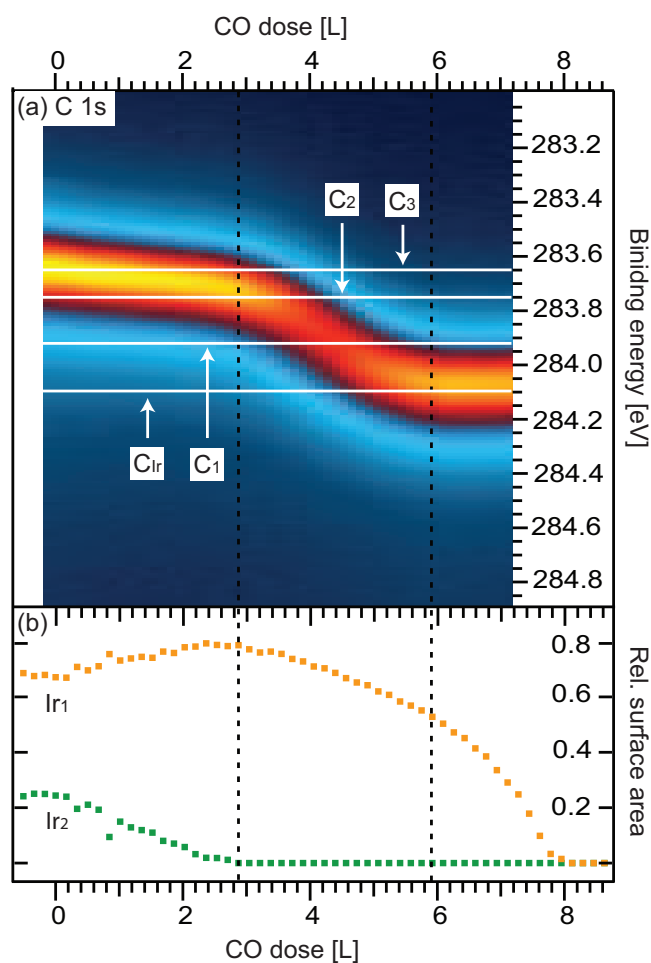
Figure 7.15 0.5 ML graphene/Ir(111) was exposed to $1{\times}10^{-5}$ mbar of O_2 for 100 sec at 410 K. After oxygen intercalation the sample was heated to 490 K and exposed to $5{\times}10^{-9}$ mbar of CO. In panel (a) the development of the C 1s peak upon CO exposure, from the initial oxygen intercalated position to the position of pristine graphene/Ir(111) is seen, and in (b) the relative surface intensity of the oxygen-induced Ir surface components is displayed. Both the Ir 4f and C 1s core levels were followed in real time.

Discussion

Shortly after the publication of our results on oxygen intercalation under graphene on Ir(111) [166], a similar study by Larciprete et al. was published [172]. Although their study is not as detailed as ours, some of their results, such as the XPS fingerprints of intercalation or that the graphene layer is decoupled from the substrate by the presence of intercalated oxygen, are in agreement with our study.

However, there is disagreement over the behavior of the closed graphene layer with respect to O_2 exposure. We showed that under an applied oxygen pressures of up to 10^{-5} mbar and for temperatures of up to $700\,\mathrm{K}$ no intercalation under a closed graphene layer takes place. Larciprete and coworkers report that complete intercalation can, indeed, be achieved by exposing the sample to 5×10^{-3} mbar O_2 at $520\,\mathrm{K}$ for 10 minutes.

The difference might be due to the different parameters used for O_2 exposure: Larciprete et al. used a 500 times higher pressure and a 3000 times larger dose. Nevertheless, the reason might also lie in their different method of preparing the graphene layer. The authors also used the TPG + CVD method, but they do not specify the time interval of the CVD step. This time interval is crucial to achieve a closed graphene layer. We found that 20 minutes CVD growth are not sufficient to close the graphene layer, and therefore extended this step to 40 minutes. We carefully checked that this recipe yields a closed layer (see Section 3.4).

7.4 Outlook: Hydrogen Intercalation

In this chapter, the intercalation of oxygen under graphene/Ir(111) has been described in detail. The question arises, if graphene is also intercalated when exposed to other gases and if the same mechanisms apply. We chose H_2 as a likely candidate because H_2 adsorbs dissociatively on the Ir(111) surface, exactly like O_2. Also, it was shown that a graphene layer on SiC can be decoupled from the substrate by intercalation of hydrogen [61, 62].
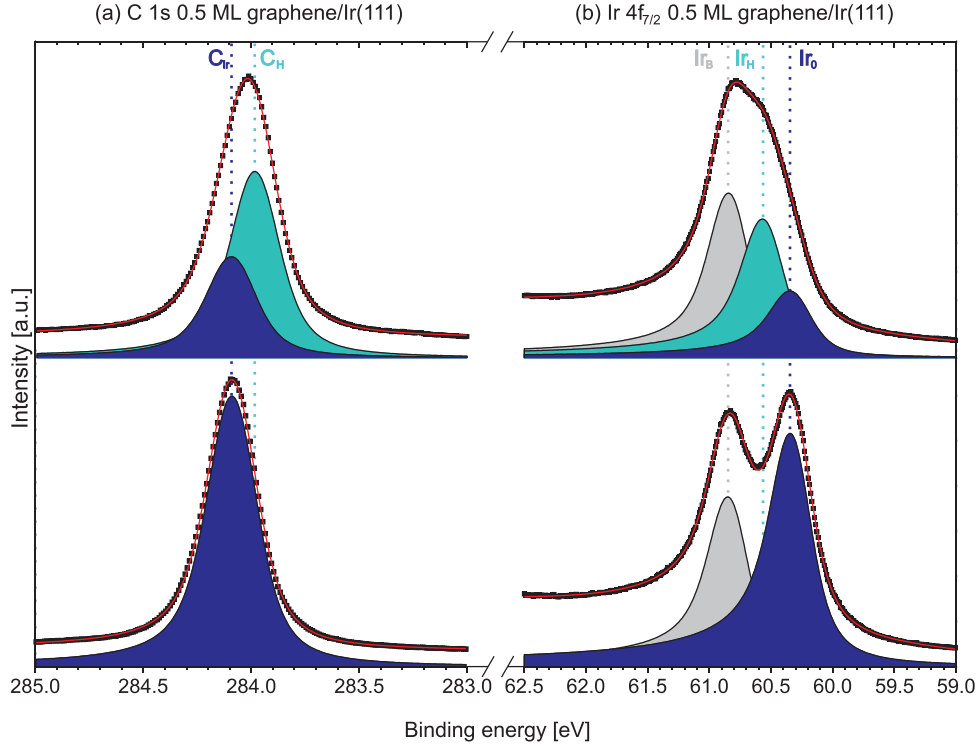
Figure 7.16 (a) C 1s and (b) Ir $4f_{7/2}$ spectra of 0.5 ML graphene/Ir(111). The lower spectra are taken before, and the upper ones after exposure to 750 L of H_2 with $p_{H_2} = 5 \times 10^{-6}$ mbar at 120 K. The experimental spectra are shown as black dots, the fits as solid red lines and the gray (Ir_B), blue (Ir_0 and C_{Ir}), and cyan (Ir_H and C_H) curves represent the components of the fit. The dashed lines are the fitted binding energy positions. Here, the Ir 4f spectra are collected with a photon energy of 120 eV.

We exposed 0.5 ML graphene flakes to 750 L of H_2 at 120 K. This temperature was chosen because hydrogen desorbs from Ir(111) between 150 K and 350 K [173].

Figure 7.16 (a) shows C 1s spectra before (lower spectrum) and after hydrogen exposure (upper spectrum). The spectrum of pristine graphene is fitted with a single component at 284.09 eV (C_{Ir}). After H_2 exposure the intensity of this component is reduced to 38 % of its initial value. A new component C_H emerges at 284.01 eV with a GFWHM that is reduced by 20 % compared to C_{Ir}. We tentatively assign this component to graphene intercalated by hydrogen.

This assignment is confirmed by the Ir 4f spectra shown in Fig. 7.16 (b). Before H_2 exposure (lower spectrum), the spectrum consists of two components: Ir_B (bulk Ir) at 60.83 eV and Ir_0 (clean Ir surface) at 60.32 eV. Note that this spectrum is recorded with a photon energy of 120 eV resulting in an increased surface sensitivity of the measurement. Therefore, the relative intensity of the Ir_0 component is higher than

e.g in Fig. Fig. 7.3. After H_2 exposure, the intensity of Ir_0 is reduced to 32% of its initial value. A new component Ir_H emerges at $60.54\,eV$, while the bulk component Ir_B is not affected. Thus, spectral weight is shifted from Ir_0 to Ir_H. The component Ir_H also emerges when an Ir surface not covered by graphene is exposed to hydrogen (data not shown) so that we can assign this component to iridium covered by hydrogen.

We conclude that under these conditions H intercalates under graphene/Ir(111). The narrowing of the C_H component signals that the graphene layer is decoupled from the substrate. However, the remaining intensity of the C_{Ir} and Ir_0 components shows that intercalation of the graphene layer is not complete.

We performed STM investigations using the cluster decoration technique. Figure 7.17 shows an STM topograph of $0.2\,ML$ graphene flakes exposed to $750\,L$ of H_2 at $90\,K$ and subsequent $0.3\,ML$ Pt deposition at the same temperature. Prior to imaging, the sample was warmed to room temperature. At this temperature, most of the hydrogen desorbs from the Ir terraces, and it is possible that H also deintercalates from under the graphene flakes. However, Pt decoration was performed at $90\,K$ and thus before desorption or deintercalation could take place.

We observe graphene islands which are mostly attached to step edges. They can be divided into two classes: Those islands with a regular cluster lattice and those with an irregular distribution of large clusters. We conclude that the presence of intercalated hydrogen inhibits sp^3 hybridization of the graphene and thus the formation of regular clusters. Similar to O intercalation, the H intercalated islands are the largest ones in the size distribution. Our STM experiments support the XPS view, namely that under the chosen conditions part of the graphene flakes are intercalated by hydrogen.

The results resemble those on oxygen intercalation: (i) We find a similar dependence of the intercalation probability on the island size. (ii) The graphene layer is decoupled from the substrate by intercalation. (iii) Cluster growth is inhibited in the intercalated areas. (iv) The edges of intercalated islands are decorated by Pt.

Nevertheless, there might be a striking difference: The probability for O intercalation can be increased by increasing the temperature at which the sample is exposed to O_2. Exposure of $0.5\,ML$ graphene to O_2 at $400\,K$ ($0.95\,ML$ at $460\,K$ respectively) leads to almost full intercalation. It is not certain if complete intercalation by hydrogen can be achieved in the same way. At temperatures higher than $120\,K$ it might be
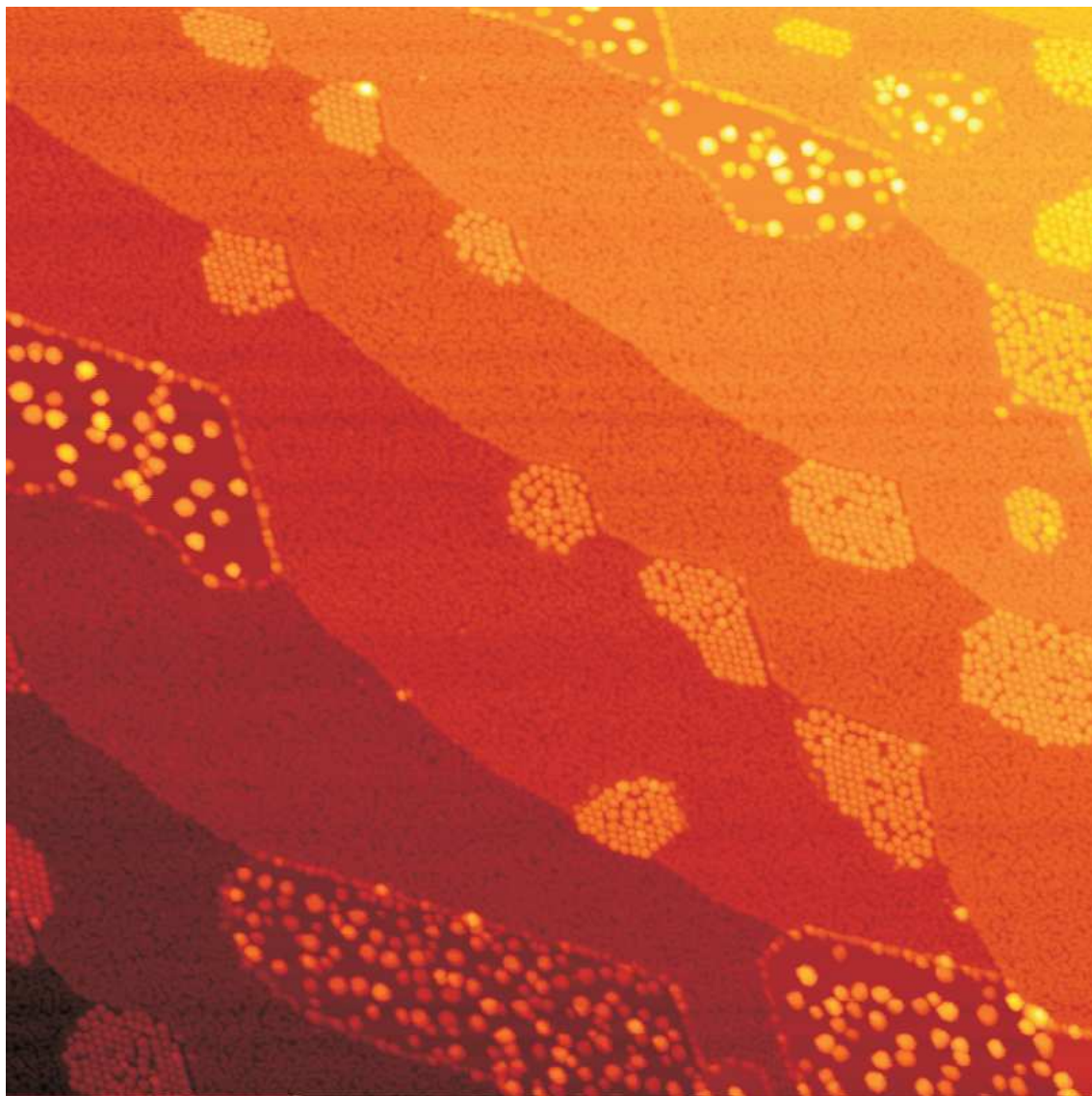
Figure 7.17 STM topograph (taken at room temperature) of Ir(111) covered with 0.5 ML graphene after exposure to 750 L of H_2 with $p_{H_2} = 1 \times 10^{-7}$ mbar at 90 K and subsequent 0.3 ML Pt deposition. Image size 250 nm x 250 nm.

more difficult to achieve H saturation of the Ir surface (and thus intercalation), as hydrogen already starts to desorb at 150 K [173]. Accordingly, the intercalation probability might decrease with increasing temperature.

Thus, further experiments are needed to point out the mechanisms of hydrogen intercalation under graphene/Ir(111) and to find the right parameters of exposure (H_2 pressure and dose, temperature) necessary to achieve full intercalation.

7.5 Conclusions

Our studies show that under an applied oxygen pressure no intercalation under a closed graphene layer takes place. Graphene on Ir(111) can be grown as an impenetrable hole-free membrane. In contrast, for 0.5 ML graphene coverage a temperature dependent intercalation behavior is observed. Up to 300 K no intercalation takes place. With increasing temperature, more and more flakes are intercalated by a dilute oxygen adatom lattice gas. This gas coexists with the dense p(2x1)-O adlayer on the bare Ir(111) terraces. Its formation is not associated with graphene flake delamination. At 355 K first small patches of an intercalated dense oxygen adlayer are observed, coexisting with the intercalated oxygen adatom lattice gas. Oxygen adlayer patches are found adjacent to substrate edges covered by graphene resulting from oxygen indiffusion along the spacious tunnel formed by the substrate step and the graphene flake. At 400 K all graphene flakes with a perimeter length larger than 80 nm are intercalated by a p(2x1)-O adsorbate layer. Flakes confined to a single Ir terrace and with a perimeter length below 80 nm resist intercalation through a dense oxygen adlayer the more likely, the shorter their perimeter length. The rate-limiting process for delamination of such graphene flakes through intercalated oxygen is thus the unbinding of the graphene flake edges from the substrate. Once unbinding took place at a location at the flake boundary, at 400 K fast delamination and intercalation of the entire flake takes place.

With XPS and STM we determined the fingerprints of the intercalated p(2x1)-O phase to be the following: (i) A -0.45 eV CLS of the C 1s peak originating from C-atoms in graphene, (ii) a 15% narrowing of the C 1s peak width, (iii) a single O 1s component with BE of 529.9 eV, (iv) disappearance of the Ir surface component and appearance of Ir_1-O and O-Ir_2-O components with Ir $4f_{7/2}$ BE of 60.62 eV and 61.11 eV, respectively, (v) a by 0.9 Å increased height of areas or entire flakes over

the one of pristine graphene, (vi) a drastically reduced apparent moiré corrugation around 0.1 Å, and (vii) the lack of a regular Pt cluster array after room temperature Pt deposition, caused by the suppression of graphene rehybridization through the intercalated oxygen. The formation of the p(2x1)-O structure with molecular oxygen is fundamentally different from the formation of the epoxy groups, esters, quinons, and lactones that has been reported to form upon exposure to atomic oxygen.

Intercalation of dense oxygen adlayers requires an applied oxygen pressure. It is necessary to exert and maintain the oxygen-induced forces on graphene flakes to enable them to unbind from the substrate. An applied oxygen pressure not only causes delamination of pure graphene from Ir(111), but also of graphene flakes with Pt cluster arrays. In the absence of an applied oxygen pressure a p(2x1)-O adlayer on the bare Ir terraces relaxes by formation of an oxygen adatom lattice gas underneath graphene flakes enabling to increase the average binding energy per oxygen adsorbate slightly. From CO titration experiments, we conclude that intercalated graphene flakes expel oxygen. Graphene energetically prefers to reside on clean Ir(111) rather than to float less bound on an intercalated dense oxygen layer.

First experiments on hydrogen intercalation indicate that hydrogen intercalates graphene island similar to oxygen.

8 Relation Between Doping of Graphene and the C 1s CLS

As mentioned in Chapter 7, intercalation of graphene can be used to decouple the graphene layer from its substrate. In this chapter we focus on another implication of graphene intercalation namely that the graphene's electronic structure is changed. As we will see the graphene layer can be doped by the presence of an intercalant.

First a few words on nomenclature: In semiconductor physics *doping* means introducing impurities into a pure semiconductor to change its electronic properties. In the present work, however, *doping of graphene* refers to a shift in its electronic band structure (as in [175], see below). The incorporation of impurities into the graphene lattice (e.g. incorporation of N into graphene/Pt(111) [176] or into graphene/Ni(111) [177]) is known as *substitutional* or *hetero atom doping*. A third possibility of graphene modification is the adsorption of molecules which is called *chemical doping* [178, 179]. Although the latter two modifications of graphene may also change its electronic structure, this work focuses on doping of graphene induced by the presence of intercalants below the graphene as well as metal clusters on top of the graphene layer.

Let us briefly recall the electronic structure of graphene. The occupied π and the unoccupied $\pi^\star$ bands show a linear dispersion around the Fermi level E_{F}. They touch

at the K-points of the first Brillouin zone where the density of states vanishes [99] -
the so-called Dirac points. As valence and conduction band touch and nonetheless
the density of states is zero at the Fermi level, graphene is often referred to as a
'zero gap semiconductor'.

Doping of graphene means shifting the Dirac point below (above) the Fermi Level
so that states of the $\pi^\star$ band become occupied (states of the π band become unoccu-
pied). This is referred to as n-doping (p-doping) of the graphene layer [175]. In this
chapter we will see that a shift of the Dirac point corresponds to a shift of the C 1s
core level and that both can be related in a rigid band model. As a consequence the
core level shift can be used to estimate the level of doping.

Shifting the Dirac point away from E_{F} increases the number of charge carriers at the
Fermi level and thereby enhances the conductivity of graphene. Due to the peculiar
band structure of graphene this effect is so large that it can, for example, be used to
detect the adsorption of single gas molecules on graphene by the adsorption-induced
change of its conductivity [7].

Primarily an enhanced conductivity of graphene is of great interest wherever its
use as a transparent electrode is envisioned, e.g. in touchscreen displays [8] or in
solar cells [9]. Actually it was shown recently that the power conversion efficiency
of a graphene based solar cell can be enhanced by a factor of 4.5 when graphene is
chemically doped by adsorbates [180].

Moreover doping of graphene might give rise to a band gap between valence and
conduction band [181]. This experimental observation by Varykhalov et al. is,
however, contradicted by their own theoretical calculations [181] as well as by the
work of Khomyakov et al. [182]. A more promising route towards opening of a band
gap in graphene is breaking the symmetry of the two carbon sublattices, e.g. by
pattern adsorption of hydrogen [92] or metal particles [104]. The question if a band
gap occurs or not is, however, beyond the scope of this work.

8.1 Origin of the C 1s Core Level Shift and Doping by Intercalation
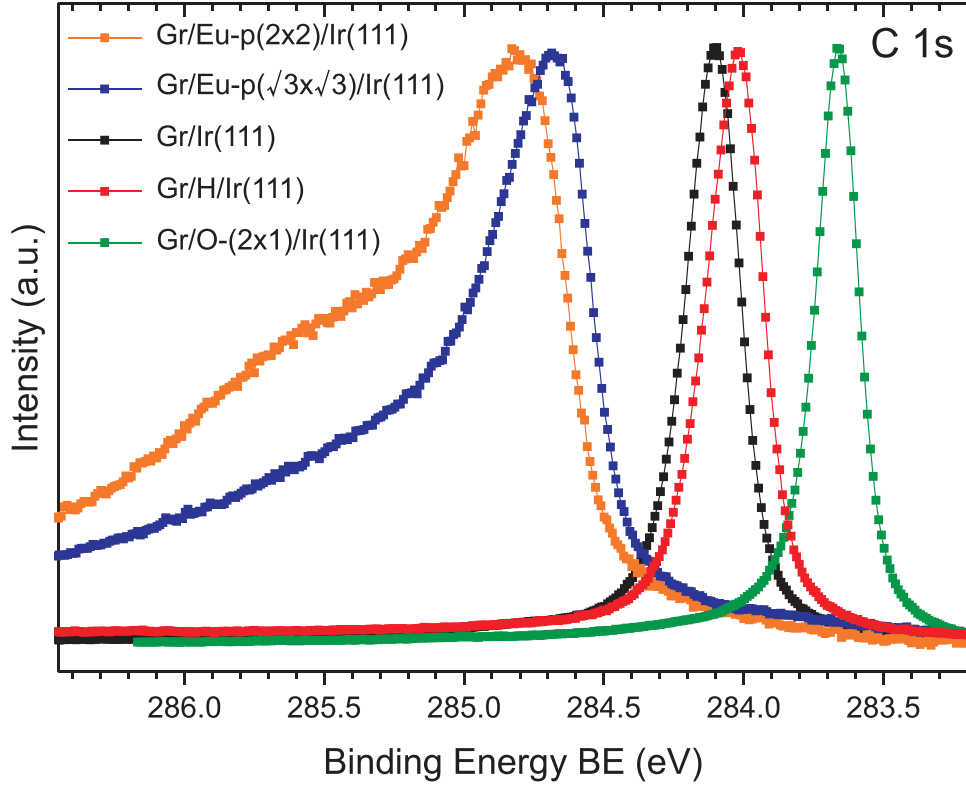
Figure 8.1 Photoemission spectra of the C 1s region of Gr/Eu-p(2×2)/Ir(111) (orange), Gr/Eu-p($\sqrt{3}\times\sqrt{3}$)R30°/Ir(111) (blue), Gr/Ir(111) (black), Gr/H/Ir(111) (red) and Gr/O-(2×1)/Ir(111) (green). Gr coverage was 1 ML for Eu, 0.95 ML for O, and 0.5 ML for H intercalation.

Figure 8.1 shows C 1s spectra of graphene on Ir(111) before and after intercalation with hydrogen, oxygen, and europium, respectively. As shown before, the C 1s spectrum of clean graphene consists of a single narrow peak located at 284.09 eV. This peak is shifted to lower binding energies after intercalation of hydrogen (- 80 meV) and oxygen (- 550 meV), whereas it is shifted to higher binding energies after intercalation of Eu. Eu can form two intercalation structures with respect to the graphene lattice: A p(2x2) and a p($\sqrt{3}$x$\sqrt{3}$)R30° structure [183]. The binding energy of the main C 1s component is 0.1 eV higher for the p(2x2) with respect to the p($\sqrt{3}$x$\sqrt{3}$)R30° structure. We note differences in the peak width which will be

discussed at the end of this section.

First of all, we want to discuss the origin of the observed core level shifts. A common explanation for core level shifts is based on changes in the Coulomb interaction between the respective electron (in this case the carbon 1s electron) and the nucleus of the atom (see for example [184]). When charge is transferred away from an atom, the screening of the positive charge on the nucleus is reduced. The remaining electrons experience therefore a stronger Coulomb interaction with the nucleus resulting in a higher binding energy of these electrons. If charge is transferred to the atom it is the other way round: more charge results in a better screening of the core thus in less Coulomb interaction and in lower binding energy. Applying this charge transfer picture to the core level shifts observed in Figure 8.1, one would conclude that graphene loses charge upon Eu intercalation and gains charge upon O intercalation.

This reasoning is, however, opposed to results from ARPES measurements concerning changes in the electronic band structure of these intercalation systems. After oxygen intercalation, the Dirac cone is located far above the Fermi level at a binding energy in between -0.64 eV [172] and -0.68 eV [174]. This corresponds to a shift of ~ 0.6 eV to lower binding energies compared to pristine graphene on Ir(111). The shift is due to an electron transfer from graphene to the intercalated oxygen (p-doping). For Eu intercalation, the Dirac cone is shifted below the Fermi level to a binding energy of ~ 1.4 eV (n-doping) [174].

The contradiction in the interpretations of ARPES and XPS data can be resolved by considering a rigid band model. In this model, the positions of the valence and conduction bands as well as the position of the core levels are fixed with respect to each other on a common binding energy scale. If valence and conduction band shift with respect to the Fermi level, this induces also a shift of the core levels. This model has been successfully used to describe the core level shifts of semiconductors [113]. The model is sketched in Figure 8.2 for the case of graphene. We consider the Dirac cone and the carbon core levels as fixed with respect to each other. In the case of O intercalation electrons are transferred from graphene to the intercalated oxygen by depleting graphene states just below the Fermi level. As the Fermi level stays aligned with that of the supporting metal, this depletion of states leads to a shift of the Dirac cone to lower binding energies. As the C 1s core level is fixed to the Dirac cone, it displays the same shift. As the binding energy scale of our XPS measurements is always calibrated with respect to the Fermi Level, we observe a
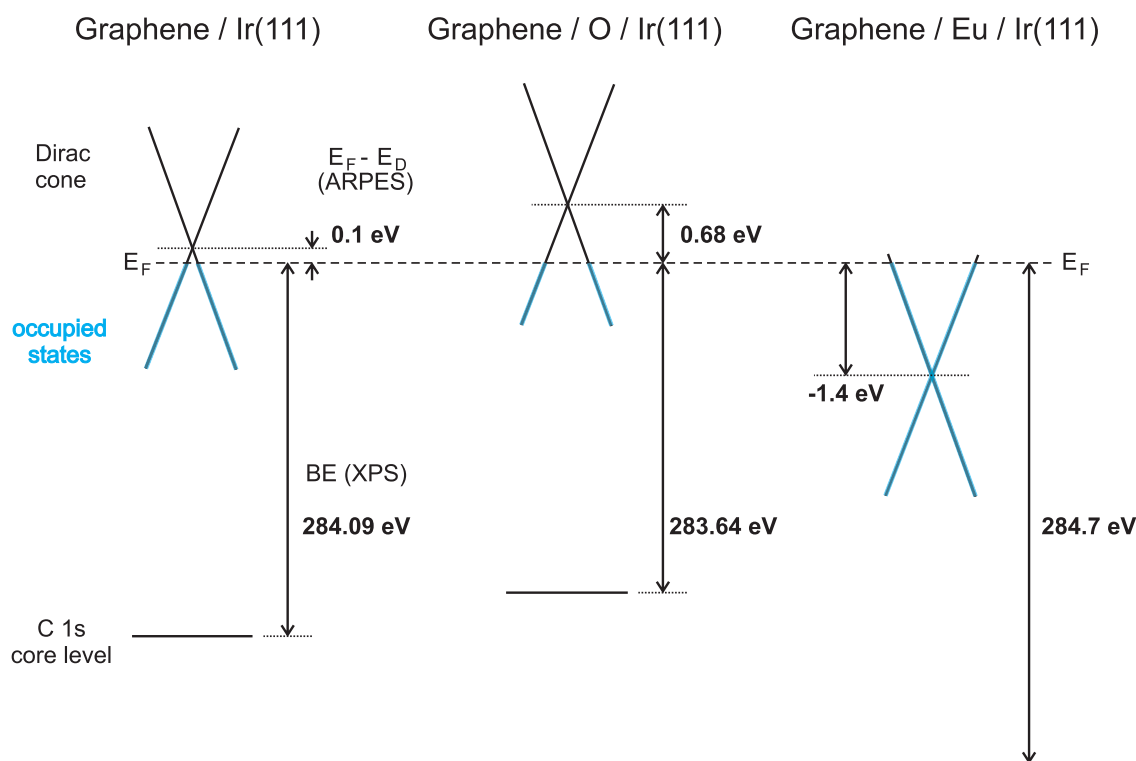
Figure 8.2 Sketch of the rigid band model showing the Dirac cone and the C 1s core level on a joint binding energy scale (non-linear). The Fermi Level E_F is indicated by the dashed line and occupied states of the Dirac cone are marked blue. The position of the Dirac cone E_D is marked by the dotted lines.

lower C 1s binding energy after O intercalation.

For the case of n-doping (e.g. by Eu intercalation) it is the other way round. The Eu gives charge to the graphene so that states above the Dirac points become populated. The Dirac point shifts down in binding energy and so does the C 1s core level.

Within the framework of the rigid band model the distance C 1s - E_D between the C 1s level Dirac point and the Dirac point should be constant for all levels of doping. To test our model we calculated C 1s - E_D for a variety of different graphene intercalation compounds (see Table 8.1).

For doping levels up to ± 0.7 eV we find a C 1s - E_D distance of (282.2 ± 0.2) eV. So C 1s - E_D varies much less than the actual level of doping. This confirms the applicability of the rigid band model to explain core level shifts of graphene. The question remains why this model is applicable to graphene, whereas usually core level shifts are explained by changes in Coulomb interaction. The answer lies in the particular electronic structure of graphene (see e.g. [99]). As the graphene bands are

linear close to the Dirac point, the density of states is low in its vicinity and vanishes at the point itself. Therefore adding or removing only very few electrons results in rather large shifts of the Fermi level without noticeable changes in the screening of the core. For example Vinogradov et al. calculated that a doping of $0.6\,\mathrm{eV}$ is caused by a hole density of $3.4 \times 10^{13}\,\mathrm{cm}^{-2}$ [78] which corresponds to a charge transfer of $\sim 0.01\,\mathrm{e}$ per carbon atom.

system	E_D (eV)	C 1s BE (eV)	C 1s - E_D
Gr/Eu-p($\sqrt{3} \times \sqrt{3}$)R30°/Ir(111)	1.43 [174]	284.68	283.25
Gr/Eu-p(2×2)/Ir(111)	1.36 [174]	284.81	283.45
Gr/Al/Ni(111)	0.64 [72]	284.65 [72]	284.01
Gr/Au/Ni(111)	0.0 [67]	284.25 [177]	284.25
graphite	0.0	284.23 [87]	284.23
Gr/Ir(111)	- 0.07 [172]	284.14 [172]	284.21
	- 0.1 [103]	284.09	284.19
Gr/H/Ir(111)		284.01	
Gr/Pt(111)	- 0.3 [102]	283.97 [87]	284.27
Gr/O/Ir(111)	- 0.64 [172]	283.60 [172]	284.24
Gr/O-(2×1)/Ir(111)	- 0.68 [174]	283.64 [166]	284.32
Gr/Cl/Ir(111)	- 0.7 [78]	283.8 [78]	284.5

Table 8.1 Overview on C 1s core level binding energy (BE) and C 1s - E_D as a function of Dirac point binding energy E_D for Gr/Pt(111), Gr/Ir(111) and several intercalation system with fcc(111) substrates. For comparison also graphite is listed.

However, the linearity of the graphene bands is only valid in the vicinity of the Dirac point. In between the Dirac points the graphene bands flatten resulting in a Van Hove singularity [185] in the density of states. Thus, considerably more charge has to be transferred to achieve higher levels of doping so that changes in screening of the core can no longer be neglected. This is reflected by the fact that for stronger doping (as observed after intercalation of Na or Eu), we find that C 1s - E_{D} deviates in a stronger way from $(282.2 \pm 0.2)\,\mathrm{eV}$.

This explains the larger C 1s CLS for Eu in the p(2x2) structure compared to Eu in the p($\sqrt{3}$x$\sqrt{3}$)R30° structure (Fig. 8.1). The ARPES data (Table 8.1) indicate that more charge is transferred by the Eu p($\sqrt{3}$x$\sqrt{3}$)R30° structure. This charge populates states in the flat part of the unoccupied $\pi^{\star}$ band without shifting the Dirac point further to lower binding energies. However, the screening is increased and the C 1s peak shifts back to a lower binding energy than for the Eu p(2x2) structure.

In Figure 8.1 we noted differences in peak width for the different intercalation compounds which will be addressed in the following. After O intercalation, the C 1s peak is narrowed compared to the one of clean graphene. In Chapter 7 we assigned this narrowing to a uniform decoupling of the graphene from the Ir substrate. After H intercalation, the shifted component is also narrower than the original peak (see Section 7.4).

For both Eu structures the C 1s peak is noticeably broader compared to the spectrum of the clean graphene layer and to those after O and H intercalation. This broadening might be due to the coexistence of different Eu phases below the graphene. Additional information is gained from the corresponding LEED images shown in Figure 8.3: (b) shows sharp but weak spots of the p(2x2) superstructure, whereas the spots of the p($\sqrt{3}$x$\sqrt{3}$)R30° structure seem to be very broad and maybe even split. The p($\sqrt{3}$x$\sqrt{3}$)R30° structure might therefore not be well ordered giving rise to a broad C 1s peak. Although the sharp spots of the p(2x2) indicate a high degree of order of this structure, non-intercalated stripes are probably present [183] and this phase coexistence broadens the C 1s peak. In addition, the carbon atoms in the p(2x2) structure are not all equivalent: 75% of the carbon atoms are part of a carbon ring centered around an Eu atom, whereas the other 25% are only neighbors to such atoms. Contrarily, in the p($\sqrt{3}$x$\sqrt{3}$)R30° structure all carbon atoms are equivalent.
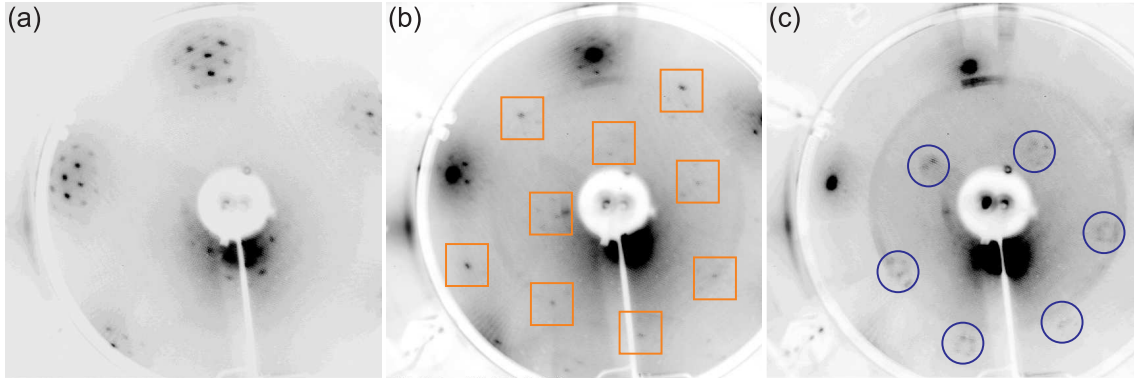
Figure 8.3 Inverted contrast LEED patterns of pristine graphene [(a), primary electron energy of 74 eV], graphene intercalated by Eu in the p(2x2) structure [(b), 74 eV, super-structure spots marked by blue squares] and the p($\sqrt{3}$x$\sqrt{3}$)R30° structure [(c), 80 eV, red circles].
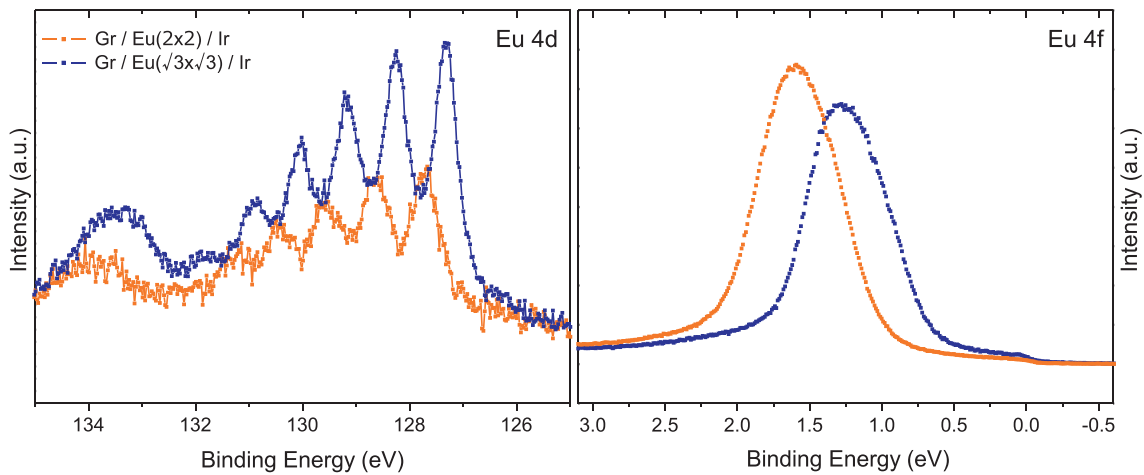
Figure 8.4 Photoemission spectra of the Eu 4d (left) and Eu 4f (right) core levels for 1 ML graphene intercalated by Europium in the p(2x2) (orange) and in the p($\sqrt{3}$x$\sqrt{3}$)R30° structure (blue), respectively. The photon energies are 360 eV (Eu 4d) and 148 eV (Eu 4f), respectively.

We conclude this section with the photoemission spectra from the Eu 4d and Eu 4f core levels of both Eu intercalation structures (Fig. 8.4).

The left panel of Figure 8.4 shows Eu 4d spectra for the p(2x2) and the p($\sqrt{3}$x$\sqrt{3}$)R30° structure, respectively. Both spectra show the known multiplet splitting of Eu 4d core level which is due to spin-orbit coupling [184]. The p(2x2) spectrum is shifted by 0.4 eV to lower binding energies compared to the p($\sqrt{3}$x$\sqrt{3}$)R30° spectrum. The Eu 4f core level displayed in the right panel shows almost the same shift (-0.3 eV).

In contrast to the C 1s core level shifts of graphene, the Eu core level shift can be explained by changes in Coulomb interaction.

For both core levels, there is a shift to higher binding energies for the p(2x2) structure than for the p($\sqrt{3}$x$\sqrt{3}$)R30°. This corresponds to a larger loss of charge *per Eu atom* in the the p(2x2) structure. This is consistent with theoretical calculations for Eu adsorption on free-standing graphene [186], which show that the charge that is transferred per Eu atom decreases with increasing Eu coverage. The *total* charge that is transferred is higher for the p($\sqrt{3}$x$\sqrt{3}$)R30° structure due to a higher Eu coverage than in the p(2x2) (compare Table 8.1).

8.2 Doping by Clusters
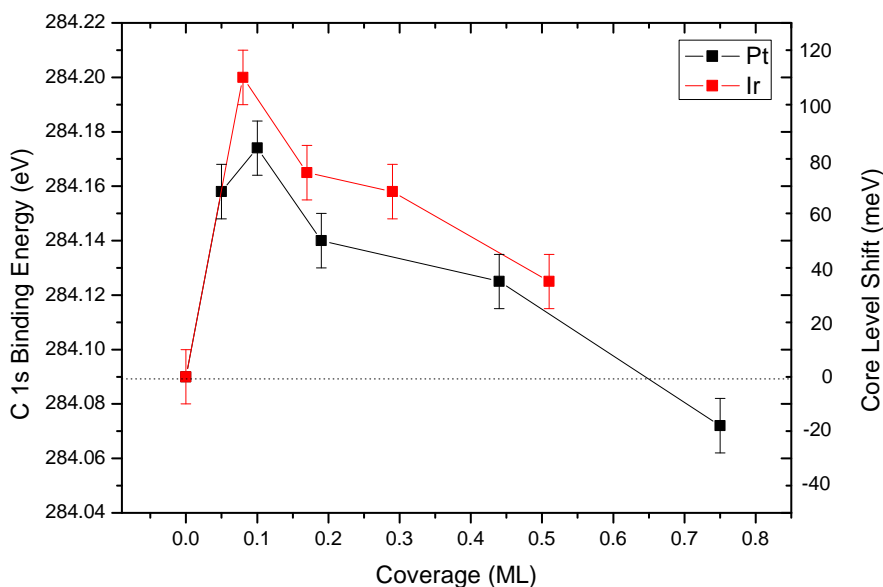
Figure 8.5 Binding energy of the C 1s main component for different Pt and Ir coverages. The peak position for clean graphene (corresponding to 0 coverage) is marked by the dotted line)

From Figure 5.4 it is obvious that the binding energy of the main C 1s component changes due to the formation of Pt clusters on the graphene layer. The shift of the C 1s core level is not constant but depends on the deposited amount of Pt. Fig. 8.5 shows the C 1s peak positions as a function of Pt and Ir coverage respectively. Before

deposition the C 1s peak is located at 284.09 eV. For low Pt coverages the peak shifts to higher binding energies. The maximum shift of $+85$ meV is observed for 0.1 ML Pt. When the amount of Pt is further increased, the peak shifts gradually back to lower binding energies. For the highest Pt coverage of 0.75 ML the peak is even shifted to a lower binding energy compared to the position for pristine graphene.

Within the framework of the rigid band model a positive core level shift of the graphene C 1s peak is related to a charge transfer of electrons to the graphene layer (n-doping). Vice versa a negative core level shift corresponds to a loss of electrons (p-doping).

The intercalation compounds described in the previous section are characterized by an intercalant-graphene interaction which is uniform over the graphene layer and leaves the sp^2-structure of graphene intact. Contrarily, the clusters induce a localized sp$^2 \rightarrow$ sp^3 rehybridization of the carbon atoms. This rehybridization breaks the symmetry of the two carbon sublattices and is thereby responsible for the opening of a band gap in graphene as reported by Rusponi et al. [104]. However, in the same article the authors report a shift of the C 1s peak by 30 meV to higher binding energies as well as a shift of the top of the σ band by the same amount and in the same direction. This observation validates the rigid band model also for the case of clusters on graphene so that we will use it in the following to discuss our results on Pt clusters.

Applying this model, a low Pt coverage (small Pt clusters) induces n-doping of graphene, whereas the highest coverage (the biggest clusters) induce p-doping. In other words the small clusters spill out charge, whereas the largest clusters attract it. This is schematically visualized in Figure 8.6.

Interestingly, the strongest n doping occurs for a coverage of 0.1 ML Pt. This coverage roughly corresponds to the transition point between the nucleation and the growth regime of the clusters (Section 5.1). Despite a slight further increase of the cluster density from 0.8 to 1 in the growth regime (for coverages higher than 0.1 ML), the core level shift is reduced. These observations can be qualitatively explained by assuming that each cluster contributes in equal shares to the total doping of the graphene layer, and most important that the charge spill-out of a cluster is inversely proportional to its size.

In the nucleation regime the cluster size increases only little with coverage, whereas the cluster density increases steeply. The increasing C 1s shift is simply due to
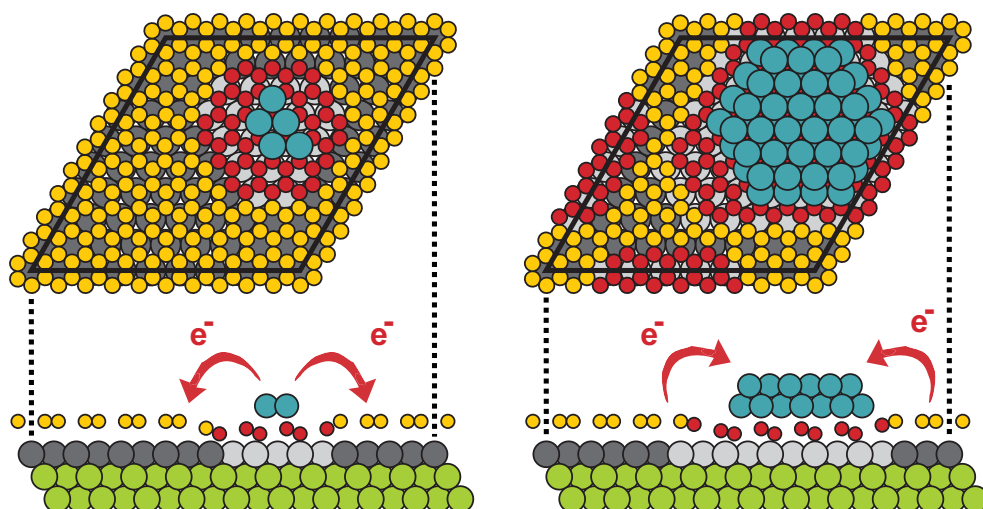
Figure 8.6 Ball modell of a Pt_5 (left) and a Pt_{64} (right) cluster representative for a coverage of 0.05 ML resp. 0.75 ML. The direction of charge transfer as inferred from the XPS data is indicated (see text). Colors as in Fig. 5.6

the increasing cluster density in this regime. In the growth regime the remaining unoccupied cells are filled gradually while the clusters noticeably increase their size. This increase in size reduces the amount of charge which is transferred and thereby the C 1s shift is also reduced.

At this point we want to mention that charge transfer from Pt clusters to graphene has recently been predicted by theory [187, 188]. Furthermore, for Pt clusters supported on carbon nanotubes, a charge transfer inversely proportional to particle size was calculated and experimentally confirmed [189]. However, the authors do not give explanations for their findings so that we can only speculate about the origin of the charge transfer. As the amount of charge transferred is inversely proportional to the particle size, it is probably proportional to the average coordination number of the metal atoms in the cluster. The lower their coordination number the stronger they interact with the graphene and the more charge is transferred.

For two reasons we can exclude that the doping of graphene by the clusters is due to a change in work function of the clusters. Firstly, the model developed by Giovannetti et al. [175] is not applicable here as the clusters bond covalently to the graphene whereas the model is only valid for weak graphene-metal-interaction. Secondly, if the model would apply, we would expect the graphene to be p-doped by the clusters, as clusters have a *larger* work function than the bulk which converges to the bulk value for increasing particle size [190].

Except for the negative shift at the highest Pt coverage we observe roughly the same core level shifts for Ir clusters (red curve in Fig. 8.5) so that we apply our considerations above also to the case of Ir clusters. We note that the shift for Ir clusters is slightly higher for all coverages compared to Pt clusters. The reason might be the stronger cluster-graphene-interaction of Ir clusters which is reflected in their higher thermal stability [15].

Finally we address the negative C 1s shift for the highest Pt coverage corresponding to a p-doping of the graphene layer. This high coverage is at the threshold for coalescence of the clusters so that we can think of the graphene layer as being sandwiched between a Pt and an Ir surface. We expect the graphene in the Pt-Gr-Ir sandwich to show a doping level between the one of graphene on Pt and the one of graphene on Ir. As graphene on Pt(111) is stronger p-doped than graphene on Ir(111) (compare table 8.1) the result of the sandwich structure should be a positive core level shift which is consistent with our data. As pointed out by Giovannetti and coworkers [175], the reason for the stronger p-doping of graphene on Pt(111) than on Ir(111) is the larger work function of Pt(111) [191, 192].

8.2.1 C 1s CLS Upon CO Exposure

In Chapter 6 we have seen that exposure of small Pt clusters to CO causes cluster diffusion and coalescence. This is accompanied by two effects in the corresponding C 1s spectrum. Firstly, the intensity of the shoulder components is reduced upon CO exposure. Secondly, the position of the C 1s main component shifts when the clusters are exposed to CO (compare Fig. 6.7). Fig. 8.7 displays the C 1s binding energy for Pt and Ir clusters before and after CO exposure as well as the relative shift in binding energy upon exposure. We note that for low Pt coverages (0.05 ML and 0.10 ML Pt) the C 1s peak shifts back towards its original position upon CO exposure. For larger coverages the peak position stays roughly constant.

Assuming that the C 1s core level shift is inversely proportional to the cluster size we can explain this 'back shift' by the coalescence of clusters upon CO exposure (Chapter 6). Accordingly small Pt clusters become mobile when saturated with CO so that they agglomerate to larger particles. This reduces the C 1s core level shift in a two-fold way: Firstly, there are less clusters after exposure which spill out charge onto the graphene layer. Secondly, the resulting clusters have increased their size and therefore each of them is spilling out less charge.
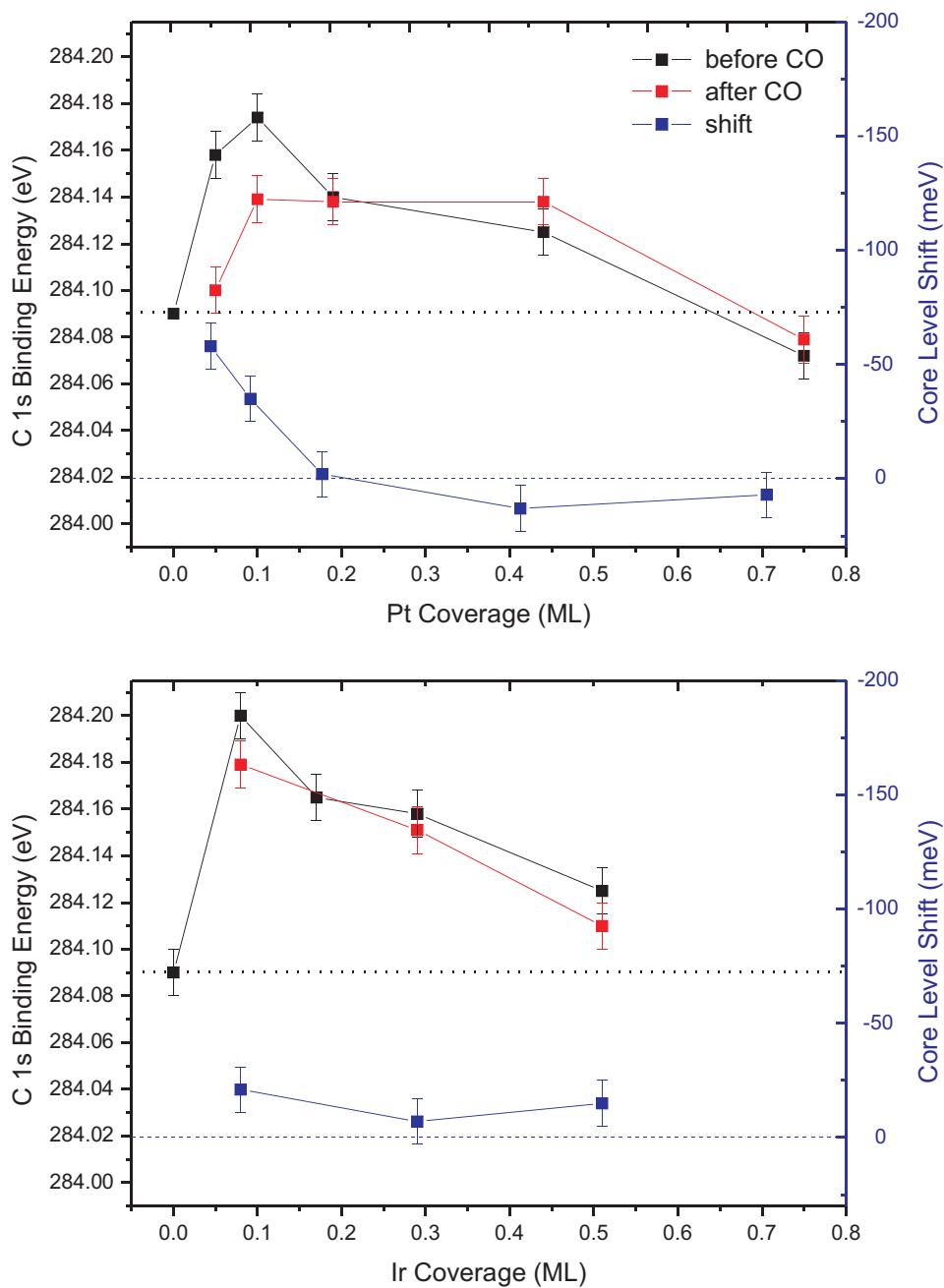
Figure 8.7 Binding energy of the C 1s main component for different Pt (top) and Ir (bottom) coverages before (black) and after (red) CO exposure as well as the respective shift of the C 1s main component (blue) upon CO exposure. The peak position for clean graphene as well as a shift of $0\,\mathrm{eV}$ are marked by a dotted and a dashed line, respectively.

We observed that larger Pt clusters are stable upon CO exposure. That means that coalescence does not take place so that we do not expect a 'back shift' for higher Pt coverages. Interestingly the decrease of shoulder intensity as reported above indicates that even for the highest Pt coverages the Pt-graphene-interaction is weakened by the adsorption of CO. Nevertheless, this weakened interaction does not manifest itself in a C 1s core level shift.

The lower panel of Fig. 8.7 shows similar data for Ir clusters. Within the limits of error the C 1s binding energy does not change upon CO adsorption which is in contrast to the case of Pt clusters. This finding is somehow puzzling as small Ir clusters (0.05 ML Ir) show almost the same mobility and coalescence when exposed to CO as small Pt clusters.

8.3 Conclusions

We have seen that intercalation of graphene leads to a change in its electronic structure. This change can be described in terms of a rigid band model. The Dirac point and the C 1s core level display the same shift. The C 1s core level shift can therefore be used to estimate the level of doping.

It was found that graphene/Ir(111) is p-doped by H and O intercalation whereas it is n-doped after Eu intercalation. It is doped in a stronger manner by the Eu $p(\sqrt{3}x\sqrt{3})R30°$ structure than by the Eu p(2x2). In the latter case, more charge is transferred to the graphene layer *per Eu atom*. This was inferred from shifts in the Eu 4d and Eu 4f core level of both structures.

The graphene layer can also be doped by Pt and Ir clusters. The smallest clusters n-dope the graphene by charge spill-out. The largest Pt coverage results in a slight p-doping of the graphene layer. When Pt clusters coalesce upon CO exposure the level of doping is reduced.

9 Summary and Outlook

9.1 Summary

Graphene/Ir(111) is a versatile template for lattices of monodispersed metal clusters on an inert support. Thereby, this system is an interesting model catalyst and an attractive laboratory for studies of nanocatalysis. A prerequisite to such studies is a profound knowledge of the system itself.

A particularity of the Graphene/Ir(111) system is the binding mechanism of clusters to the graphene moiré. Prior to this thesis, a DFT based scenario of cluster binding, based on graphene rehybridization, was developed. Despite its plausibility, there has been no experimental evidence for this scenario, beyond the agreement of the calculated and of the experimentally-determined binding site preference of the metal clusters. In the course of this thesis, strong experimental evidence supporting the calculations was found.

The DFT picture was confirmed by comparing calculated core level spectra to XPS measurements. For pristine graphene, DFT and XPS agree on a 140 meV modulation of the C 1s CLS, which correlates with the height modulation of the graphene layer above the Ir surface. With Pt clusters adsorbed, measured Pt 4f CLS of the adsorbed clusters further support the calculations. The modulation of the C 1s spectrum is strengthened after Pt deposition, and C atoms both under and in the vicinity of the Pt clusters can be experimentally distinguished as a broad shoulder of positive C 1s CLS. The calculations suggest that the sp^2 to sp^3 rehybridization of graphene displaces the involved C atoms closer to the Ir(111) surface, implying chemical bond formation. The signature of these bonds in the Ir 4f spectrum was identified. Furthermore, the calculations imply a 1.1 eV CLS splitting between Pt- and Ir-bonded C atoms, which is also also consistent with the XPS data. In later chapters, the C 1s shoulder and the Ir 4f signature of cluster binding were successfully used to trace the binding strength of the clusters to the graphene layer.

As as a basis for further studies, the growth of Pt clusters, their structure, and their interaction with the graphene layer were studied as a function of Pt coverage. STM measurements revealed that once Pt clusters are two-layered, their further growth is restricted to two dimensions. The threshold for sintering was found to be at 0.75 ML Pt, so that the upper size limit for Pt clusters arranged in a lattice is 65 atoms. The cluster-graphene interaction, as well as the graphene-Ir surface interaction was investigated with spectra of the C 1s and the Ir 4f regions, respectively. It was found that the related components, namely the C 1s shoulder and the Ir interface component, agree regarding their relative intensities. The intensities were corrected for damping by the Pt clusters. Combining the STM and the XPS data, schematic representations of the clusters and their binding geometry with the graphene layer was derived. The Pt 4f spectra were found to be a superposition of several components. The resulting spectra are of complex shape and were not further investigated.

A requirement for reaction studies is the investigation of the stability of the cluster/support system at elevated temperatures and in the presence of reactants, i.e. under reaction conditions.

Therefore, cluster arrays were tested for their stability with respect to gas exposure, with a focus on Pt clusters exposed to CO. The stability of the clusters and adsorption-induced processes were analyzed as a function of cluster size. Small clusters containing fewer than 10 atoms are unstable upon CO adsorption. They sinter through Smoluchowski ripening - cluster diffusion and coalescence - rather than the frequently reported Ostwald ripening mediated by metal-adsorbate complexes. Larger clusters remain immobile upon CO adsorption, but become more three-dimensional. An implication of the CO-induced cluster mobility is the sensitivity of Pt cluster array growth to the CO background pressure.

The study was extended to the adsorption of other gases (H_2, O_2) on Pt clusters, as well as to the adsorption of CO on other metal clusters (Ir, Au). We have seen that adsorption of H_2 and O_2 does not destabilize small Pt clusters. As CO is the molecule which interacts the strongest with the clusters, we used it to test the stability of Ir and Au clusters. We showed that small Ir clusters sinter upon CO exposure, paralleled by a decrease of C 1s shoulder intensity. Both observations are the same as for Pt clusters. Au clusters behave differently: Although they are much weaker bound to the graphene compared to Ir and Pt clusters, they are not destabilized by CO adsorption. This is explained by the much weaker interaction

of CO with Au surfaces compared to Ir and Pt surfaces. Finally, medium sized Ir clusters were tested for their stability under ambient conditions. It was shown that the clusters are stable, even after they have been exposed to air at atmospheric pressure for weeks, and after cleaning with alcohol.

We conclude that large clusters ($s_{av} \geq 40$ atoms) are stable when exposed to gases, be it the very reactive CO or even air at atmospheric pressures. In contrast, smaller clusters are unstable when exposed to CO and not suitable for reaction studies.

Furthermore, the impact of oxygen exposure on the graphene itself was studied. Our studies show that under an applied oxygen pressure no intercalation under a closed graphene layer takes place. Graphene on Ir(111) can be grown as an impenetrable, hole-free membrane. In contrast, for 0.5 ML graphene coverage a temperature dependent intercalation behavior is observed. Up to 300 K, no intercalation takes place. With increasing temperature, more and more flakes are intercalated by a dilute oxygen adatom lattice gas. This gas coexists with the dense p(2x1)-O adlayer on the bare Ir(111) terraces. At 355 K, first small patches of an intercalated dense oxygen adlayer are observed. At 400 K, all graphene flakes with a perimeter length larger than 80 nm are intercalated by a p(2x1)-O adsorbate layer. Flakes confined to a single Ir terrace and with a perimeter length below 80 nm resist intercalation the more likely, the shorter their perimeter length. The rate-limiting process for delamination of such graphene flakes is thus the unbinding of the graphene flake edges from the substrate. Once unbinding took place at a location at the flake boundary, at 400 K fast delamination and intercalation of the entire flake takes place.

One important consequence of the dense p(2x1)-O adlayer below graphene is the lack of regular Pt cluster arrays after room temperature Pt deposition, caused by the suppression of graphene rehybridization through the intercalated oxygen.

Intercalation of dense oxygen adlayers requires an applied oxygen pressure. It is necessary to exert and maintain the oxygen-induced forces on graphene flakes to enable them to unbind from the substrate. An applied oxygen pressure not only causes delamination of pure graphene from Ir(111), but also of graphene flakes with Pt cluster arrays. From CO titration experiments, we conclude that intercalated graphene flakes expel oxygen. Graphene energetically prefers to reside on clean Ir(111) rather than to float less strongly bound on an intercalated dense oxygen layer. First experiments on hydrogen intercalation indicate that hydrogen intercalates graphene islands similar to oxygen.

Intercalation of graphene often leads to its doping. Comparing XPS and ARPES data for various systems, it was found that the Dirac point and the C 1s core level display the same shift. These shifts can be described in terms of a rigid band model and the C 1s core level shift may be used to estimate the level of doping. It was found that graphene/Ir(111) is p-doped by H and O intercalation, whereas it is n-doped after Eu intercalation. The graphene layer is also doped by Pt and Ir clusters on top of it. The smallest clusters n-dope the graphene by charge spill out. The largest Pt coverage results in a slight p-doping of the graphene layer. When Pt clusters coalesce upon CO exposure, the level of doping is reduced.

9.2 Outlook

DFT calculations played a crucial role in the comprehension of cluster binding to the graphene moiré. These calculations predicted a number of facts which could be verified experimentally: The preferred binding site within the moiré unit cell, the sp^2 to sp^3 rehybridization of graphene atoms associated with the development of a high-binding-energy shoulder in the C 1s spectrum, and the Pt 4f core level shifts. However, other observations are not in agreement with the results of the calculations: DFT overestimates the intensity of the C 1s shoulder component, and predicts a negative shift of the C 1s main peak. These discrepancies might be overcome by an improved functional, e.g. one that includes van der Waals interactions.

Also, DFT was only partial helpful to interpret our discovery of CO-induced cluster mobility. The calculations showed that CO adsorption can mobilize Pt clusters. However, only CO adsorbed in 2-fold coordinated bridge sites mobilizes the clusters, whereas experimentally, 1-fold coordinated adsorption is observed. Either we believe that DFT underestimates the effect of CO adsorbed on 1-fold coordinated island-edge sites on the bonding of the Pt to the graphene below, or we must assume that a CO-decorated island can adopt a transient structure in which Pt-graphene bonds are broken and the island is mobilized. As an experimental confirmation of a possible transient configurations is a demanding task, we hope that improved functionals will also solve this problem.

Pt clusters were found to be stable when exposed to H_2 and O_2. Thus, Pt clusters in the presence of these gases behave different from clusters in the presence of CO. This behavior was tentatively attributed to differences in adsorption geometry

and in adsorption energy. Another peculiarity is that Au clusters are stable upon CO adsorption, even though they are only weakly bound to the graphene layer. Theoretical input might help to obtain a deeper understanding of these issues.

The structure of Pt clusters on the graphene/Ir(111) moiré was investigated by means of STM and XPS. Ball models were created to visualize these results schematically. Of course, DFT calculations for all cluster sizes or SXRD measurements would be desirable for confirmation of these models. Employing the latter technique, details of the clusters' atomic structure would be gained, such as the stacking of the particles or the presence of intraparticle strain.

The brief study of hydrogen intercalation yielded results resembling those on oxygen intercalation. Nevertheless, there might be a striking difference: The probability for O intercalation can be increased by increasing the temperature at which the sample is exposed to O_2. Exposure of $0.5\,\mathrm{ML}$ graphene to O_2 at $400\,\mathrm{K}$ ($0.95\,\mathrm{ML}$ at $460\,\mathrm{K}$ respectively) leads to almost full intercalation. It is not certain if complete intercalation by hydrogen can be achieved in the same way. At temperatures higher than $120\,\mathrm{K}$, the sticking probability of H_2 is reduced, as hydrogen already starts to desorb at $150\,\mathrm{K}$. Accordingly, the intercalation probability might decrease with increasing temperature. Thus, further experiments are needed to point out the mechanisms of hydrogen intercalation under graphene/Ir(111) and to find the right parameters of exposure (H_2 pressure and dose, temperature) necessary to achieve full intercalation.

We emphasized that clusters on Graphene/Ir(111) are an interesting model catalyst. In the course of this thesis, profound knowledge of this system was gained: The binding of the clusters to the graphene as well as their structure was thoroughly studied. Furthermore, we learned much about the interaction of graphene and of cluster arrays when exposed to CO, H_2 and O_2. To study a catalytic reaction on the clusters, however, was beyond the scope of this work. The indispensable tests of the stability of the system we performed will help to guide further studies. For reaction studies, attention should be paid to the following issues:

- The preparation of an absolutely closed monolayer of graphene is necessary. Otherwise, gases (H_2, O_2) may intercalate below the graphene layer, and thereby destroy the cluster lattice.

- If reactions including CO are studied (such as CO oxidation, or NO_x reduction), large clusters ($s_{av} \geq 40$ atoms) should be used, in order to guarantee

their stability.

- The temperatures of the reaction should be below $450\,\mathrm{K}$, because thermally activated cluster motion sets in at higher temperatures [15].

These guidelines are valid for reactions carried out under partial pressures $p_{\mathrm{CO}} \leq 1 \times 10^{-8}\,\mathrm{mbar}$, $p_{\mathrm{O_2}} \leq 1 \times 10^{-5}\,\mathrm{mbar}$ and $p_{\mathrm{H_2}} \leq 5 \times 10^{-6}\,\mathrm{mbar}$, respectively. In the near future, instruments like the ambient-pressure XPS setup [193] or the reactor STM [194] will hopefully be used to study the stability of clusters and their reactivity under higher pressures, and thus closer to realistic conditions.

Bibliography

[1] A. K. Geim, K. S. Novoselov, *The Rise of Graphene*, Nature Mater. **6**, 183 (2007)

[2] A. K. Geim, *Graphene: Status and Prospects*, Science **324**, 1530 (2009)

[3] K. S. Novoselov, A. K. Geim, S. V. Morozov, D. Jiang, Y. Zhang, S. V. Dubonos, I. V. Grigorieva, A. A. Firsov, *Electric Field Effect in Atomically Thin Carbon Films*, Science **306**, 666 (2004)

[4] K. S. Novoselov, A. K. Geim, S. V. Morozov, D. Jiang, M. I. Katsnelson, I. V. Grigorieva, S. V. Dubonos, A. A. Firsov, *Two-Dimensional Gas of Massless Dirac Fermions in Graphene*, Nature **438**, 197 (2005)

[5] Y. Zhang, Y.-W. Tan, H. L. Stormer, P. Kim, *Experimental Observation of the Quantum Hall Effect and Berry's Phase in Graphene*, Nature **438**, 201 (2005)

[6] Y.-M. Lin, C. Dimitrakopoulos, K. A. Jenkins, D. B. Farmer, H.-Y. Chiu, A. Grill, P. Avouris, *100-GHz Transistors from Wafer-Scale Epitaxial Graphene*, Science **327**, 662 (2010)

[7] F. Schedin, A. K. Geim, S. V. Morozov, E. W. Hill, P. Blake, M. I. Katsnelson, K. S. Novoselov, *Detection of Individual Gas Molecules Adsorbed on Graphene*, Nature Mater. **6**, 652 (2007)

[8] S. Bae, H. Kim, Y. Lee, X. Xu, J.-S. Park, Y. Zheng, J. Balakrishnan, T. Lei, H. R. Kim, Y. I. Song, Y.-J. Kim, K. S. Kim, B. Özyilmaz, J.-H. Ahn, B. H. Hong, S. Iijima, *Roll-to-Roll Production of 30-Inch Graphene Films for Transparent Electrodes*, Nature Nanotech. **5**, 574 (2010)

[9] X. Li, H. Zhu, K. Wang, A. Cao, J. Wei, C. Li, Y. Jia, Z. Li, X. Li, D. Wu, *Graphene-on-Silicon Schottky Junction Solar Cells*, Adv. Mater. **22**, 2743 (2010)

[10] J. Wintterlin, M.-L. Bocquet, *Graphene on Metal Surfaces*, Surf. Sci. **603**, 1841 (2009)

[11] M. Batzill, *The Surface Science of Graphene: Metal Interfaces, CVD Synthesis, Nanoribbons, Chemical Modifications, and Defects*, Surf. Sci. Rep. **67**, 83 (2012)

[12] J. Coraux, A. T. NDiaye, C. Busse, T. Michely, *Structural Coherency of Graphene on Ir(111)*, Nano Lett. **8**, 565 (2008)

[13] R. van Gastel, A. T. N'Diaye, D. Wall, J. Coraux, C. Busse, N. M. Buckanie, F.-J. Meyer zu Heringdorf, M. Horn-von Hoegen, T. Michely, B. Poelsema, *Selecting a Single Orientation for Millimeter Sized Graphene Sheets*, Appl. Phys. Lett. **95**, 121901 (2009)

[14] C. Herbig, M. Kaiser, N. Bendiab, S. Schumacher, D. F. Förster, J. Coraux, K. Meerholz, T. Michely, C. Busse, *Mechanical Exfoliation of Epitaxial Graphene on Ir(111) Enabled by Br_2 Intercalation*, J. Phys.: Condens. Matter **24**, 314208 (2012)

[15] A. T. N'Diaye, T. Gerber, C. Busse, J. Myslivecek, J. Coraux, T. Michely, *A Versatile Fabrication Method for Cluster Superlattices*, New J. Phys. **11**, 103045 (2009)

[16] E. Roduner, *Size Matters: Why Nanomaterials Are Different*, Chem. Soc. Rev. **35**, 583 (2006)

[17] S. N. Khanna, A. W. Castleman, editors, *Quantum Phenomena in Clusters and Nanostructures*, Springer-Verlag, Berlin (2003)

[18] A. J. Cox, J. G. Louderback, S. E. Apsel, L. A. Bloomfield, *Magnetism in 4d-Transition Metal Clusters*, Phys. Rev. B **49**, 12295 (1994)

[19] M. Haruta, N. Yamada, T. Kobayashi, S. Iijima, *Gold Catalysts Prepared by Coprecipitation for Low-Temperature Oxidation of Hydrogen and of Carbon Monoxide*, J. Catal. **115**, 301 (1989)

[20] U. Heiz, U. Landman, editors, *Nanocatalysis*, Springer-Verlag, Berlin (2007)

[21] C. R. Henry, *Surface Studies of Supported Model Catalysts*, Surf. Sci. Rep. **31**, 231 (1998)

[22] A. T. Bell, *The Impact of Nanoscience on Heterogeneous Catalysis*, Science **299**, 1688 (2003)

[23] U. Heiz, A. Sanchez, S. Abbet, W.-D. Schneider, *Catalytic Oxidation of Carbon Monoxide on Monodispersed Platinum Clusters: Each Atom Counts*, J. Am. Chem. Soc. **121**, 3214 (1999)

[24] B. Yoon, H. Häkkinen, U. Landman, A. S. Wörz, J.-M. Antonietti, S. Abbet, K. Judai, U. Heiz, *Charging Effects on Bonding and Catalyzed Oxidation of CO on Au_8 Clusters on MgO*, Science **307**, 403 (2005)

[25] L. M. Molina, B. Hammer, *Active Role of Oxide Support during CO Oxidation at* Au/MgO, Phys. Rev. Lett. **90**, 206102 (2003)

[26] L. M. Molina, B. Hammer, *Some Recent Theoretical Advances in the Understanding of the Catalytic Activity of Au*, Appl. Catal. A **291**, 21 (2005)

[27] E. Yoo, T. Okata, T. Akita, M. Kohyama, J. Nakamura, I. Honma, *Enhanced Electrocatalytic Activity of Pt Subnanoclusters on Graphene Nanosheet Surface*, Nano Lett. **9**, 2255 (2009)

[28] E. Yoo, T. Okada, T. Akita, M. Kohyama, I. Honma, J. Nakamura, *Sub-Nano-Pt Cluster Supported on Graphene Nanosheets for CO Tolerant Catalysts in Polymer Electrolyte Fuel Cells*, J. Power Sources **196**, 110 (2011)

[29] C. Xu, X. Wang, J. Zhu, *Graphene-Metal Particle Nanocomposites*, J. Phys. Chem. C **112**, 19841 (2008)

[30] Z. Luo, L. A. Somers, Y. Dan, T. Ly, N. J. Kybert, E. J. Mele, A. T. C. Johnson, *Size-Selective Nanoparticle Growth on Few-Layer Graphene Films*, Nano Lett. **10**, 777 (2010)

[31] K. M. McCreary, K. Pi, A. G. Swartz, W. Han, W. Bao, C. N. Lau, F. Guinea, M. I. Katsnelson, R. K. Kawakami, *Effect of Cluster Formation on Graphene Mobility*, Phys. Rev. B **81**, 115453 (2010)

[32] A. Charrier, A. Coati, T. Argunova, F. Thibaudau, Y. Garreau, R. Pinchaux, I. Forbeaux, J.-M. Debever, M. Sauvage-Simkin, J.-M. Themlin, *Solid-State Decomposition of Silicon Carbide for Growing Ultra-Thin Heteroepitaxial Graphite Films*, J. Appl. Phys. **92**, 2479 (2002)

[33] M. Hupalo, X. Liu, C.-Z. Wang, W.-C. Lu, Y.-X. Yao, K.-M. Ho, M. C. Tringides, *Metal Nanostructure Formation on Graphene: Weak versus Strong Bonding*, Adv. Mater. **23**, 2082 (2011)

[34] E. Cho, E. N. Yitamben, E. V. Iski, P. Guisinger, Nathan, T. Kuech, *Atomic-Scale Investigation of Highly Stable Pt Clusters Synthesized on a Graphene Support for Catalytic Applications*, J. Phys. Chem. C **116**, 26066 (2012)

[35] Y. Pan, M. Gao, L. Huang, F. Liu, H.-J. Gao, *Directed Self-Assembly of Monodispersed Platinum Nanoclusters on Graphene Moiré Template*, Appl. Phys. Lett. **95**, 093106 (2009)

[36] K. Donner, P. Jakob, *Structural Properties and Site Specific Interactions of Pt with the Graphene/Ru(0001) Moiré Overlayer*, J. Chem. Phys **131**, 164701 (2009)

[37] Z. Zhou, F. Gao, D. W. Goodman, *Deposition of Metal Clusters on Single-Layer Graphene/Ru(0001): Factors that Govern Cluster Growth*, Surf. Sci. **604**, L31 (2010)

[38] E. Sutter, P. Albrecht, B. Wang, M.-L. Bocquet, L. Wu, Y. Zhu, P. Sutter, *Arrays of Ru Nanoclusters with Narrow Size Distribution Templated by Monolayer Graphene on Ru*, Surf. Sci. **605**, 1676 (2011)

[39] A. K. Engstfeld, H. E. Hoster, R. J. Behm, L. D. Roelofs, X. Liu, C.-Z. Wang, Y. Han, J. W. Evans, *Directed Assembly of Ru Nanoclusters on Ru(0001)-Supported Graphene: STM Studies and Atomistic Modeling*, Phys. Rev. B **86**, 085442 (2012)

[40] A. K. Engstfeld, S. Beckord, C. D. Lorenz, R. J. Behm, *Growth of PtRu Clusters on Ru (0001)-Supported Monolayer Graphene Films*, ChemPhysChem **13**, 33133319 (2012)

[41] Q. Liao, H. Zhang, K. Wu, H. Li, S. Bao, P. He, *Nucleation and Growth of Monodispersed Cobalt Nanoclusters on Graphene Moiré on Ru (0001)*, Nanotechnology **22**, 125303 (2011)

[42] H. Zhang, Q. Fu, Y. Cui, D. Tan, X. Bao, *Fabrication of Metal Nanoclusters on Graphene Grown on Ru(0001)*, Chin. Sci. Bull. **54**, 2446 (2009)

[43] M. Sicot, S. Bouvron, O. Zander, U. Ruediger, Y. S. Dedkov, M. Fonin, *Nucleation and Growth of Nickel Nanoclusters on Graphene Moiré on Rh(111)*, Appl. Phys. Lett. **96**, 093115 (2010)

[44] A. T. N'Diaye, S. Bleikamp, P. J. Feibelman, T. Michely, *Two-Dimensional Ir Cluster Lattice on a Graphene Moiré on Ir(111)*, Phys. Rev. Lett. **97**, 215501 (2006)

[45] C. Vo-Van, S. Schumacher, J. Coraux, V. Sessi, O. Fruchart, N. B. Brookes, P. Ohresser, T. Michely, *Magnetism of Cobalt Nanoclusters on Graphene on Iridium*, Appl. Phys. Lett. **99**, 142504 (2011)

[46] A. Cavallin, M. Pozzo, C. Africh, A. Baraldi, E. Vesselli, C. Dri, G. Comelli, R. Larciprete, P. Lacovig, S. Lizzit, D. Alfè, *Local Electronic Structure and Density of Edge and Facet Atoms at Rh Nanoclusters Self-Assembled on a Graphene Template*, ACS Nano **6**, 3034 (2012)

[47] C. T. Campbell, S. C. Parker, D. E. Starr, *The Effect of Size-Dependent Nanoparticle Energetics on Catalyst Sintering*, Science **298**, 811 (2002)

[48] C. H. Bartholomew, *Mechanisms of Catalyst Deactivation*, Appl. Catal. A **212**, 17 (2001)

[49] J. Sehested, J. A. Gelten, I. N. Remediakis, H. Bengaard, J. K. Nørskov, *Sintering of Nickel Steam-Reforming Catalysts: Effects of Temperature and Steam and Hydrogen Pressures*, J. Catal. **223**, 432 (2004)

[50] A. Berkó, J. Szöko, F. Solymosi, *Effect of CO on the Morphology of Pt Nanoparticles Supported on TiO$_2$(110)-(1 x n)*, Surf. Sci. **566**, 337 (2004)

[51] J. Raskó, *CO-Induced Surface Structural Changes of Pt on Oxide-Supported Pt Catalysts Studied by DRIFTS*, J. Catal. **217**, 478 (2003)

[52] A. Berkó, F. Solymosi, *CO-Induced Changes of Ir Nanoparticles Supported on TiO₂ (110)-(1 x 2) Surface*, Surf. Sci. **411**, L900 (1998)

[53] A. Berkó, F. Solymosi, *Effects of Different Gases on the Morphology of Ir Nanoparticles Supported on the TiO₂ (110)-(1 x 2) Surface*, J. Phys. Chem. B **104**, 10215 (2000)

[54] F. Solymosi, E. Novak, A. Molnar, *Infrared Spectroscopic Study on Carbon Monoxide-Induced Structural Changes of Iridium on an Alumina Support*, J. Phys. Chem. **94**, 7250 (1990)

[55] A. Berkó, F. Solymosi, *Adsorption-Induced Structural Changes of Rh Supported by TiO₂ (110)-(1 x 2): An STM Study*, J. Catal. **183**, 91 (1999)

[56] P. J. Feibelman, *Formation and Diffusion of S-Decorated Cu Clusters on Cu(111)*, Phys. Rev. Lett. **85**, 606 (2000)

[57] W. L. Ling, N. C. Bartelt, K. Pohl, J. de la Figuera, R. Q. Hwang, K. F. McCarty, *Enhanced Self-Diffusion on Cu(111) by Trace Amounts of S: Chemical-Reaction-Limited Kinetics*, Phys. Rev. Lett. **93**, 166101 (2004)

[58] J. Kibsgaard, K. Morgenstern, E. Lægsgaard, J. V. Lauritsen, F. Besenbacher, *Restructuring of Cobalt Nanoparticles Induced by Formation and Diffusion of Monodisperse Metal-Sulfur Complexes*, Phys. Rev. Lett. **100**, 116104 (2008)

[59] M. Di Vece, D. Grandjean, M. J. Van Bael, C. P. Romero, X. Wang, S. Decoster, A. Vantomme, P. Lievens, *Hydrogen-Induced Ostwald Ripening at Room Temperature in a Pd Nanocluster Film*, Phys. Rev. Lett. **100**, 236105 (2008)

[60] S. B. Simonsen, I. Chorkendorff, S. Dahl, M. Skoglundh, J. Sehested, S. Helveg, *Direct Observations of Oxygen-Induced Platinum Nanoparticle Ripening Studied by In Situ TEM*, J. Am. Chem. Soc **132**, 7968 (2010)

[61] C. Riedl, C. Coletti, T. Iwasaki, A. A. Zakharov, U. Starke, *Quasi-Free-Standing Epitaxial Graphene on SiC Obtained by Hydrogen Intercalation*, Phys. Rev. Lett. **103**, 246804 (2009)

[62] J. A. Robinson, M. Hollander, M. LaBella, K. A. Trumbull, R. Cavalero, D. W. Snyder, *Epitaxial Graphene Transistors: Enhancing Performance via Hydrogen Intercalation*, Nano Lett. **11**, 3875 (2011)

[63] S. Oida, F. R. McFeely, J. B. Hannon, R. M. Tromp, M. Copel, Z. Chen, Y. Sun, D. B. Farmer, J. Yurkas, *Decoupling Graphene from SiC(0001) via Oxidation*, Phys. Rev. B **82**, 041411 (2010)

[64] P. Sutter, J. T. Sadowski, E. A. Sutter, *Chemistry under Cover: Tuning Metal-Graphene Interaction by Reactive Intercalation*, J. Am. Chem. Soc. **132**, 8175 (2010)

[65] E. Starodub, N. C. Bartelt, K. F. McCarty, *Oxidation of Graphene on Metals*, J. Phys. Chem. C **114**, 5134 (2010)

[66] H. Zhang, Q. Fu, D. T. Yi Cui, X. Bao, *Growth Mechanism of Graphene on Ru(0001) and O_2 Adsorption on the Graphene/Ru(0001) Surface*, J. Phys. Chem. C **113**, 8296 (2009)

[67] A. Varykhalov, J. Sánchez-Barriga, A. M. Shikin, C. Biswas, E. Vescovo, A. Rybkin, D. Marchenko, O. Rader, *Electronic and Magnetic Properties of Quasifreestanding Graphene on Ni*, Phys. Rev. Lett. **101**, 157601 (2008)

[68] C. Enderlein, Y. S. Kim, A. Bostwick, E. Rotenberg, K. Horn, *The Formation of an Energy Gap in Graphene on Ruthenium by Controlling the Interface*, New J. Phys. **12**, 033014 (2010)

[69] I. Gierz, T. Suzuki, R. T. Weitz, D. S. Lee, B. Krauss, C. Riedl, U. Starke, H. Höchst, J. H. Smet, C. R. Ast, K. Kern, *Electronic Decoupling of an Epitaxial Graphene Monolayer by Gold Intercalation*, Phys. Rev. B. **81**, 235408 (2010)

[70] L. Jin, Q. Fu, R. Mu, D. Tan, X. Bao, *Pb Intercalation Underneath a Graphene Layer on Ru(0001) and its Effect on Graphene Oxidation*, Phys. Chem. Chem. Phys. **13**, 16655 (201!)

[71] M. Gyamfi, T. Eelbo, M. Waśniowska, R. Wiesendanger, *Impact of Intercalated Cobalt on the Electronic Properties of Graphene on Pt(111)*, Phys. Rev. B **85**, 205434 (2012)

[72] E. N. Voloshina, A. Generalov, M. Weser, S. Böttcher, K. Horn, Y. S. Dedkov, *Structural and Electronic Properties of the Graphene/Al/Ni(111) Intercalation System*, New J. Phys. **13**, 113028 (2011)

[73] N. Rougemaille, A. T. N'Diaye, J. Coraux, C. Vo-Van, O. Fruchart, A. K. Schmid, *Perpendicular Magnetic Anisotropy of Cobalt Films Intercalated under Graphene*, Appl. Phys. Lett. **101**, 142403 (2012)

[74] J. Mao, L. Huang, Y. Pan, M. Gao, J. He, H. Zhou, H. Guo, Y. Tian, Q. Zou, L. Zhang, H. Zhang, Y. Wang, S. Du, X. Zhou, A. H. C. Neto, H.-J. Gao, *Silicon Layer Intercalation of Centimeter-Scale, Epitaxially Grown Monolayer Graphene on Ru(0001)*, Appl. Phys. Lett. **100**, 093101 (2012)

[75] L. Meng, R. Wu, H. Zhou, G. Li, Y. Zhang, L. Li, Y. Wang, H.-J. Gao, *Silicon Intercalation at the Interface of Graphene and Ir(111)*, Appl. Phys. Lett. **100**, 083101 (2012)

[76] K. V. Emtsev, A. A. Zakharov, C. Coletti, S. Forti, U. Starke, *Ambipolar Doping in Quasifree Epitaxial Graphene on SiC(0001) Controlled by Ge Intercalation*, Phys. Rev. B. **84**, 125423 (2011)

[77] S. Lizzit, R. Larciprete, P. Lacovig, M. Dalmiglio, F. Orlando, A. Baraldi, L. Gammelgaard, L. Barreto, M. Bianchi, E. Perkins, P. Hofmann, *Transfer-Free Electrical Insulation of Epitaxial Graphene from its Metal Substrate*, Nano Lett. **12**, 4503 (2012)

[78] N. A. Vinogradov, K. A. Simonov, A. V. Generalov, A. S. Vinogradov, D. V. Vyalikh, C. Laubschat, N. Mårtensson, A. B. Preobrajenski, *Controllable p-Doping of Graphene on Ir(111) by Chlorination with $FeCl_3$*, J. Phys.: Condens. Matter **24**, 314202 (2012)

[79] P. J. Feibelman, *Pinning of Graphene to Ir(111) by Flat Ir Dots*, Phys. Rev. B **77**, 165419 (2008)

[80] P. J. Feibelman, *Onset of Three-Dimensional Ir Islands on a Graphene/Ir(111) Template*, Phys. Rev. B **80**, 085412 (2009)

[81] J. Coraux, A. T. N'Diaye, M. Engler, C. Busse, D. Wall, N. Buckanie, F.-J. Meyer zu Heringdorf, R. van Gastel, B. Poelsema, T. Michely, *Growth of Graphene on Ir(111)*, New J. Phys. **11**, 023006 (2009)

[82] S. Lizzit, A. Baraldi, *High-Resolution Fast X-ray Photoelectron Spectroscopy Study of Ethylene Interaction with Ir(111): From Chemisorption to Dissociation and Graphene Formation*, Catal. Today **154**, 68 (2010)

[83] H. Hattab, A. T. NDiaye, D. Wall, G. Jnawali, J. Coraux, C. Busse, R. van Gastel, B. Poelsema, T. Michely, F.-J. Meyer zu Heringdorf, M. Horn-von Hoegen, *Growth Temperature Dependent Graphene Alignment on Ir(111)*, Appl. Phys. Lett. **98**, 141903 (2011)

[84] J. Knudsen, P. J. Feibelman, T. Gerber, E. Grånäs, K. Schulte, P. Stratmann, J. N. Andersen, T. Michely, *Clusters Binding to the Graphene Moiré on Ir(111): X-ray Photoemission Compared to Density Functional Calculations*, Phys. Rev. B **85**, 035407 (2012)

[85] C. Busse, P. Lazić, R. Djemour, J. Coraux, T. Gerber, N. Atodiresei, V. Caciuc, R. Brako, A. T. N'Diaye, S. Blügel, J. Zegenhagen, T. Michely, *Graphene on Ir(111): Physisorption with Chemical Modulation*, Phys. Rev. Lett. **107**, 036101 (2011)

[86] A. T. N'Diaye, J. Coraux, T. N. Plasa, C. Busse, T. Michely, *Structure of Epitaxial Graphene on Ir(111)*, New. J. Phys. **10**, 043033 (2008)

[87] A. B. Preobrajenski, M. L. Ng, A. S. Vinogradov, N. Mårtensson, *Controlling Graphene Corrugation on Lattice-Mismatched Substrates*, Phys. Rev. B **78**, 073401 (2008)

[88] B. Wang, M. Caffio, C. Bromley, H. Früchtl, R. Schaub, *Coupling Epitaxy, Chemical Bonding, and Work Function at the Local Scale in Transition Metal-Supported Graphene*, ACS Nano **4**, 5773 (2010)

[89] B. Wang, M.-L. Bocquet, S. Marchini, S. Günther, J. Wintterlin, *Chemical Origin of a Graphene Moiré Overlayer on Ru(0001)*, Phys. Chem. Chem. Phys. **10**, 3530 (2008)

[90] P. Lacovig, M. Pozzo, D. Alfè, P. Vilmercati, A. Baraldi, S. Lizzit, *Growth of Dome-Shaped Carbon Nanoislands on Ir(111): The Intermediate between Carbidic Clusters and Quasi-Free-Standing Graphene*, Phys. Rev. Lett. **103**, 166101 (2009)

[91] Y. Li, D. Subramaniam, N. Atodiresei, P. Lazic, V. Caciuc, C. Pauly, A. Georgi, C. Busse, M. Liebmann, S. Blügel, M. Pratzer, M. Morgenstern, R. Mazzarello, *Absence of Edge States in Covalently Bonded Zigzag Edges of Graphene on Ir(111)*, accepted by Adv. Mater. (2013)

[92] R. Balog, B. Jørgensen, L. Nilsson, M. Andersen, E. Rienks, M. Bianchi, M. Fanetti, E. Lægsgaard, A. Baraldi, S. Lizzit, Z. Sljivancanin, F. Besenbacher, B. Hammer, T. Pedersen, P. Hofmann, L. Hornekær, *Bandgap Opening in Graphene Induced by Patterned Hydrogen Adsorption*, Nature Mater. **9**, 315 (2010)

[93] M. L. Ng, R. Balog, L. Hornekær, A. B. Preobrajenski, N. A. Vinogradov, N. Mårtensson, K. Schulte, *Controlling Hydrogenation of Graphene on Transition Metals*, J. Phys. Chem. C **114**, 18559 (2010)

[94] E. A. Juarez-Arellano, B. Winkler, A. Friedrich, D. J. Wilson, M. Koch-Müller, K. Knorr, S. C. Vogel, J. J. Wall, H. Reiche, W. Crichton, M. Ortega-Aviles, M. Avalos-Borja, *Reaction of Rhenium and Carbon at High Pressures and Temperatures*, Z. Kristallogr. **223**, 492 (2008)

[95] J. A. M. Simoes, J. L. Beauchamp, *Transition Metal-Hydrogen and Metal-Carbon Bond Strengths: The Keys to Catalysis*, Chem. Rev. **90**, 629 (1990)

[96] C. Puzzarini, K. A. Peterson, *Multiple Bonds to Gold: A Theoretical Investigation of XAuC (X = F, Cl, Br, I) Molecules*, Chem. Phys. **311**, 177 (2005)

[97] D. Tzeli, A. Mavridis, *Theoretical Investigation of Iron Carbide, FeC*, J. Chem. Phys. **116**, 4901 (2002)

[98] K.-C. Lau, Y. C. Chang, X. Shi, C. Y. Ng, *High-Level Ab-Initio Predictions for the Ionization Energy, Bond Dissociation Energies, and Heats of Formation of Nickel Carbide (NiC) and its Cation (NiC$^+$)*, J. Chem. Phys. **133**, 114304 (2010)

[99] A. H. Castro Neto, N. M. R. Peres, K. S. Novoselov, A. K. Geim, *The Electronic Properties of Graphene*, Rev. Mod. Phys. **81**, 109 (2009)

[100] A. Grüneis, D. V. Vyalikh, *Tunable Hybridization Between Electronic States of Graphene and a Metal Surface*, Phys. Rev. B **77**, 193401 (2008)

[101] P. Sutter, M. S. Hybertsen, J. T. Sadowski, E. Sutter, *Electronic Structure of Few-Layer Epitaxial Graphene on Ru(0001)*, Nano Lett. **9**, 2654 (2009)

[102] P. Sutter, J. T. Sadowski, E. Sutter, *Graphene on Pt(111): Growth and Substrate Interaction*, Phys. Rev. B **80**, 245411 (2009)

[103] I. Pletikosić, M. Kralj, P. Pervan, R. Brako, J. Coraux, A. T. N'Diaye, C. Busse, T. Michely, *Dirac Cones and Minigaps for Graphene on Ir(111)*, Phys. Rev. Lett. **102**, 056808 (2009)

[104] S. Rusponi, M. Papagno, P. Moras, S. Vlaic, M. Etzkorn, P. M. Sheverdyaeva, D. Pacilé, H. Brune, C. Carbone, *Highly Anisotropic Dirac Cones in Epitaxial Graphene Modulated by an Island Superlattice*, Phys. Rev. Lett. **105**, 246803 (2010)

[105] M. Dresselhaus, G. Dresselhaus, *Intercalation Compounds of Graphite*, Adv. Phys. **30**, 139 (1981)

[106] S. A. Solin, *The Nature and Structural Properties of Graphite Intercalation Compounds*, Adv. Chem. Phys. **49**, 455 (1982)

[107] Y. S. Dedkov, M. Fonin, U. Rüdiger, C. Laubschat, *Rashba Effect in the Graphene/Ni(111) System*, Phys. Rev. Lett. **100**, 107602 (2008)

[108] J. Rusz, A. B. Preobrajenski, M. L. Ng, N. A. Vinogradov, N. Mårtensson, O. Wessely, B. Sanyal, O. Eriksson, *Dynamical Effects in X-ray Absorption Spectra of Graphene and Monolayered h-BN on Ni(111)*, Phys. Rev. B **81**, 073402 (2010)

[109] A. T. NDiaye, *Epitaxial Graphene and Cluster Lattices on Iridium(111)*, Ph.D. thesis, RWTH Aachen (2010)

[110] P. Feulner, D. Menzel, *Simple Ways to Improve Flash Desorption Measurements from Single Crystal Surfaces*, J. Vac. Sci. Technol. **17**, 662 (1980)

[111] C. Busse, *Nucleation and Stacking-Faults on the Iridium(111) Surface*, Ph.D. thesis, RWTH Aachen (2003)

[112] F. Reinert, S. Hüfner, *Photoemission Spectroscopy - From Early Days to Recent Applications*, New J. Phys. **7**, 97 (2005)

[113] W. F. Egelhoff, *Core-Level Binding-Energy Shifts at Surfaces and in Solids*, Surf. Sci. Rep. **6**, 253 (1987)

[114] A. Damascelli, *Probing the Electronic Structure of Complex Systems by ARPES*, Phys. Scr. **2004**, 61 (2004)

[115] M. P. Seah, W. A. Dench, *Quantitative Electron Spectroscopy of Surfaces: A Standard Data Base for Electron Inelastic Mean Free Paths in Solids*, Surf. Interface Anal. **1**, 2 (1979)

[116] *https://www.maxlab.lu.se*

[117] *http://www.wikipedia.org*

[118] M. Kralj, I. Pletikosić, M. Petrović, P. Pervan, M. Milun, A. T. N'Diaye, C. Busse, T. Michely, J. Fujii, I. Vobornik, *Graphene on Ir(111) Characterized by Angle-Resolved Photoemission*, Phys. Rev. B **84**, 075427 (2011)

[119] I. Horcas, R. Fernández, J. M. Gómez-Rodríguez, J. Colchero, J. Gómez-Herrero, A. M. Baro, *WSXM: A Software for Scanning Probe Microscopy and a Tool for Nanotechnology*, Rev. Sci. Instrum. **78**, 013705 (2007)

[120] S. Doniach, M. Sunjic, *Many-Electron Singularity in X-ray Photoemission and X-ray Line Spectra from Metals*, J. Phys. C **3**, 285 (1970)

[121] G. Kresse, J. Furthmüller, *Efficiency of Ab-Initio Total Energy Calculations for Metals and Semiconductors Using a Plane-Wave Basis Set*, Comput. Mater. Sci. **6**, 15 (1996)

[122] G. Kresse, J. Furthmüller, *Efficient Iterative Schemes for Ab-Initio Total-Energy Calculations Using a Plane-Wave Basis Set*, Phys. Rev. B **54**, 11169 (1996)

[123] D. M. Ceperley, B. J. Alder, *Ground State of the Electron Gas by a Stochastic Method*, Phys. Rev. Lett. **45**, 566 (1980)

[124] J. P. Perdew, A. Zunger, *Self-Interaction Correction to Density-Functional Approximations for Many-Electron Systems*, Phys. Rev. B **23**, 5048 (1981)

[125] P. E. Blöchl, *Projector Augmented-Wave Method*, Phys. Rev. B **50**, 17953 (1994)

[126] G. Kresse, D. Joubert, *From Ultrasoft Pseudopotentials to the Projector Augmented-Wave Method*, Phys. Rev. B **59**, 1758 (1999)

[127] M. Methfessel, A. T. Paxton, *High-Precision Sampling for Brillouin-Zone Integration in Metals*, Phys. Rev. B **40**, 3616 (1989)

[128] J. Neugebauer, M. Scheffler, *Adsorbate-Substrate and Adsorbate-Adsorbate Interactions of Na and K Adlayers on Al(111)*, Phys. Rev. B **46**, 16067 (1992)

[129] E. Miniussi, M. Pozzo, A. Baraldi, E. Vesselli, R. R. Zhan, G. Comelli, T. O. Menteş, M. A. Niño, A. Locatelli, S. Lizzit, D. Alfè, *Thermal Stability of Corrugated Epitaxial Graphene Grown on Re(0001)*, Phys. Rev. Lett. **106**, 216101 (2011)

[130] E. Starodub, A. Bostwick, L. Moreschini, S. Nie, F. E. Gabaly, K. F. McCarty, E. Rotenberg, *In-Plane Orientation Effects on the Electronic Structure, Stability, and Raman Scattering of Monolayer Graphene on Ir(111)*, Phys. Rev. B **83**, 125428 (2011)

[131] T. Balasubramanian, J. N. Andersen, L. Walldén, *Surface-Bulk Core-Level Splitting in Graphite*, Phys. Rev. B **64**, 205420 (2001)

[132] S. Lizzit, G. Zampieri, L. Petaccia, R. Larciprete, P. Lacovig, E. D. L. Rienks, G. Bihlmayer, A. Baraldi, P. Hofmann, *Band Dispersion in the Deep 1s Core Level of Graphene*, Nature Phys. **6**, 345 (2010)

[133] M. Bianchi, D. Cassese, A. Cavallin, R. Comin, F. Orlando, L. Postregna, E. Golfetto, S. Lizzit, A. Baraldi, *Surface Core Level Shifts of Clean and Oxygen Covered Ir(111)*, New J. Phys. **11**, 063002 (2009)

[134] O. Björneholm, A. Nilsson, H. Tillborg, P. Bennich, A. Sandell, B. Hernnäs, C. Puglia, N. Mårtensson, *Overlayer Structure from Adsorbate and Substrate Core Level Binding Energy Shifts: CO, CCH_3 and O on Pt(111)*, Surf. Sci. **315**, L983 (1994)

[135] The error bars are statistical errors depending on the size of the considered ensemble (~ 600 moiré cells) and on n [195]. An exception is the 0.05 ML Pt experiment: is was repeated several times and values for n ranging from 0.53 to 0.82 were found. Therefore the larger error bar. If the bar is not visible it is smaller than the symbol.

[136] C. Kittel, *Einführung in die Festkörperphysik - 14. Auflage*, Oldenbourg, München (2006)

[137] D. Franz, S. Runte, C. Busse, S. Schumacher, T. Gerber, T. Michely, M. Mantilla, V. Kilic, J. Zegenhagen, A. Stierle, *Atomic Structure and Crystalline Order of Graphene-Supported Ir Nanoparticle Lattices*, Phys. Rev. Lett. **110**, 065503 (2013)

[138] T. Gerber, J. Knudsen, P. J. Feibelman, E. Grånäs, P. Stratmann, K. Schulte, J. N. Andersen, T. Michely, *CO-Induced Smoluchowski Ripening of Pt Cluster Arrays on the Graphene/Ir(111) Moiré*, ACS Nano **7**, 2020 (2013)

[139] P. J. Feibelman, *Rebonding Effects in Separation and Surface-Diffusion Barrier Energies of an Adatom Pair*, Phys. Rev. Lett. **58**, 2766 (1987)

[140] R. Stumpf, *H-Enhanced Mobility and Defect Formation at Surfaces: H on Be(0001)*, Phys. Rev. B **53**, R4253 (1996)

[141] S. Horch, H. Lorensen, S. Helveg, E. Laegsgaard, I. Stensgaard, K. Jacobsen, J. Nørskov, F. Besenbacher, *Enhancement of Surface Self-Diffusion of Platinum Atoms by Adsorbed Hydrogen*, Nature **398**, 134 (1999)

[142] *http://pubs.acs.org/doi/suppl/10.1021/nn400082w*

[143] B. Tränkenschuh, N. Fritsche, T. Fuhrmann, C. Papp, J. F. Zhu, R. Denecke, H.-P. Steinrück, *A Site-Selective In Situ Study of CO Adsorption and Desorption on Pt(355)*, J. Chem. Phys. **124**, 074712 (2006)

[144] J. G. Wang, W. X. Li, M. Borg, J. Gustafson, A. Mikkelsen, T. M. Pedersen, E. Lundgren, J. Weissenrieder, J. Klikovits, M. Schmid, B. Hammer, J. N. Andersen, *One-Dimensional PtO$_2$ at Pt Steps: Formation and Reaction with CO*, Phys. Rev. Lett. **95**, 256102 (2005)

[145] B. Tränkenschuh, C. Papp, T. Fuhrmann, R. Denecke, H.-P. Steinrück, *The Dissimilar Twins-A Comparative, Site-Selective In Situ Study of CO Adsorption and Desorption on Pt(322) and Pt(355)*, Surf. Sci. **601**, 1108 (2007)

[146] P. Gruene, A. Fielicke, G. Meijer, D. M. Rayner, *The Adsorption of CO on Group 10 (Ni, Pd, Pt) Transition-Metal Clusters*, Phys. Chem. Chem. Phys. **10**, 6144 (2008)

[147] J. Lauterbach, R. W. Boyle, M. Schick, W. J. Mitchell, B. Meng, W. H. Weinberg, *The Adsorption of CO on Ir(111) Investigated with FT-IRAS*, Surf. Sci. **350**, 32 (1996)

[148] B. Hammer, O. H. Nielsen, J. K. Nørskov, *Structure Sensitivity in Adsorption: CO Interaction with Stepped and Reconstructed Pt Surfaces*, Catal. Lett. **46**, 31 (1997)

[149] G. Blyholder, *Molecular Orbital View of Chemisorbed Carbon Monoxide*, J. Phys. Chem. **68**, 2772 (1964)

[150] A. Föhlisch, M. Nyberg, J. Hasselström, O. Karis, L. G. M. Pettersson, A. Nilsson, *How Carbon Monoxide Adsorbs in Different Sites*, Phys. Rev. Lett. **85**, 3309 (2000)

[151] A. Föhlisch, M. Nyberg, P. Bennich, L. Triguero, J. Hasselström, O. Karis, L. G. M. Pettersson, A. Nilsson, *The Bonding of CO to Metal Surfaces*, J. Chem. Phys. **112**, 1946 (2000)

[152] P. J. Feibelman, B. Hammer, J. K. Nørskov, F. Wagner, M. Scheffler, R. Stumpf, R. Watwe, J. Dumesic, *The CO/Pt(111) Puzzle*, J. Phys. Chem. B **105**, 4018 (2001)

[153] H.-J. Butt, K. Graf, M. Kappl, *Physics and Chemistry of Interfaces*, Wiley-VCH, Weinheim (2003), chap. 7, p. 118 ff.

[154] F. Tao, S. Dag, L.-W. Wang, Z. Liu, D. R. Butcher, H. Bluhm, M. Salmeron, G. A. Somorjai, *Break-Up of Stepped Platinum Catalyst Surfaces by High CO Coverage*, Science **327**, 850 (2010)

[155] T. Michely, J. Krug, *Islands, Mounds and Atoms: Patterns and Processes in Chrystal Growth Far from Equilibrium*, Springer-Verlag, Berlin (2004)

[156] J. Lee, J. P. Cowin, L. Wharton, *He Diffraction from Clean Pt(111) and (1 x 1)H/Pt(111) Surface*, Surf. Sci. **130**, 1 (1983)

[157] H. Steininger, S. Lehwald, H. Ibach, *Adsorption of Oxygen on Pt(111)*, Surf. Sci. **123**, 1 (1982)

[158] Y. Y. Yeo, L. Vattuone, D. A. King, *Calorimetric Heats for CO and Oxygen Adsorption and for the Catalytic CO Oxidation Reaction on Pt(111)*, J. Chem. Phys. **106**, 392 (1997)

[159] N. A. Vinogradov, K. Schulte, M. L. Ng, A. Mikkelsen, E. Lundgren, N. Mårtensson, A. B. Preobrajenski, *Impact of Atomic Oxygen on the Structure of Graphene Formed on Ir(111) and Pt(111)*, J. Phys. Chem. C **115**, 9568 (2011)

[160] R. Larciprete, S. Fabris, T. Sun, P. Lacovig, A. Baraldi, S. Lizzit, *Dual Path Mechanism in the Thermal Reduction of Graphene Oxide*, J. Am. Chem. Soc. **133**, 17315 (2011)

[161] C. J. Weststrate, A. Resta, R. Westerstrom, E. Lundgren, A. Mikkelsen, J. N. Andersen, *CO Adsorption on a Au/CeO$_2$ (111) Model Catalyst*, J. Phys. Chem. C **112**, 6900 (2008)

[162] G. Ertl, M. Neumann, K. Streit, *Chemisorption of CO on the Pt(111) Surface*, Surf. Sci. **64**, 393 (1977)

[163] B. Hammer, J. K. Nørskov, *Why Gold is the Noblest of All the Metals*, Nature **376**, 238 (2005)

[164] B. Hammer, Y. Morikawa, J. K. Nørskov, *CO Chemisorption at Metal Surfaces and Overlayers*, Phys. Rev. Lett. **76**, 2141 (1996)

[165] N. Lopez, T. Janssens, B. Clausen, Y. Xu, M. Mavrikakis, T. Bligaard, J. Nørskov, *On the Origin of the Catalytic Activity of Gold Nanoparticles for Low-Temperature CO Oxidation*, J. Catal. **223**, 232 (2004)

[166] E. Grånäs, J. Knudsen, U. A. Schröder, T. Gerber, C. Busse, M. A. Arman, K. Schulte, J. N. Andersen, T. Michely, *Oxygen Intercalation under Graphene on Ir(111): Energetics, Kinetics, and the Role of Graphene Edges*, ACS Nano **6**, 9951 (2012)

[167] Y. B. He, A. Stierle, W. X. Li, A. Farkas, N. Kasper, H. Over, *Oxidation of Ir(111): From O-Ir-O Trilayer to Bulk Oxide Formation*, J. Phys. Chem. C **112**, 11946 (2008)

[168] D. Hagen, B. Nieuwenhuys, G. Rovida, G. Somorjai, *Low-Energy Electron Diffraction, Auger Electron Spectroscopy, and Thermal Desorption Studies of Chemisorbed CO and O_2 on the (111) and Stepped [6(111)x(l00)] Iridium Surfaces*, Surf. Sci. **57**, 632 (1976)

[169] *http://pubs.acs.org/doi/suppl/10.1021/nn303548z*

[170] S. D. Miller, N. Inoglu, J. R. Kitchin, *Configurational Correlations in the Coverage Dependent Adsorption Energies of Oxygen Atoms on Late Transition Metal fcc(111) Surfaces*, J. Chem. Phys. **134**, 104709 (2011)

[171] E. Grånäs et al., to be published

[172] R. Larciprete, S. Ulstrup, P. Lacovig, M. Dalmiglio, M. Bianchi, F. Mazzola, L. Hornekær, F. Orlando, A. Baraldi, P. Hofmann, S. Lizzit, *Oxygen Switching of the Epitaxial Graphene-Metal Interaction*, ACS Nano **6**, 9551 (2012)

[173] C. J. Hagedorn, M. J. Weiss, W. H. Weinberg, *Dissociative Chemisorption of Hydrogen on Ir(111): Evidence for Terminal Site Adsorption*, Phys. Rev. B **60**, R14016 (1999)

[174] T. Gerber, M. Petrović, E. Grånäs, S. Schumacher, S. Runte, F. Craes, D. F. Förster, U. A. Schröder, J. Coraux, C. Vo-Van, J. Zegenhagen, P. Pervan, J. N. Andersen, C. Busse, M. Kralj, J. Knudsen, T. Michely, *Understanding Core Level Shifts of Graphene*, submitted to New J. Phys. (2013)

[175] G. Giovannetti, P. A. Khomyakov, G. Brocks, V. M. Karpan, J. van den Brink, P. J. Kelly, *Doping Graphene with Metal Contacts*, Phys. Rev. Lett. **101**, 026803 (2008)

[176] G. Imamura, K. Saiki, *Synthesis of Nitrogen-Doped Graphene on Pt(111) by Chemical Vapor Deposition*, J. Phys. Chem. C **115**, 10000 (2011)

[177] R. J. Koch, M. Weser, W. Zhao, F. Vines, K. Gotterbarm, S. M. Kozlov, O. Höfert, M. Ostler, C. Papp, J. Gebhardt, H.-P. Steinrück, A. Görling,

T. Seyller, *Growth and Electronic Structure of Nitrogen-Doped Graphene on Ni(111)*, Phys. Rev. B **86**, 075401 (2012)

[178] D. Z. Hongtao Liu, Yunqi Liu, *Chemical Doping of Graphene*, J. Mater. Chem. **21**, 3335 (2011)

[179] B. Guo, L. Fang, B. Zhang, J. R. Gong, *Graphene Doping: A Review*, Insciences J. **1**, 80 (2011)

[180] X. Miao, S. Tongay, M. K. Petterson, K. Berke, A. G. Rinzler, B. R. Appleton, A. F. Hebard, *High Efficiency Graphene Solar Cells by Chemical Doping*, Nano Lett. **12**, 2745 (2012)

[181] A. Varykhalov, M. Scholz, T. Kim, O. Rader, *Effect of Noble-Metal Contacts on Doping and Band Gap of Graphene*, Phys. Rev. B **82**, 121101(R) (2010)

[182] P. A. Khomyakov, G. Giovannetti, P. C. Rusu, G. Brocks, J. van den Brink, P. J. Kelly, *First-Principles Study of the Interaction and Charge Transfer between Graphene and Metals*, Phys. Rev. B **79**, 195425 (2009)

[183] D. F. Förster, *EuO and Eu on Metal Crystals and Graphene: Interface Effects and Epitaxial Films*, Ph.D. thesis, Universität zu Köln (2011)

[184] S. Hüfner, *Photoelectron Spectroscopy : Principles and Application*, Springer-Verlag, Berlin, 3 edition (1995)

[185] L. Van Hove, *The Occurrence of Singularities in the Elastic Frequency Distribution of a Crystal*, Phys. Rev. **89**, 1189 (1953)

[186] D. F. Förster, T. O. Wehling, S. Schumacher, A. Rosch, T. Michely, *Phase Coexistence of Clusters and Islands: Europium on Graphene*, New. J. Phys. **14**, 023022 (2012)

[187] I. Fampiou, A. Ramasubramaniam, *Binding of Pt Nanoclusters to Point Defects in Graphene: Adsorption, Morphology, and Electronic Structure*, J. Phys. Chem. C **116**, 6543 (2012)

[188] D.-H. Lim, J. Wilcox, *DFT-Based Study on Oxygen Adsorption on Defective Graphene-Supported Pt Nanoparticles*, J. Phys. Chem. C **115**, 22742 (2011)

[189] D. H. Chi, N. T. Cuong, N. A. Tuan, Y.-T. Kim, H. T. Bao, T. Mitani, T. Ozaki, H. Nagao, *Electronic Structures of Pt Clusters Adsorbed on (5,5) Single Wall Carbon Nanotube*, Chem. Phys. Lett. **432**, 213 (2006)

[190] E. Roduner, *Electronic structure*, in *Nanoscopic Materials*, The Royal Society of Chemistry, London (2006)

[191] H. L. Skriver, N. M. Rosengaard, *Surface Energy and Work Function of Elemental Metals*, Phys. Rev. B **46**, 7157 (1992)

[192] H. B. Michaelson, *The Work Function of the Elements and its Periodicity*, J. Appl. Phys. **48**, 4729 (1977)

[193] J. Schnadt, J. Knudsen, J. N. Andersen, H. Siegbahn, A. Pietzsch, F. Hennies, N. Johansson, N. Mårtensson, G. Öhrwall, S. Bahr, S. Mähl, O. Schaff, *The New Ambient-Pressure X-ray Photoelectron Spectroscopy Instrument at MAX-lab*, J. Synchrotron Rad. **19**, 701 (2012)

[194] P. B. Rasmussen, B. L. M. Hendriksen, H. Zeijlemaker, H. G. Ficke, J. W. M. Frenken, *The 'Reactor STM': A Scanning Tunneling Microscope for Investigation of Catalytic Surfaces at Semi-Industrial Reaction Conditions*, Rev. Sci. Instrum. **69**, 3879 (1998)

[195] T. Gerber, *Geordnete Metallcluster auf dem Graphen/Iridium(111)-Moirémuster*, Diplomarbeit, Universität zu Köln (2009)

Appendix

In this Appendix, some additional results will be briefly described. Due to a lack of time, these topics were not further pursued.
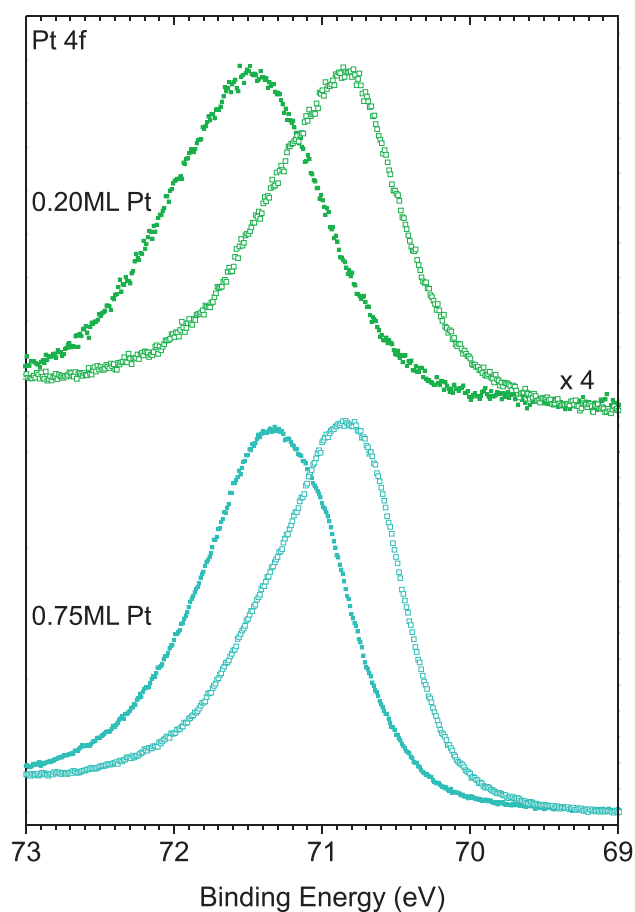
Pt 4f Spectra after CO Exposure

Figure A.1 Pt 4f before (open symbols, reproduction of the data shown in Figure 5.7) and after (full symbols) 10 L CO exposure for 0.20ML Pt (top, multiplied by a factor of 2) and 0.75ML Pt (bottom).

Figure A.1 shows Pt 4f spectra of 0.20 ML and 0.75 ML Pt clusters, before and after CO exposure, respectively. The spectra of the clean particles are already hard to deconvolute due to several components (compare Chapter 4). After CO exposure, the peaks are shifted to higher binding energies by 0.5 - 0.6 eV. The shifts are similar for all Pt coverages that were studied. However, this shift is much smaller than the shift of 1.4 eV reported by Björneholm et. al. [134] for CO adsorbed atop on the Pt(111) surface.

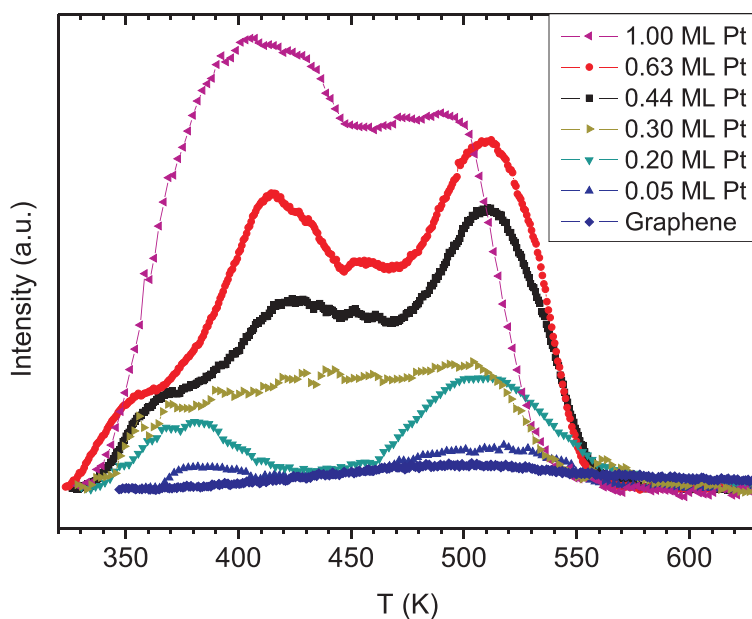# Thermal Desorption Spectroscopy of CO from Pt Clusters

Figure A.2 TDS of CO from Pt clusters of the indicated coverages. Clusters were saturated by dosing 12 L to 100 L CO at room temperature. Heating rate 5 K/s.

Figure A.2 shows thermal desorption spectroscopy (TDS) data of CO desorption from Pt clusters. We observe three desorption features at roughly 375 K, 420 K and 510 K, respectively. As the cluster lattice is probably destroyed after being exposed to CO, together with additional heating to over 550 K, this data was not further evaluated.
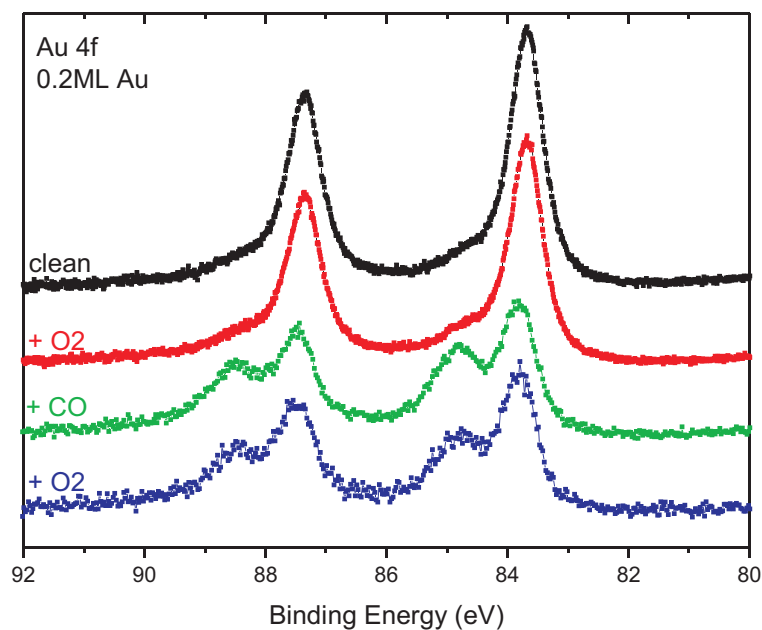
Absence of CO Oxidation on Au Clusters

Figure A.3 Au 4f spectra of 0.2 ML Au clusters after deposition (black, top) after dosing $10\,\text{L}$ O_2 (red), after dosing $10\,\text{L}$ CO (green), after additional dosing of $45\,\text{L}$ O_2 (blue, bottom). All exposures done at T $= 120\,\text{K}$ with $p_{\text{CO},O_2} \leq 1 \times 10^{-7}\,\text{mbar}$.

Small Au clusters on oxide surfaces are known to catalyze the oxidation of CO. We tested this reaction on Au clusters on graphene/Ir(111). Figure A.3 shows a series of Au 4f spectra. The spectrum does not change when the clean particles are exposed to O_2. Thus, O_2 adsorption is absent. The spectrum does change after exposure to CO. A new component at higher binding energies develops and the original peaks shifts a bit to higher binding energies (compare Section 6.6.2). Both features indicate CO adsorption. After additional exposure to O_2, the spectrum does not change further. We conclude that the CO is not reacted away by oxygen. Thus, Au clusters supported by graphene seem to be inactive for CO oxidation.

Growth of Rh Clusters
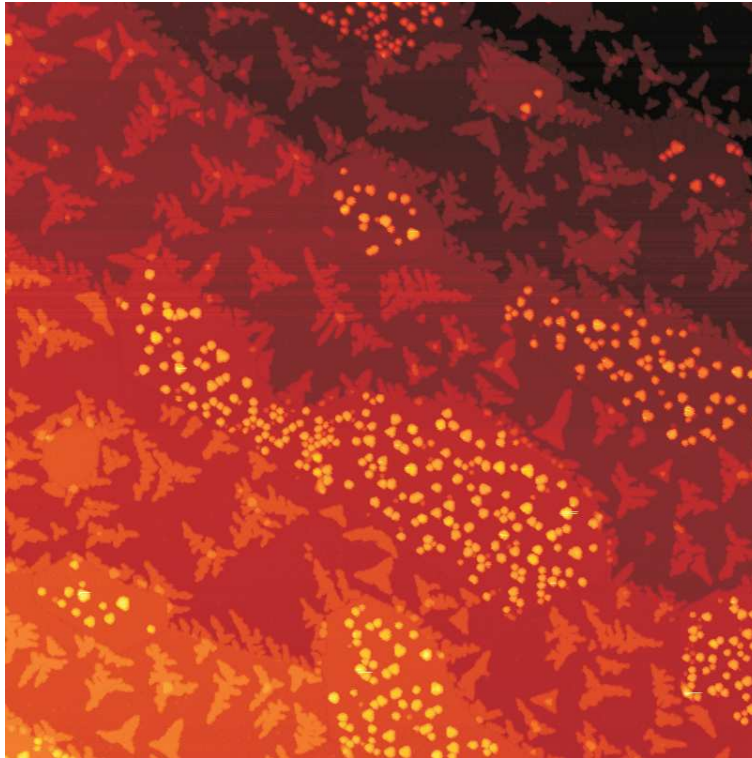
Figure A.4 0.3 ML Rh deposited at room temperature on a partially graphene-covered Ir surface. Picture size 2500 Å x 2500 Å.

In the beginning of this thesis, the growth of Rh clusters was studied, but these clusters were not further investigated. Figure A.4 shows the result of room temperature deposition of 0.3 ML Rh on a partially graphene-covered surface. Although, we observe some short range ordered clusters, long range order is absent and the filling is below 0.5.

A regular lattice can be obtained by low temperature Rh deposition (Fig. A.5). The clusters grown in this way are even stable up to 400 K.

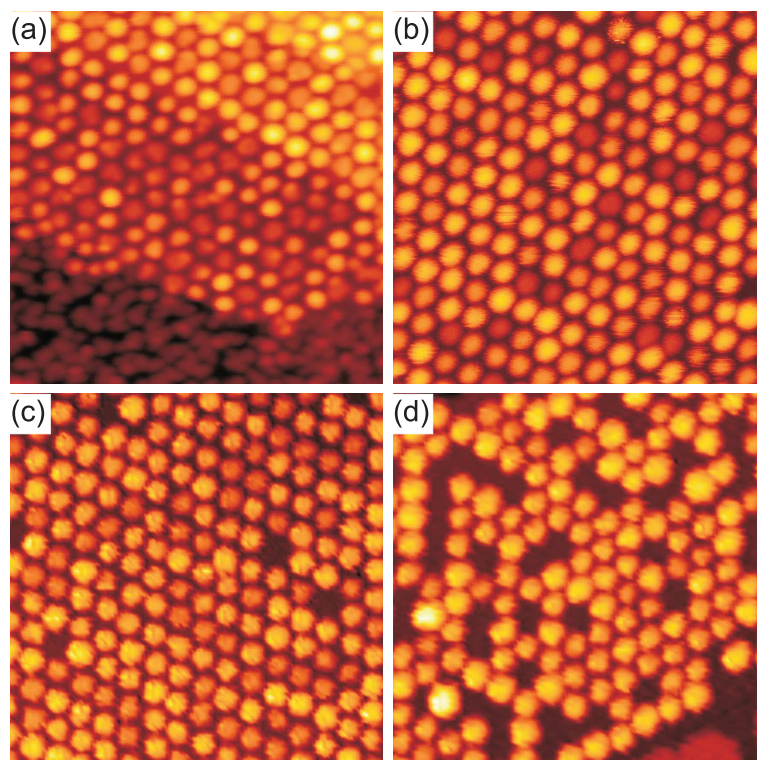**Figure A.5** Deposition of 0.33 ML Rh on partially graphene-covered Ir(111) at 90 K. (a) imaged at 90 K, (b) annealed and imaged at 300K, (c) annealed at 400K, imaged at 300K, (d) annealed at 500K, imaged at 300K. Picture size is 340 Å x 340 Å.

Publications

Parts of the results presented in this thesis can be found in the following publications:

1. J. Knudsen, P. J. Feibelman, T. Gerber, E. Grånäs, K. Schulte, P. Stratmann, J. N. Andersen, T. Michely
   Clusters Binding to the Graphene Moiré on Ir(111):
   X-ray Photoemission Compared to Density Functional Calculations
   Phys. Rev. B **85**, 035407 (2012)

2. T. Gerber, J. Knudsen, P. J. Feibelman, E. Grånäs, P. Stratmann, K. Schulte, J. N. Andersen, T. Michely
   CO-Induced Smoluchowski Ripening of
   Pt Cluster Arrays on the Graphene/Ir(111) Moiré
   ACS Nano **7**, 2020 (2013)

3. E. Grånäs, J. Knudsen, U. A. Schröder, T. Gerber, C. Busse, M. A. Arman, K. Schulte, J. N. Andersen, T. Michely
   Oxygen Intercalation under Graphene on Ir(111):
   Energetics, Kinetics, and the Role of Graphene Edges
   ACS Nano **6**, 9951 (2012)

4. T. Gerber, M. Petrovic, E. Grånäs, S. Schumacher, S. Runte, F. Craes, D. F. Förster, U. A. Schröder, J. Coraux, C. Vo-Van, J. Zegenhagen, P. Pervan, J. N. Andersen, C. Busse, M. Kralj, J. Knudsen, T. Michely
   Understanding Core Level Shifts of Graphene
   submitted to New J. Phys. (2013)

Further publications that are not part of this thesis:

5. A. T. NDiaye, T. Gerber, C. Busse, J. Myslivecek, J. Coraux, T. Michely
   A Versatile Fabrication Method for Cluster Superlattices
   New J. Phys. **11**, 103045 (2009)

6. C. Busse, P. Lazic, R. Djemour, J. Coraux, T. Gerber, N. Atodiresei,
   V. Caciuc, R. Brako, A. T. NDiaye, S. Blügel, J. Zegenhagen, T. Michely
   Graphene on Ir(111): Physisorption with Chemical Modulation
   Phys. Rev. Lett. **107**, 036101 (2011)

7. D. Franz, S. Runte, C. Busse, S. Schumacher, T. Gerber, T. Michely,
   M. Mantilla, V. Kilic, J. Zegenhagen, A. Stierle
   Atomic Structure and Crystalline Order of
   Graphene-Supported Ir Nanoparticle Lattices
   Phys. Rev. Lett. **110**, 065503 (2013)

Symbols and Abbreviations

α	asymetry parameter of the Doniach-Sunjic function
ARPES	angular resolved photoemission spectroscopy
CE	circle equivalent diameters
CLS	core level shift
CVD	chemical vapor deposition
DFT	density functional theory
DS	Doniach-Sunjic
E_F	Fermi Energy
fcc	face-centered cubic
GFWHM	Gaussian full width at half maximum
hcp	hexagonal close-packed
HOPG	highly ordered pyrolytic graphite
I	intensity
L	Langmuir i.e. 1.33×10^{-6} mbar·s
LEED	low energy electron diffraction
LEEM	low energy electron microscopy
LFWHM	Lorentzian full width at half maximum
ML	monolayer
STM	scanning tunneling microscopy
SXRD	surface X-ray diffraction
Θ	fractional surface coverage
TEM	transmission electron microscopy
TPG	temperature programmed growth
UHV	ultra high vacuum
vdW	van der Waals
XPS	X-ray photoemeission spectroscopy
XSW	X-ray standing waves

Acknowledgements - Danksagung

An dieser Stelle möchte ich mich bei all denen bedanken, die zum Gelingen dieser Arbeit beigetragen haben.

This work has greatly benefited from several people which I want to acknowledge.

- Bei Thomas Michely, für die Möglichkeit an diesem interessanten Thema, in Kooperation mit anderen Forschungseinrichtungen und Partnern, zu arbeiten. Außerdem für die vielen Diskussionen und Anregungen, und das damit verbundene Vorantreiben der Arbeit.

- Bei Andreas Stierle, für das Interesse an der Arbeit und die Übernahme des Zweitgutachtens. Außerdem für einen Einblick in die Technik der oberflächensensitiven Röntgenbeugung.

- Bei Joachim Krug, für seine Bereitschaft den Vorsitz der Prüfungskommission zu übernehmen.

- Bei Carsten Busse, für die Übernahme des Beisitzes. Außerdem für die sehr angenehme Zeit, in der wir das Büro teilten.

- Bei Ulrike Schröder und Patrick Stratmann, die im Rahmen ihrer Master- bzw. Diplomarbeit zu dieser Arbeit beigetragen haben.

- Bei allen Korrekturlesern: Sebastian, Brocks, Fabian Craes, Sebastian Standop, sowie besonders bei Ingrid Hageleit und Ulrike Schröder.

This work was in large parts done in the context of cooperations and I want to express my gratitude to all collaborators.

- *Jan Knudsen, Elin Grånäs, Karina Schulte and Jesper N. Andersen from the Division of Synchrotron Radiation Research and the MAX IV Laboratory in*

Lund, Sweden, who taught me how to acquire XPS spectra and how to analyze them. I enjoyed there hospitality during several stays in Lund, and their companion during countless shifts at Max-lab. Furthermore, Jan and Elin contributed a lot to the articles that are a part of this thesis.

- *Peter J. Feibelman who performed DFT calculations on the core level shifts related to cluster binding and on the mobility of CO decorated Pt clusters, and who contributed to the articles that are a part of this thesis.*

Besonderer Dank geht an Norbert Henn, für das Lösen vieler technischer Probleme, und für das stete Streben nach Verbesserungen der Anlage.

Des Weiteren möchte ich mich bei allen bisher ungenannten Mitgliedern der Arbeitsgruppe für die freundliche und produktive Arbeitsatmosphäre bedanken: Martin Engler, Daniel Förster, Charlotte Herbig, Felix Huttmann, Wouter Jolie, Jürgen Klinkhammer, Sven Macko, Alpha N'Diaye, Sven Runte, Stefan Schumacher.

Außerdem bei Beate Neugebauer, Carmen Handels, Dorothea Hochscheid, Andrea Helldörfer, Ralf Müller, Rolf Dommel, den Werkstätten, sowie allen weiteren Mitarbeitern des II. Physikalischen Instituts.

Zu guter Letzt, möchte ich mich herzlichst bei Familie und Freunden bedanken. Für deren Unterstützung und vor allem, dafür dass es sie gibt!

Deutsche Kurzzusammenfassung

Die Wechselwirkung von Graphen und darauf angeordneten Clustergittern, mit CO, H_2 and O_2 wurde mittels Rastertunnelmikroskopie (RTM) und Röntgenphotoelektronenspektroskopie (PES) untersucht. Die experimentellen Daten wurden durch Berechnungen mittels Dichtefunktionaltheorie (DFT) ergänzt. Als Voraussetzung für Studien der Gas-Wechselwirkung wurde der Bindungsmechanismus der Cluster an das Graphen sowie das Wachstum und die Struktur der Pt-Cluster im Detail untersucht.

Die Bildung von Clustergittern auf Graphen auf Ir(111) wurde durch Rehybridisierung des Graphens erklärt. Dieses DFT Modell wurde nun durch den Vergleich von berechneten und gemessenen Photoelektronenspektren bestätigt. Für Graphen ohne Cluster finden sowohl DFT als auch PES eine 140 meV Modulation des C 1s-Niveaus, die mit der Höhenmodulation der Graphenschicht über der Ir(111)-Oberfläche korreliert. Die gemessenen Verschiebungen des Pt 4f-Niveaus der adsorbierten Cluster untermauern die Berechnungen. Die Modulation des C 1s-Niveaus wird durch die Cluster verstärkt. Die Kohlenstoffatome unterhalb und in der Nähe der Pt-Cluster lassen sich experimentell als breite Schulter im C 1s-Spektrum nachweisen. Die sp^2 zu sp^3 Rehybridisierung des Graphens bringt die beteiligten Kohlenstoffatome näher an die Ir-Oberfläche, was auf chemische Bindung hindeutet. Die Signatur dieser Bindung konnte im Ir 4f-Spektrum identifiziert werden.

Das Wachstum von Pt-Clustern, deren Struktur und deren Wechselwirkung mit der Graphenschicht wurde als Funktion der Pt-Bedeckung untersucht. RTM-Messungen ergaben, dass das weitere Wachstum von Pt-Clustern auf zwei Dimensionen beschränkt bleibt, sobald diese zweilagig sind. Sintern von Clustern setzt ab einer Bedeckung von 0,75 ML Pt ein, so dass die Größe von in Gittern angeordneten Pt-Clustern auf 65 Atome beschränkt ist. Die Cluster-Graphen-, sowie die Graphen-Ir-Wechselwirkung, wurde mit C 1s und Ir 4f-Spektren untersucht. Die entsprechenden Komponenten, nämlich die C 1s-Schulter und die Ir-Grenzflächen-Komponente, stimmen hin-

sichtlich ihrer relativen Intensität überein. Durch Kombination dieser Ergebnisse wurde eine schematische Darstellungen der Cluster und ihrer Bindung an die Graphenschicht abgeleitet.

Die Stabilität von Pt-Clustern bei CO Begasung wurde untersucht. Cluster-Stabilität und durch Adsorption induzierte Prozesse wurden als Funktion der Cluster-Größe analysiert. Kleine Cluster mit weniger als zehn Atomen werden durch CO Adsorption instabil. Sie sintern durch Smoluchowski-Reifung – Diffusion von Clustern und deren Verschmelzung – und nicht durch die häufig beobachtete Ostwald-Reifung über Metall-Adsorbat-Komplexe. Größere Cluster bleibt nach CO-Adsorption unbeweglich, werden allerdings dreidimensional. Eine Implikation der CO-induzierten Clustermobilität ist die Empfindlichkeit des Wachstum der Pt-Cluster auf den CO Hintergrunddruck. Die Untersuchung wurde auf die Adsorption von anderen Gasen (H_2 and O_2) auf Pt-Clustern, sowie die Adsorption von CO auf anderen Metallclustern (Ir, Au) erweitert.

Sauerstoff-Interkalations-Phasen unter Graphen auf Ir(111) wurden in Abhängigkeit von Temperatur und Zeit der O_2-Begasung sowie der Flockengröße untersucht. Ein O_2-Hintergrunddruck treibt den auf unbedeckten Ir-Terrassen gebildeten atomaren Sauerstoff unter die Graphenflocken. Der Einfluss der Stufenkanten des Substrats sowie der des Ablösens von Graphenflocken-Kanten auf die Interkalation wurde untersucht. Mit Hilfe von CO-Titration zur selektiven Entfernung von Sauerstoff von den unbedeckten Ir-Terrassen wurde die Energetik der Interkalation aufgedeckt. Cluster-Dekorations-Techniken wurden als effizientes Mittel zur Visualisierung der Interkalation verwendet. Die Studie wurde auf die Interkalation von Wasserstoff ausgedehnt.

Interkalation von Graphen führt oft zur Dotierung des Graphens. Beim Vergleich von C 1s-Niveau und Bandstruktur-Messungen verschiedener Systeme wurde festgestellt, dass der Dirac-Punkt und das C 1s-Niveau die gleiche Verschiebung zeigen. Diese Verschiebungen können mit Hilfe eines 'rigid band model' beschrieben werden. Außerdem ist es möglich, die Dotierung des Graphens anhand der Verschiebung des C 1s-Niveaus abzuschätzen. Graphen auf Ir(111) wird durch H- und O-Interkalation p-dotiert, während es durch Eu-Interkalation n-dotiert wird. Das Graphen wird auch von Pt- und Ir-Clustern dotiert. Die kleinsten Cluster verursachen eine n-Dotierung des Graphens, die größte Pt-Bedeckung führt zu leichter p-Dotierung. Wenn Pt-Cluster durch CO-Begasung verschmelzen, wird die Dotierung reduziert.

Erklärung

Ich versichere, dass ich die von mir vorgelegte Dissertation selbständig angefertigt, die benutzten Quellen und Hilfsmittel vollständig angegeben und die Stellen der Arbeit - einschließlich Tabellen, Karten und Abbildungen -, die anderen Werken im Wortlaut oder dem Sinn nach entnommen sind, in jedem Einzelfall als Entlehnung kenntlich gemacht habe; dass diese Dissertation noch keiner anderen Fakultät oder Universität zur Prüfung vorgelegen hat; dass sie - abgesehen von den angegebenen Teilpublikationen - noch nicht veröffentlicht worden ist, sowie, dass ich eine solche Veröffentlichung vor Abschluss des Promotionsverfahrens nicht vornehmen werde. Die Bestimmungen der Promotionsordnung sind mir bekannt. Die von mir vorgelegte Dissertation ist von Prof. Dr. Thomas Michely betreut worden.

Köln, den 25. März 2013

Timm Gerber

Lebenslauf

Name	Gerber
Vorname	Timm
Geburtsdatum	22.02.1982
Geburtsort	Offenbach am Main
Staatsangehörigkeit	deutsch
05/2001	Abitur, Otto-Hahn-Gymnasium Bensberg, Note 2,3
08/2001 - 05/2002	Zivildienst, Integrative Kindertagesstätte Rosenhof, Bergisch Gladbach
10/2002 - 06/2009	Physik- und Mathematikstudium Universität zu Köln
04/2005	Vordiplom, Noten 1,4 (Physik) und 1,5 (Mathematik)
09/2006 - 03/2007	Erasmus-Programm Université de Versailles Saint-Quentin-en-Yvelines Frankreich
07/2009	Diplomarbeit in Physik, "Geordnete Metallcluster auf dem Graphen/Iridium(111)-Moirémuster", Note 1,3
09/2009 - 03/2013	Promotionsstudent bei Prof. Dr. Thomas Michely II. Physikalisches Institut, Universität zu Köln